THE DYNAMICS AND CONTROL OF THE CUBESAIL MISSION—A SOLAR SAILING DEMONSTRATION

BY

ANDRZEJ PUKNIEL

DISSERTATION

Submitted in partial fulfillment of the requirements
for the degree of Doctor in Philosophy in Aerospace Engineering
in the Graduate College of the
University of Illinois at Urbana-Champaign, 2010

Urbana, Illinois

Doctoral Committee:

Professor Victoria Coverstone, Chair
Professor John Prussing
Professor Rodney Burton
Professor Gary Swenson

ABSTRACT

The proposed study addresses two issues related to the slow emergence of solar sailing as a viable space propulsion method. The low technology readiness level and complications related to stowage, deployment, and support of the sail structure are both addressed by combining the CU Aerospace and University of Illinois-developed UltraSail and CubeSat expertise to design a small-scale solar sail deployment and propulsion experiment in low Earth orbit. The study analyzes multiple aspects of the problem from initial sizing and packaging of the solar sail film into two CubeSat-class spacecraft, through on-orbit deployment dynamics, attitude control of large and flexible space structure, and predictions of performance and orbital maneuvering capability.

ACKNOWLEDGEMENTS

The following work would have not been possible without the continuous support and encouragement of my advisor, Professor Coverstone. Her patience, scientific insight, and enthusiasm are a rare combination that fosters a unique research environment. It allows the students to develop both as highly competent engineers as well as young individuals. Few advisors sincerely care for their students' personal development as much as Professor Coverstone and I consider myself privileged to be part of her research group.

I would also like to thank Professors Rod Burton and Gary Swenson as well as Dr. David Carroll for excellent advice and insightful discussions. Their questions and experience often steered my research and increased my understanding of the problem at hand.

Professor Prussing has been an inspiration starting with my early undergraduate years, and is largely responsible for my interest in astrodynamics. It is a privilege to have him serve on my committee.

CubeSail team members Alex Ghosh and Julia Laystrom-Woodard were essential throughout the project and performed majority of the hardware development, modeling, and testing. I wish them the best of luck as they continue to support this and future solar sailing efforts.

Lastly, I would like to acknowledge NASA Marshall Space Flight Center and specifically Les Johnson for his continuous support of the solar sailing endeavors at the University of Illinois.

TABLE OF CONTENTS

CHAPTER 1

INTRODUCTION

1.1 History of Solar Sailing

The concept of solar sailing is nearing its century mark and although a true solar sailing mission is yet to fly, there is wealth of conceptual designs, missions, and subsystem demonstrations that have been performed throughout the years. A detailed description of every solar sailing mission is beyond the scope of this dissertation, however it is the hope of the author that a brief history combined with the overview of the current solar sailing missions will demonstrate how rich and vibrant this field of research is today.

The concept of spacecraft propelled by solar pressure dates back to 1920s and ideas of the father of Russian astronautics, Konstantin Tsiolkovsky.[1,2] Tsiolkvosky's early writing on propulsion methods that utilize light inspired his co-worker, Fridrickh Tsander, who in 1924 published the first account of practical solar sailing as means to propel spacecraft using light. In his work, Tsander wrote about "tremendous mirrors of very thin sheets, capable of…using the pressure of sunlight to attain cosmic velocities."[3]

The next three decades were marked by relative obscurity of solar sailing from public or scientific interest. It was not until 1951 that the first technical paper on solar sailing as means of propelling a spacecraft was written by Carl Wiley, under a pseudonym of Russell Sanders.[4] Wiley, an aeronautical engineer, published the article in May of 1951 in the *Astounding Science Fiction*, detailing design of a feasible solar sail and strategies for orbit raising. The article, although well received and accurate, spurred little interest in the scientific community. Interestingly, during later years when

solar sailing was no longer regarded as science fiction and Wiley no longer worried about losing his scientific credibility, he attended several of the technical presentation at Jet Propulsion Laboratory (JPL).[5]

The first publication in a technical journal in the United States appeared in 1958 in *Jet Propulsion* and was written by Richard Garwin.[6] Garwin included preliminary calculations on performance of a 'solar sailing' vehicle—a term he coined—and expounded the elegance of a continuously-accelerating, propellantless mode of space transportation.

Unlike Wiley's early publication, Garwin's article sparked wide interest in solar sailing research and led to numerous studies that were undertaken during the late 1950s and early 1960s. In 1960, the first master's thesis on solar sail design was published at Massachusetts Institute of Technology (MIT) by Philippe Villers.[7] That same year, NASA Langley Research Center organized a first meeting on the subject and a year later a short course on solar sailing was offered at University of California at Los Angeles (UCLA).[5]

Between 1965 and 1967 Richard MacNeal and John Hedgepath, building on ideas of spinning solar sails initially developed by Ted Cotter in 1958, invented the Heliogyro, shown in Figure 1. The helicopter-like design envisioned multi-kilometer long blades and used centrifugal force to deploy and to maintain the proper shape of the sail. The main goal of this system was to reduce the complexity of the stowage and deployment of a large sail from the launch vehicle. It is important to note that the Heliogyro served as a basis for the University of Illinois at Urbana-Champaign (UIUC)

design of the UltraSail—the precursor of the CubeSail mission described in this dissertation.

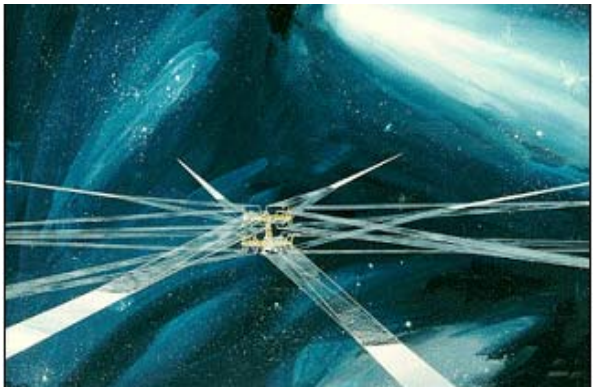

Figure 1. Artist's conception of the Heliogyro.

As the Apollo program was coming to an end in the early 1970s, the US space program was adjusting to lower levels of funding and majority of solar sailing research was halted. The only funded research during this time was done under a NASA contract performed by Jerome Wright at Battelle laboratories in Ohio. Although the study focused on launch vehicles and propulsion requirements for a variety of missions which were currently under consideration, part of Wright's analysis included solar sailing trajectory to rendezvous with the Halley comet. The results revealed solar sail flight times of only four years, allowing for a comet intercept in the mid 1980s—a drastic improvement from the seven- to eight-year mission times designed using solar electric propulsion (SEP). The favorable flight times allowed for more-reasonable development and fabrications schedule and resulted in the final go-ahead from NASA management in September of 1976 under the guidance of the Jet Propulsion Laboratory (JPL).[8]

The initial design for the Halley comet rendezvous considered an 800x800m three-axis stabilized square solar sail configuration, but was quickly dropped due to high-risk associated with deployment. The alternative configuration chosen by the

designers was a spin-stabilized Heliogyro with twelve 7.5 km blades rotating around a central hub. The blades were deployed using centrifugal force and spun continuously at high rates to keep the blades relatively flat. In September of 1977 NASA re-evaluated the performance estimates of the SEP design and ultimately rejected the solar sailing concept due to higher associated risk. Ironically, the solar-electric concept for a Halley comet rendezvous was dropped soon after due to escalating cost estimates. Although a scaled-down fly-by mission was proposed shortly after, by then the launch widow for a successful intercept elapsed and a NASA mission to intercept the Halley comet was never flown. Interestingly, the comet was intercepted by a series of Soviet, Japanese, and European spacecraft.[8]

Although the Halley comet intercept mission was never launched, it sparked an unparallel interest in solar sailing technology and led to numerous mission analysis as well as discovery of a host of new trajectories previously unachievable with SEP. The initial studies investigated traditional low-thrust trajectories spiraling out from a circular Earth orbit and onwards to escape. The studies quickly progressed to more exotic missions such as non-Keplarian orbits, multi-destination Earth asteroid visits, or missions to both Inner and Outer Solar System. The last two decades have seen an increased interest in utilizing the benefits of solar sailing and several missions have been designed specifically for its use. These include missions that provide early detection and warning of solar events (Heliostorm)[9], missions to conduct detailed analysis of helioseismology and heliomagnetism (Solar Polar Imager)[10], or mission to explore our local galactic neighborhood beyond the heliopause (Interstellar Probe)[11].

Until May of 2010, no successful solar sailing mission has ever been flown[*]. There have been, however, several noteworthy tests of particular solar sailing subsystems and deployment methods, as well as numerous planned missions.

In 1992, the Russian Federal Space Agency launched two experimental spin-stabilized thin-film mirrors named Znamya 2 and Znamya 2.5. The first was a 20 m circular disk launched from the Progress resupply vehicle and controlled from the MIR space station (Figure 1). The second was a larger, 25 m, reflector launched only three months after its predecessor, however the film material snagged on an antenna and failed to deploy. Although both spacecraft utilized highly reflective thin films and were stabilized in a fashion similar to ideas of Ted Cotter, their ultimate purpose was illumination of high latitude spots on Earth and demonstration of Space Solar Power (SSP).[12]

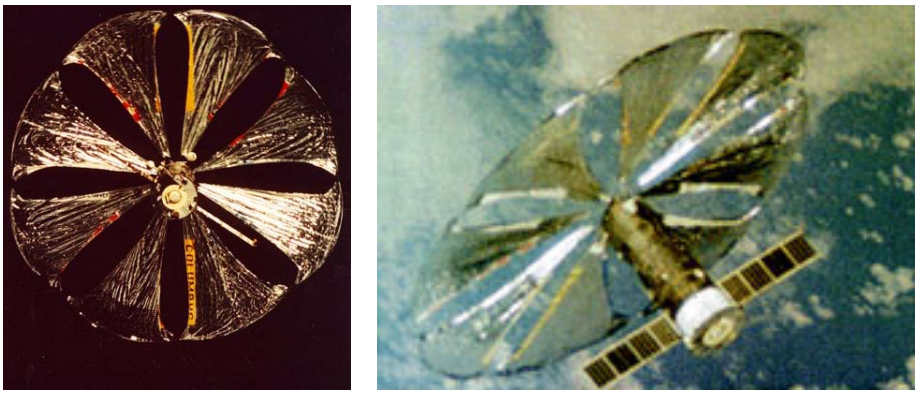

Figure 2. Znamya 2 solar reflector deployed in low Earth orbit.

The cancellation of the Halley comet rendezvous mission was seen by many as the start of larger withdrawal of the US from space exploration. Louis Friedman recalls: "Solar sailing, Halley's Comet missions, the search for extraterrestrial intelligence, the continued exploration of Mars, and mission to the edge of the solar system were all

[*] On May 21, 2010, the Japanese Aerospace Exploration Agency, JAXA launched and successfully deployed a solar sailing spacecraft named IKAROS, described in some detail later in this section.

dropped from U.S. plans within a three-year period."[5] This shift prompted Friedman, along with Carl Sagan and Bruce Murray, to form the Planetary Society in an attempt to reverse this trend. By 2005, the group has built and attempted to launch the first "fully functional solar sail spacecraft," named Cosmos1, however due to the launch vehicle failure, the spacecraft was lost on June 21 of that year. Fortunately, an anonymous $1 million donation allowed the Planetary Society to continue its solar sailing endeavors and plans to launch LightSail-1, shown in Figure 3, as the first in a series of increasingly complex missions. This first demonstration envisions deploying a 3 meter square sail from a 10x10x30 cm CubeSat and plans to launch in low Earth orbit by the end of 2010. LightSail-2 will build on its predecessor's design with an enlarged sail area, larger payload of scientific instruments, and longer mission duration. LightSail-3 intends to sail to the Earth-sun L1 Lagrange point and demonstrate solar wind monitoring for geomagnetic storm forecasting.[13]

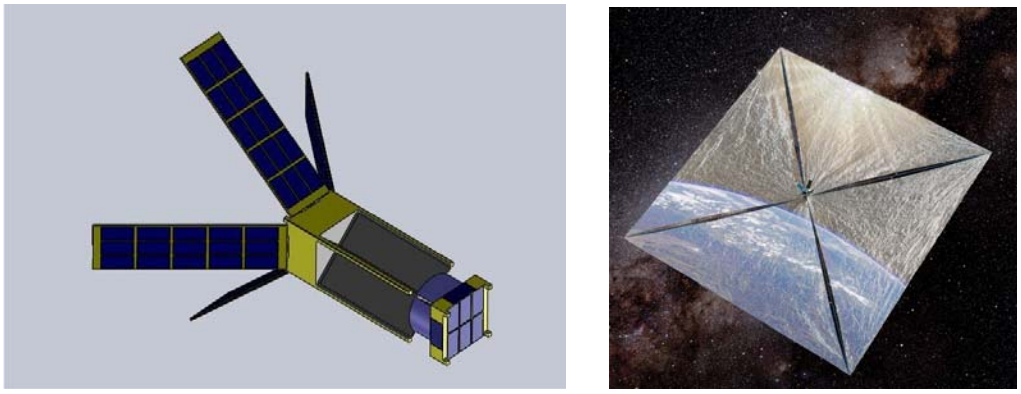

Figure 3. Planetary Society's LightSail-1. Spacecraft prior to sail deployment (left), artist depiction of a fully deployed LightSail-1 sail (right).[13]

A NASA design similar to LightSail-1 named NanoSail-D envisioned deployment of 10 m^2 square sail from a three-unit (3U) CubeSat, shown in Figure 4.[14] The spacecraft was launched on August 2, 2008 on Falcon 1 rocket, but due to launch vehicle failure, it was lost. NASA Marshall Space Flight Center (MSFC) plans to launch

the backup NanoSail-D as payload on the FASTSAT-HSV01 (Fast, Affordable Science and Technology Satellite) mission and is manifested for launch in 2010.[15]

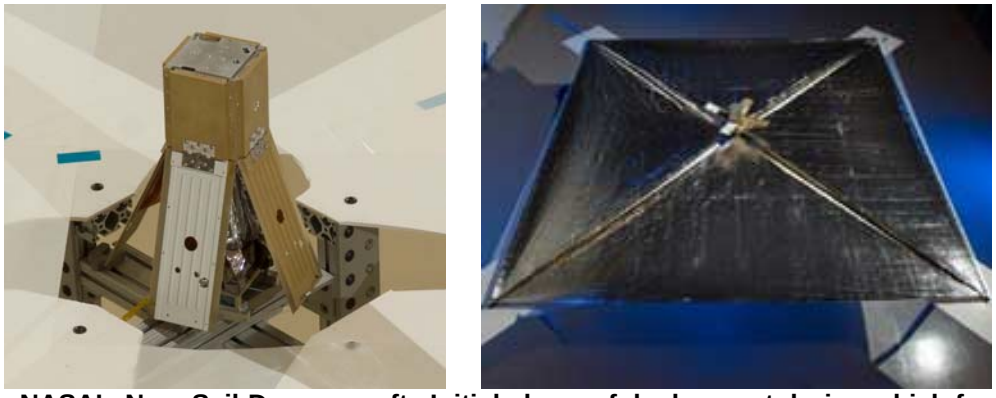

Figure 4. NASA's NanoSail-D spacecraft. Initial phase of deployment during which four hinged doors retract (left), sail at full deployment (right).[14]

The Japan Aerospace Exploration Agency (JAXA), plans to test fly a square sail with a diagonal distance of 20 m. The Interplanetary Kite-craft Accelerated by Radiation Of the Sun, IKAROS, mission will launch as secondary payload to Venus Climate Orbiter, "AKATSUKI"(PLANET-C), using an H-IIA launch vehicle. IKAROS offers a unique design, shown in Figure 5, by combining spin deployment and stabilization with classical square sail geometry[16]

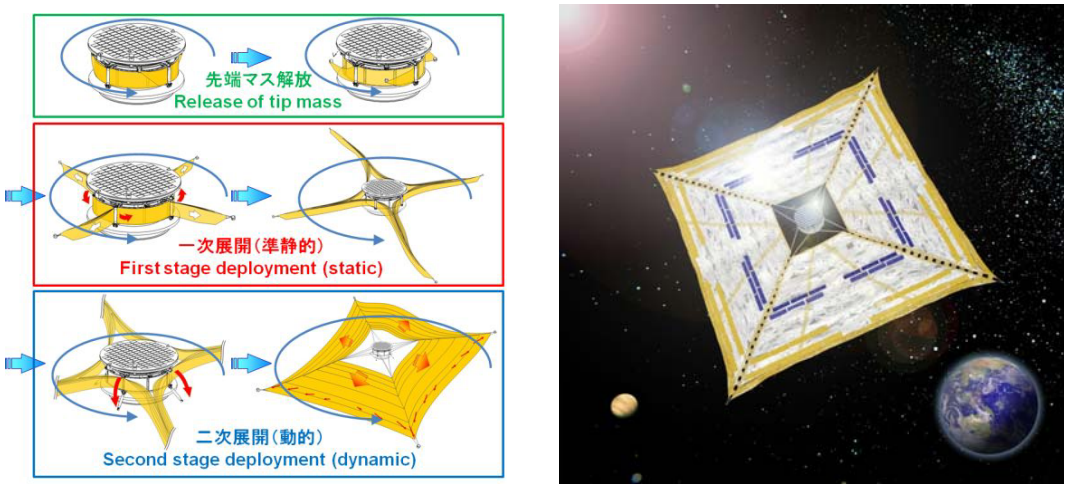

Figure 5. JAXA's IKAROS spacecraft. Deployment sequence (left), artists depiction of a fully deployed IKAROS sail (right).

The above three missions, as well as the CubeSail demonstration discussed in this dissertation attest to the 'renaissance' of solar sailing. After several unsuccessful attempts at raising funds for a large-scale solar sailing missions, numerous developers are pursuing a reduced-scale or incremental development strategy. The design of smaller, less expensive missions that can be launched as secondary payloads and into less-than-ideal orbits, allows for testing and validation of several solar sailing technologies and allows for risk reduction in future, more complex, missions. CubeSail design follows this paradigm with the first demonstration described in this dissertation.

1.2 Solar Sail Design Challenges

The single most important characteristic of solar sails is their large size—often measured in kilometers—necessary to achieve acceptable accelerations and transfer times. At the same time, limitations on payload fairing size of a launch vehicle necessitate packaging and subsequent deployment schemes which are both autonomous and reliable. Once deployed, the film must remain relatively flat (unbillowed) in order to maximize its propulsive capability and thus requires a stiffening method that is scalable with the sail size. The packaging, deployment, and stiffening methods remain one of the most difficult challenges of solar sail design.

Historically, stiffening and deployment methods, which often accomplish both tasks, include: the mast/boom architecture shown in Figure 6, the stay design shown in Figure 7, and the spinning method shown in Figure 1 and Figure 8. The mast/boom architecture suffers from scalability issues due to Euler buckling at long lengths and large structural mass for larger spacecraft, resulting in reduced payload mass and increased transfer times. The stay design is difficult to implement reliably and number

of the designs envision assisted (either human or robotic) deployment or on orbit assembly. The spinning architecture allows for easier scalability and eliminates the need for booms, mast, or stays and is thus selected for the UltraSail and CubeSail designs.

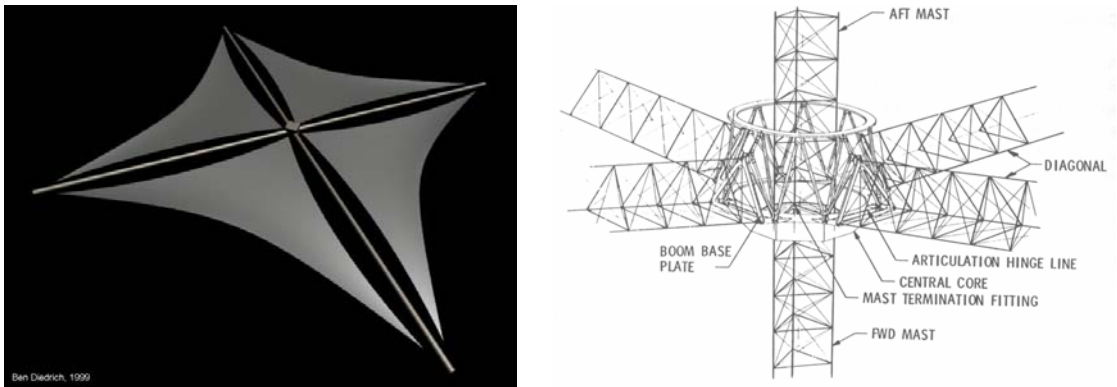

Figure 6. Boom-supported square sail.[17,18]

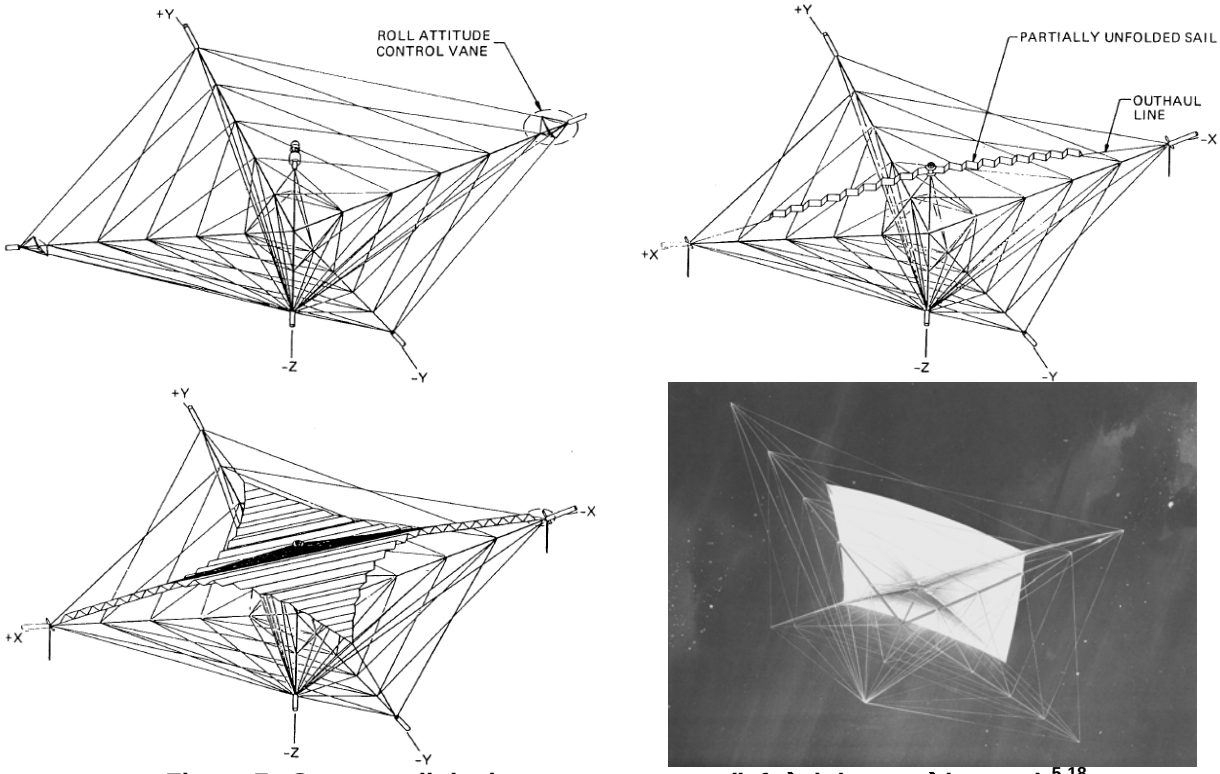

Figure 7. Square sail deployment sequence (left→right, top→bottom).[5,18]

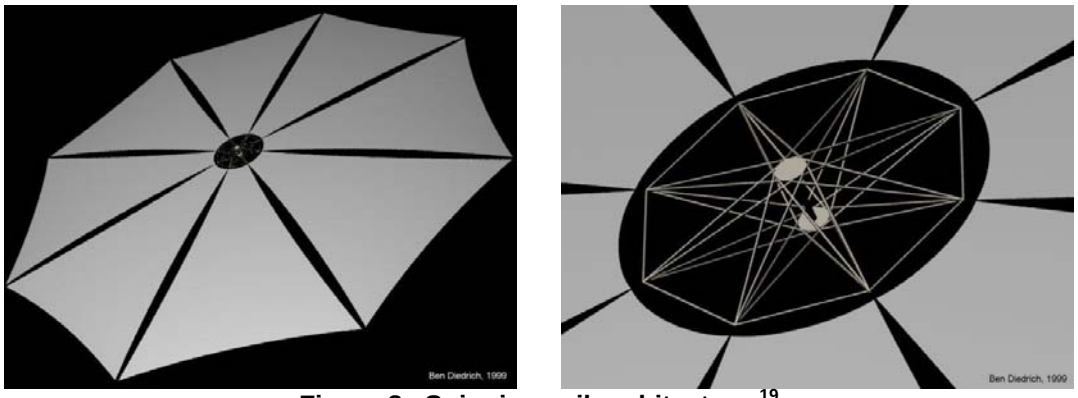

Figure 8. Spinning sail architecture.[19]

The packaging of the large structure is largely dependent on the deployment method, with several methods presented in the literature. Square sails are typically folded using, for example, the "Miura-Ori"[20] or MFPP[21] method. Regardless of the folding method, the sail is subject to numerous creases (Figure 9), which weaken the substrate material and often damage the high-reflectivity coating, reducing its efficiency.

Figure 9. U3P sail during zero-g unfolding testing.[21]

Spinning configurations can utilize the centrifugal force to deploy sail sections that are folded in an accordion-like fashion, or, in the case of the Heliogyro, unrolled from a mandrel. Storage and deployment from a reel enables high efficiency packaging of long blades as well as avoids creasing associated with folding and is therefore used in both the UltraSail and the CubeSail design.

The final challenge facing current solar sailing efforts is the high cost, combined with high risk-factor associated with poorly characterized technology. Several of the solar sailing subsystems, including the previously-discussed stowage/deployment/ stiffening of the sail film as well as control methods of large, flexible structures in space, have low technology readiness level (TRL). In addition, their large size and desired insertion orbits away from the Earth often necessitate large launch vehicles with highly-capable upper stages. Adding to the cost of the launch vehicle is the non-trivial cost associated with fabricating large quantities of the film, which must include a high reflectivity coating on the front, high emissivity coating on the back, and rip-stop to prevent tear propagation. Much of these technologies require extensive testing and validation, especially in the space environment.

1.3 UltraSail Heritage Design

The UltraSail concept[22,23,24,25,26], shown in Figure 10, was developed to address several of the above-mentioned challenges. The design was initially developed under a NASA STTR study by a team at CU Aerospace partnered with the University of Illinois and included Rodney Burton, Victoria Coverstone, and David Carroll. The UltraSail system builds on the Heliogyro design of MacNeal and consists of a central hub with narrow solar sail blades radiating outward from the hub. The major difference between the Heliogyro and UltraSail is the addition of formation-flying tip microsatellites attached to the end of each of the UltraSail blades. These tip satellites deploy each of the blades, as well as maneuver the blades to provide attitude control. The UltraSail blades are initially stored on a reel and are unrolled, utilizing the onboard propulsion of the tip satellite. The unrolling of the film in this manner has an advantage over the classic

square sail configuration as the film does not need to be folded in the stored configuration. The additional benefit of this tip satellite system is elimination of the need for large sail supporting structures present in many previous solar sailing designs.

The final task of the UltraSail STTR study was to develop a concept for a small, low-cost demonstration to reduce the technical risk associated with the mission. This final task was further analyzed under the 2008 NASA SBIR contract and forms the foundation of the CubeSail design presented here.

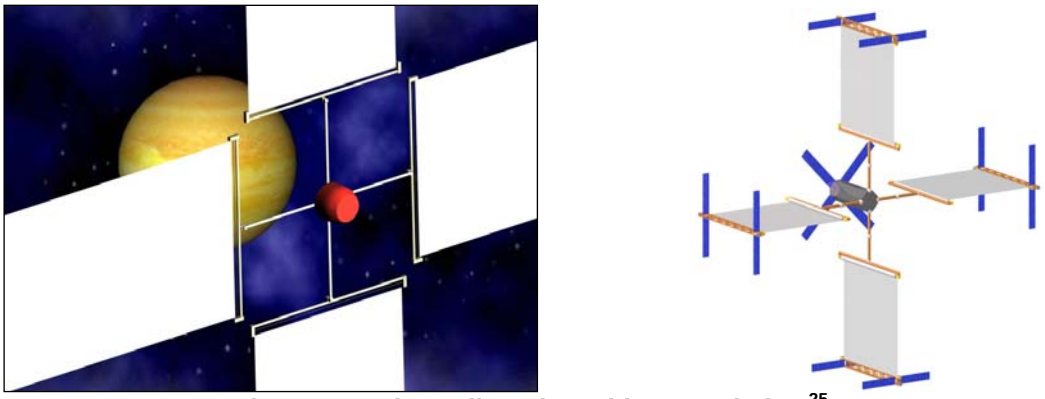

Figure 10. UltraSail Design with Four Blades.[25]

1.4 CubeSat Program

The CubeSat Program originated in 1999 as a collaborative effort between California Polytechnic State University (Cal-Poly) and Stanford University. The driving force behind this partnership was the standardization of design for nanosatellite and the development of a reliable mechanical deployment system. This, in turn, would ensure easy multi-satellite integration and instill confidence to launch providers and primary payload developers. This design would also streamline the cumbersome process of obtaining export licenses and launch approvals that conform to all International Traffic in Arms Regulations (ITAR). Cal Poly also organizes final delivery of the integrated systems to the launch site.

All satellites participating in the CubeSat Program must conform to the specific CubeSat Standard[27]. Each satellite must be a 10cm cube with maximum weight of 1kg. The deviation of center of mass from the geometrical center, location of the power flight pull pin, and the location and size of the deployment switches are also specified. In addition, it is possible to "stack" as many as three cubes together to form a single satellite. Upon completion, the participating CubeSat satellites are delivered to CalPoly and then loaded and deployed from the Poly-Picosatellite Orbital Deployer (P-POD), which is a spring loaded mechanism shown in Figure 11. This standard, reliable, and flight proven deployment system is designed to protect the main payload from the CubeSats while minimizing the packing volume launching three CubeSats.

Figure 11. P-POD Deployer.[28]

The CubeSat program was initiated at the University of Illinois in 2001 as part of the Illinois Tiny Satellite Initiative (ITSI) by Professors Gary Swenson and Victoria Coverstone. The work on the first satellite, named Illinois Observing Nanosatellite (ION), began that same year and in April of 2005, the Illinois team delivered a complete and functional ION to Cal-Poly for the July 26th, 2006 Dnepr (Belka) launch.

From Cal-Poly, ION and 13 other CubeSats were transported to the Baikonur Cosmodrome launch site in Kazakhstan for integration with the main payload and the

launch vehicle. The launch attempt occurred at 19:43:00 UTC on July 26 with all the pre-flight preparations, the rocket lift-off, and the propulsion unit mode engagement occurring normally. However, 73.9 seconds after lift-off, the rocket trajectory deviation control system issued a command for the motors emergency shutdown due to the loss of the rocket in-flight stability. The emergency was caused by a short-time malfunctioning of the pumping hydraulic drive of a combustion chamber of the first stage propulsion unit. All 18 satellites onboard were destroyed.

Since the 2006 launch failure and loss of ION, the Illinois team has been working on the next generation satellite and has made significant improvement in the bus design. The new design, IlliniSat-2, is now completely modular and fits into a 10x10x10 cm volume and provides all the necessary support for a wide range of payloads. This built-in versatility to accommodate various payloads, combined with an active 3-axis attitude control system, makes the next generation Illinois CubeSat a prime choice for the scaled-down, low-cost CubeSail demonstration.

1.5 CubeSail Mission

The CubeSail design thus builds upon the original UltraSail's storage, deployment, and control ideas and combines them with the advanced capability in nanosatellite design and attitude control from the Illinois CubeSat program to realize an on-orbit, autonomous solar sail deployment experiment. The relatively low cost and high frequency of secondary payload launch opportunities for the CubeSat-class spacecraft enables a demonstration that significantly reduces both cost and risk. At the same time, the demonstration will test and characterize numerous aspect of the

CubeSail design (stowage, deployment, and sail dynamics with no stiffening hardware) and thus advance the overall technology readiness level of this solar sailing technology.

The CubeSail mission utilizes an existing spacecraft bus for communication, data handling, and power as well as an in-house expertise on nanosatellite control with magnetic torque actuation to deploy 20 m^2 of aluminized Mylar film in low Earth orbit. A detailed model of the CubeSail tip satellite is shown in Figure 12 and Figure 13 and of the combined assembly in Figure 14.

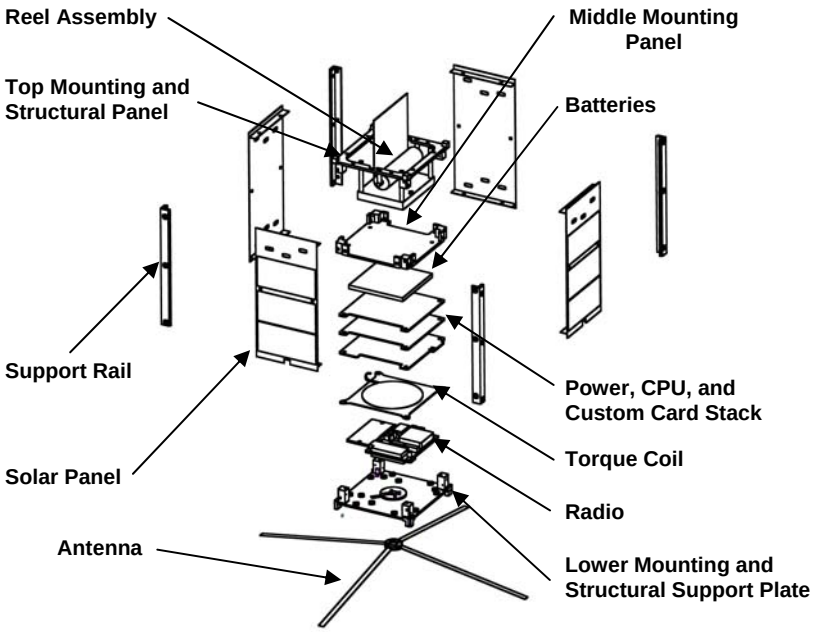

Figure 12. Exploded view of the CubeSail tip satellite.

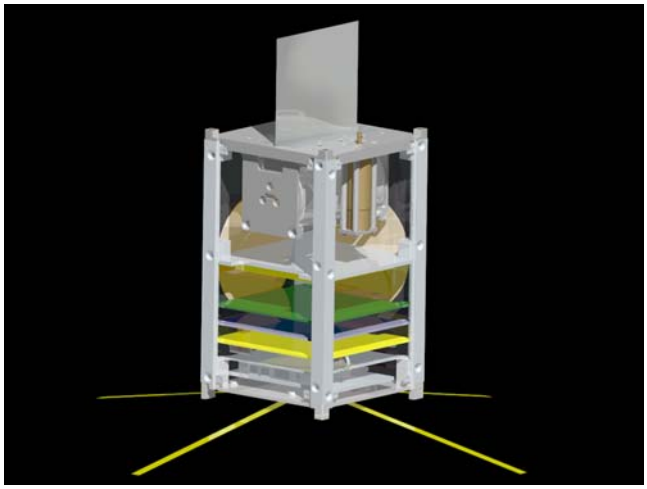

Figure 13. Assembled view of the CubeSail tip satellite.

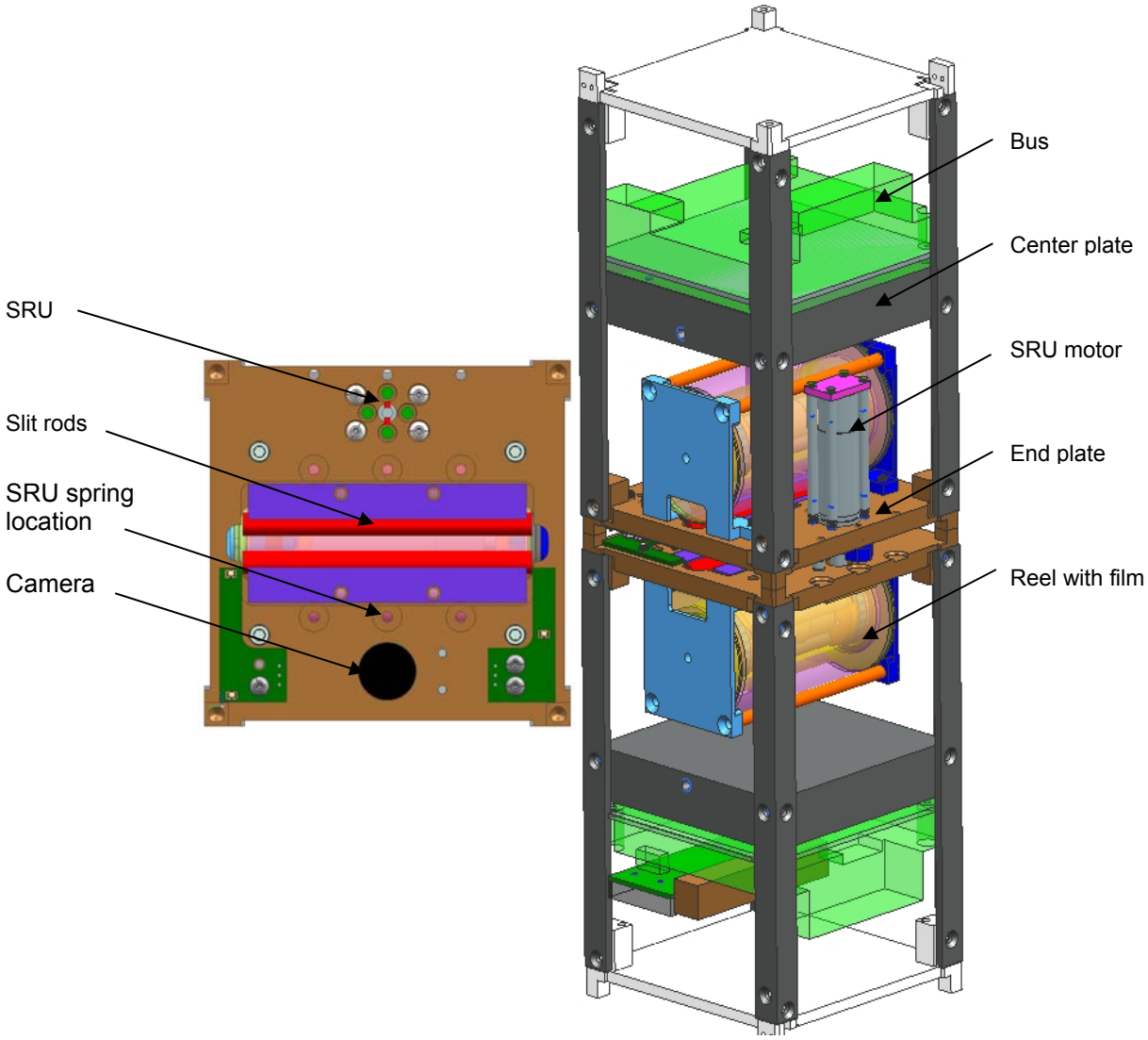

Figure 14. CubeSail assembly model drawing.

The film deployment will occur between two nearly-identical 10x10x15 cm CubeSats using a single strip of film, 78 mm wide and 250 m long, stored on two reels and unrolled via gravity gradient force. A conceptual drawing of the deployment is shown in Figure 15. The attitude of the blade is controlled via the two tip-satellites using magnetic torquers onboard each of the spacecraft. It is the intent of this study to present a design and analysis necessary for successful launch on one of the numerous secondary launch opportunities available to CubeSat-class spacecraft.

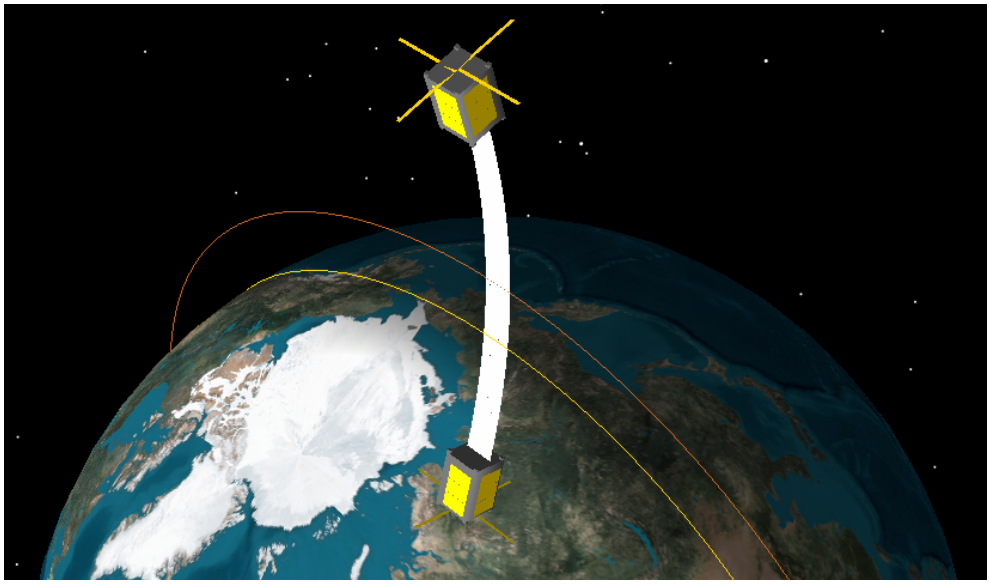

Figure 15. CubeSail spacecraft during deployment.

1.6 Research Objectives

The presented work analyzes several aspects of the CubeSail mission from initial sizing and packaging of the solar sail film into two CubeSat-class spacecraft, through selection of the method and in-depth analysis of the deployment of a 20 m^2 solar sail in low Earth orbit, and lastly predictions of performance and orbital maneuvering capability.

The most difficult aspects of this design, which also make this analysis unique and novel, are the deployment of a non-rigid large-area solar sail into a non-drag-free environment, control of the sail dynamics via nanosatellites with magnetic torque

actuation, and achieving desired orbital maneuvering performance in a presence of varying lighting conditions and non-conservative forces. The presented work includes:

(1) Identification of a solar sail deployment mechanism that eliminates current stowage and deployment difficulties. The experiment assumes that no external sail stiffening hardware such as booms, stays, or guy-wires are utilized, while guaranteeing film flatness. Stowage of a 20 m^2 sail is considered within two 10x10x6 cm payload bays of two 1.5U CubeSat nanosatellites.

(2) Analysis of the dynamics and development of the attitude control algorithms for initial stabilization of the combined CubeSail assembly after ejection from the upper stage of the launch vehicle but prior to sail deployment. Due to size and mass constraints, only magnetic torque actuation is considered as attitude control means.

(3) Identification and preliminary analysis of two deployment schemes: the spin induced deployment and gravity gradient induced deployment.

(4) Selection of desired insertion orbit.

(5) Detailed analysis of the gravity gradient deployment dynamics of a flexible solar sail in the presence of residual aerodynamic drag and solar radiation pressure forces.

(6) Prediction of solar sail performance (eg. Spacecraft lifetime, sail equilibrium temperature, etc.) during nominal operations.

(7) Analysis of propulsive capability for orbital maneuvers.

(8) Final mission design that is fully compatible with the UIUC CubeSat specifications such as mass, power, volume, attitude determination and control capability, typical orbit insertion parameters and hardware interfaces.

The presented research represents majority of the technology necessary for a successful on-orbit experiment and ensure that University of Illinois remains at the forefront of cutting-edge science.

CHAPTER 2

ATTITUDE DETERMINATION AND CONTROL PRIOR TO FILM DEPLOYMENT

2.1 CubeSail Mission Sequence

The top-level sequence of the CubeSail mission is given below and depicted pictorially in Figure 16:

1. Satellite is launched as a single, rigidly-combined unit utilizing secondary payload opportunity. Spacecraft must not be powered during this phase.
2. Upon ejection from the P-POD, satellite's main computer is booted up and the communication antenna is deployed. Basic health checks, battery charging, and beacon transmission are all initiated at this time. In addition, automatic detumbling of the satellite is initiated with pre-computed orbital ephemeris and control weight matrices. High accuracy is not expected at this stage.
3. After the satellite signal has been acquired by the ground station, a series of tests aimed at verifying spacecraft health is initiated. Depending on the results, this 'commissioning' phase may last from several days to few weeks. During this phase, more accurate ephemeris and orbit-specific control weight matrices are uploaded to the spacecraft in order achieve high accuracy detumbling and stabilization of the assembly. The rotational velocity is reduced to zero and the spacecraft is oriented with its long side along the local vertical. After the attitude maneuvers are completed, the batteries are allowed to re-charge.
4. At this time, the film deployment is initiated by first unwinding it by an amount slightly longer than the engagement distance of Separation Release Unit (SRU) lead screw, but less than the compressed length of the spring.
5. The SRU motor is engaged and is run until the satellites are separated. Film is in tension at this point and the SRU springs are compressed sufficiently to provide the desired separation velocity. Guide rails ensure both spacecraft are locked in the pitch direction and that the separation occurs linearly.
6. The reel motors on both satellites are started and operated at the prescribed rate until full sail deployment is reached. The rate of the reel motors is slightly larger than the natural separation dynamics to avoid loss of energy from the deploying system which can lead to zero relative velocity prior to full film deployment or, worse, snap-back and entanglement of the sail. Gravity gradient ensures sufficient tension in the film to prevent excessive billowing due to aerodynamic drag and solar radiation pressure.
7. Once the film is fully deployed, the spacecraft enters nominal operations mode. A reaction wheel on each spacecraft is used to keep the film pitch at zero (edge on to the velocity direction). The tip satellites are not actively controlled in the roll and yaw directions, but rather allowed to align themselves with the film in the minimum energy state (zero torque). This is done in order to prevent damage to film and to conserve energy.
8. After the nominal operations mode is completed, the spacecraft executes a long-duration orbital maneuver to raise its altitude and make a small inclination correction. During this phase, the reaction wheels are used to keep the relative pitch angle at a prescribed value.
9. The mission concludes with a de-orbiting maneuver that presents maximum surface area into the velocity direction.

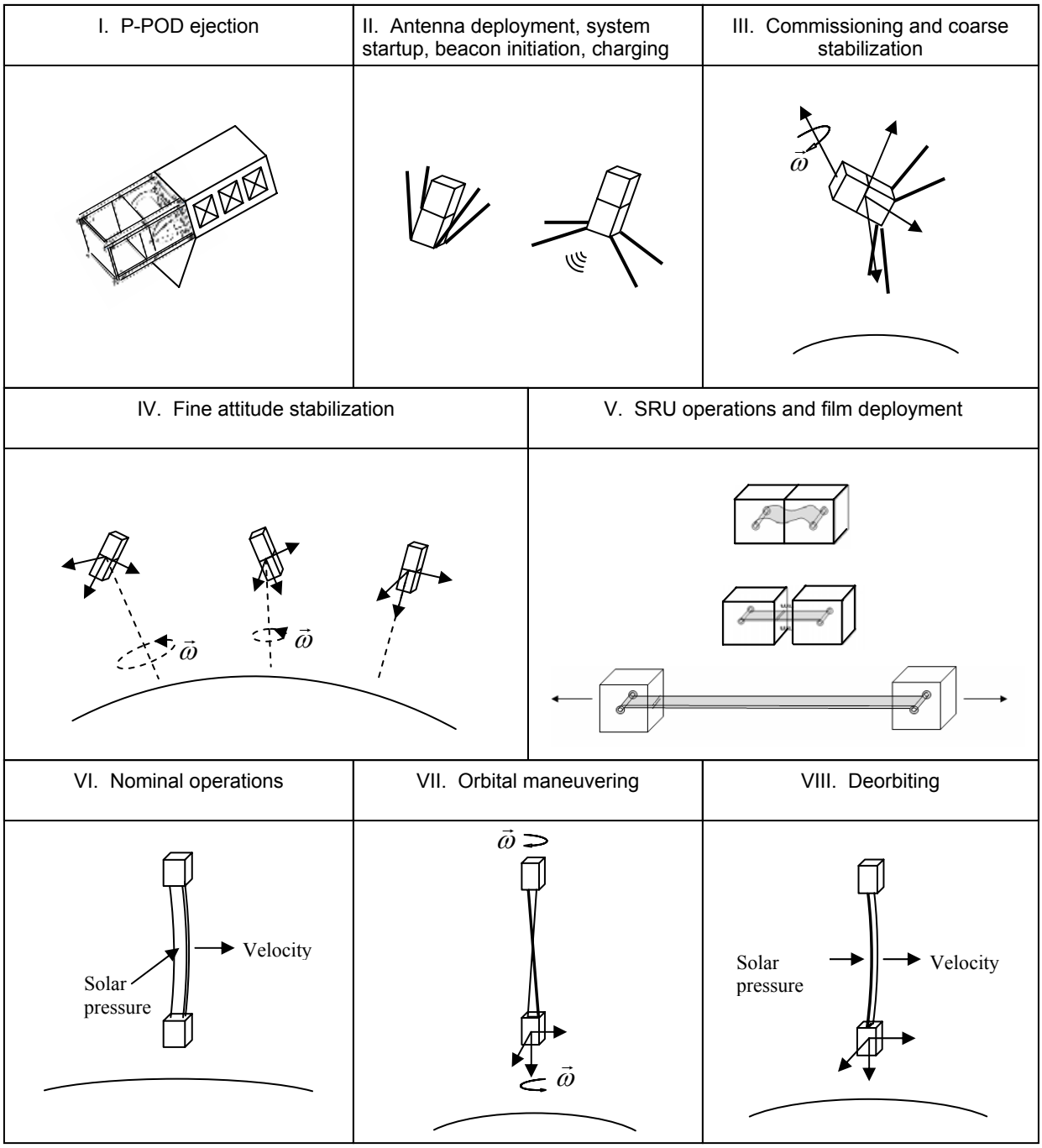

Figure 16. Top-level CubeSail mission sequence.

The analysis of the dynamics and control strategies of the above sequence forms the basis of this dissertation and is presented in the same order whenever possible.

2.2 Attitude Determination

The CubeSail mission utilizes the IlliniSat-2 bus, which includes the necessary attitude determination (AD) hardware and software. Details regarding the IlliniSat-2 AD subsystems are presented in a master's thesis by Warner[29] , and are included here only in cursory fashion.

IlliniSat-2 hardware includes a 3-axis magnetometer, a coarse sun sensor, and two rate gyros for complete 3-axis rate computation. The magnetometer and rate gyro specifications are listed in Table 1 and Table 2 respectively. Table 2 lists three potential rate gyros, but depending on the desired redundancy and power budget, only two will be selected. The specific sun sensor has not been selected yet, and options range from extracting sun vector information from the solar panel voltage readings to commercially available sensors.

Table 1. Honeywell magnetometer characteristics.

Part Number	Sensitivity [μGauss]	Range [±Gauss]	Size [mm]	Power [mW]
HMC6343	85	2	9x9x1.9	14.9

Table 2. Invensense rate gyro characteristics.

Part Number	Measurement Axis	Range [± º/sec]	Size [mm]	Power [mW]
IDG-1215	Pitch and Roll	67	4x5x1.2	21
ISZ-1215	Yaw	67	4x5x1.2	13.5
IXZ-500	Pitch and Yaw	110	4x5x1.2	19.5

The top level attitude determination algorithm is shown in Figure 17. The information from the sun sensor and the magnetometer are used to directly obtain the attitude knowledge using the TRIAD algorithm[30,31]. The rate information is obtained directly from the rate gyros. Hardware testing demonstrated that sensor noise is a non-negligible source of error and requires the use of filtering. The IlliniSat-2 employs either a simple moving average (SMA) or an extended Kalman filter (EKF)—depending on the

desired accuracy, predicted spacecraft rates, and available power—to minimize the impact of hardware noise on rate information. [29,32]

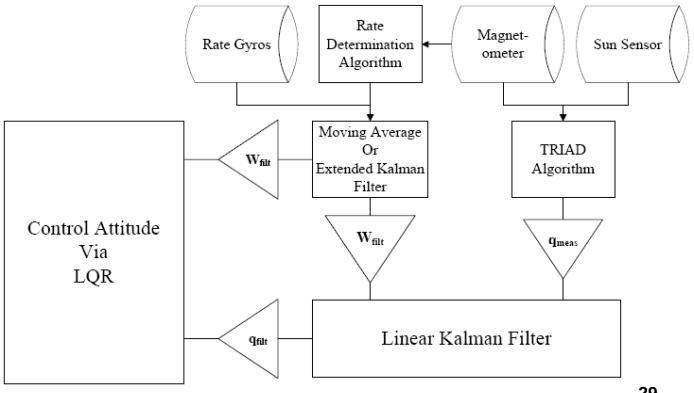

Figure 17. Attitude determination flow diagram.[29]

The implementation of the above attitude determination scheme results in the 1-σ accuracy of less than 0.5° per axis in the attitude knowledge and approximately 0.01°/sec (magnitude) in the angular rate knowledge.

2.3 Attitude Control

The separation of the spacecraft from the upper stage of the launch vehicle usually results in residual torques being imparted onto the spacecraft. These torques cause the spacecraft to be inserted into its orbit with a non-nominal attitude and often with angular velocity that causes a three-axis tumble. In practice, it is very difficult to accurately predict the spacecraft's initial attitude and rotational rates as it is deployed, and requires the design of a robust controller that is capable of handling a wide range of initial attitudes and body rates.

Historically, the final stage and the Poly-Picosatellite Orbital Deployer for a CubeSat-class spacecraft imparts at most 2.5 deg/sec angular velocity to all three axes. Since initial despinning and stabilization of the CubeSail is critical to mission success, the controller is designed with 100% margin and is capable of handling 5 deg/sec

rotational rates on all three axes. In simulation, this will typically be referred to as the worst-case scenario.

In order to demonstrate that the proposed design is capable of stabilizing the combined CubeSail assembly, a Matlab-based simulator was written that solves the optimal control problem of despinning and re-orienting the spacecraft from any initial attitude and maximum rotational rate of 5 deg/sec.

2.3.1 Torque Coil Theory and Design

The CubeSail attitude control is accomplished with three-axis, variable-strength magnetic torquers. The actuators consist of a novel design that imprints consecutive copper loops in a circular wind-down pattern on a flexible circuit board, four layers deep, shown in Figure 18. The flexible torquers are mounted behind the solar panels and include all necessary control circuitry.

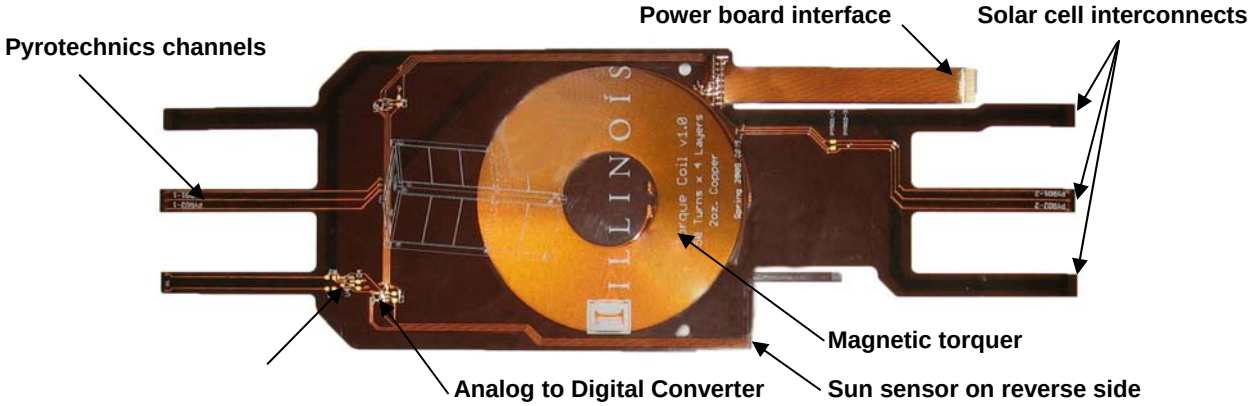

Figure 18. CubeSail's flexible, variable-strength magnetic torquer board.

Control authority of magnetic actuators is typically described using the magnetic dipole moment, $\mathbf{m}$, generally defined as:

$$\mathbf{m} = N \cdot I \cdot A \cdot \hat{\mathbf{a}}_n \qquad [1]$$

where N is the number of loops, I is the current flowing through the wire, A is the cross-sectional area, and $\hat{\mathbf{a}}_n$ is the direction normal to the coil and is determined according to the right-hand-rule. When the coil is immersed in an external magnetic field, say that of the Earth, it produces a torque. The torque is generated by the interaction of the two magnetic fields and is governed by the following equation:

$$\vec{M}_B = \mathbf{m} \times \mathbf{b}_e \quad [2]$$

Intuitively, the magnetic moment tends to align itself in the direction of the external magnetic field. When the two vectors align, the cross product in the above equation is equal to zero and no torque is exerted on the coil. The coil thus reaches a state of stable equilibrium and rejects any deviations as long as the coil maintains its dipole moment.

The above equation for magnetic dipole moment must be corrected for continuously decreasing surface areas as the copper trace winds down:

$$\mathbf{m} = 4 \cdot I \cdot \pi \cdot \sum_{i=1}^{N} \left(r_i^2 \right) \cdot \hat{\mathbf{a}}_n \quad [3]$$

where r_i is the radius of the i^{th} loop and the multiplier '4' accounts for the number of layers. Table 3 provides specifics of the torque coils used on the CubeSail spacecraft; all three coils are identical.

Table 3. Torque coil parameters.

Coil Property	Value
Radius of outer-most loop [m]	0.0342
Trace thickness [m]	4.2×10^{-4}
Number of turns	50
Number of layers	4
Nominal voltage [V]	7.4
Maximum current [A]	0.25
Maximum dipole moment [Am^2]	0.192

With the above properties and correcting for decreasing area at each loop, the CubeSail's torque coils are capable of producing maximum magnetic dipole moments of 0.096 A-m^2 (at $I_{\max} = 0.25\ A$). Since both satellites have identical attitude control capability and the torquers can be fired simultaneously, the initial detumbling and stabilization can be accomplished using a maximum dipole moment of 0.192 A-m^2.

2.3.2 Earth Magnetic Field Model

In order to calculate the torque generated by the magnetic actuators, the external magnetic field, in this case of the Earth, $\mathbf{b}_e$, must be calculated. Figure 19 shows total intensity contour lines of Earth's magnetic field projected onto a Mercator map and demonstrates dependence of $\mathbf{b}_e$ on the spacecraft position. Although it is readily obvious that the field is non-uniform, what is not shown is that the field is also time-varying—a fact which makes its computation difficult.

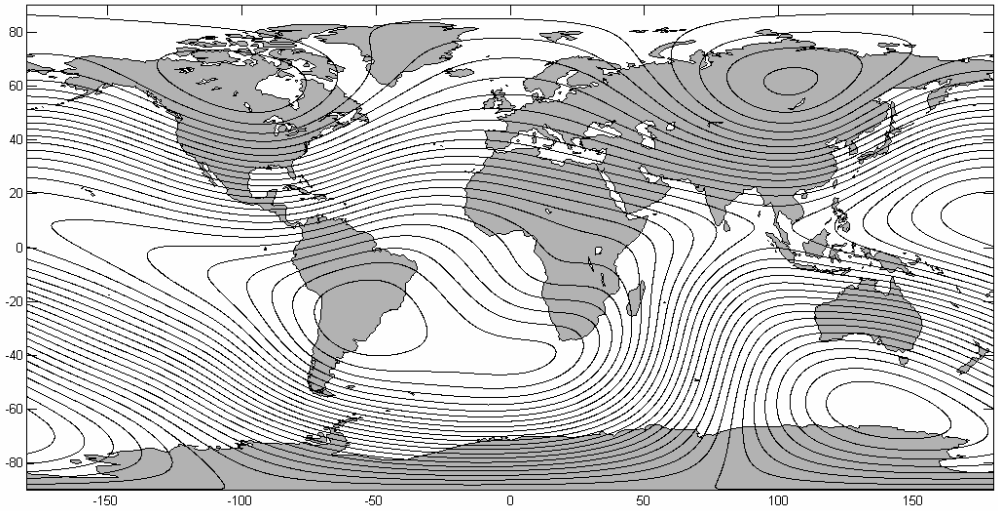

Figure 19. Geomagnetic total intensity lines at surface. Year = 2010. Model = IGRF11.

The International Association of Geomagnetism and Aeronomy (IAGA) developed a description of the Earth's main magnetic field, now in its 11th generation, called International Geomagnetic Reference Field (IGRF). The IGRF is a series of

mathematical models of the Earth's main field and its annual rate of change (secular variation). The main field coefficients are functions of time and for the IGRF the change is assumed to be linear over five-year intervals. It is thus possible to accurately calculate the magnetic field up to the IGRF epoch year and, secondly, to extrapolate the coefficients for five years past the IGRF epoch year.

A specific field model is referred to by including either the epoch year or the generation in the name. In addition, there are definitive coefficient sets (DGRF) for which no further revisions are anticipated. The most recently published result is the IGRF2010 (IGRF11) set, which consists of definitive coefficient sets for 1945 thru 2005 and preliminary sets for 2010 and for extrapolating from 2010 to 2015. More information on the IGRF models can be found on the IAGA website[33].

It is most convenient to compute the geomagnetic field in the Earth-Centered Fixed (ECF) coordinate system. This can be done by writing the magnetic field as a sum of spherical harmonics, in the following form:

$$\mathbf{b}_e^{ECF} = \sum_{n=1}^{\infty} \sum_{m=0}^{n} \mathbf{b}_{n,m} \qquad [4]$$

In the above equation, the vector $\mathbf{b}_e^{ECF}$ is the calculated magnetic field in the ECF reference frame, and $\mathbf{b}_{n,m}$ is the spherical harmonic of degree n and order m. The components of $\mathbf{b}_{n,m}$ are found by the following equation:

$$\mathbf{b}_{n,m} = \frac{K_{n,m} a^{n+2}}{r^{n+m+1}} \begin{Bmatrix} \dfrac{g_{n,m} C_m + h_{n,m} S_m}{r} \left[\left(u A_{n,m+1}(u) + (n+m+1) A_{n,m}(u) \right) \hat{\mathbf{r}} - A_{n,m+1}(u) \hat{Z}^{ECF} \right] \\ -m A_{n,m}(u) \left[\left(g_{n,m} C_{m-1} + h_{n,m} S_{m-1} \right) \hat{X}^{ECF} + \left(h_{n,m} C_{m-1} - g_{n,m} S_{m-1} \right) \hat{Y}^{ECF} \right] \end{Bmatrix} \qquad [5]$$

The parameters $g_{n,m}$ and $h_{n,m}$ are the Gauss coefficients of degree *n* and order *m*, as published by the IGRF. The parameter a is the mean radius of the Earth and is equal to 6371.2 km. The parameter r is simply the magnitude of $\mathbf{r}$, the desired position in the ECF frame. The unit vector $\hat{\mathbf{r}}$ is in the direction of $\mathbf{r}$. The parameter u is the third component of $\hat{\mathbf{r}}$ which may be found as follows:

$$u = \hat{\mathbf{r}} \bullet \hat{Z}^{ECF} \qquad [6]$$

The remaining terms can be determined recursively through the following recursions:

$$\begin{gathered} K_{n,0} = K_{1,1} = 1 \quad \forall \quad n \in \{1,...,\infty\} \\ K_{n,m} = \left(\frac{n-m}{m+m}\right)^{1/2} K_{n-1,m} \quad \forall \quad m \in \{1,...,\infty\}, \;\; n > m \\ K_{n,m} = \left((n+m)(n-m+1)\right)^{-1/2} K_{n,m-1} \quad \forall \quad m \in \{2,...,\infty\}, \;\; n \geq m \end{gathered} \qquad [7]$$

$$\begin{gathered} A_{0,0}(u) = 1 \\ A_{n,n}(u) = (1)(3)(5)...(2n-1) \quad \forall \quad n \in \{1,...,\infty\} \\ A_{n,m}(u) = \frac{1}{n-m}\left[(2n-1)uA_{n-1,m}(u) - (n+m-1)A_{n-2,m}(u)\right] \quad \forall \quad \mathrm{m} \in \{0,...,\infty\}, \;\; n > m \end{gathered} \qquad [8]$$

$$\begin{array}{lll} S_0 = 0 & C_0 = 1 & S_m = S_1 C_{m-1} + C_1 S_{m-1} \\ S_1 = \mathbf{r} \bullet \hat{Y}^{ECF} & C_1 = \mathbf{r} \bullet \hat{X}^{ECF} & C_m = C_1 C_{m-1} - S_1 S_{m-1} \end{array} \qquad [9]$$

$K_{n,m}$ are known as the Schmitt coefficients, while $A_{n,m}$ are derived Legendre polynomials. S_m and C_m are related to the Schmitt coefficients, but are separated as a means of simplifying the recursions.

It is important to note that the Schmitt coefficients are independent of the desired position. Thus, if the magnetic field is to be calculated for a number of points, the Schmitt coefficients need only be calculated once, and may be reused for each subsequent calculation. However, the rest of the parameters are location dependent,

and must be recalculated for each desired location. A useful reference concerning the derivation of the above equations can be found in texts by Campbell [34] and by Roithmayr[35].

2.4 Linear Quadratic Regulator

The linear quadratic (LQ) control problem is an optimal control problem. It is covered in most modern control texts, such as Bryson and Ho[36] or Brogan[37]. In the LQ problem, it is assumed that there is a system in which the state dynamics are governed by a linear differential equation with constant coefficients in the state, but time-varying input dynamics:

$$\dot{\mathbf{x}} = \mathbf{A}\mathbf{x} + \mathbf{B}(t)\mathbf{u} \quad \text{given} \quad \mathbf{x}(t_0) \qquad [10]$$

For the LQ problem, the following cost function is assigned:

$$\mathbf{J} = \frac{1}{2}\int_{t_0}^{t_f} \left(\mathbf{x}^T\mathbf{Q}\mathbf{x} + \mathbf{u}^T\mathbf{R}\mathbf{u}\right) d\tau + \frac{1}{2}\mathbf{x}\left(t_f\right)^T \mathbf{P}_T\mathbf{x}\left(t_f\right) \quad \text{given} \quad \mathbf{x}(t_0) = \mathbf{x}_0 \qquad [11]$$

The matrix $\mathbf{Q}$ may be thought of as a penalty on the state vector to discourage the state from deviating too large from the desired state, $\mathbf{R}$ as a matrix to penalize using excessive control effort, and $\mathbf{P}_T$ as a penalty on the final state. All of these are constant matrices. From the point of view of the designer, unless these matrices have some a priori designation, they may be viewed as a means of changing the characteristics of the system dynamics. Thus, these matrices provide a quantitative way of trading off state deviation with control energy. All of $\mathbf{Q}$, $\mathbf{R}$, and $\mathbf{P}_T$ are assumed to be positive definite.

The goal of the linear quadratic regulator is to find the optimal control to minimize the cost function given these various matrices and an initial state condition. It is a well-

known result that the optimal solution to the LQ problem is a full state feedback controller of the following form:

$$\mathbf{u}^* = \mathbf{F}\mathbf{x} = -\mathbf{R}^{-1}\mathbf{B}(t)^T \mathbf{P}(t)\mathbf{x} \qquad [12]$$

The matrix $\mathbf{P}(t)$ is found by the following differential equation:

$$\dot{\mathbf{P}}(t) = \mathbf{Q} + \mathbf{P}(t)\mathbf{A} + \mathbf{A}^T\mathbf{P}(t) - \mathbf{P}(t)\mathbf{B}(t)\mathbf{R}^{-1}\mathbf{B}(t)^T \mathbf{P}(t) \quad \text{given} \quad \mathbf{P}(t_f) = \mathbf{P}_T \qquad [13]$$

In principle, this equation may be evaluated in closed form or analytically, to find the time varying matrix $\mathbf{P}(t)$, which in turn specifies $\mathbf{u}^*$.

2.4.1 Asymptotic Periodic Linear Quadratic Regulator

A special case of the quadratic linear regulator is where the matrix $\mathbf{B}(t)$ is periodic. In this case, for some value of T and all t,

$$\mathbf{B}(t) = \mathbf{B}(t+T) \qquad [14]$$

In this case, if $\mathbf{P}_T$ is properly chosen, it can be shown that the solution to Equation 13 results in a $\mathbf{P}(t)$ that is also periodic with a period T. This periodicity in the feedback matrix can be used to show that, in the case of some very general conditions on the penalty matrix $\mathbf{Q}$, $\mathbf{P}(t)$ approaches a steady state matrix $\mathbf{P}_{ss}$ as $\mathbf{R}$ approaches infinity[38]. Thus, for large values of $\mathbf{R}$, it can be expected that this $\mathbf{P}_{ss}$ matrix may be used as a reasonable approximation for $\mathbf{P}(t)$ for all values of t. In this case, the optimal control law becomes

$$\mathbf{u}^* = \mathbf{F}\mathbf{x} = -\mathbf{R}^{-1}\mathbf{B}(t)^T \mathbf{P}_{ss}\mathbf{x} \qquad [15]$$

To find $\mathbf{P}_{ss}$, note that the following long average over one period can be made:

$$\mathbf{B}(t)\mathbf{R}^{-1}\mathbf{B}(t)^T \approx \mathbf{C} = \frac{1}{T}\int_0^T \mathbf{B}(\tau)\mathbf{R}^{-1}\mathbf{B}(\tau)^T \, d\tau \qquad [16]$$

These approximations greatly simplify the implementation for the linear quadratic regulator. Inserting this approximation into the differential equation found in Equation 13, it is possible to solve the following algebraic Riccati equation for $\mathbf{P}_{ss}$:

$$\mathbf{0} = \mathbf{Q} + \mathbf{P}_{ss}\mathbf{A} + \mathbf{A}^T\mathbf{P}_{ss} - \mathbf{P}_{ss}\mathbf{C}\mathbf{P}_{ss} \qquad [17]$$

2.4.2 CubeSail's Asymptotic Periodic LQR Design

To apply the linear quadratic regulator to the CubeSail's attitude control system, a state vector consisting of the integral of the attitude, the attitude, and angular velocity of the Fixed Body coordinate system with respect to the Orbital Reference frame is defined. The attitude is represented using quaternions, denoted by $\mathbf{q}$, and consists of only the first three elements. It is important to note that the dynamics in Equation 10 do not include the evolution of the fourth element of the quaternion, but are nevertheless a function of this element. When evaluating along the nominal trajectory, it will be necessary to know the nominal value of this fourth element. However, using the quaternion constraint equation ($\|\mathbf{q}\| = 1$) it is possible to show that this nominal value is simply one. The integral of the attitude is used due to its many benefits, notably its stabilizing tendencies and noise reduction. The new state vector, which includes the integral control, can be written as:

$$\tilde{x}_{lqr} = \begin{bmatrix} \int \mathbf{q}^{B/R} & \mathbf{q}^{B/R} & \omega^{B/R} \end{bmatrix}^T \qquad [18]$$

and the augmented dynamics can be written as:

$$\dot{\tilde{\mathbf{x}}}_{lqr} = \tilde{\mathbf{A}}\tilde{\mathbf{x}}_{lqr} + \tilde{\mathbf{B}}(t)\mathbf{u} \qquad [19]$$

$$\tilde{\mathbf{A}} = \begin{bmatrix} \mathbf{0}_3 & \mathbf{I}_3 & \mathbf{0}_3 \\ \mathbf{0}_3 & & \mathbf{A} \end{bmatrix} \qquad \tilde{\mathbf{B}}(t) = \begin{bmatrix} \mathbf{0}_6 \\ -\tilde{\mathbf{I}}^{-1}\mathbf{b}^{\times}(t) \end{bmatrix} \qquad [20]$$

$$\mathbf{A} = \begin{bmatrix} & & & \mathbf{0} & \frac{1}{2}\mathbf{I} & \\ \omega_0\tilde{\mathbf{I}}^{-1} & \begin{matrix} 8\omega_0(I_z - I_y) & -6\omega_0 I_{xy} & 2I_{xz} \\ -8\omega_0 I_{xy} & 6\omega_0(I_z - I_x) & -2\omega_0 I_{yz} \\ 8\omega_0 I_{xz} & 6\omega_0 I_{yz} & 2\omega_0(I_x - I_y) \end{matrix} & \begin{matrix} 0 & -2I_{yz} & I_x - I_y + I_z \\ 2I_{yz} & 0 & -2I_{xy} \\ -I_x + I_y - I_z & 2I_{xy} & 0 \end{matrix} \end{bmatrix} \qquad [21]$$

where $\tilde{\mathbf{I}}$ represents the 3x3 moment of inertia of the spacecraft, $\mathbf{b}^{\times}(t)$ is the skew symmetric-matrix formed from the geomagnetic field vector[39] expressed in the fixed body coordinate system, and $\mathbf{A}$ is the linearized system dynamics about the nominal nadir-pointing trajectory[40].

The input, $\mathbf{u}$, is the magnetic moment generated by the magnetorquers onboard each of the spacecraft. The parameter ω_0 is the magnitude of the orbital angular velocity of the reference coordinate system with respect to the inertial coordinate system. There is some slight deviation of the angular velocity for noncircular orbits. However, the average orbital angular velocity may be used in the calculations. Also, the above system dynamics take into account the gravity-gradient effects when computing the linearized system.

2.5 Attitude Control Simulator

The above LQR control scheme is combined with the CubeSail system dynamics, magnetic field model, simple aerodynamic drag model, and gravity gradient model to form the attitude control simulator. The simulator was initially developed for the ION1 spacecraft and has been adapted for use for the slightly larger CubeSail mission. The details pertaining to each of the models used for the initial detumbling and orientation of

the combined assembly can be found in the author's master's thesis[40]. It is important to note that due to minimal surface area and relatively short length of the spacecraft at this stage of the mission, the simulation uses simpler models for aerodynamic drag and gravity gradient than those used during film deployment and during nominal operations.

The general diagram of the simulation is shown in Figure 20. The simulation is initiated by applying the tip-off quaternion $\vec{q}_0$ and rotation rate $\vec{\omega}_0$ to the satellite dynamics in order to propagate the state forward in time by a short time (typically orders of tens of seconds), denoted by T_{LQR}. The resultant attitude and rotational rate ($\vec{q}$ and $\vec{\omega}$) are used by the LQR to compute an optimum duty cycle (% of maximum current) and direction of current flow necessary to despin and orient the spacecraft along the nadir. The computed duty cycle is then used in the 'magnetic torquers' block, which computes the magnetic torque on the spacecraft given torque coil parameters and external magnetic field vector. The magnetic torque is combined with the gravity gradient and the aerodynamic drag torque to form a total torque which is then applied to the satellite in order to obtain the updated state. The updated state is used to compute a new optimal duty cycle and the process is repeated until final time is reached.

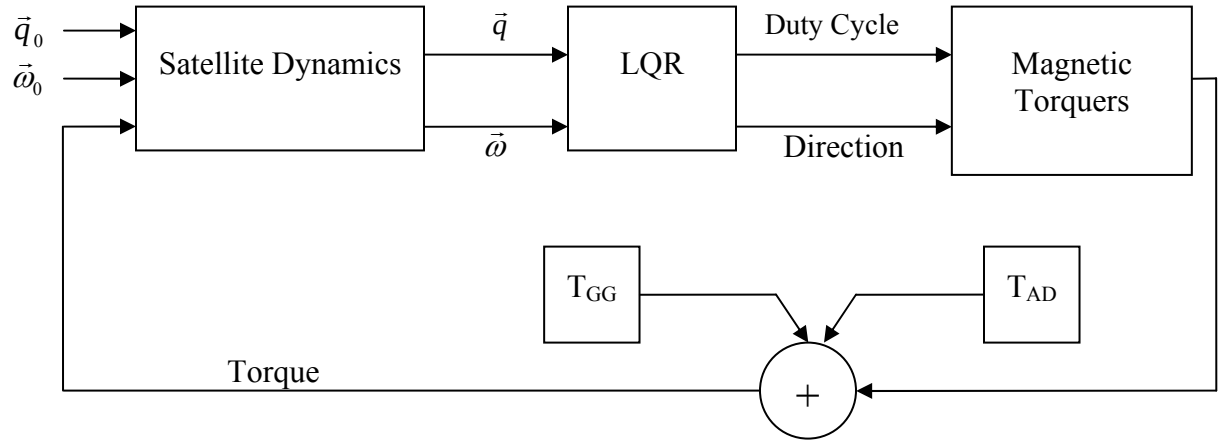

Figure 20. Attitude control diagram.

Each optimal duty cycle is held constant for the prescribed duration T_{LQR}, which is currently set at 15 seconds. Longer update times result in less optimal magnetic torques being applied to the spacecraft as it travels along its orbital track and through a spatially-varying magnetic field. In contrast, very short update times result in a frequently switching torque profile that requires additional power (due to ramp up and ramp down of the LTC1799 and coils) and puts larger computational burden on the processor. Author's experience with the simulator shows that a T_{LQR} between 15 and 60 second results in good performance and acceptable run times on a standard desktop PC of approximately 5 seconds per run (15 hour simulation time).

The development of the attitude control simulation code is critical to two aspects of the CubeSail detumbling process. First, it allows for quick evaluation and tuning of the LQR performance by modifying the $\mathbf{Q}$ and $\mathbf{R}$ penalty matrices. Second, it provides means to test the robustness of the controller by running large Monte Carlo simulations with randomly varying initial tip-off attitudes. Experience gained during ION1 LQR development showed that selection of the penalty matrices by 'educated guess' method produces non-robust results. As a result, the simulation code is used in conjunction with a Genetic Algorithm (GA) algorithm to find a near-optimal set of $\mathbf{Q}$ and $\mathbf{R}$ matrices to minimize a certain cost function (usually despinning and orientation times). Details of this approach are described in detail in the following section.

All simulations of the initial detumbling and stabilization of the CubeSail spacecraft use the following assumptions. The spacecraft is assumed to be a rigid body with the dimension of 327x100x100 mm and mass of 3 kg. The less than 340.5 mm length stated in the CubeSat Design Specification document[27] is a result of a

requirement of having top and bottom separation feet (340.5 – 6.5 – 7.0 = 327 mm). Due to their minimal size, the feet are not included in the overall height or mass properties of the spacecraft. At this time, the center of mass is assumed to coincide perfectly with the geometrical center of the two-satellite assembly. This is seen as an acceptable assumption since the CubeSat Design Specification[27] requires them to be within 20 mm of each other and the reel mount has been designed to allow small positional adjustments. Moreover, a parameter that represents any such deviation is already incorporated in the simulation code. The principal moments of inertia can therefore be calculated as:

$$\tilde{\mathbf{I}} = \begin{bmatrix} 0.029232 & 0 & 0 \\ 0 & 0.029232 & 0 \\ 0 & 0 & 0.005 \end{bmatrix} kg \cdot m^2 \qquad [22]$$

The spacecraft was assumed to be inserted into a typical CubeSat orbit, here set to be a 750 km altitude circular low Earth orbit inclined at 98°. The orbit was propagated for 15 hours and included gravity gradient and aerodynamic drag disturbance torques, as well as the applied magnetic control torque. The coefficient of drag was chosen to be 2.2 and the aerodynamic density was chosen to be the mean of solar maximum and solar minimum densities at 750 km, or 4.476×10^{-14} kg/m^3. The atmospheric density values were calculated using NRLMSISE00 code developed by the Naval Research Laboratory (NRL)[41,42].

All simulations assume the worst case tip-off rotational rate of 5 °/sec on all three axes. Initial attitude is typically computed by creating a random 4x1 vector representing the quaternion. The exception to this rule occurs during tuning of the $\mathbf{Q}$ and $\mathbf{R}$

matrices when the attitude quaternion is selected to represent 'difficult to stabilize' initial conditions. Details regarding these special cases are discussed in the following section.

2.5.1 Q and R Matrix Computation with Genetic Algorithm

A Genetic Algorithm is a metaheuristic method of solving global optimization problems which typically have large search spaces. The foundation of this method is derived from the process of biological evolution where a population evolves through the processes of selection, mutation, cross-over, and inheritance towards a better state.

Analogous to the physical behavior, the GA generates a population of candidate solutions and evolves it towards an optimal solution. The algorithm begins with a randomly generated population of individuals, whose fitness is evaluated at each generation. Three main types of rules are used to create a subsequent generation. The first rule is the *selection*, in which a portion of the current population, called parents, is selected to contribute to the next generation. A fitness-based process is employed to select the parents, where individuals with higher fitness are more likely to be selected. The fitness-based process is typically stochastic so that a small portion of individuals with lower fitness is selected, thus preserving diversity and avoiding premature convergence to a sub-optimal solution. The second rule is the *crossover* or *recombination*, in which two parents are combined in order to form children for the next generation. The third rule is the *mutation*, in which a random change is applied to an individual parent in order to introduce diversity and avoid converging to local minima.[43] The stopping criteria for the algorithm can vary from reaching a limit on the average change in the objective function, maximum number of generations, or run time. The CubeSail GA algorithm stopping criterion is set to 50 generations.

The CubeSail mission utilizes a Genetic Algorithm to find a set of near-optimal $\mathbf{Q}$ and $\mathbf{R}$ matrices for initial detumbling and stabilization of the combined assembly. A Genetic Algorithm is well suited for this problem due to the fitness function's dependence on spacecraft mass properties, torque coil parameters, general orbit parameters (ex.: polar vs. equatorial), external magnetic field, disturbance torques, and initial tip-off attitude and rotational rates. Selection of $\mathbf{Q}$ and $\mathbf{R}$ is further complicated by varying units in the state vector ($\tilde{x}_{lqr} = \begin{bmatrix} \int \mathbf{q}^{B/R} & \mathbf{q}^{B/R} & \omega^{B/R} \end{bmatrix}^T$), natural coupling of the dynamics between the three body axes, and the fact that the optimal solution is computed using the $\mathbf{P}_{ss}$ matrix, which is obtained by solving the algebraic Riccati equation.

Lastly, the Genetic Algorithm optimizes the weight matrices for a single tip-off case, but must perform well for virtually any (bounded) initial conditions. Although it is true that larger initial angular velocities are more difficult to stabilize, an equivalent statement is difficult to form for the initial attitude. Depending on spacecraft orientation, its torquing capability, and external magnetic field, some attitudes are more difficult to stabilize than others. Since initial detumbling and stabilization is critical to mission success, the robustness of the weight matrices for virtually any initial attitude is a mission requirement. It is also important to note that the GA-optimization must be performed at least twice—once for the candidate orbit and again after launch when improved orbit parameters are obtained from tracking.

The CubeSail Genetic Algorithm optimizes the state vector, x^{GA}, of 12 variables that are diagonal values of the two weight matrices:

$$x^{GA} = \begin{bmatrix} Q_{11} & Q_{22} & Q_{33} & Q_{44} & Q_{55} & Q_{66} & Q_{77} & Q_{88} & Q_{99} & R_{11} & R_{22} & R_{33} \end{bmatrix} \quad [23]$$

subject to either detumbling or tracking cost function, depending on which mode the satellite is in. The detumbling mode emphasizes reducing the rotational rates on all three axes to below a prescribed threshold of 0.1 º/sec as quickly as possibly, and de-emphasizes the nadir pointing orientation. The cost function can therefore be written as:

$$J_{Detumbling} = \left\{ t_{Detumble} : \vec{\omega}^{B/R} \left(t_{Detumble} < t \le t_f \right) \le 0.1^\circ / \sec \right\} \quad [24]$$

The tracking mode, which begins at $t_{Detumble}$, emphasizes alignment with the nadir pointing direction below the prescribed angle of 5º for all three Euler angles (θ, ϕ, ψ). Initial attempts at formulating an analogous cost function using the tracking time—time at which all three angles are below the 5º threshold from $t_{Detumble}$ until end of simulation time—resulted in limited success and a new method has been adopted. An accumulated error for all Euler angles above the 5º threshold from $t_{Detumble}$ to t_f, as shown in Figure 21, is computed and then added together to form the new tracking cost function shown below. The deployment of the sail along the nadir with its edge oriented in the orbital velocity direction ensures minimal drag profile, resulting in each of the three Euler having equal weights in the cost function.

$$J_{Tracking} = \sum_{t_{Detumble}}^{t_f} \left\{ \left| \theta(t) \right| : \left| \theta(t) \right| > 5^\circ \right\} + \sum_{t_{Detumble}}^{t_f} \left\{ \left| \phi(t) \right| : \left| \phi(t) \right| > 5^\circ \right\} + \sum_{t_{Detumble}}^{t_f} \left\{ \left| \psi(t) \right| : \left| \psi(t) \right| > 5^\circ \right\} \quad [25]$$

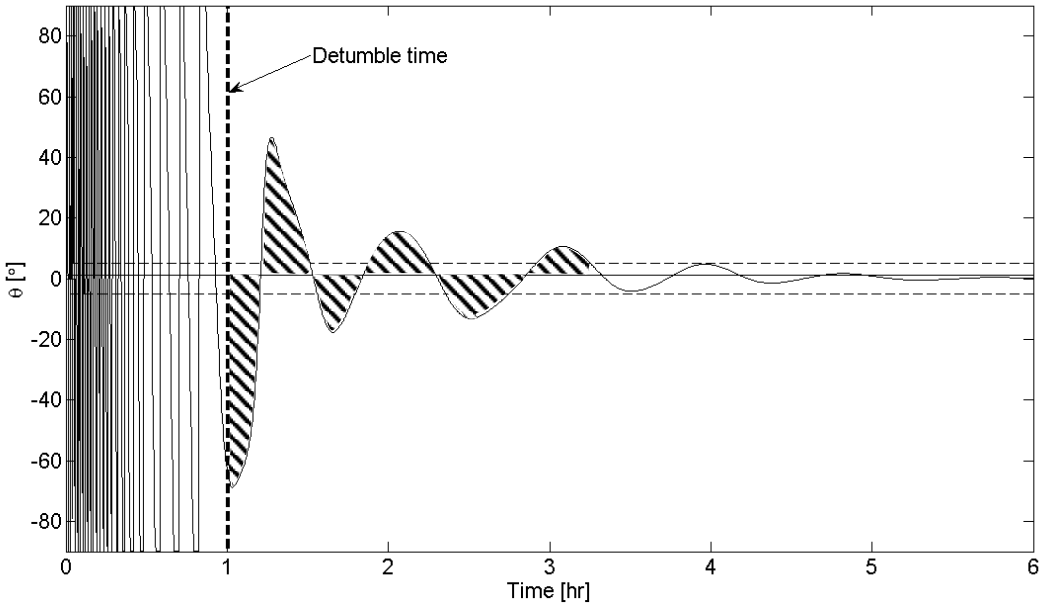

Figure 21. Graphical representation of tracking cost function.

A Matlab-based Genetic Algorithm[44] with default settings has been applied to the previously-discussed attitude control simulator and yielded the following results for the detumbling and tracking modes:

$$x_{Detumbling}^{GA} = \left[9.9902\times10^{-8} \;\; 8.8807\times10^{-7} \;\; 3.7887\times10^{-7} \;\; 8.1223\times10^{2} \;\; 5.1812\times10^{3} \;\; 4.6502\times10^{3} \right.$$
$$\left. 2.0665\times10^{2} \;\; 9.3325\times10^{2} \;\; 8.8855\times10^{2} \;\; 9.3973\times10^{8} \;\; 8.0773\times10^{8} \;\; 8.0687\times10^{7} \right]$$
$$x_{\text{Tracking}}^{GA} = \left[3.4335\times10^{-7} \;\; 5.4315\times10^{-7} \;\; 4.9135\times10^{-7} \;\; 7.0081\times10^{3} \;\; 9.7211\times10^{3} \;\; 1.6692\times10^{4} \right. \quad [26]$$
$$\left. -5.4157\times10^{1} \;\; 7.5313\times10^{2} \;\; -2.8717\times10^{2} \;\; 7.4764\times10^{7} \;\; 8.0728\times10^{8} \;\; 3.1255\times10^{7} \right]$$

2.5.2 Robust Results of Initial Detumbling and Stabilization of CubeSail Assembly

The above steps were performed for the previously-described sample orbit in order to find an GA-optimized set of $\mathbf{Q}$ and $\mathbf{R}$ matrices for both detumbling and tracking modes. These were then used to run a final 1000-case simulation with varying initial attitudes, all assuming the worst-case scenario with initial rotational rate of 5 º/sec

on all three axes. Figure 22 through Figure 24 are a representative sample of the output from a single run.

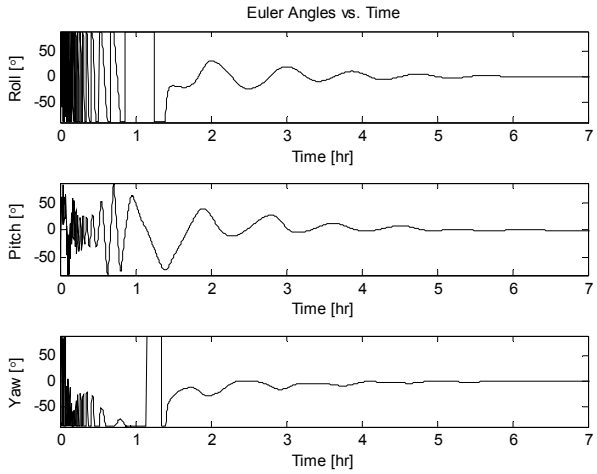

Figure 22. Offset from nadir pointing direction (left) and Euler angle history (right).

As can be seen in Figure 22, the spacecraft is stabilized in approximately 2 hours. The rotational rates are reduced to under 1 º/sec in 0.5 hours and further reduced to near zero in the next 1.5 hours as seen in Figure 23 (left). Figure 23 (right) shows the controller used almost 100% of available power initially to reduce the rotational rates and then used finer control to achieve the nadir-pointing attitude. The magnitude of torques applied to the spacecraft, which include magnetic, aerodynamic, and gravity gradient, are shown in Figure 24. It is worth pointing out that prior to sail deployment, the drag force is nearly negligible. This is due to the assumption that center of mass is aligned with the geometrical center, causing the center of gravity and center of pressure to coincide and produce no torque.

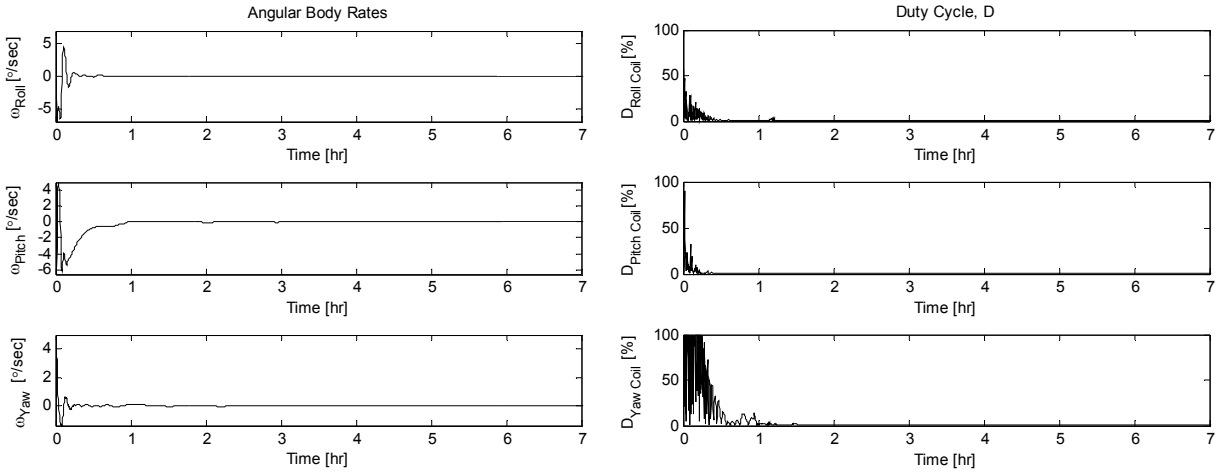

Figure 23. Angular body rates (left) and duty cycle (right).

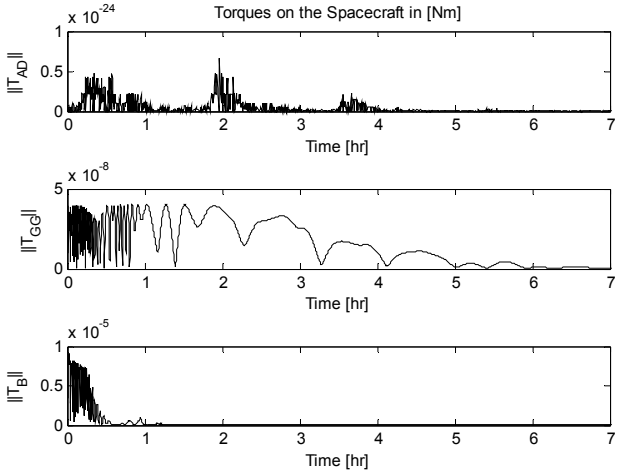

Figure 24. Torques on the spacecraft.

The Monte Carlo simulation with randomly varying initial attitudes confirmed existence of initial quaternions which are easily stabilizable and those that are not. The 1000-run simulation is seen as a reasonable statistical sampling that avoids biasing of certain attitudes. It is therefore possible to compute with reasonable accuracy the most likely detumbling and tracking times expected for the CubeSail spacecraft. The histograms of $t_{Detumble}$ and $t_{Tracking}$ from the Monte Carlo simulation are shown in Figure 26. The mean detumbling time is 1.23 hours with standard variation of 0.28 hours, while the mean tracking time is 2.70 hours with standard variation of 1.27 hours.

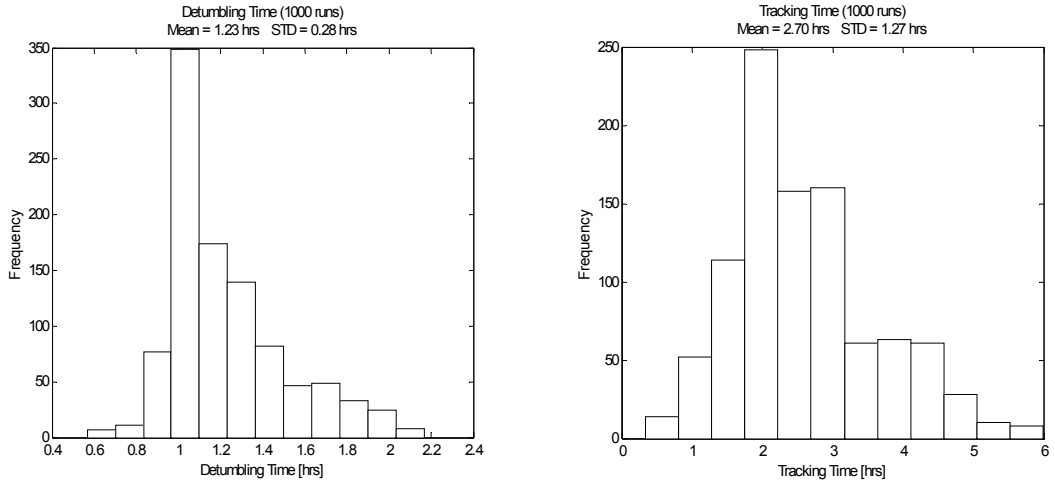

Figure 25. Histogram of detumbling time (left) and tracking time (right) from a 1000 run simulation. Simulation randomly varied initial quaternions and assumed worst-case angular rate of 5 º/sec on all three axis.

2.5.3 Energy Usage During Initial Detumbling and Stabilization of CubeSail Assembly

The general diagram of the interface between the CubeSail's attitude control system and the power system is shown in Figure 26. The current generated by the solar panels is fed into the LT1512 Single-Ended Primary Inductance Converter (SEPIC), which charges the two lithium-ion batteries onboard the spacecraft. The attitude control system uses the LTC1779 current mode step-down DC/DC converter to control the current to the three torque coils depending on the desired duty cycle.

Although the ACS uses the unregulated line and can therefore draw power either from the batteries or directly from the solar panels, this analysis assumes a constant voltage provided from the two batteries of 7.4 V. This is seen as an acceptable assumption since detumbling and reorientation will always be performed starting with fully charged batteries. In addition, the favorable discharge characteristics of lithium ion batteries (Figure 27) show a small decrease in voltage, especially in the first 20% of the discharge, which is the predicted range of operation.

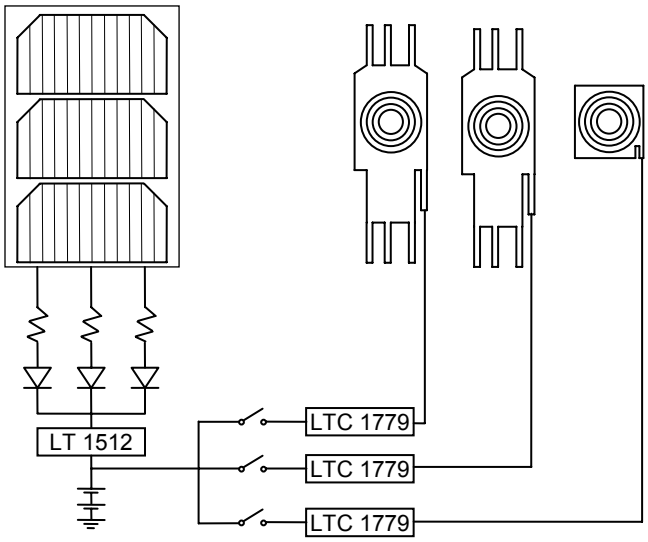

Figure 26. CubeSail ACS power system.

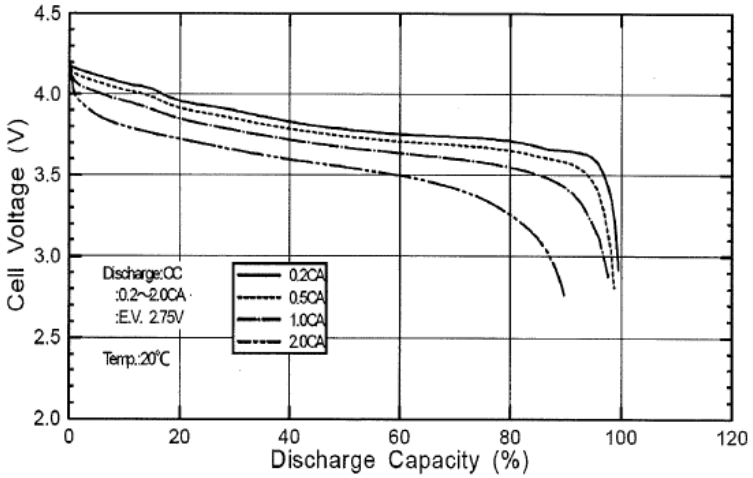

Figure 27. Discharge characteristics of a typical lithium ion battery.[45]

In order to obtain realistic power consumption during the initial detumbling and reorientation of the CubeSail assembly, the duty cycle computed by the LQR must be corrected for efficiency losses in the power system. The major source of inefficiency is the LTC1779 controller and as such it will be the focus of this analysis. The efficiency of the controller depends on the input voltage and the load current as shown in Figure 28.

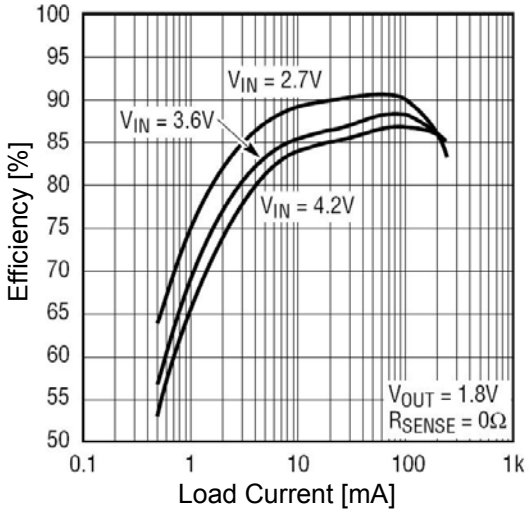

Figure 28. LTC 1779 efficiency vs. load current.[46]

Since the plot does not contain a curve for 7.4 V, the values of efficiencies vs. the load current are extracted directly from the plot using the *grabit.m* program47 for the 3.6 and 4.2 V curves. As a first step, the efficiency data is linearly interpolated over the load current interval of 0.5 to 250 mA in order to obtain equal number of data points (n, currently set at 1000). Next, the mean value of the difference between interpolated efficiencies is obtained according to the following equations:

$$\Delta\eta = \eta_{4.2\,V}(I) - \eta_{3.6\,V}(I)$$
$$\overline{\Delta\eta} = \frac{1}{n}\sum_{k=1}^{n}\Delta\eta_k \qquad [27]$$

Next, the mean value of the difference in efficiencies, $\overline{\Delta\eta}$, is divided by the change in voltage between the two curves (4.2 - 3.6 = 0.8 V), in order to obtain an average drop in efficiency per unit volt. It is assumed that the magnitude of the change remains constant in the range of the load current. Lastly, the average drop in efficiency from the 4.2 V to the desired 7.4 V curve can be estimated by multiplying by the change in voltage of 3.2 V (7.4 – 4.2 = 3.2). The final equation for the desired efficiency curve can therefore be written as:

$$\eta_{7.4\,V}(I) = \eta_{4.2\,V}(I) + \overline{\Delta\eta} \cdot \frac{7.4 - 4.2}{4.2 - 3.6} \qquad [28]$$

The resulting efficiency vs. load current curve for the 7.4 V input voltage is shown in Figure 29.

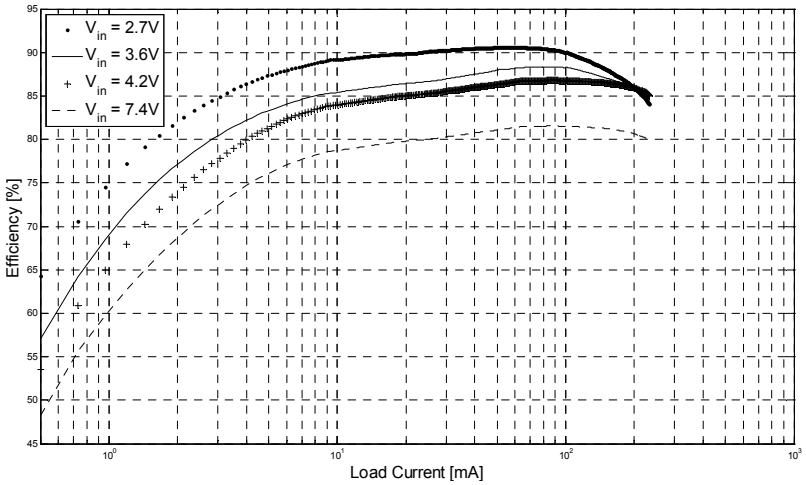

Figure 29. LTC1779 efficiency vs. load current for V_{in} = 7.4V .

The LQR simulation outputs an optimal set of duty cycles ($I = I_{\max} \cdot DutyCycle$) that need to be applied to each of the three coils ($k = 1, 2, 3$) for a prescribed duration, T_{LQR}, in order to stabilize the spacecraft. The total energy expended by the three torque coils can therefore be written as:

$$E = \sum_{k=1}^{3} \sum_{j=1}^{N} I_{\max} \cdot DutyCycle(k, j) \cdot \eta_{7.4V}(I) \cdot V \cdot T_{LQR} \qquad [29]$$

Where $N = (t_f - t_0) / T_{LQR}$ and T_{LQR} is assumed constant and equal for all three coils. The function $\eta_{7.4V}(I)$ is found by Equation 28 evaluated at the desired load current.

Similarly to statistical analysis of the detumbling and tracking times, the Monte Carlo simulation results are used to compute average expected power consumption during the initial stabilization of the CubeSail assembly. The energy from each run is computed from Equation 29 and shown as a histogram in Figure 30. The mean energy

consumption is 0.17 W-hr with a standard deviation of 0.03 W-hr. Since each tip satellite uses two LI-2DS1P-2200 batteries[48] with a total energy storage of 32.56 W-hr per satellite, these results demonstrate that even for the worst-case scenario of 5 º/sec rotation on each axis, the spacecraft can be detumbled and stabilized without intermediate recharging of the batteries.

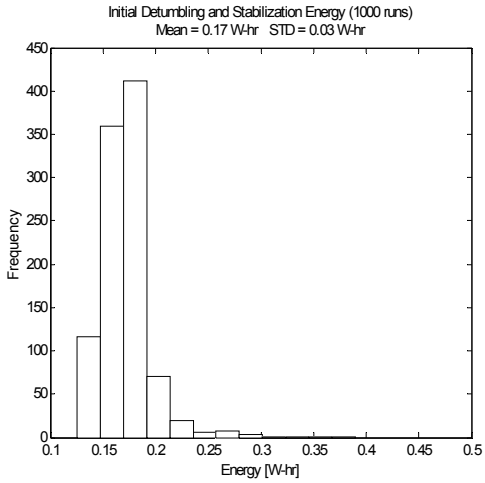

Figure 30. Histogram of energy usage during initial stabilization and detumbling from a 1000 run simulation. Simulation randomly varied initial quaternions and assumed worst-case angular rate of 5 º/sec on all three axis.

CHAPTER 3

DEPLOYMENT METHODS AND SELECTION

3.1 Preliminary Analysis of Deployment Strategies

Analysis performed during Phase I effort under the NASA SBIR contract (NNX08CC85P) revealed two viable deployment methods: the spin induced deployment and the gravity gradient induced deployment. In the first method, shown in Figure 31 (left), the mated satellites are spun together and then released using the Separation Release Unit—discussed in detail in a later chapter. The film is unwound until the rotational rate of the system decreases to a prescribed threshold level that ensures the film does not billow out excessively. At this time, the tip satellites rotate in opposite directions along the long axis of each spacecraft inducing a twist in the film. If properly oriented relative to the sun, the resultant pitch in the blade forces the system to act as a 'propeller' and spin up. Once the desired rotational velocity is achieved, the satellites return to their zero-pitch attitude and more film is unwound. This process is repeated until the final spin rate and deployment length are achieved. The centrifugal force of the rotating system provides the tension necessary to keep the film relatively flat. The challenge of this approach resides in the complicated dynamics of two independent CubeSats connected by a non-rigid tether.

The second deployment method, shown in Figure 31 (right), utilizes a gravity gradient between the two tip satellites to provide the necessary tension in the film. The mated satellites are oriented into a nadir pointing attitude and separated using a spring mechanism. The film is unwound using the built-in motor in each nanosatellite until the entire sail length is deployed at which point the gravity gradient force is at the maximum

and provides the required tension. The advantage of this method is the passive attitude stabilization of the system. The following sections describe preliminary analysis of each of the methods and describe their advantages.

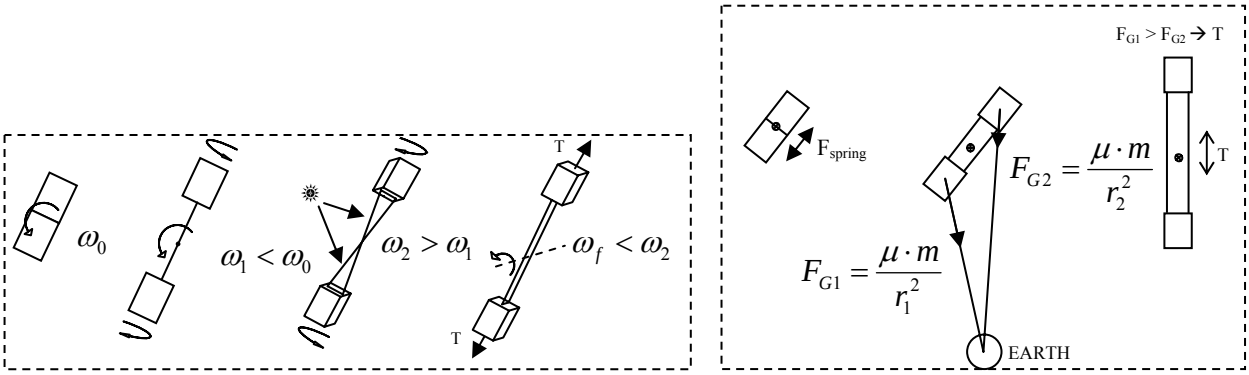

Figure 31. Sail deployment options: spinning (left) and gravity gradient (right).

3.1.1 Preliminary Analysis of Spin Induced Deployment

The preliminary analysis of the spin induced deployment is performed assuming that the spacecraft is inserted into a sun-synchronous terminator orbit. The selection of this orbit was motivated by complicated dynamics during the spin-up maneuvers and limited responsiveness of the magnetic attitude control system and result in elimination of orbits with varying lighting conditions.

The desired nominal orientation throughout the deployment is illustrated in Figure 32, with the minimal cross-sectional area presented to the sun and with the spin vector normal to the orbital velocity vector. It is important that the spacecraft rotation occur through the sail width and not the sail thickness in the event that the satellites are not perfectly aligned with the film as shown in Figure 33. If such a situation were to occur, the satellite will exert a torque on the film and it is desired that the torque be applied over the film width (78 mm) rather than the sail thickness (6.2 μm) to prevent damage to the film.

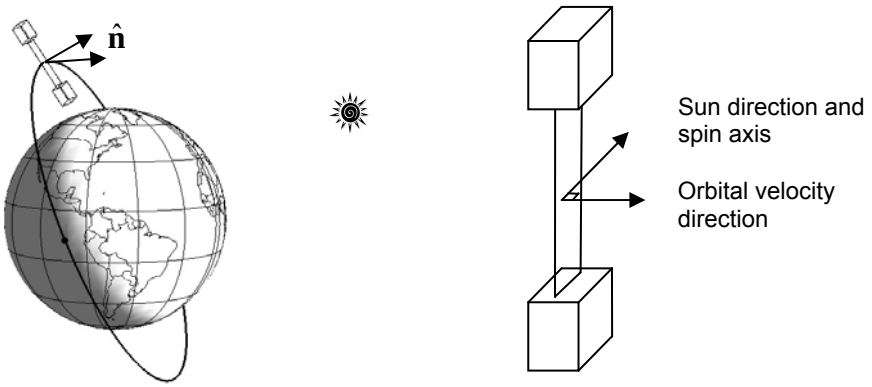

Figure 32. On orbit CubeSail configuration for spin induced deployment.

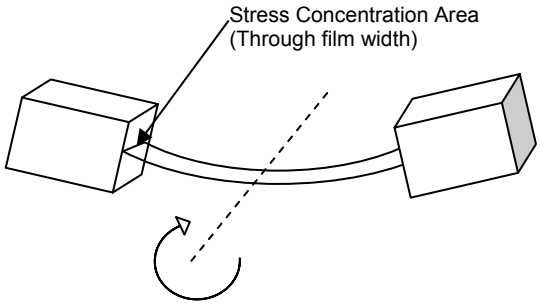

Figure 33. Exaggerated behavior of sail-satellite system during spin deployment.

This rotation will unfortunately result in either time-varying cross-sectional area presented into the velocity direction (when spin axis points towards the sun) or a time-varying cross-sectional area presented to the sun (when spin axis points towards the orbital velocity direction). Since the main attribute of the sun-synchronous terminator orbit is the constant lighting condition, the latter of the two scenarios is chosen and the spacecraft must be launched into sufficiently high altitude to make the aerodynamic drag effects manageable.

The initial spin-up is achieved while the two satellites are held rigidly together by the SRU. Magnetic torquers on both spacecraft are used to rotate the assembly around the sun-pointing axis, to a maximum rate of 6 °/sec (1 RPM). The maximum rate is dictated by the magnetic dipole moment of the coils and the strength of Earth's magnetic field. The final rotational rate at full deployment is dictated by the requirement

that the film remain relatively flat. Previous studies found that for a spinning solar sail configuration, a spin rate that guarantees acceptable sail flatness is achieved when the force ratio (FR) of centrifugal force to a 'billowing force' (either solar pressure or aerodynamic drag) is between 3:1 and 5:1.[25] Given the proposed design, this corresponds to an angular rate at full 260 m deployment of 1.274 rev/hr (FR=5).

The preliminary analysis assumes an undeformed (flat) sail with physical parameters of the sail-satellite system defined in Figure 34 and the origin of the coordinate system at the center of mass of the system. In this notation, l_{sail} varies between 0 and 260 m, $\omega_{\min} \le \omega \le \omega_{\max}$, and the system rotates around the y-axis. Although the choice of this spin axis creates an unfavorable drag profile, it was chosen purposely to spread the stress on the film induced if the two satellites are not perfectly co-boresighted. In general, this torque is desirable since it re-aligns the satellite with the film material, but during film deployment this torque must act through the width of the slit to avoid damage to the film.

Lastly, it is important to notice that as the spacecraft makes one full revolution, it will encounter maximum and minimum drag profiles resulting in periodic straightening and billowing-out of the sail. The effects of this accordion-like behavior are not investigated in this preliminary analysis.

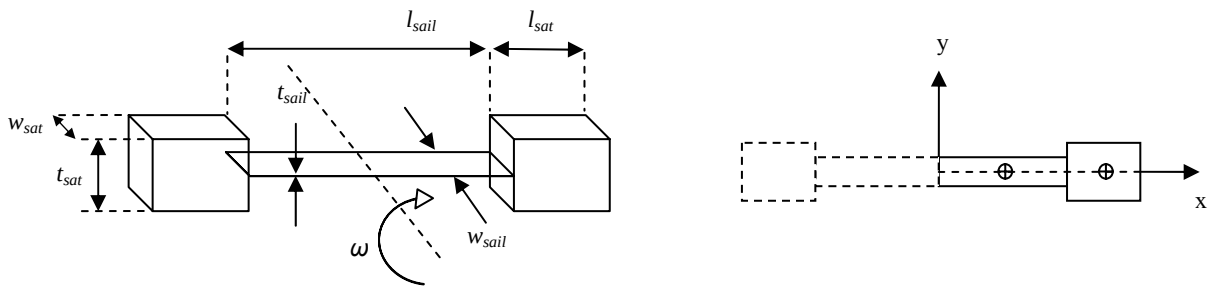

Figure 34. Physical parameters of CubeSail spacecraft.

The moment of inertia of this system, computed individually for the sail and each satellite, can be written as:

$$\mathrm{I}_{yy,sail}\left(l_{sail}\right)=\frac{m_{sail}\cdot l_{sail}^{2}}{12}=\frac{\rho_{sail}\cdot l_{sail}^{3}\cdot w_{sail}\cdot t_{sail}}{12} \quad [30]$$

$$I_{yy,sat}\left(l_{sail}\right)=\frac{2m_{sat}-\rho_{sail}\cdot l_{sail}\cdot w_{sail}\cdot t_{sail}}{24}\left(l_{sat}^{2}+w_{sat}^{2}\right)+\frac{1}{8}\left(2m_{sat}-\rho_{sail}\cdot l_{sail}\cdot w_{sail}\cdot t_{sail}\right)\left(l_{sail}+l_{sat}\right)^{2} \quad [31]$$

where m_{sail} is the mass of the deployed sail and ρ_{sail} is the sail density. It should be noted that the sail density appears in the equation for the moment of inertia of the satellite since m_{sat} is defined as the satellite mass including the film and must be adjusted as the film is deployed.

The principle of conservation of angular momentum about the center of mass can be written as:

$$I_{0}\cdot\omega_{0}=\left[\sum_{i=1}^{m}I_{i}\left(l\right)\cdot\omega_{i}\left(l\right)\right]\Bigg|_{l=l_{sail}} \quad [32]$$

For the first spin up maneuver when the two satellites are still mated, the two satellites can be treated as a single rigid body with a moment inertia I_0 spinning at a rate ω_0. The system moment of inertial is computed according to the following equation:

$$I_{0}=m_{sat}\cdot\left(\left(2\cdot l_{sat}\right)^{2}+w_{sat}^{2}\right)/6 \quad [33]$$

The right hand side of Equation 32 represents the system when a length of sail, l_{sail}, has been deployed. At this point of the study, the system is considered as three rigid bodies (m = 3) rotating around the origin. It is therefore possible to rewrite Equation 32 as:

$$I_0 \cdot \omega_0 = \omega(l_{sail}) \cdot \left[I_{sail}(l_{sail}) + I_{sat,1}(l_{sail}) + I_{sat,2}(l_{sail}) \right] \quad [34]$$

where I_{sail} has been defined in Equation 30. The two satellites are identical and their moment of inertia around the system origin is defined by Equation 31. The dependence of all the variables on a single independent variable, l_{sail}, is repeated for emphasis. Solving for the rotational velocity, $\omega(l_{sail})$, results in the following equation:

$$\omega(l_{sail}) = \frac{I_0 \cdot \omega_0}{I_{sail} + 2 \cdot I_{sat}} \quad [35]$$

It is now necessary to determine the upper and lower bounds on the rotational velocity. The minimum angular velocity, $\omega_{\min}$, can be determined from the previously discussed force ratio of centrifugal to aerodynamic drag force. Assuming a flat sail, the aerodynamic drag force can be written as a function of deployed sail length as:

$$F_{AD} = \frac{1}{2} \rho_{atm} \cdot v^2 \cdot C_D \cdot A = \frac{1}{2} \rho \cdot v^2 \cdot C_D \cdot w_{sail} \cdot l_{sail} \quad [36]$$

where C_D is the coefficient of drag and is assumed to be equal to 2.2. The parameter ρ_{atm} is the atmospheric density and is assumed to be the mean density at 750 km between solar maximum and solar minimum and is equal to 4.48x10^{-14} kg/m^3. Lastly, v is the orbital velocity which, for a circular orbital with an altitude at 750 km, is equal to 7.48 km/s.

The centrifugal force at the center of mass of one of the satellites can be written as:

$$F_{centr} = \sum_i m_i \cdot \omega_i^2 \cdot r_i$$

$$F_{centr} = \left[\frac{m_{sail}}{2} \cdot \omega^2 \cdot \frac{l_{sail}}{4} + \left(m_{sat} - \frac{m_{sail}}{2} \right) \cdot \omega^2 \left(\frac{l_{sail}}{2} + \frac{l_{sat}}{2} \right) \right] \quad [37]$$

$$F_{centr}(l_{sail}, \omega) = \frac{\rho_{sail} \cdot t_{sail} \cdot w_{sail} \cdot \omega^2 \cdot l_{sail}^2}{8} + \frac{1}{2} \cdot \left(m_{sat} - \frac{\rho_{sail} \cdot t_{sail} \cdot w_{sail} \cdot l_{sail}}{2} \right) \cdot \omega^2 \cdot (l_{sail} + l_{sat})$$

The optimality condition on sail flatness is simply written as:

$$F_{centr} / F_{AD} \geq k_{FR} \qquad [38]$$

where k_{FR} is the force ratio constant. As mentioned previously, the historical optimal value of k_{FR} was found to be between 3 and 5 with the latter value used in the subsequent analysis.

After substitution of the above results for the aerodynamic and centrifugal forces, the flatness condition can be written as:

$$\frac{\frac{\rho_{sail} \cdot t_{sail} \cdot \omega^2 \cdot l_{sail}}{2} + 2 \cdot \left(\frac{m_{sat}}{w_{sail} \cdot l_{sail}} - \frac{\rho_{sail} \cdot t_{sail}}{2} \right) \cdot \omega^2 \cdot \left(l_{sail} + l_{sat} \right)}{\rho \cdot v^2 \cdot C_D} \geq 5 \qquad [39]$$

The minimum angular velocity is therefore found iteratively in two steps. In the first step, given a deployed sail length l_{sail}, the angular velocity of the system is found using Equation 35. In the second step, the computed angular velocity and l_{sail} are used to determine whether the condition in Equation 39 has been violated. If the condition is not violated, the sail is deployed further; if it is violated, the sail deployment is halted and a pitching maneuver is executed to spin-up the sail-satellite assembly. In other words, the value of ω at some l_{sail} that makes Equation 39 equal to k_{FR} is by definition $\omega_{\min}$.

Alternatively, $\omega(l_{sail})$ from Equation 35 is substituted into Equation 39 and solved for l_{sail} when it is exactly equal to k_{FR}. This result could then be substituted back into Equation 35 to find $\omega_{\min}$.

The maximum force the sail can withstand can be written as:

$$F_{\max} = \sigma_{yield} \cdot A_{cs} = \sigma_{yield} \cdot w_{sail} \cdot t_{sail} \quad [40]$$

Assuming that the only force acting in the plane of the sail film is the centrifugal force, it is possible to equate Equations 37 and 40 and solve for ω, which now becomes $\omega_{\max}$, the maximum angular velocity the film can withstand before it rips. Although the centrifugal force is not the only force acting on the sail, it will be shown later that the system will be spun-up to approximately 1% of this value and since other forces are relatively weaker, this assumption is seen as acceptable. The maximum rotation velocity can therefore be written as:

$$\omega_{\max} = \sqrt{\frac{8 \cdot \sigma_{yield}}{\rho_{sail} \cdot l_{sail,f}^2 + \left(\frac{4 \cdot m_{sat}}{w_{sail} \cdot t_{sail}} - 2 \cdot \rho_{sail} \cdot l_{sail,f} \right) \cdot \left(l_{sail,f} + l_{sat} \right)}} \quad [41]$$

In the above equation, $l_{sail,f}$ is the final length of the sail deployed when the system reaches $\omega_{\min}$. The yield strength for Mylar—a typical solar sailing film substrate material—is equal to 172 MPa.

The simulation is therefore run in the following sequence:

1. Given an initial rotational velocity, ω_0, initial moment of the inertia of the system, I_0, and initial length of the deployed sail, l_{sail}, use Equation 35 to compute $\omega(l_{sail})$.
2. Use the computed value of ω in Equation 39 to check if FR exceeds k_{FR}.
3. If FR > 5, set $l_{sail} = l_{sail} + \Delta l_{sail}$ and repeat steps 1 and 2.
4. If FR ≤ 5 and l_{sail} < 250 must perform a spin-up maneuver:
    a. Set $l_{sail} = l_{sail,f}$ and use Equation 41 to find $\omega_{\max}$.
    b. Set $\omega_0 = 0.01 \cdot \omega_{\max}$ (1% of maximum angular velocity).
    c. Use Equations 30 and 31 and $l_{sail,f}$ to compute $\mathrm{I}_{yy,sail}\left(l_{sail,f}\right)$ and $I_{yy,sat}\left(l_{sail,f}\right)$.
    d. Set $I_0 = \mathrm{I}_{yy,sail}\left(l_{sail,f}\right) + 2 \cdot I_{yy,sat}\left(l_{sail,f}\right)$.
5. If l_{sail} < 260m, go to step 1.

The above steps are used to compute crucial information about the spin induced deployment such as number of spin-up maneuvers, initial and final rotational rates of the system, and sail length deployed at each maneuver. An additional value that is often of interest to the designer is the duration of full deployment. The computation of this duration takes into account time necessary to unwind the film and time needed to spin-up the assembly, however it does not account for the satellite pitching maneuvers.

The time to deploy a sail of length l_{sail} is computed by assuming a constant deployment rate $\dot{l}_{sail}$ of 5 cm/sec (each roll deploys at 2.5 cm/sec) and using Equation 42 below.

$$t_{deploy}\left(l_{sail}\right) = l_{sail} / \dot{l}_{sail} \qquad [42]$$

The time for the system to spin up to the some final angular velocity ω_f is found in the following way. Assuming that the blade pitch angle at the origin is zero and varies linearly to some final value θ_{tip} at one satellite and $-\theta_{tip}$ at the other satellite, it is possible to write the torque on the sail as[25]:

$$\tau = \frac{P \cdot w_{sail} \cdot l_{sail}^{2\ 2}}{8 \cdot \theta_{tip}} \left[-\cos\left(\theta_{tip}\right) - \frac{1}{3}\cos\left(3\theta_{tip}\right) + \frac{\sin\left(\theta_{tip}\right)}{\theta_{tip}} + \frac{\sin\left(3\theta_{tip}\right)}{9\theta_{tip}} \right] \qquad [43]$$

where P is the solar pressure whose value at 1 AU is equal to 9.1×10^{-6} N/m^2. Although the maximum of this function occurs at 47.33°, the simulation assumes a slightly smaller pitch angle of 35° for all pitching maneuvers. The torque on the system can also be written as:

$$\begin{aligned} \tau &= I \cdot \dot{\omega} \\ \dot{\omega} &= \tau / I = const \end{aligned} \qquad [44]$$

where $I = I_{yy,sail} + 2 \cdot I_{yy,sat}$ and is defined as before by Equations 30 and 31. The rotational velocity can be written as:

$$\omega(t) = \dot{\omega} \cdot t + \omega(0) \qquad [45]$$

Evaluating Equation 45 at the final time when the system is spun-up to ω_f and solving for t, yields the following result for the spin-up time:

$$t_{spin-up} = \frac{\omega_f - \omega(0)}{\dot{\omega}} = \frac{\left(\omega_f - \omega(0)\right) \cdot I}{\tau} \qquad [46]$$

Typically, for each maneuver, ω_f is a percentage of the maximum angular velocity found in Equation 41 and $\omega(0)$ is the minimum angular velocity the system achieved by deploying a length of film l_{sail} without violating the flatness condition.

It is now possible to simulate the film deployment exactly as described in steps 1 through 5. The results of this simulation ran for three different values of ω_0 are presented below in Table 4.

Table 4. Results of spin induced film deployment.

	$\omega_0 = 10\% \cdot \omega_{\max}$	$\omega_0 = 1\% \cdot \omega_{\max}$	$\omega_0 = 0.5\% \cdot \omega_{\max}$
Number of Deployment Maneuvers	3	4	4
l_{sail} deployed at each maneuver [m]	[2.2, 80.0, 167.8]	[2.2, 23.7, 133.3, 90.9]	[2.2, 16.1, 68.2, 163.6]
ω_0 at each maneuver [deg/sec]	[6.0, 47.0, 8.0]	[6.0, 4.7, 1.4, 0.6]	[6.0, 2.3, 0.8, 0.4]
$\omega_{\min} = \omega_{final}$ at each maneuver [deg/sec]	[.037, .038, .885]	[.037, .038, .038, .236]	[.037, .038, .038, .048]
t_{deploy} at each maneuver [sec]	[44, 1600, 3357]	[44, 473, 2666, 1817]	[44, 321, 1364, 3271]
$t_{spin-up}$ at each maneuver [hrs]	[275, 41]	[27, 7, 3]	[14, 4, 2]
Total deployment time [hrs]	335.7	39.7	21.8

Interestingly, although the scenarios with lower spin-up velocity require one additional spin-up maneuver, they take significantly less time to complete the full film deployment. This is due to the fact that the angular acceleration during spin-up is relatively low resulting in long spin-up times. It is therefore quicker to spin up the

system to a lower angular velocity more times, than to have few large spin-up maneuvers. It is also important to note that $\omega_{\max} \propto \sqrt{\sigma}$; as a result, for $\omega_0 = 10\% \cdot \omega_{\max}$ $\sigma = 1\% \cdot \sigma_{yield}$ and similarly for $\omega_0 = 1\% \cdot \omega_{\max}$ $\sigma = 0.01\% \cdot \sigma_{yield}$.

3.1.2 Preliminary Analysis of Gravity Gradient Induced Deployment

Preliminary analysis of the gravity gradient deployment was performed for spacecraft in a co-planar ecliptic orbit. In this case, and if the sail deployment occurs edge on as shown in Figure 35, the effects of solar radiation pressure and drag can be neglected in the formulation.

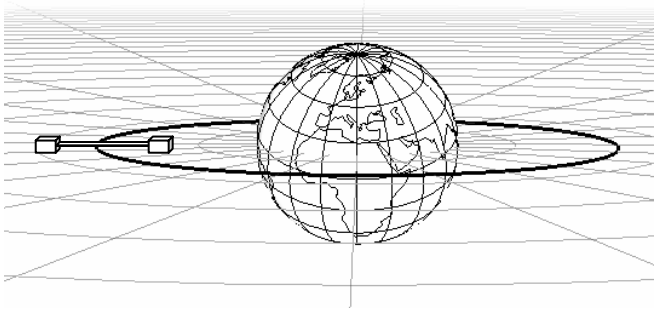

Figure 35. Gravity gradient sail deployment in a co-planar ecliptic orbit.

The relative motion of the tip satellites (assumed to be point masses) is formulated through the use of 'reduced mass' defined as:

$$m_1' = \frac{m_1 m_2}{m_1 + m_2} \quad \text{and} \quad m_2' = m_1 + m_2 \qquad [47]$$

It is possible to show that the correct kinetic energy relative to an inertial frame at the center of mass is obtained by assuming m_2 is fixed and using the reduced mass m_1' in place of m_1 in the standard equations for the kinetic energy. Similarly, the correct potential energy can be obtained by substituting reduced masses m_1' and m_2' in place of

m_1 and m_2 respectively and the calculation of the forces, relative motions, and energies of the system will be correct.[49]

Figure 36 forms the basis of the following formulation. It is assumed that the tether is inextensible and massless and that the center of mass of the system travels along a circular orbit with no perturbations. This assumption is seen as an acceptable first order approximation, especially given that typical deployment times are relatively short and guarantee small perturbations due to oblateness or third body effects.

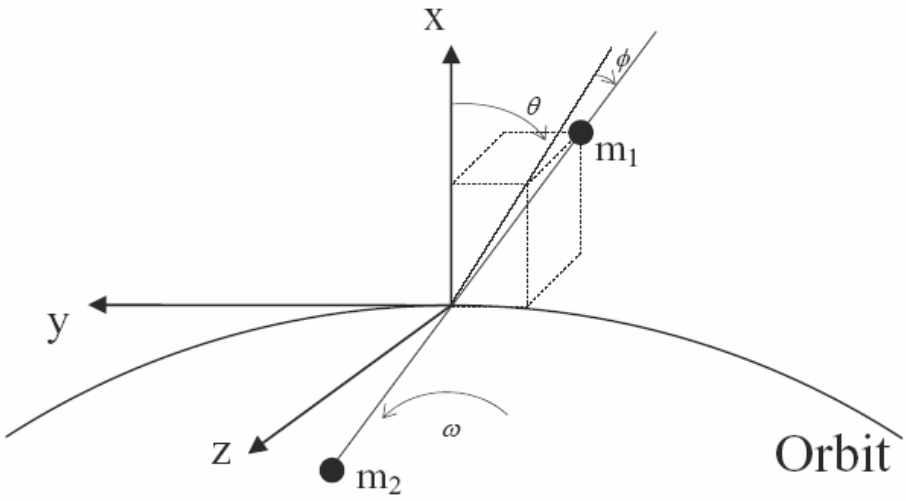

Figure 36. Gravity-gradient deployment configuration.

The equations of motion are obtained by first forming the Lagrangian function as follows:

$$L = T - V \qquad [48]$$

where

$$\begin{aligned} T &= \frac{m_1'}{2}\left[\dot{l}^2 + l^2\left\{\left(\dot{\theta}+\omega\right)^2\cos^2\phi + \dot{\phi}^2\right\}\right] \\ V &= \frac{m_1'}{2}\omega^2 l^2\left(1 - 3\cos^2\theta\cdot\cos^2\phi\right) \end{aligned} \qquad [49]$$

and then writing the Lagrange equations for each of the generalized coordinates as follows[50,51,52]:

$$\frac{d}{dt}\left(\frac{\partial L}{\partial \dot{q}_i}\right)-\frac{\partial L}{\partial q_i}=Q_i \text{ with } q_i=(l,\theta,\phi) \quad for \quad i=1,\ 2,\ 3 \tag{50}$$

The resultant EOM are as follows:

$$\begin{aligned}
\ddot{l} &= \frac{T}{m_1'}+l\left[\left(\dot{\theta}+\omega\right)^2\cos^2\phi+\dot{\phi}^2\right]-\omega^2 l\left(1-3\cos^2\theta\cdot\cos^2\phi\right)\\
\ddot{\theta} &= -2\frac{\dot{l}}{l}\left(\dot{\theta}+\omega\right)+2\dot{\phi}\left(\dot{\theta}+\omega\right)\tan\phi-3\omega^2\cos\theta\cdot\sin\theta\\
\ddot{\phi} &= -2\frac{\dot{l}}{l}\dot{\phi}-\left(\dot{\theta}+\omega\right)^2\cos\phi\cdot\sin\phi-3\omega^2\cos^2\theta\cdot\cos\phi\cdot\sin\phi
\end{aligned} \tag{51}$$

The problem is solved as a two-point boundary value problem (2PBVP) by first rewriting the above second order differential equations (ODEs) as a system of first-order ODEs:

$$\begin{aligned}
\dot{x}_1 &= x_4\\
\dot{x}_2 &= x_5\\
\dot{x}_3 &= x_6\\
\dot{x}_4 &= \frac{T}{m_1'}+x_1\left[\left(x_5+\omega\right)^2\cos^2\left(x_3\right)+x_6^2\right]-\omega^2 x_1\left[1-3\cos^2\left(x_2\right)\cdot\cos^2\left(x_3\right)\right]\\
\dot{x}_5 &= -2\frac{x_4}{x_1}\left(x_5+\omega\right)+2x_6\left(x_5+\omega\right)\tan\left(x_3\right)-3\omega^2\cos\left(x_2\right)\cdot\sin\left(x_2\right)\\
\dot{x}_6 &= -2\frac{x_4}{x_1}\cdot x_6-\left(x_5+\omega\right)^2\cos\left(x_3\right)\cdot\sin\left(x_3\right)-3\omega^2\cos^2\left(x_2\right)\cdot\cos\left(x_3\right)\cdot\sin\left(x_3\right)
\end{aligned} \tag{52}$$

The simulations assume a deployment of CubeSail spacecraft into a 750 km circular orbit, resulting in the orbital angular rate of 0.001049 rad/s. The initial deployment conditions are as follows:

$$\begin{aligned}
\left[l\quad\theta\quad\phi\quad\dot{l}\quad\dot{\theta}\quad\dot{\phi}\right]^T_{t=t_0} &= \left[1\,m\quad 5^\circ\quad 5^\circ\quad \dot{l}_0\quad 0\quad 0\right]^T\\
\left[l\quad\theta\quad\phi\quad\dot{l}\quad\dot{\theta}\quad\dot{\phi}\right]^T_{t=t_f} &= \left[260\,m\quad 0\quad 0\quad 0\quad 0\quad 0\right]^T
\end{aligned} \tag{53}$$

The initial deployment rate, $\dot{l}_0$, and constant tension, T, are solved using a built-in Matlab 2PBVP solver[53] to satisfy the boundary conditions shown above.

Figure 37 (left) shows that the sail is fully deployed in approximately 1.25 hours and that the deployment rate is never negative, indicating that the motor does not need to be reversed. The in- and out-of-plane angle time histories are shown in Figure 37 (right) and demonstrate that even with initial perturbations of ±5º away from the nadir direction, they quickly return to the desired configuration. The specific values of the initial deployment rate and tension are 0.175 m/s and 6.44x10^{-4} N respectively.

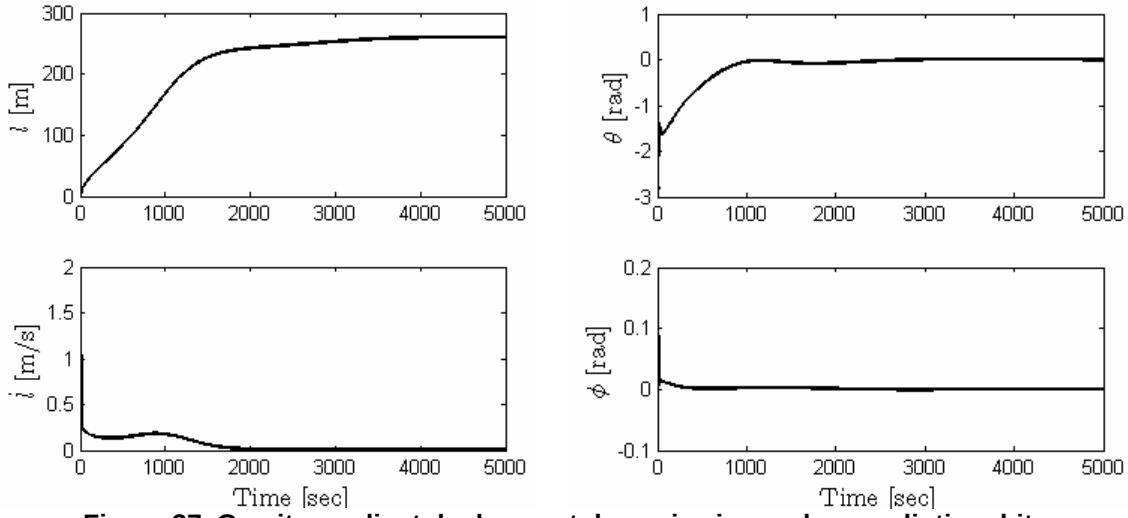

Figure 37. Gravity gradient deployment dynamics in co-planar ecliptic orbit.

It is important to note that gravity gradient deployment is not constrained to the co-ecliptic orbit. Figure 38 demonstrates edge on deployment into non-co-ecliptic orbit and shows that the above presented Lagrangian equations must be modified to include force terms due to solar radiation pressure. If the film deployment occurs edge on, the aerodynamics force can be neglected in the first-order analysis.

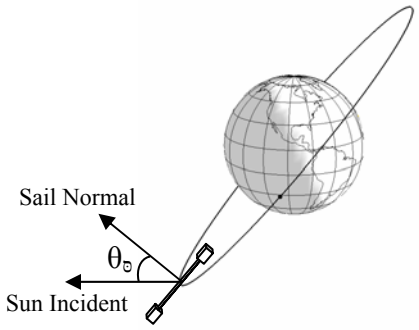

Figure 38. Gravity gradient deployment into non-co-ecliptic orbit.

3.2 Selection of Deployment Method for the First CubeSail Demonstration

Preliminary analysis of the spin induced and the gravity gradient deployment methods demonstrated that both are viable options. In order to systematically select the most optimum method, two tools have been utilized. The first is a qualitative method widely used in the field of decision analysis called the 'force field diagram.' The second method, often used in systems engineering, is more quantitative in nature and aims at identifying key mission drivers and technological solutions that best satisfy them. Both methods are described in the subsequent sections and applied to determine most optimal deployment method—in terms of mission success.

3.2.1 Deployment Method Selection using Force Field Diagrams

Force field diagrams are a qualitative tool often used in decision analysis in situations when there is a large number of arguments for and against a decision, when there exists a need to identify risks associated with a planned action and to develop a strategy for counteracting them, or when there exists a need to identify key causes of successful or unsuccessful action. Force field diagrams visually organize and display the arguments by presenting each argument or a reason as an arrow pointing towards a line. The arguments on the left of the line are in favor of the particular decision or action

and the arguments on the right are against it. The vertical location along the line indicates the importance, or weight, of that particular argument to the decision with higher arrows having larger weight. The underlying idea of the force field diagrams is of two forces pushing against each other, with the greatest overall force winning. The combination of weight of each argument and number of arguments constitutes the overall force for that side and represents the attitude of the team towards a particular decision.[54,55]

Figure 39 is the force field diagram for the gravity gradient deployment method and lists arguments in favor and against using this method. The discussion of these arguments and explanation of the relative importance of each is discussed next.

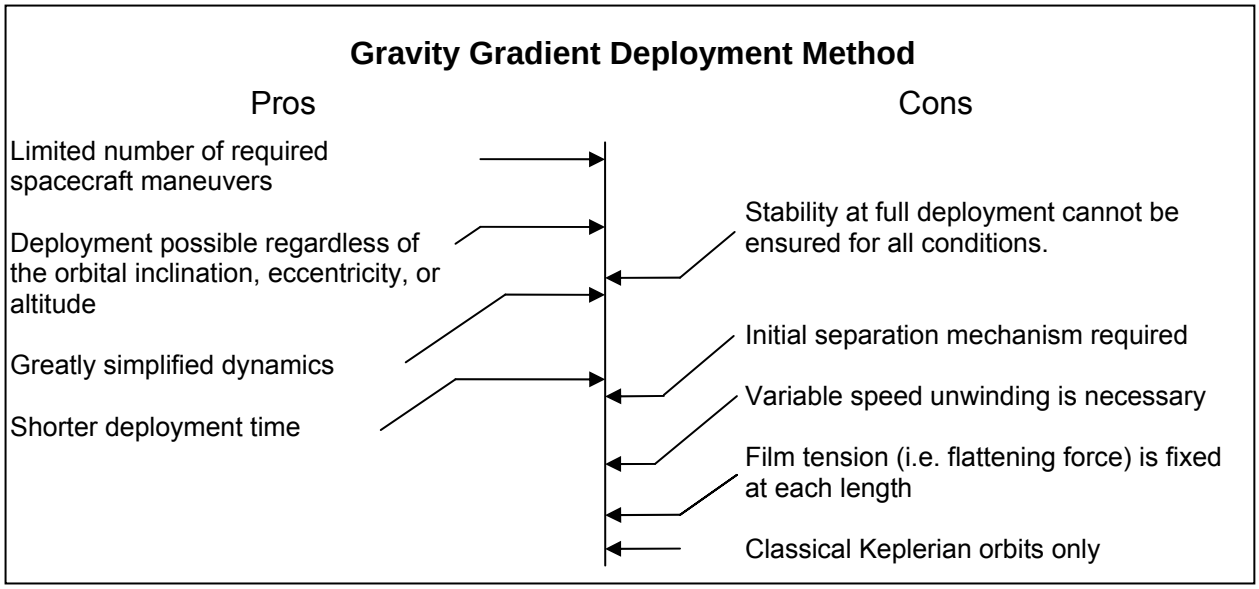

Figure 39. Force field diagram for the gravity gradient deployment method.

In the gravity gradient deployment method, the limited number of required spacecraft maneuvers is seen is a positive attribute due to previously discussed limitations of the attitude control system. The limited responsiveness of the system and restricted power that is available for maneuvering, create a system that favors a design with less active actuation. In addition, the ability to deploy into a wide range of

Keplerian orbits (based on inclination, eccentricity, and altitude) allows for increased number of launch opportunities resulting in an on-schedule demonstration. Due to the non-rotating nature of the gravity gradient deployment in the presence of non-conservative forces, the dynamics of the sail-satellite behavior are simpler and are less sensitive to modeling errors. This approach also creates 'reliability through simplicity' since there are less points of potential failure.[56] Lastly, the deployment time for gravity gradient is on the order of 2 hours, while the spin induced deployment takes approximately 20 hours to complete (assuming sufficient onboard power exists and no recharging is necessary).

Although there are several arguments against using the gravity gradient method, all are ranked relatively low due to ease of solving these issues. The conditions necessary to keep the film in tension must be found, however previous studies in tethered space systems guarantee the existence of these conditions. The necessity for a mechanism which provides initial separation velocity is resolved by placing two or more compressed springs between the spacecraft—a simple and reliable method. The need of variable deployment speeds has been anticipated with the purchase of a variable speed motor during the Phase I program. In addition, the ability to control the initial separation velocity through a proper selection of stiffness constants of the separation springs, allows for a design of a system whose relative velocity will not exceed the maximum speed of the motor.

The inherent nature of the gravity gradient method dictates that the flattening force is fixed at each sail length during the deployment. This effect will be most pronounced in the performance of the sail during orbital maneuvering when the solar

radiation pressure may have to be throttled down (through attitude adjustments) to prevent excessive billowing. This, in turn, will result in longer transfer times—a qualitative impact of which must be assessed. Regardless of the severity of the impact, the key technologies will be validated prior to any orbital maneuvering and longer transfer times are seen as secondary effect with an acceptable impact on overall system performance.

Lastly, the argument that the gravity gradient method works only in a Keplerian orbit is placed as least important on the force field diagram. The premise of a low cost technology validation demonstration through secondary payload opportunities limits the potential orbit to a low Earth (Keplerian) orbit. It should be noted that although a full scale UltraSail mission might involve a non-Keplerian orbit, this is not the goal of the technology validation demonstrations and thus this argument is regarded as unimportant at this stage of the design.

Figure 40 shows the force field diagram for the spin induced deployment method and lists arguments in favor and against using this method. As before, the following paragraphs contain a discussion of these arguments and explanation of the relative importance of each.

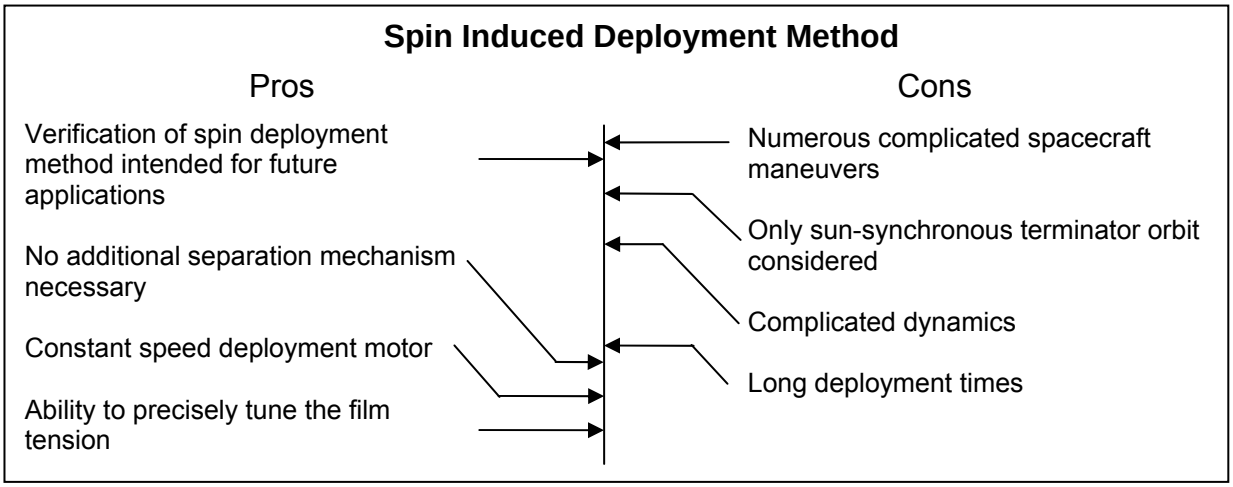

Figure 40. Force field diagram for the spin induced deployment method.

The disadvantages of using the spin induced method include the necessity of multiple pitching and de-pitching maneuvers in a rapidly rotating frame and complicated sail dynamics. Due to constantly changing lighting conditions and drag profile, the insertion orbit should be restricted to the sun synchronous terminator orbit.

The major advantage of using the spin induced deployment method is characterization of the sail dynamics and validation of the control algorithms for future UltraSail missions. Since this is seen as one of the crucial demonstrations necessary prior to a full-scale UltraSail mission, yet there are already a number of technology validations occurring during this demonstration, we propose a two-step demonstration tactic. In the first step, the spacecraft will be inserted into any of the acceptable low Earth orbits and deployed via the gravity gradient method. The mission goals will include validation of the following: spacecraft bus, deployment mechanism including reel/motor/slit assembly, separation release unit, attitude control algorithms, dynamical models, and sail performance—many of which are difficult to test accurately on the ground. The CubeSail team believes that a success of a gravity gradient deployment

will instill confidence in our design and serve as a stepping stone to a more complicated mission, demonstrating the spin-induced deployment.

After evaluation of the gravity gradient deployment method and any necessary redesigns, a second small scale demonstration mission will be launched into a sun-synchronous terminator orbit with a minimum altitude of 850 km and be deployed via the spin-induced method. The mission goals for this demonstration will include: validation of spin dynamical models of the sail-satellite system, responsiveness of the attitude control for a rotating system (which may be augmented with reaction wheels, electric or cold gas thrusters), and orbital performance of a system that is similar to the UltraSail geometry. It should be noted that the deployment into an orbit above 850 km in altitude is meant to minimize effects of drag, which would normally not be present in an interplanetary mission.

3.2.2 Deployment Method Selection using Matrix Diagrams

The matrix diagram is another tool often used in the decision analysis process to set the priorities and basic principles upon which the design philosophy and choices will be based. In the first step of this method, the team makes a list of the requirements for a specific mission and ranks them by importance according to the following scale:

1) Not important
2) Somewhat important
3) Fairly important
4) Very important
5) Critical to meet → Design driver

Since typically there are more than five requirements, the raking numbers (1-5) will be used more than once. It is important, however, that the average ranking of all requirements be near 3.0 (2.5-3.5 range is acceptable), so that the designer avoids making every requirement critical.

In the second step, the designer indicates how well each engineering solution satisfies the requirement by filling in the matrix with the following numerical rankings.

Weight	Relationship
9	Strong
3	Medium
1	Small

Table 5 shows a complete matrix diagram and lists the requirements and their importance as seen by the CubeSail team as well as how each of the two deployment methods satisfies the requirements.

Table 5. Matrix diagram for two deployment methods.

Requirements ↓ / Engineering Solutions →	Importance	Gravity Gradient Deployment	Spin Induced Deployment
Flexibility in orbit insertion parameters	3	9	1
Minimal sensitivity launch date due to solar flux variations	3	9	3
Availability of secondary payload launches to desired orbit	3	9	3
Minimal power usage by attitude control subsystem	3	3	1
Minimal complexity in achieving initial deployment configuration	3	9	3
Minimal number of necessary deployment maneuvers	4	9	1
Constant speed of film deployment	1	1	9
Minimal deployment time	1	9	3
Minimal complexity of separation mechanism	2	3	9
Fine-tuning of flattening force	3	1	9
Simple deployment dynamics	5	9	1
Region of stability at full deployment	5	3	9
Technology validation leading to full-scale UltraSail demonstration	4	3	9
Minimal sensitivity to attitude errors during deployment	3	3	3
Mission Risk Reduction (MRR): film twisting prevention	4	9	9
MRR: film damage prevention due to attitude errors	4	9	3
MRR: through simplicity of deployment method	5	9	1
Maximum orbital lifetime of the system	2	9	3
Ability to test solar propulsive performance	4	9	9
Average Importance	**3.26**		
Importance Rating		**424**	**284**

The above analysis using both force field diagrams as well as matrix diagram suggest that the gravity gradient deployment method is the preferred way for the first

technology demonstration. The large number of technologies which must be validated combined with reduced mission risk ranks this method above the spin induced deployment. Nonetheless, validation of the spinning geometry is seen as necessary prior to a full scale UltraSail mission. As a result, we suggest that the gravity gradient technology validation demonstration be followed by a second small-scale demonstration in low Earth orbit at altitudes above 850 km and preferably in a sun-synchronous terminator orbit, using a spin-induced deployment and stabilization method.

3.3 Preliminary Orbit Maneuvering Analysis

Preliminary analysis of the orbital maneuvering is performed using the Edelbaum low-thrust orbit transfers model and neglects aerodynamic drag. The model is valid under the following assumptions: (1) the transfer occurs between nearly circular orbits, (2) the thrust vector yaw angle is constant within each revolution, and (3) the magnitude of the acceleration is constant. The last assumption will be relaxed slightly while providing good first-order results for the transfer time and time histories of key variables. With these assumptions, Edelbaum derived the following set of equations for the low-thrust orbit transfer[57,58]:

$$\Delta V = f \cdot t \qquad [54]$$

$$\beta = \tan^{-1}\left[\frac{V_0 \sin(\beta_0)}{V_0 \cos(\beta_0) - f \cdot t}\right]$$

$$V = \sqrt{\left(V_0^2 - 2 \cdot V_0 \cdot f \cdot t \cdot \cos(\beta_0) + f^2 \cdot t^2\right)} \qquad [55]$$

$$\Delta i = \frac{2}{\pi}\left[\tan^{-1}\left[\frac{f \cdot t - V_0 \cos(\beta_0)}{V_0 \sin(\beta_0)}\right] + \frac{\pi}{2} - \beta_0\right]$$

where $V_0 = (\mu / a_0)^{1/2}$ with a_0 as the semi-major axis of the initial orbit, f is the magnitude of the acceleration vector, β is the out-of-plane or thrust yaw angle, and Δi

is the total inclination change desired. The components of the thrust acceleration vector along the tangent, normal, and out-of-plane directions are indicated by f_t, f_n, and f_h, with the normal direction oriented toward the center of attraction. With this notation, the acceleration components can be written as $f_t = \cos(\beta)$ and $f_h = \sin(\beta)$. The initial angle β_0 is found from the following equation:

$$\tan\beta_0 = \frac{\sin\left(\frac{\Delta i \cdot \pi}{2}\right)}{\frac{V_0}{V_f} - \cos\left(\frac{\Delta i \cdot \pi}{2}\right)} \quad [56]$$

A typical simulation begins by computing the initial thrust yaw angle, β_0, from Equation 56. Next, knowing the total desired change in inclination, Δi, it is possible to compute the total change in velocity, ΔV_{tot}, using the following equation:

$$\Delta V_{tot} = V_0 \cos(\beta_0) - \frac{V_0 \sin(\beta_0)}{\tan\left(\frac{\Delta i \cdot \pi}{2} + \beta_0\right)} \quad [57]$$

Once the total change in velocity is known, it is possible to rewrite Equation 54 to compute the transfer time as $t_f = \Delta V_{tot} / f$. The variations with time of the remaining variables are then computed using Equations 55 between the initial time, t_0, and the final time, t_f.

Lastly, the acceleration provided by the CubeSail is computed based on work completed for the Ultra Large Solar Sail study[25]. The average solar pressure along the blade in body frame can be written as:

$$\vec{P} = \frac{P}{l_{sail}} \cdot \left[0 \quad \int_0^{l_{sail}} \cos^2\theta \cdot \sin\theta \cdot dx \quad \int_0^{l_{sail}} \cos^3\theta \cdot dx \right]^T \quad [58]$$

where the angle θ is the pitch angle of the sail and is varied linearly starting from zero at the blade center along the blade length until a final value of θ_{tip}:

$$\theta = \theta_{tip} \cdot \left(\frac{x}{l_{sail}} \right) \quad [59]$$

It is important to note that this linear variation in the pitch angle is adopted as a first approximation to allow use of the previously-derived solar radiation pressure equations. The UltraSail geometry allowed for pitching actuation only at one end of the blade, whereas the CubeSail design will typically be actuated at both ends. Conveniently, after integration of the solar pressure vector, the dependence on the sail length vanishes. If the two tip satellites are pitched in the same direction, it is possible to correct for this discrepancy by calculating the force for only half the sail (equivalent to assuming final length is equal to $l_{sail}/2$) and then multiplying by 2. This results is equivalent to multiplying the solar pressure vector by the total area of $l_{sail} \cdot w_{sail}$.

After integrating Equation 58 and multiplying by the sail surface area, the force components are:

$$\vec{F}_{SP} = \frac{w_{sail} \cdot l_{sail} \cdot P}{12 \cdot \theta_{tip}} \cdot \left[0 \quad \cos\left(3\theta_{tip}\right) + 3\cos\left(\theta_{tip}\right) - 4 \quad \sin\left(3\theta_{tip}\right) + 9\sin\left(\theta_{tip}\right) \right]^T \quad [60]$$

The magnitude of the acceleration is computed using Equation 61 where m is the spacecraft mass (3 kg).

$$f = \left\| \mathbf{F}_{SP} \right\| / m \quad [61]$$

The above equations are propagated between the initial time t_0 and final time t_f for three cases: 100 km orbit raise, 5º inclination change, and combination of the first

two maneuvers. The results are shown in Table 6. It should be noted that the change in the magnitude of acceleration, due to changes in the β angle, is approximately 0.3×10^{-8} km/s or 8% in one year, which is seen as an acceptable deviation from the constant acceleration assumption used by Edelbaum. Also, it is apparent that even modest inclination changes require approximately eight months of transfer time due to minimal film area and hence available thrust.

Table 6. Transfer times for three orbital maneuvers.

Scenario	Δi [º]	Δalt [km]	Transfer time [days]
(1)	0.4	100	22.6
(2)	5	0	239.8
(3)	5	100	239.3

3.4 Preliminary Orbit Selection

The above analysis assumed deployment either into a sun-synchronous terminator orbit or the co-ecliptic orbit due to favorable lighting and drag conditions. The following section describes methodology behind down-selecting the orbit to the sun-synchronous terminator orbit and provides analysis to compute minimum insertion altitude.

3.4.1 Spacecraft Orbital Lifetime Analysis

Initial orbital lifetime analysis is performed for the gravity gradient stabilized configuration and assumes an undeformed sail. The problem is highly sensitive to the spacecraft attitude, insertion altitude, and launch date within the solar cycle. Since all three variables have large search spaces, initial analysis bounds the problem between worst- and base-case scenarios. The best and worst case attitudes occur when the sail is edge-on and face-on to the velocity vector respectively. The best and worst case launch date are given by solar minimum and solar maximum years respectively.

Insertion altitude is chosen as a free variable and orbital lifetime as an equivalent cost function.

Figure 41 (left) illustrates the variations in solar flux over the 11 year sun cycle with the solar minima years occurring in mid 2008 (and then every 2019 + n*11yrs) and solar maxima years occurring in 2014 + n*11yrs. The effects of this large variation in the solar flux have a significant impact on the density of Earth's atmosphere as is shown Figure 41 (right). For example, at the altitude of 750 km, the density varies by two orders of magnitude between solar maximum and solar minimum years. This, in turn, results in significantly reduced orbital lifetime of the spacecraft as is shown in Table 7 and Figure 42. The shaded areas in Table 7 represent altitudes at which the spacecraft will survive at least 1 year before deorbiting, for each of the described attitudes. It is important to note that for the worst case scenario when the sail is face-on to the velocity vector, the spacecraft must be deployed into a 800 km orbit during solar minimum and 900km orbit during solar maximum.

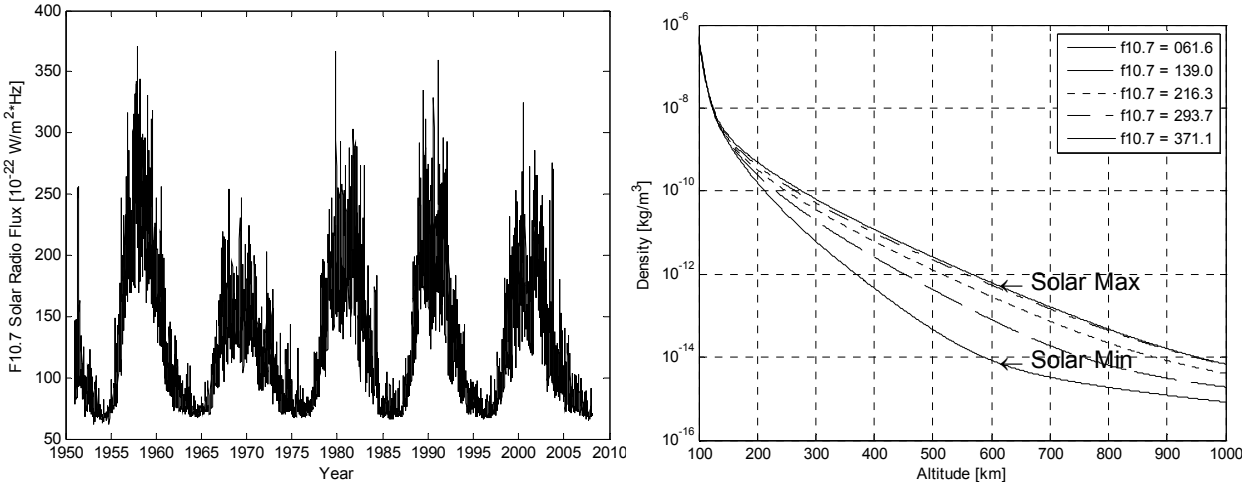

Figure 41. Solar cycle (left) and atmospheric density vs. altitude (right).

Table 7. Orbital Lifetime vs. altitude and configuration

Altitude [km]	Orbital Lifetime [yrs]			
	Edge-on Solar Min	Edge-on Solar Max	Face-on Solar Min	Face-on Solar Max
400	1.4	0.6	0.004	0.0012
500	6.7	4.9	0.034	0.0073
600	27.2	22.4	0.176	0.0036
700	106	92.5	0.508	0.137
800	317	316	1.169	0.386
900	>300	>300	2.044	1.108

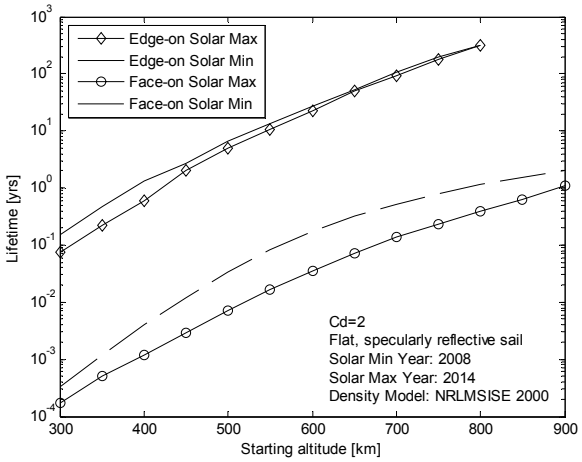

Figure 42. Orbital Lifetime for edge-on and face-on configurations during solar extrema

Although the launch date within the solar cycle has a significant effect on the orbital lifetime, the sail attitude with respect to the velocity direction has an even greater impact. From the above table, during a solar maximum period, if the film is deployed with the sail normal perpendicular to the velocity direction (edge-on) and must survive for at least one year, it must be deployed into a minimum initial altitude of 500 km. In contrast, if the sail is deployed in the face-on configuration during the same period, it must be inserted into a 900 km initial orbit. As a result of this strong dependence of orbital lifetime on CubeSail attitude, the spacecraft is nominally flown in the zero pitch (edge-on) configuration.

3.4.2 Spacecraft Orbital Lighting Analysis

The two candidate orbits are evaluated based on the performance in the presence of the two external forces—aerodynamic drag (AD) and solar radiation pressure (SRP). The sail axes are chosen with $\hat{Z}^{Sail}$ axis in the direction normal to the film surface, $\hat{Y}^{Sail}$ axis in the direction tangential to the film along its width, and $\hat{X}^{Sail}$ axis in the direction tangential to the film along its length.

In the first case, the spacecraft is inserted into a sun-synchronous terminator orbit with the sail $\hat{Y}^{Sail}$ axis nominally oriented into the velocity direction as shown in Figure 43. This 'SRP-face-on/AD-edge-on' configuration creates a minimum drag profile and ensures the longest orbital lifetime when the spacecraft is in its nominal operating mode. In addition, the sun-synchronous terminator orbit offers constant lighting conditions and thus eliminates accordion-like billowing effects when the spacecraft comes in and out of shadow and allows for less complicated orbital maneuver planning. This configuration is therefore selected as most desirable for the CubeSail spacecraft.

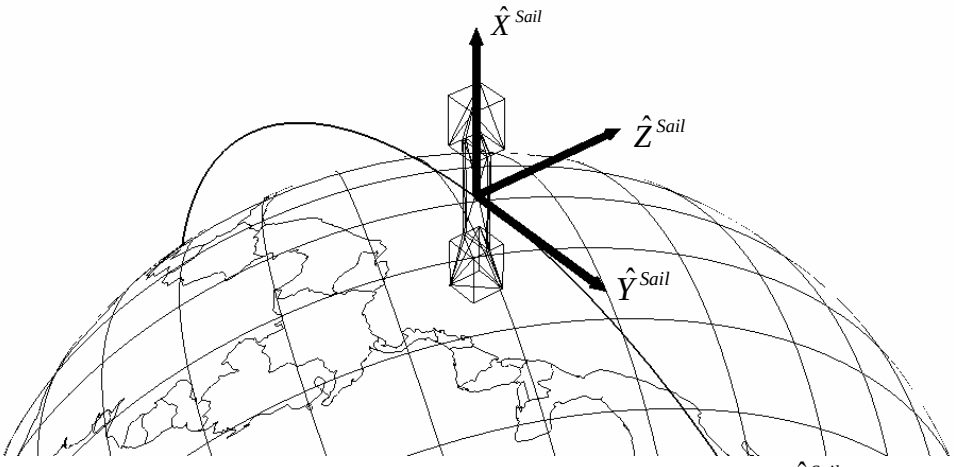

Figure 43. CubeSail in a sun synchronous terminator orbit with nominal $\hat{Y}^{Sail}$ axis oriented into the velocity direction.

In the second case, the spacecraft is inserted into an ecliptic orbit (spacecraft orbital and the ecliptic planes are co-planar) and the sail is nominally oriented with its $\hat{Y}^{Sail}$ axis pointed into the velocity direction as shown in Figure 44. This 'SRP-edge-on/AD-edge-on' configuration creates minimum drag profile and ensures the longest orbital lifetime when the spacecraft is in its nominal operating mode. Although this case creates no billowing in the film during normal operations, the spacecraft does go in and out of shadow, thus complicating orbital maneuver planning, causing time-varying billowing of the sail, and has undesired thermal effects as the film is warmed and cooled. This configuration is seen as the second-best option for the CubeSail spacecraft.

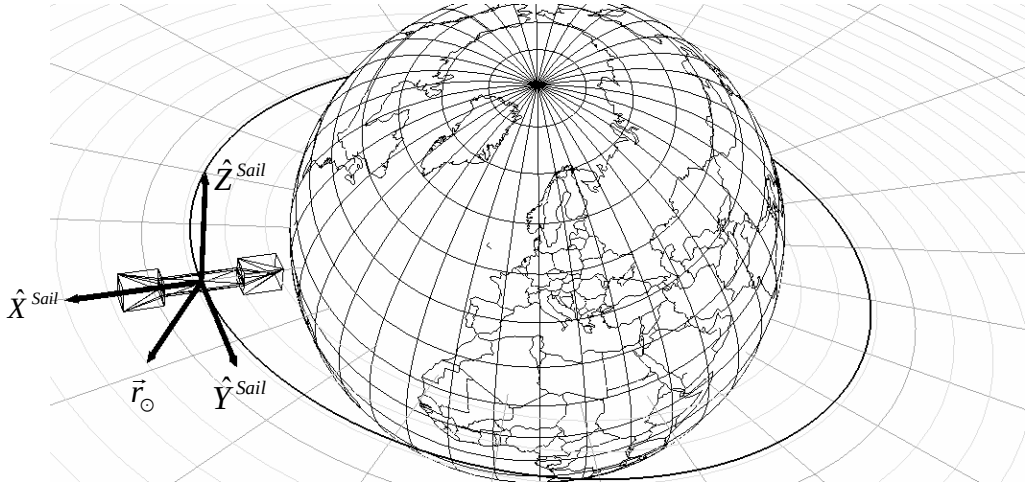

Figure 44. CubeSail in ecliptic orbit with nominal $\hat{Y}^{Sail}$ axis oriented into the velocity direction.

In the third case, the spacecraft is inserted into a sun-synchronous terminator orbit, with the nominal $\hat{Z}^{Sail}$ axis oriented into the velocity direction as shown in Figure 45. This 'SRP-edge-on/AD-face-on' configuration causes the sail to be continuously billowed out in the $-\hat{Z}^{Sail}$ direction and thus have short orbital lifetime. The aerodynamic drag force remains relatively constant during nominal operations, which, along with constant lighting conditions offered by the sun-synchronous terminator orbit, reduce

time-varying temperature effect and billowing dynamics. This configuration is therefore ranked as the 3rd best.

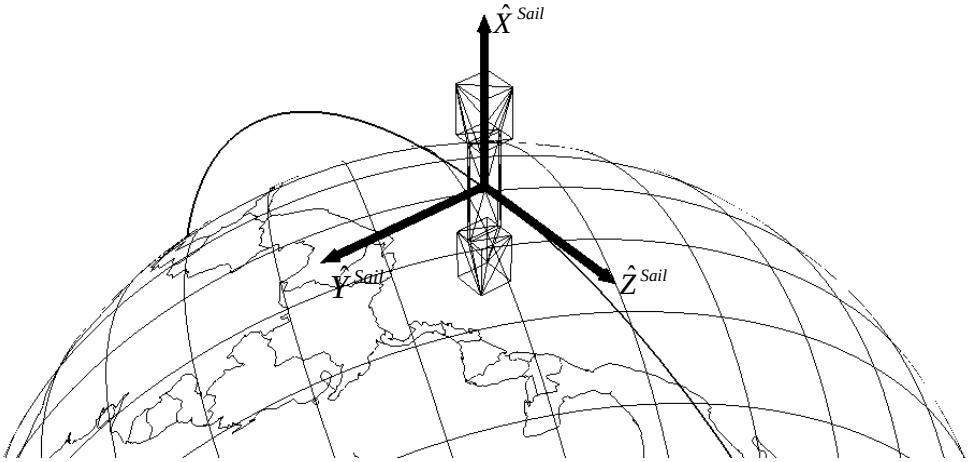

Figure 45. CubeSail in a sun synchronous terminator orbit with nominal $\hat{Z}^{Sail}$ axis oriented into the velocity direction.

In the fourth case, the spacecraft is inserted into an ecliptic orbit, but in contrast to the second case, is deployed with $\hat{Z}^{Sail}$ axis nominally oriented in the velocity direction. This 'SRP-face-on/AD-face-on' configuration creates maximum billowing in the sail caused by both solar radiation pressure and aerodynamic drag. The orbital lifetime degradation can be helped somewhat by pointing the non-reflective side as the spacecraft approaches the sun as shown in Figure 46. Since the back side of the film is non-reflective, only half as much momentum will be imparted onto the film by the incoming photons on the way towards the sun as on the way away. This configuration will further complicate the accordion-like behavior not only as the spacecraft come in and out of shadow, but also as it transfers through the solar apoapse. Similarly, the thermal considerations of switching between high reflectivity front coating and high emissivity back coating are further complicated as is maneuver planning. Due to the

added complications, this is the least favorable configuration, but it is analyzed is some detail to demonstrate the 'worst-case scenario.'

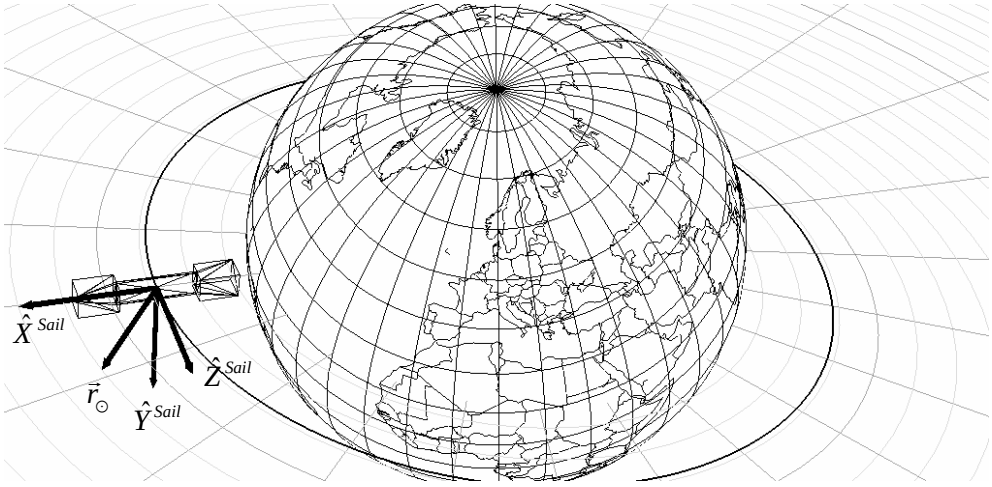

Figure 46. CubeSail in an ecliptic orbit with nominal $\hat{Z}^{Sail}$ axis oriented into the velocity direction.

All four cases are summarized in Table 8 along with the performance ranking for each orbit and nominal flight attitude.

Table 8. Summary of CubeSail candidate orbits and attitudes.

Sail attitude with respect to force	Force		Sample orbit	Associated Figure	Performance Rating (1 = Best)
	SRP	AD			
	Face On	Edge On	Sun Synchronous Terminator with nominal $\hat{Y}^{Sail}$ axis oriented into the velocity direction.	Figure 43	1
	Edge On	Edge On	Ecliptic with nominal $\hat{Y}^{Sail}$ axis oriented into the velocity direction.	Figure 44	2
	Edge On	Face On	Sun Synchronous Terminator with nominal $\hat{Z}^{Sail}$ axis oriented into the velocity direction.	Figure 45	3
	Face On	Face On	Section of ecliptic orbit with nominal $\hat{Z}^{Sail}$ axis oriented into the velocity direction.	Figure 46	4

CHAPTER 4

Detailed Analysis of Gravity Gradient Deployment

4.1 Separation Release Unit Design

The Separation Release Unit (SRU) is shown Figure 47. The design allows the two tip satellites to be rigidly mated during launch and initial detumbling, but to separate with high reliability just prior to film deployment. The basis of this design is the Faulhaber 1524-012SR DC micromotor [59] along with the Faulhaber 15/5 262:1 gearbox[60], which is rigidly attached to a ¼''x20 brass screw, called the 'lead screw.' The lead screw is screwed into a threaded plate on the opposite satellite by three full turns, and allows for easy alignment, repeated mating and de-mating during testing, and rigid connection between the two satellites. In addition, the SRU includes multiple separation springs that provide initial separation velocity during film deployment. The dynamical response of the system to the separation, as well as selection of specific springs is discussed in the following two sections.

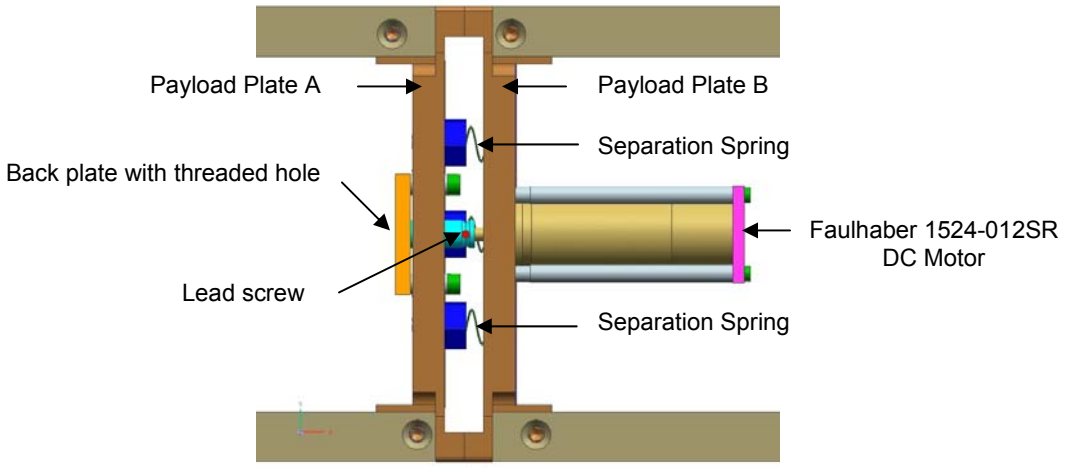

Figure 47. Separation Release Unit Design Diagram.

4.1.1 Impact of SRU Operations on Satellite Dynamics

During the separation maneuver, the motion of the screw around the long axis of the satellite will cause an opposite rotation of the two rigidly-mated satellites. The impact of this rotation on the satellite attitude is analyzed by taking into account the contribution to the system's angular momentum from the lead screw. The analysis disregards, however, any contributions from the internal workings of the gearbox (whose exact gear sizes and weights are unknown), stiction in the motor, and stiction between the lead screw and the back plate.

The satellites are assumed to be rigidly mated throughout the separation maneuver, which is accomplished through the use of alignment pins in the feet and spring alignment sockets on the payload plates. The moment of inertia of the satellite is estimated as a rectangular prism of uniform density and 3 kg mass according to the following formula and Figure 48:

$$I_{sat} \triangleq I_{xx,sat} = \frac{m}{12}\left(y_{sat}^2 + z_{sat}^2\right) \qquad [62]$$

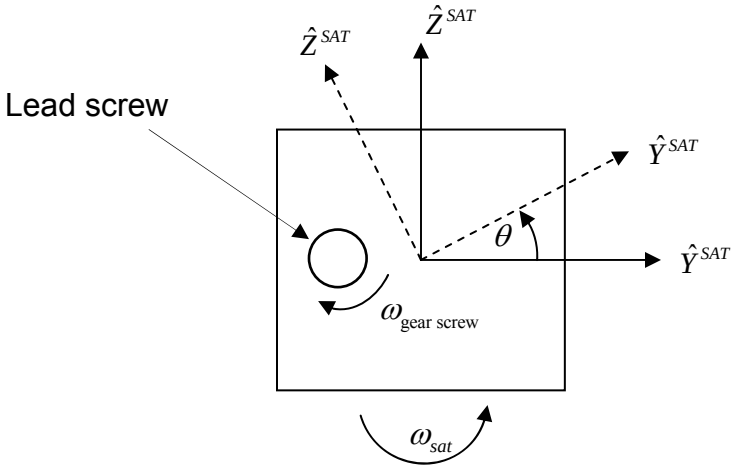

Figure 48. Satellite and lead screw rotation notation.

Given that the gear box output is 24 RPM and the lead screw is inserted by three threads (3 full turns), the SRU motor must operate for at least 7.5 seconds. An additional 2.5 seconds are allowed as a safety margin to ensure full separation.

The lead screw is a ¼''x20 brass screw shown in Figure 49. The moment of inertia of the screw is computed assuming that the threaded shaft is a solid cylinder and that the head cap is thick-walled hollowed cylinder. The appropriate moment of inertia equations and associated diagrams are given below and in Figure 50.

$$I_{xx,\text{ solid cylinder}} = \frac{1}{2}mr^2 \qquad I_{xx,\text{ thick-wall cylinder}} = \frac{1}{2}m\left(r_1^2 + r_2^2\right) \qquad [63]$$

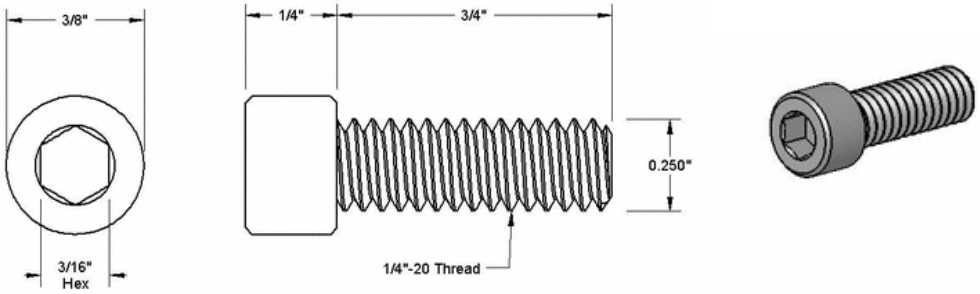

Figure 49. 1/4x20 cap socket screw used for the worm screw.

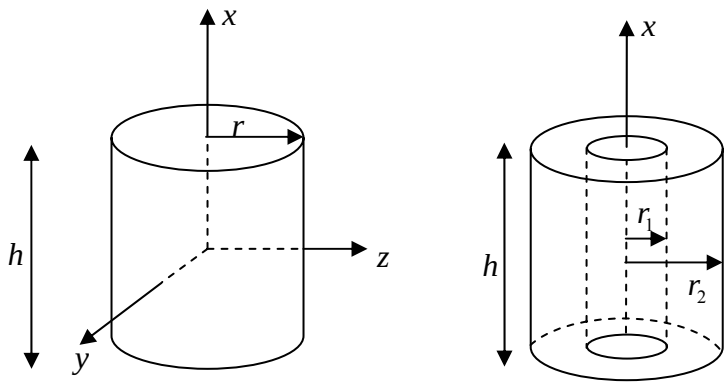

Figure 50. Solid (left) and thick-walled hollow (right) cylinder geometry.

The masses of individual segments are found using the density of stainless steel (18 Cr-8Ni) of 8 g/cm^3. Table 9 summarizes the mass properties of the lead screw.

Table 9. Lead screw mass properties.

Part	Volume [m^3]	Density [kg/m^3]	Mass [kg]	I_{xx} [kg-m^2]
Cap Socket	$2\cdot\pi\cdot r_2\cdot h\cdot(r_2-r_1)=1.81\times10^{-6}$	8000	0.0145	8.21×10^{-7}
Threaded Shaft	$\pi\cdot r^2\cdot h=2.41\times10^{-6}$	8000	0.0193	3.89×10^{-7}

The rotation of the screw occurs in the negative (counter clock-wise) direction around the $\hat{X}^{SAT}$ axis, causing a positive θ rotation of the satellite as shown in Figure 48. The equation for angular momentum and the rotational angle during three phases of the SRU motor operations have been derived and are presented in Equations 64 and 65. The details of the derivation are given in Appendix A. The motor is assumed stationary at time t_1 and is accelerated at a constant rate of 1x10^5 rad/sec^2 until it reaches a maximum rotational velocity at time t_2. Between t_2 and t_3 the motor rotates at a constant rotational velocity of 26 RPM until the two tip satellites are separated, and then decelerates until it reaches zero rotational velocity at t_4.

$$H_{sat}(t)=\begin{cases} I_{\text{lead screw}}\cdot\alpha_{\text{lead screw}}\cdot(t-t_1) & \forall\ t_1\le t\le t_2 \\ I_{\text{lead screw}}\cdot\omega_{\text{lead screw}}(t_2) & \forall\ t_2<t\le t_3 \\ -I_{\text{lead screw}}\cdot\alpha_{\text{lead screw}}\cdot(t-t_3)+H_{sat}(t_3) & \forall\ t_3<t\le t_4 \end{cases} \quad [64]$$

$$\theta_{sat}(t)=\begin{cases} \dfrac{I_{\text{lead screw}}\cdot\alpha_{\text{lead screw}}\cdot(t-t_1)^2}{2I_{sat}} & \forall\ t_1\le t\le t_2 \\ \dfrac{I_{\text{lead screw}}\cdot\alpha_{\text{lead screw}}\cdot(t_2-t_1)\cdot(t-t_2)}{I_{sat}}+\theta_{sat}(t_2) & \forall\ t_2<t\le t_3 \\ -\dfrac{I_{\text{lead screw}}\cdot\alpha_{\text{lead screw}}\cdot(t-t_3)^2}{2I_{sat}}+\dfrac{H_{sat}(t_3)\cdot(t-t_3)}{I_{sat}}+\theta_{sat}(t_3) & \forall\ t_3<t\le t_4 \end{cases} \quad [65]$$

The above results are applied to the CubeSail spacecraft for $t_1=0$ sec, $t_2=0.0066$ sec, $t_3=10$ sec, $t_3=10.0066$ sec. Interestingly, during the separation process, the assembly will rotate by only 0.35º as shown in Figure 51. This small rotation is attributed to the

minimal moment of inertia of the lead screw as compared to the two satellites. In addition, the motor acceleration is sufficiently high that a step-input behavior for the rotational velocity is an acceptable approximation. It is important to emphasize that this rotation is of the entire assembly (as opposed to relative rotation of the tip satellites) since the satellites are held together using the film, alignment pins in the feet, and alignment sockets for the separation springs.

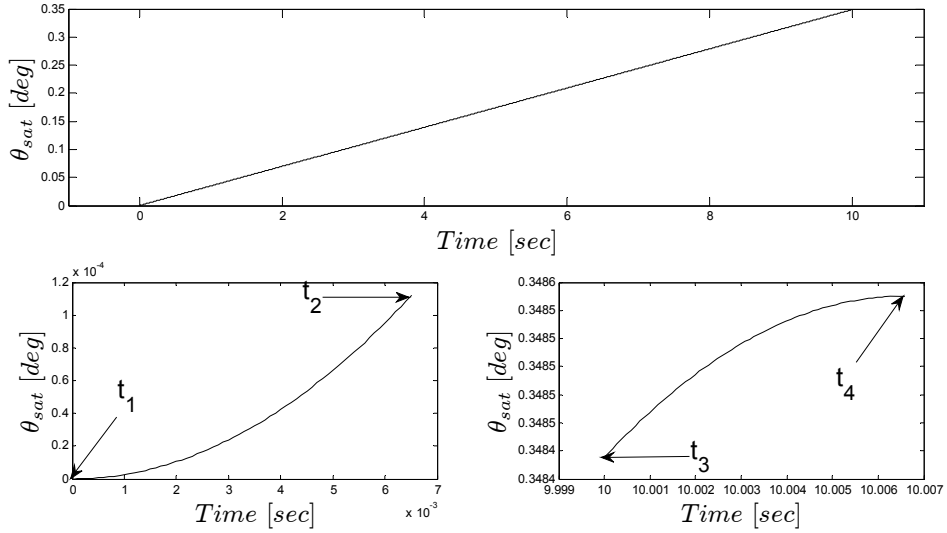

Figure 51. Satellite pitch angle during SRU operation.

4.1.2 Spring Selection for Initial Spacecraft Separation

A system of two springs in parallel can be described equivalently by a single spring system whose constant is simply the sum of the two springs as shown in Figure 52. In order to minimize non-linear deployment, the springs are identical and the total force can therefore be written as:

$$F_{total} = \left(k_1 + k_2\right) \cdot x = 2 \cdot k \cdot x \qquad [66]$$

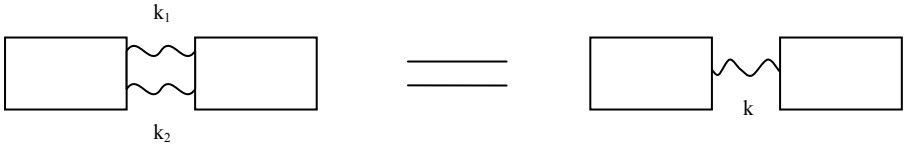

Figure 52. Equivalent spring-mass systems

The maximum force that the film can withstand before breaking is computed as:

$$F_{\max} = \sigma_{yield} \cdot A_{cs} \qquad [67]$$

During the stage of deployment when the lead screw has disengaged but the springs are still compressed, the film is in tension which is induced primarily by the springs. For a 6.3 micron-thick Mylar film ($\sigma_{yield,\,Mylar} = 172\ MPa$) with a width of 78 mm, this maximum tensile force (including 30% safety margin) is 83.18 N. The corresponding maximum spring constant is found by solving Equation 66 for k, which results in $k_{\max} = 4159\ N/m$ for the spring that is compressed by 1 cm. This is the upper bound on the spring constant for the CubeSail mission. Further refinements to this value are computed based on the desired separation dynamics.

The initial deployment velocity is computed using conservation of energy principle. At the end of a stroke, all the potential energy stored in the spring is converted into kinetic energy of the two satellites. This can be written as:

$$U_{spring} = \frac{1}{2} k \cdot x^2 = \frac{1}{2} m \cdot V_{rel}^2$$
$$V_{rel} = \sqrt{\frac{k \cdot x^2}{m}} \qquad [68]$$

where V_{rel} is the relative velocity of one satellite with respect to the second one and m is the initial mass of a single tip satellite. Using the previously-computed spring constant of 4159 N/m, stroke distance of 1 cm, and satellite mass of 1.5 kg, the initial maximum relative velocity is $V_{rel,\,\max} = 0.527\ m/s$. This is the upper bound on the separation velocity, whose exact value is determined in a later section.

4.2 CubeSail Reference Frames

In order to fully characterize its behavior, CubeSail will utilize six reference frames. The frames are abbreviated as: ECI, ECF, ORB, SatL, SatU, and Sail are defined below.

4.2.1 Earth Centered Inertial Reference Frame

The Earth Centered Inertial (ECI) frame, shown in Figure 53, is defined with its origin at the center of Earth and with the $\hat{X}^{ECI}$ unit vector pointing in the direction of First Point of Aries or vernal equinox. This point, however, precesses around the pole of the Earth's orbit about the Sun with a period of 26,000 years. This precession of equinoxes causes a shift in the position of vernal equinox relative to the fixed stars with a rate of $0.014\ °/yr$ and forces an addition of corresponding date to accurately define the position of the vernal equinox. The system used for CubeSail's attitude control system was chosen to be the J2000 with epoch time on January 1st, 2000 at 12:00:00.000. In this frame, the vector $\hat{Z}^{ECI}$ is defined from the center of Earth to the North Pole. Consequently, vector $\hat{Y}^{ECI}$, which completes the orthonormal triad, is found using the cross product.

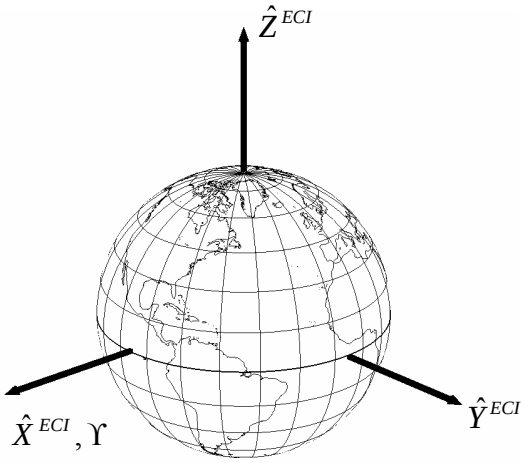

Figure 53. Earth Centered Inertial Reference Frame

4.2.2 Earth Centered Fixed Reference Frame

The Earth Centered Fixed (ECF) frame, shown in Figure 54, is defined with its origin at the center of Earth and, in contrast with the ECI frame, rotates with it. The unit vector $\hat{X}^{ECF}$ is pointing in the direction of the Prime Meridian (also referred to as the Greenwich Meridian) and lies in the equatorial plane. The vector $\hat{Z}^{ECF}$ is defined from the center of Earth to the North Pole and the vector $\hat{Y}^{ECF}$ is computed, as previously, using the cross product.

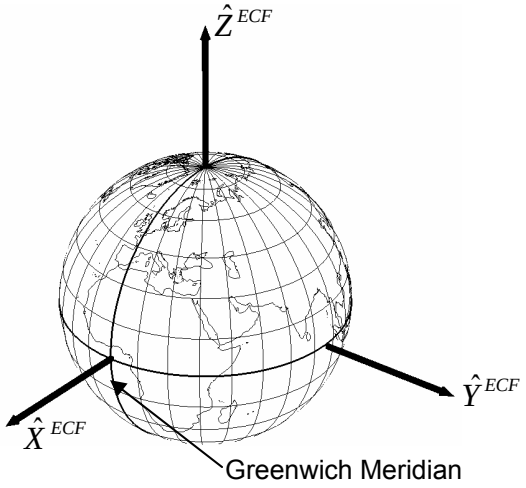

Figure 54. Earth Centered Fixed Reference Frame

4.2.3 Orbital Reference Frame

The Orbital reference frame, also referred to as the Local Vertical Local Horizontal (LVLH) frame, is denoted by letters ORB. The frame is centered—and moves along with—the CubeSail's center of mass. The unit vector $\hat{X}^{ORB}$ points from the Earth's center along the radius vector toward the spacecraft. The unit vector $\hat{Z}^{ORB}$ is normal to the orbital plane and unit vector $\hat{Y}^{ORB}$ completes the orthonormal triad. It is

important to note that $\hat{Y}^{ORB}$ is typically not aligned with the velocity direction except for circular orbits or at apogee and perigee for elliptical orbits.

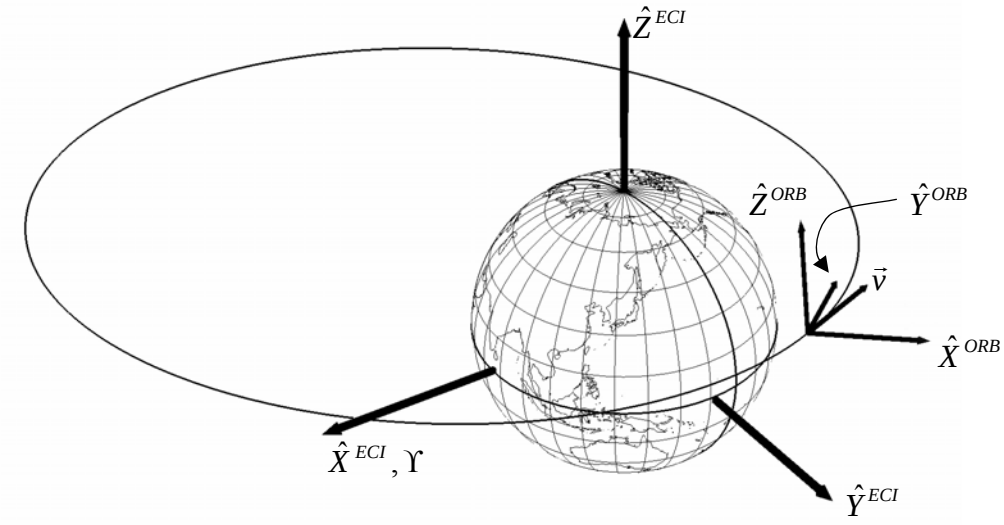

Figure 55. Local Vertical Local Horizontal Reference Frame

4.2.4 SatL and SatU Reference Frames

The SatL and SatU frames refer to the 'Lower' and 'Upper' of the two satellites. It is important to notice that the satellites are not identical and the lower of the two spacecrafts has the Separation Release Unit including the motor and lead screw and is thus slightly heavier. Both SatL and SatU reference frames are located at the center of mass of the respective satellites with the $\hat{X}^{SAT}$ axis pointing away from Earth when the spacecraft is in nominal orientation (through the payload interface plate for the lower satellite and through the bus end plate for the top satellite). The $\hat{Y}^{SAT}$ axis of both satellites is directed parallel to the bobbins' spin axis (along the film surface through its thickness when the film is undeformed). Lastly, the $\hat{Z}^{SAT}$ axis of both satellites completes the triad and, in the case of undeformed sail, is normal to the film.

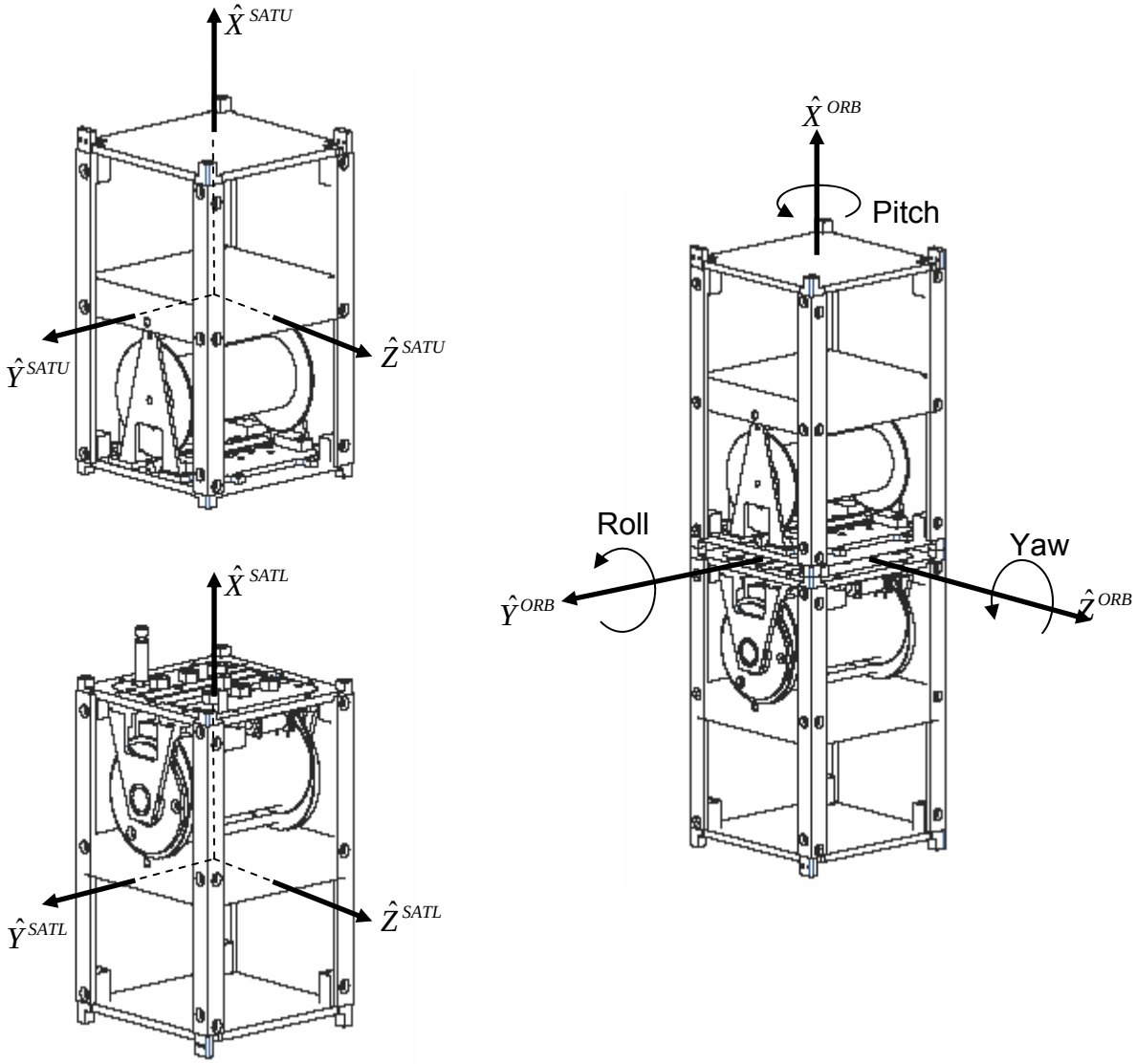

Figure 56. SatL and SatU Reference Frames (left) and roll/pitch/yaw definition (right).

4.2.5 'Sail' Reference Frame

The 'Sail' reference frame actually corresponds to *n* slightly different reference frames, each having their origin located on the film, equidistant from the film edges and separated a distance Δr along the film. The sail is thus divided into *n* sections each 78 mm in width and Δr in height. Each of the 'Sail' frames, illustrated in Figure 57, has its $\hat{Z}_i^{Sail}$ opposite the direction of the surface normal of the i^{th} section, its $\hat{Y}_i^{Sail}$ axis in the

chord-wise tangential direction of the i^{th} section, and the $\hat{X}_i^{Sail}$ axis completes the right-handed system ($\hat{Y}_i^{Sail} \times \hat{Z}_i^{Sail}$) and lies in the plane of the i^{th} section.

Special Case: Flat Plate Sail Reference Frame

A special case when the sail film is neither billowed out, nor pitched (has no twist) results in a 'flat plate' representation of the sail seen in Figure 57. In this simplified case, the sail normal ($\hat{Z}^{Sail}$) is always aligned with the satellite $\hat{Z}^{SAT}$ axis and the sail tangential along the sail chord ($\hat{Y}^{Sail}$) is always aligned with satellite $\hat{Y}^{SAT}$ axis.

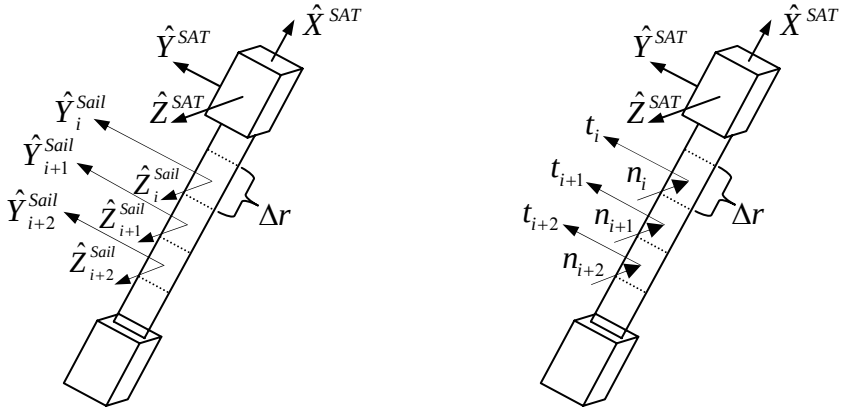

Figure 57. Sail geometry with no billowing and no twist ('flat plate' geometry).

General Case: Billowed and Pitched 'Sail' Reference Frame

Typical CubeSail operations in low Earth orbit will result in the film being both billowed out and often twisted. In order to accurately represent the forces and torques on the spacecraft, the sail is divided into *n* section as before, with each section rotated around the $\hat{X}^{SAT}$ axis by and angle θ_i^{Sail} that represents to the sail pitch and then rotated by an angle ϕ_i^{Sail} around the $\hat{Y}^{SAT}$ axis that represents the billowing of the film. Figure 58 depicts the above-described geometry. It is assumed that the angle θ_i^{Sail} varies linearly from its maximum value of θ^{Sat} at the upper satellite ($x = 0$) to zero pitch at the

sail mid-section ($x = l_{sail} / 2$), to finally $-\theta^{Sat}$ at the lower satellite ($x = l_{sail}$) where l_{sail} is the length of deployed sail, which can also be written as:

$$\theta^{Sail}(x) = \theta^{Sat} \cdot \left(1 - \frac{2 \cdot x}{l_{sail}}\right) \quad [69]$$

In order to obtain the shape of a billow-out sail that includes the effects from aerodynamic drag, solar radiation pressure, and gravity gradient forces, an equilibrium configuration is found at each point along the orbit and given the attitude of both tip satellites. As before, it is assumed that there is no chord-wise billowing and each section of width 78 mm and height Δr is displaced by the same amount as the chord-midpoint.

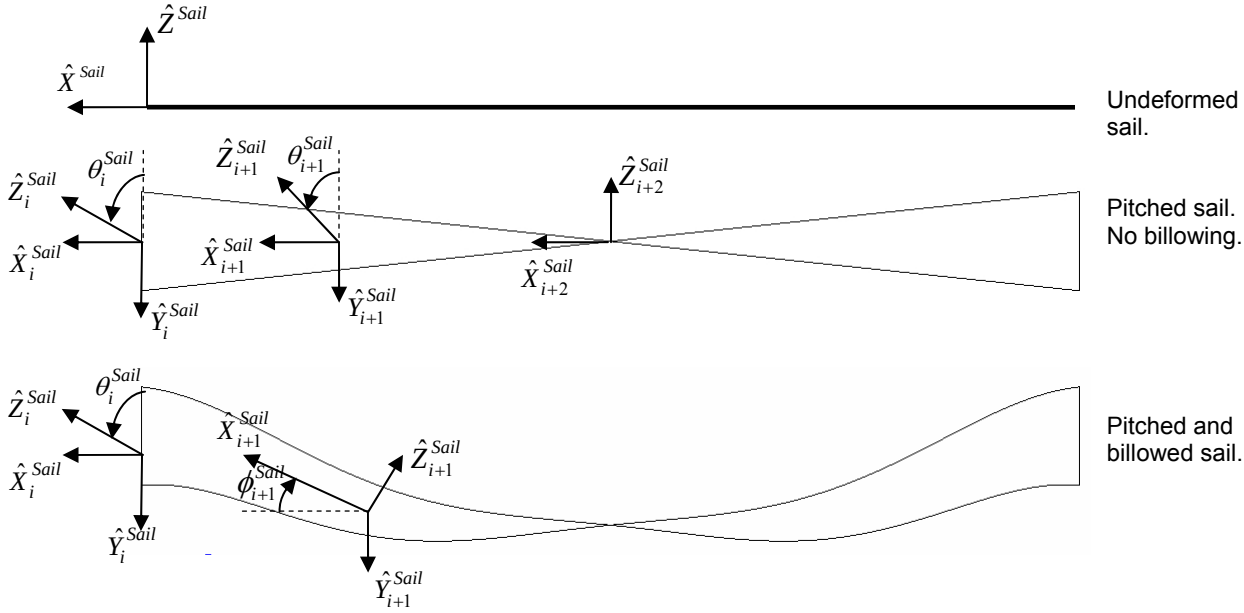

Figure 58. Sail reference frame with pitching and billowing.

4.2.6 Transformation between ECI and ECF Reference Frames

Since both the Earth Centered Inertial and Earth Centered Fixed reference frames have their z-axis pointed in the direction of the North Pole, the transformation between these two frames can be reduced to simple rotation around that axis by an

angle θ_{GMST}, known as the Greenwich Mean Sidereal Time, and is shown in Figure 59. The Earth rotates about its pole axis at a rate of one rotation for every 23h, 56min, and 4.1s. Since the ECF coordinate system's axes are fixed within the Earth, they also rotate at this same rate. Thus, Greenwich Mean Sidereal Time also rotates at this rate and can be found as a function of time according to the following equation[83]:

$$\begin{aligned}\theta_{GMST} &= 67{,}310.53841^{s} + \left(876{,}600^{h} + 8{,}640{,}184.812866^{s}\right)\cdot T_{UT1} \\ &\quad + 0.093104\cdot T^{2}{}_{UT1} - 6.2\times 10^{-6}\cdot T^{3}{}_{UT1}\end{aligned} \qquad [70]$$

T_{UT1} is computed by first calculating the Julian Date, JD_{UT1}, from the time stamp associated with the position vector (typically given as [$year$, $month$, day, $hour$, min, sec]) using the following equation:

$$\begin{aligned}JD_{UT1} &= 367\cdot year - INT\left\{\frac{7\cdot\left[year + INT\left(\frac{month+9}{12}\right)\right]}{4}\right\} \\ &\quad + INT\left(\frac{275\cdot month}{9}\right) + day + 1{,}721{,}013.5 + \frac{hr}{24} + \frac{\min}{1440} + \frac{s}{86{,}400}\end{aligned} \qquad [71]$$

Then using the Julian Date to find T_{UT1} from:

$$T_{UT1} = \frac{JD_{UT1} - 2{,}451{,}545.0}{36{,}525} \qquad [72]$$

The above equation yields the Greenwich Mean Sidereal Time in the units of seconds, which can be converted to degrees by dividing it by 240 ($1^{s} = 1/240°$) and then removing multiples of $360°$ (conveniently done using the *wrapTo360* function in Matlab).

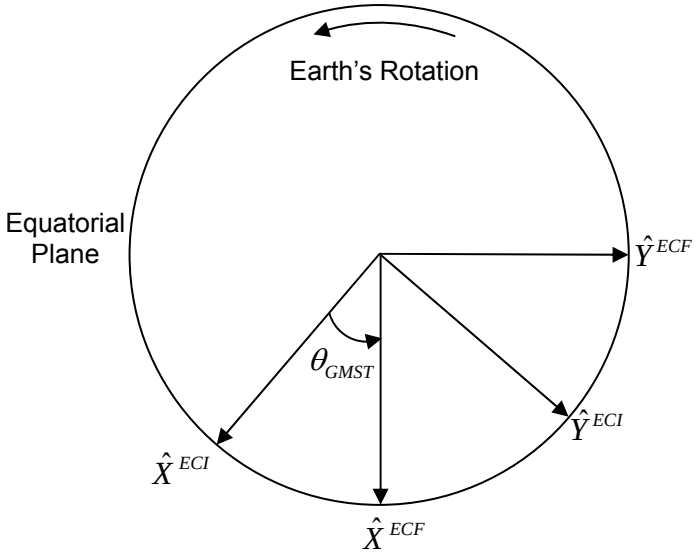

Figure 59. ECI to ECF Reference Frame Transformation

Once θ_{GMST} has been calculated, the transformation between the ECF and ECI frames can be calculated as the following transformation matrix:

$$A_{ECI}^{ECF} = \begin{bmatrix} \cos(\theta_{GMST}) & \sin(\theta_{GMST}) & 0 \\ -\sin(\theta_{GMST}) & \cos(\theta_{GMST}) & 0 \\ 0 & 0 & 1 \end{bmatrix} \quad [73]$$

Therefore, given a vector in the ECI frame, it suffices to pre-multiply it by the above A_{ECI}^{ECF} matrix to obtain an equivalent vector in the ECF frame.

4.2.7 Transformation between ECI and Orbital Reference Frames

The local vertical local horizontal vectors are easily defined from the position and velocity vectors (given in the ECI frame) from the following equations:

$$\hat{X}^{ORB} = \frac{\vec{r}^{ECI}}{|\vec{r}^{ECI}|} \qquad \hat{Z}^{ORB} = \frac{\vec{r}^{ECI} \times \vec{v}^{ECI}}{|\vec{r}^{ECI} \times \vec{v}^{ECI}|} \qquad \hat{Y}^{ORB} = \hat{Z}^{ORB} \times \hat{X}^{ORB} \quad [74]$$

The transformation matrix from the ECI to the Orbital frame can therefore be written as:

$$A_{ECI}^{ORB} = \begin{bmatrix} \hat{X}^{ORB} & \hat{Y}^{ORB} & \hat{Z}^{ORB} \end{bmatrix}^T \quad [75]$$

where the $\hat{X}^{ORB}$, $\hat{Y}^{ORB}$, and $\hat{Z}^{ORB}$ are column vectors and the following properties were used:

$$\left(A_{ORB}^{ECI}\right)^{T} = \left(A_{ORB}^{ECI}\right)^{-1} = A_{ECI}^{ORB} \quad [76]$$

4.2.8 Transformation between Orbital and SatL and SatU reference frames

The CubeSail attitude is represented using the roll ϕ^{SAT}, pitch θ^{SAT}, and yaw ψ^{SAT} angles as shown in Figure 56 (right). When all three Euler angles are identically zero, the Orbital and Sat reference frames coincide. It is important to note that the definition used in Figure 56 differs from the classical representation (where the rotation around the radial direction is typically the yaw axis). This departure was made to preserve the historical definition that a twist in the sailing film is referred to as pitch. To transform between the Orbital and Sat frames, we use an Euler 1-2-3 rotation sequence (rotation around the $\hat{X}^{ORB}$ axis through the angle θ^{SAT}, followed by a rotation about the new y' axis through the angle ϕ^{SAT}, and a final rotation about the new z'' axis through the angle ψ^{SAT}).

$$A_{ORB}^{SAT} = R_3\left(\psi^{SAT}\right) \cdot R_2\left(\phi^{SAT}\right) \cdot R_1\left(\theta^{SAT}\right) \quad [77]$$

with

$$R_1\left(\theta^{SAT}\right) = \begin{bmatrix} 1 & 0 & 0 \\ 0 & \mathrm{c}\left(\theta^{SAT}\right) & \mathrm{s}\left(\theta^{SAT}\right) \\ 0 & -\mathrm{s}\left(\theta^{SAT}\right) & \mathrm{c}\left(\theta^{SAT}\right) \end{bmatrix} \qquad R_2\left(\phi^{SAT}\right) = \begin{bmatrix} \mathrm{c}\left(\phi^{SAT}\right) & 0 & -\mathrm{s}\left(\phi^{SAT}\right) \\ 0 & 1 & 0 \\ \mathrm{s}\left(\phi^{SAT}\right) & 0 & \mathrm{c}\left(\phi^{SAT}\right) \end{bmatrix}$$

$$R_3\left(\psi^{SAT}\right) = \begin{bmatrix} \mathrm{c}\left(\psi^{SAT}\right) & \mathrm{s}\left(\psi^{SAT}\right) & 0 \\ -\mathrm{s}\left(\psi^{SAT}\right) & \mathrm{c}\left(\psi^{SAT}\right) & 0 \\ 0 & 0 & 1 \end{bmatrix} \quad [78]$$

Resulting in:

$$A_{ORB}^{SAT} =$$

$$\begin{bmatrix} \mathrm{c}(\phi^{SAT})\mathrm{c}(\psi^{SAT}) & \mathrm{c}(\theta^{SAT})\mathrm{s}(\psi^{SAT})+\mathrm{c}(\psi^{SAT})\mathrm{s}(\phi^{SAT})\mathrm{s}(\theta^{SAT}) & \mathrm{s}(\psi^{SAT})\mathrm{s}(\theta^{SAT})-\mathrm{c}(\psi^{SAT})\mathrm{c}(\theta^{SAT})\mathrm{s}(\phi^{SAT}) \\ -\mathrm{c}(\phi^{SAT})\mathrm{s}(\psi^{SAT}) & \mathrm{c}(\psi^{SAT})\mathrm{c}(\theta^{SAT})-\mathrm{s}(\phi^{SAT})\mathrm{s}(\psi^{SAT})\mathrm{s}(\theta^{SAT}) & \mathrm{c}(\psi^{SAT})\mathrm{s}(\theta^{SAT})+\mathrm{c}(\theta^{SAT})\mathrm{s}(\phi^{SAT})\mathrm{s}(\psi^{SAT}) \\ \mathrm{s}(\phi^{SAT}) & -\mathrm{c}(\phi^{SAT})\mathrm{s}(\theta^{SAT}) & \mathrm{c}(\phi^{SAT})\mathrm{c}(\theta^{SAT}) \end{bmatrix} \quad [79]$$

Where the ‘s’ and ‘c’ in the above equations represent sine and cosine functions respectively.

The above discussion was generalized to either of the two satellites (Upper or Lower). In order to accurately describe the attitude of each of the spacecraft, the roll, pitch, and yaw angles will use superscripts ‘U’ and ‘L’ for Upper and Lower satellite Euler angles respectively, thus forming corresponding rotation matrices A_{ORB}^{SATU} and A_{ORB}^{SATL}.

4.2.9 Transformation between Satellite and Sail reference frames

In the special case when the sail is neither billowed out nor pitched, the satellite axis ($\hat{X}^{SAT}$, $\hat{Y}^{SAT}$, $\hat{Z}^{SAT}$) and the sail axis ($\hat{X}^{Sail}$, $\hat{Y}^{Sail}$, $\hat{Z}^{Sail}$) coincide and the transformation matrix between them is simply the identity matrix.

In the general case when the sail is billowed out and pitched, it is necessary to both rotate between the two frames (when computing the force) and also to offset the origin (when computing the torques).

One of the assumptions used throughout the CubeSail dynamical derivation is the film does not experience plastic or elastic deformation. As a result, the only permissible deformations that are considered are the longitudinal bending and twisting shown in Figure 60. The non-permissible deformation is shown in Figure 61 and results in non-uniform tension along the film by creating zones of compression and tension.

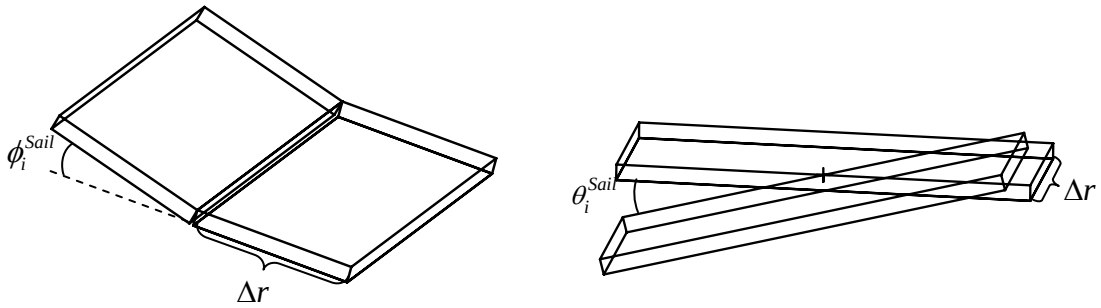

Figure 60. Permissible sail deformations. Longitudinal bending (left), twisting (right).

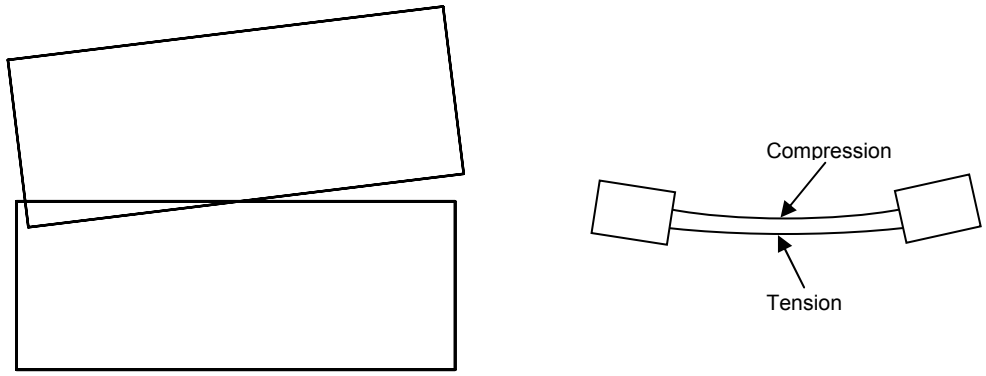

Figure 61. Non-permissible deformation geometry (lateral bending).

As a result, the transformation between the SAT and 'Sail' frames reduces to two sequential orthogonal rotations. The first occurs around the $\hat{X}^{Sail}$ axis by the angle θ^{Sail}, followed by the rotation around the new $\hat{Y}^{Sail}$ axis by the angle ϕ^{Sail}. The resultant transformation matrix from the SAT to the Sail frame is:

$$R_1\left(\theta^{Sail}\right)=\begin{bmatrix}1 & 0 & 0\\ 0 & \cos\left(\theta^{Sail}\right) & \sin\left(\theta^{Sail}\right)\\ 0 & -\sin\left(\theta^{Sail}\right) & \cos\left(\theta^{Sail}\right)\end{bmatrix} \qquad R_2\left(\phi^{Sail}\right)=\begin{bmatrix}\cos\left(\phi^{Sail}\right) & 0 & -\sin\left(\phi^{Sail}\right)\\ 0 & 1 & 0\\ \sin\left(\phi^{Sail}\right) & 0 & \cos\left(\phi^{Sail}\right)\end{bmatrix} \quad [80]$$

$$A_{SAT}^{Sail}=R_2\left(\phi^{Sail}\right)\cdot R_1\left(\theta^{Sail}\right)=\begin{bmatrix}\cos\left(\phi^{Sail}\right) & \sin\left(\phi^{Sail}\right)\sin\left(\theta^{Sail}\right) & -\sin\left(\phi^{Sail}\right)\cos\left(\theta^{Sail}\right)\\ 0 & \cos\left(\theta^{Sail}\right) & \sin\left(\theta^{Sail}\right)\\ \sin\left(\phi^{Sail}\right) & -\cos\left(\phi^{Sail}\right)\sin\left(\theta^{Sail}\right) & \cos\left(\phi^{Sail}\right)\cos\left(\theta^{Sail}\right)\end{bmatrix} \quad [81]$$

The transformation from any given frame to the sail frame can thus be accomplished by knowing the orbital position (in order to find A_{ECI}^{ORB}), the attitude of the

satellites (in order to find A_{ORB}^{SAT} and θ^{Sail}), and finally the forces on the sail in order to iteratively compute ϕ^{Sail} (in order to find A_{SAT}^{Sail}).

4.3 Modeling of Forces and Torques on the Spacecraft

4.3.1 Aerodynamic Drag

Figure 62 demonstrates relative magnitudes of environmental torques on a sample spacecraft in a circular low Earth orbit. These particular results are for a 1.52 m diameter circular cylinder, 9.14 m in length. The magnetic torque was evaluated assuming a 1 Amp current in a single loop of wire around the length of the cylinder oriented to give the maximum torque. The aerodynamic torque was computed using free-molecular flow theory, and the radiation torque was computed using a reflectivity of one.[61]

As shown in the figure, at the altitudes of interest (approximately 800 km), the aerodynamic, gravity gradient, and magnetic torques are all of the same order of magnitude. Although the solar radiation pressure is shown to be an order of magnitude smaller, one must keep in mind that the sample satellite was not a solar sailing spacecraft.

The comparable strength of these torques illustrates the need to accurately model the disturbance torques in order to properly size the magnetic control authority. The below discussion focuses on the aerodynamic drag torque and presents a suitable model to calculate the coefficient of drag of the sail. The aerodynamic drag model used for the two tip satellites is the same one used for the ION1 spacecraft and is covered in detail in Ref [40].

The goal of this derivation is to arrive at the force equation in the normal and tangential directions applicable at each of the elemental section of height Δr and width of 78 mm as seen in Figure 57.

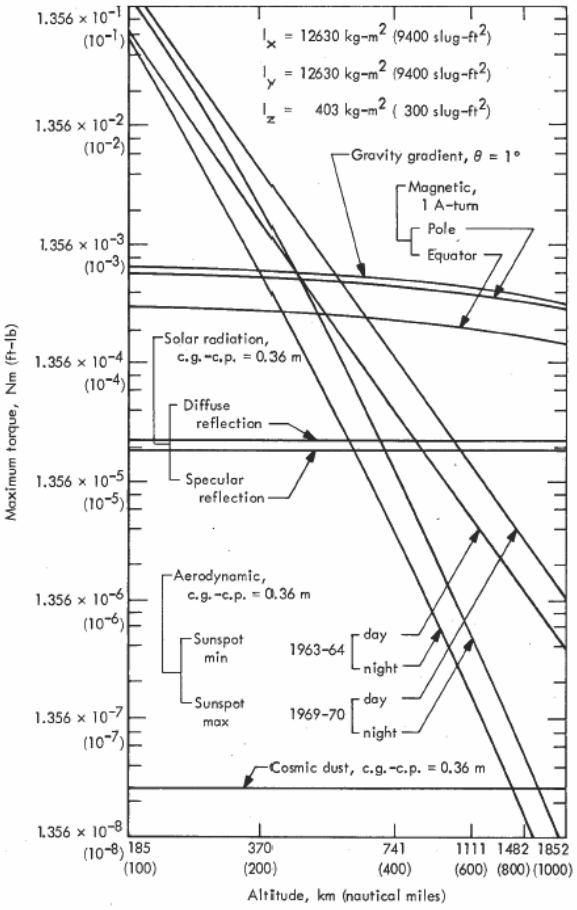

Figure 62. Relative magnitudes of the environmental torques on an Earth satellite.[61,62]

The magnitude of the aerodynamic force acting on a spacecraft can be written as:

$$F_{AD} = \frac{1}{2}\rho_{atm} \cdot V_R^{\,2} \cdot C_D \cdot A_{cs} \qquad [82]$$

In order to accurately predict the aerodynamic force, each of the terms in Equation 82 must be estimated. The magnitude of relative velocity of the incoming particles, V_R, can be computed with high accuracy from orbital mechanics. The atmospheric density, ρ_{atm}, is typically dependent on several factors including altitude,

latitude of the subsatellite point, period within the solar cycle, as well as the day of the year and time of the day. A high fidelity atmospheric density model called the NRLMSISE00 is being used and was described previously. The cross sectional area, A_{cs}, of the sail presented into the velocity direction depends on the exact shape of the film and will be addressed in more detail in a subsequent section.

Lastly, the coefficient of drag must be estimated. Historically, many designers assumed a constant value of 2.2 during the design phase and often adjusted its value while performing orbit determination analysis after the vehicle has been launched. The actual coefficient of drag is dependent on a number of factors. The number and type of molecules impacting the surface, as seen in Figure 63, varies over several orders of magnitude with altitude. For example, at 200 km, N_2 and O are the major constituents of the thermosphere and have approximately the same density. In contrast, at 800 km, He and O densities are comparable, while the O_2, Ar, and N_2 densities have dropped significantly.

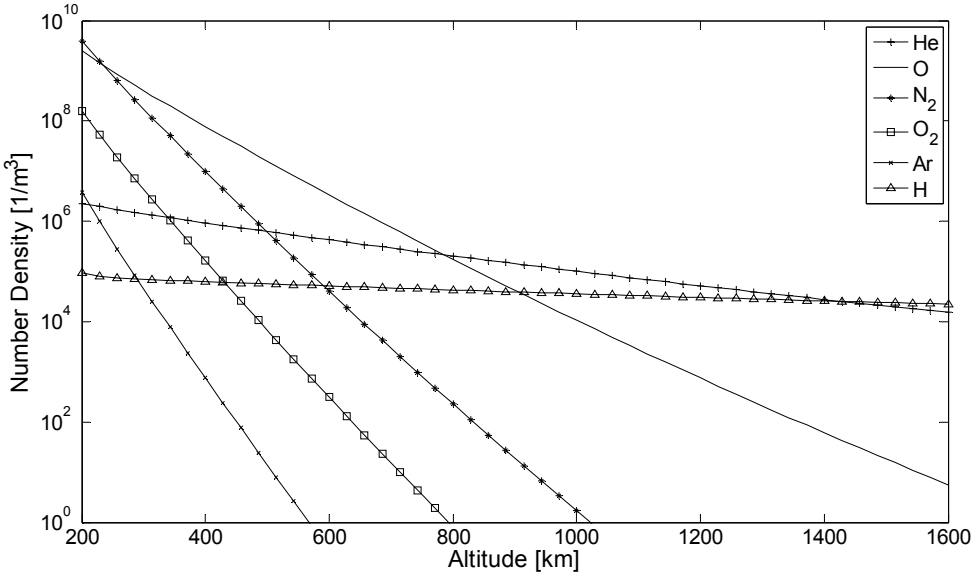

Figure 63. Molecule number density from NRLMSISE00 model. Lat = 60º, Lon = 200º, and default solar flux values.

The importance of these thermospheric constituents is illustrated in Figure 64 and shows the widely varying kinetic energies that will dictate the energy transfer as the molecules impact the surface.

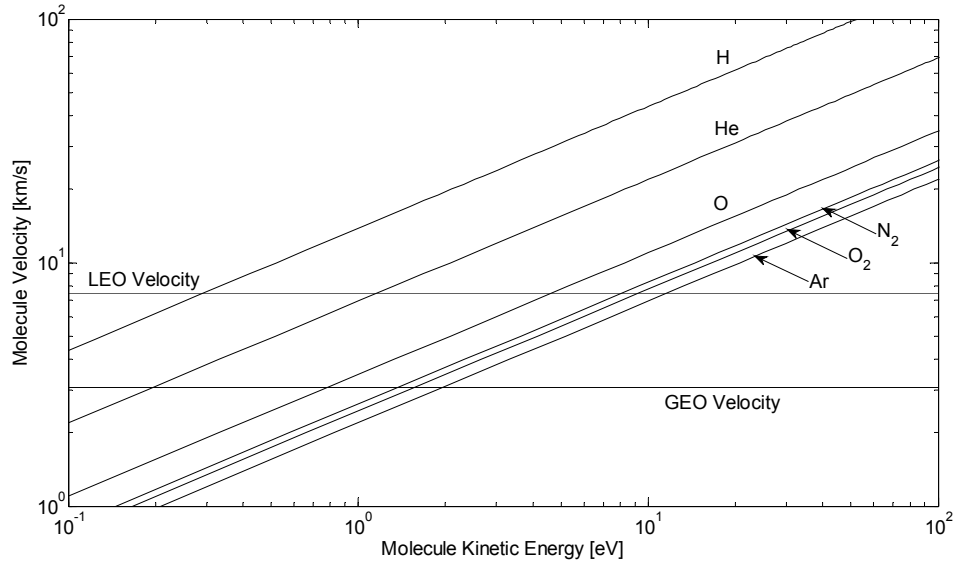

Figure 64. Velocity vs. kinetic energy for various thermospheric constituents.[63]

Other factors that affect the aerodynamic drag coefficient include the type of surface (here assumed aluminum due to the sail film coating), the level of contamination of the surface, the temperature of the incident molecules, the temperature of the surface, the angle of incidence and molecular reflection model. The last two dependencies are shown for a sample flat plate in Figure 65 with α as the thermal accommodation coefficient, and illustrate that the coefficient of drag varies between 1 and 4—a significant disparity.

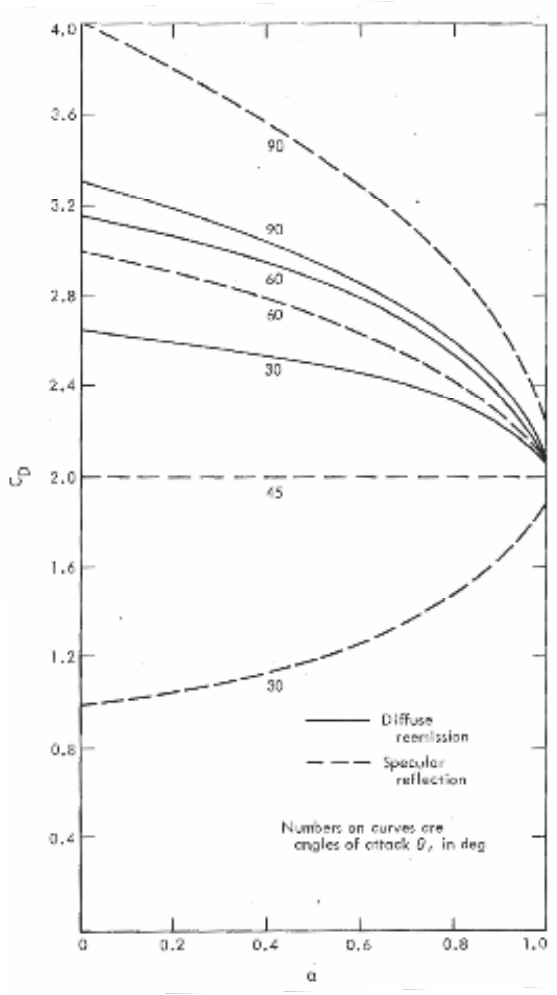

Figure 65. Sample variation of the drag coefficient for a flat plate in hyperthermal free-molecule flow as a function of incidence angle and reflection model.[62] α is the thermal accommodation coefficient and angle of attack $\theta \propto \overline{\alpha}^{AD}$.

At the current time, a general quantum-based theory of these interactions is not sufficiently developed to predict the exact exchange of energy and momentum, and macroscopic averages must be taken. The formulation is typically done through the use of accommodation coefficients and the particular derivation presented below is adopted from Ref [39].

Before starting the derivation, it is useful to define specular and diffuse reflections. Specular reflection, seen in Figure 66 (left), is a concept where each molecule bounces off the surface with no change in energy. The angle of incidence equals the angle of

reflection and the incoming velocity, reflected velocity, and plane normal are all co-planar. The momentum transfer is normal to the surface and equals twice the normal component of the incoming momentum. In practice, very few molecules experience pure specular reflection. Instead, the incoming molecule tends to be, at least partially, *accommodated* to the surface. The diffuse reflection model assumes that the molecule becomes completely accommodated to the surface and 'loses all memory' of its incoming direction and energy. While it is completely accommodated, it interacts with other molecules on the surface and eventually detaches with a probabilistic kinetic energy characteristic of surface temperature and a probabilistic direction governed by a "cosine" distribution as shown in Figure 66 (right).[39]

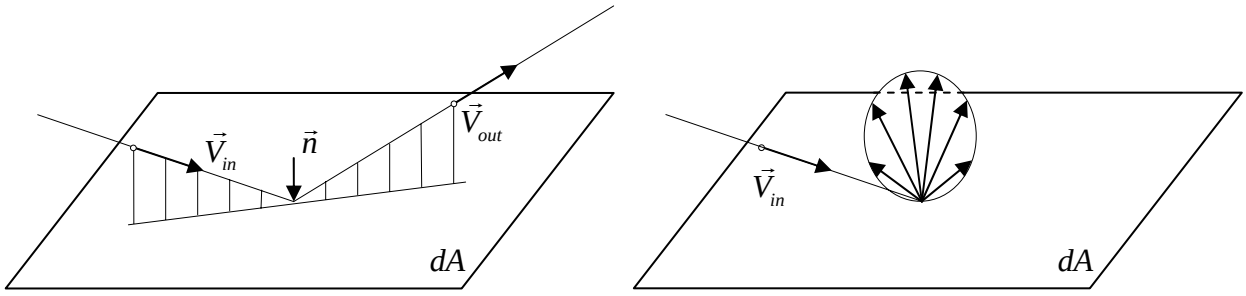

Figure 66. Specular (left) and diffuse (right) molecular reflection.

The actual molecular behavior falls somewhere between purely specular and purely diffuse reflection. Using partial accommodation theory, the force acting on surface element dA will have components in both inward normal facing direction ($\vec{n}$) and in the tangential direction ($\vec{t}$). We can therefore write the force on a single area element broken into normal and tangential components as follows:

$$d\vec{f} = d\vec{f}_n + d\vec{f}_t \qquad [83]$$

The elemental area projected onto the normal direction can be written using the angle of incidence, shown in Figure 67, as $\cos(\alpha^{AD}) \cdot dA$. Similarly, the elemental area

projected onto the tangential direction is $\sin(\alpha^{AD}) \cdot dA$. The superscript AD is used to indicate angle of incidence of the thermospheric constituent particles and not the photons used in the solar radiation pressure calculation.

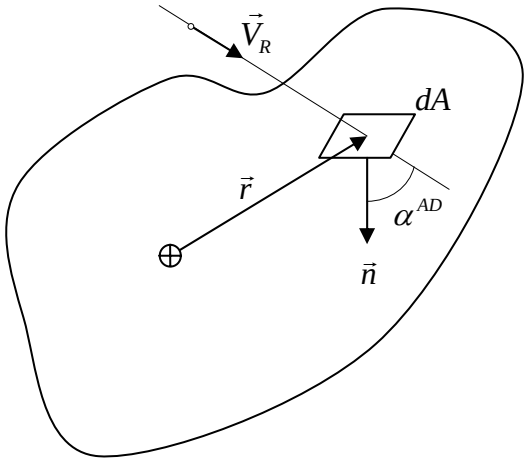

Figure 67. Incident molecule on element of spacecraft's surface.

The angle of attack can be found from the dot product of the local atmospheric velocity vector, $\vec{V}_R$, and the surface normal, $\vec{n}$:

$$\cos(\alpha^{AD}) = \hat{V}_R \bullet \vec{n} \quad \text{where} \quad \hat{V}_R = \frac{\vec{V}_R}{\|\vec{V}_R\|} \qquad [84]$$

The relative velocity between the spacecraft and incoming molecules is dominated by the orbital velocity and the rotation of the atmosphere, as shown in Figure 68.

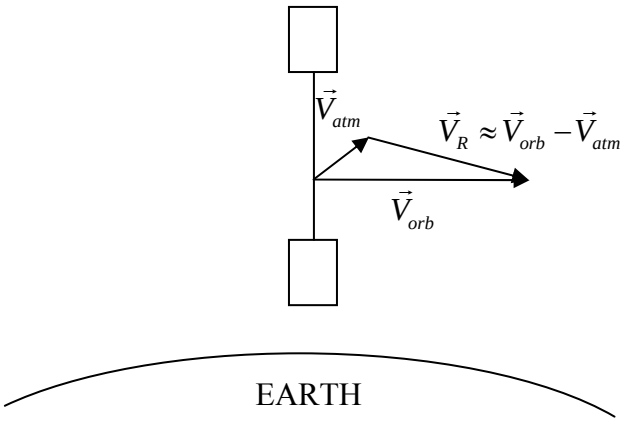

Figure 68. Local atmospheric velocity vector diagram.

Contributions to $\vec{V}_R$ from random thermal motion of individual molecules are small and are thus ignored. Ravindran and Hughes[64] provide a compact equation for the relative velocity of the incoming particles in the body frame (in this case the 'Sail' frame), $\vec{V}_R^{Sail}$, that takes into account the orbital speed and rotation of the atmosphere as:

$$\vec{V}_R^{Sail} = V_{orb}\left(1 - \frac{\omega_E \cdot R \cdot \cos i}{V_{orb}}\right) \cdot A_{SAT}^{Sail} \cdot A_{ORB:CubeSail}^{SAT} \cdot A_{ORB:Ravindran}^{ORB:CubeSail} \cdot \begin{bmatrix} -1 \\ \left(\frac{\omega_E \cdot R}{V_{orb}}\right) \cdot \sin i \cdot \cos f \\ 0 \end{bmatrix} \quad [85]$$

In the above equation V_{orb} is the magnitude of the orbital velocity, ω_E is the rotational rate of the Earth, R is the magnitude of orbital radius, i is the orbital inclination, and f is the orbital true anomaly. The matrix $A_{ORB:Ravindran}^{ORB:CubeSail}$ is applied to correct for differently defined orbital reference frames between the Ravindran/Hughes and CubeSail frames. The orbital reference frame in Ref [64], shown in Figure 69, is defined with the z-axis in the inward radial direction, the x-axis in the general velocity direction in the orbital plane, and the y-axis as normal to the orbital plane in the right-handed coordinate system.

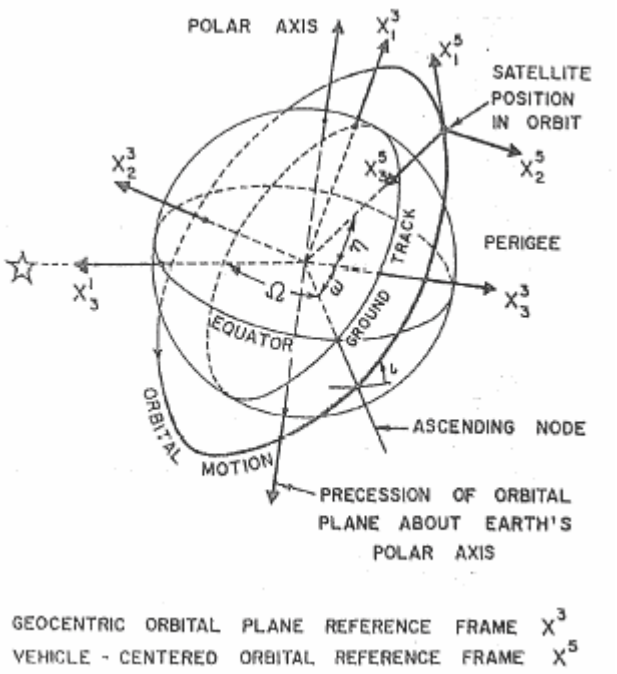

Figure 69. Ravindran and Hughes Orbital Reference Frame.[64]

The transformation matrix between these two orbital reference frames can therefore be written from observation as:

$$A_{ORB:Ravindran}^{ORB:CubeSail} = \begin{bmatrix} 0 & 1 & 0 \\ 0 & 0 & -1 \\ -1 & 0 & 0 \end{bmatrix}^T \qquad [86]$$

Henceforth, the 'ORB' frame will always refer to the CubeSail orbital reference frame.

Returning to the elemental force development, we first look at the limit case of completely diffuse reflection when all molecules are fully accommodated. The incoming mass flux on dA can be written as $\rho_{atm} \cdot V_R \cdot \cos(\alpha^{AD}) \cdot dA$. The momentum flux through dA, which is also the force imparted to dA, in the $\vec{n}$ and the $\vec{t}$ directions can therefore be written as:

$$\left(\rho_{atm} \cdot V_R \cdot \cos(\alpha^{AD}) \cdot dA\right) \cdot \left(V_R \cdot \cos(\alpha^{AD})\right) \vec{n} \qquad [87]$$

and

$$\left(\rho_{atm} \cdot V_R \cdot \cos\left(\alpha^{AD}\right) \cdot dA\right) \cdot \left(V_R \cdot \sin\left(\alpha^{AD}\right)\right)\vec{t} \qquad [88]$$

Although the molecules leaving the wall have no mean motion in the tangential direction, they do have mean velocity in the $-\vec{n}$ direction with a magnitude denoted by V_b. The kinetic theory of gasses provides us with the following equation for V_b as a function of surface temperature, T_b ,:

$$V_b = \left(\frac{\pi \bar{R} T_b}{2 m_{gas}}\right)^{\frac{1}{2}} \qquad [89]$$

Here the variable $\bar{R}$ is the universal gas constant ($\bar{R} = 8.314 \times 10^3 \ J / kg \cdot mole \cdot °C$) and m_{gas} is the molecular weight of the gas. Since CubeSail will most likely be deployed into orbits between 600 and 1000 km in altitude, the dominant species will be helium (He) and atomic oxygen (AO) and V_b is approximately 5% of V_R.

It is therefore possible to write the elemental force on dA in the normal and tangential directions as:

$$\begin{aligned} d\vec{f}_n^{\,Diffuse} &= \rho_{atm} \cdot V_R \cdot \cos\left(\alpha^{AD}\right) \cdot \left(V_R \cdot \cos\left(\alpha^{AD}\right) + V_b\right) \cdot \vec{n} \cdot dA \\ d\vec{f}_t^{\,Diffuse} &= \rho_{atm} \cdot V_R^2 \cdot \sin\left(\alpha^{AD}\right) \cdot \cos\left(\alpha^{AD}\right) \cdot \vec{t} \cdot dA \end{aligned} \qquad [90]$$

The other limiting case is if all molecules reflect purely specularly. Since the molecules leave the surface with no change in the velocity and angle of incidence equals the angle of reflection, it is possible to write the elemental force as:

$$\begin{aligned} d\vec{f}_n^{\,Specular} &= 2 \cdot \rho_{atm} \cdot V_R^2 \cdot \cos^2\left(\alpha^{AD}\right) \cdot \vec{n} \cdot dA \\ d\vec{f}_t^{\,Specular} &= \vec{0} \end{aligned} \qquad [91]$$

Since the real molecule-to-surface interactions lie between these two limiting cases, it is convenient to define two factors: σ_n and σ_t called the *accommodation*

coefficients for normal and tangential momentum exchange. It is therefore possible to write the force components as:

$$\begin{aligned} d\vec{f}_n &= \sigma_n \cdot d\vec{f}_n^{\,Diffuse} + (1-\sigma_n) \cdot d\vec{f}_n^{\,Specular} \\ d\vec{f}_t &= \sigma_t \cdot d\vec{f}_t^{\,Diffuse} + (1-\sigma_t) \cdot d\vec{f}_t^{\,Specular} \end{aligned} \quad [92]$$

Substituting and collecting terms, it is possible to write:

$$\begin{aligned} d\vec{f}_{AD} = &\left\{ \rho_{atm} \cdot V_R^2 \cdot \cos(\alpha^{AD}) \cdot \left[\left(\frac{V_b}{V_R} - \cos(\alpha^{AD}) \right) \cdot \sigma_n + 2\cos(\alpha^{AD}) \right] \right\} \vec{n} \cdot dA \\ &+ \left\{ \rho_{atm} \cdot V_R^2 \cdot \cos(\alpha^{AD}) \cdot \sin(\alpha^{AD}) \cdot \sigma_t \right\} \vec{t} \cdot dA \end{aligned} \quad [93]$$

To obtain the total force in the normal and tangential directions, the above equations must be integrated over the entire sail area. In normal operations, the sail will often be both billowed out and pitched (twisted), resulting in a non-uniform angle α^{AD} along the blade. The deformed shape is divided into n sections, as was done in Figure 57, and the incidence angle of the incoming molecules is computed for each of the differential areas, dA. The corresponding accommodation coefficients are then calculated using Equations 95 and 96 (discussed shortly) and integrated over the length of the blade to obtain the total force. It is important to note that since the shape of the sail is dependent on the force and vice-versa the force depends on the sail shape, this is done iteratively.

The final remaining step is to write the above equations in the *Sail* frame. A small difficulty arises when determining the sign of the force, which depends on the direction of incoming particles. The aerodynamic drag acts on the sail regardless of which side is presented into the velocity direction and at this point the difference between the reflective and emissive sides is not taken into account. The correct signs for the aerodynamic drag force are obtained by first limiting the incidence angle such

that $0 \le \alpha^{AD} \le 90^{\circ}$ (note that it is still possible to apply either positive or negative pitch) and then using the signum function of the appropriate components of the incoming particle vector expressed in the Sail frame, $\hat{V}_R^{Sail}$. Using Figure 70 to aid in the visualization of the aerodynamic drag geometry, it is possible to write the differential force components in the *Sail* frame as:

$$d\vec{f}_{AD}^{\,Sail} = \begin{bmatrix} 0 \\ sign\left(V_{R,y}^{Sail}\right) \cdot \rho_{atm} \cdot V_R^2 \cdot \cos\left(\alpha^{AD}\right) \cdot \sin\left(\alpha^{AD}\right) \cdot \sigma_t \cdot dA \\ sign\left(V_{R,z}^{Sail}\right) \cdot \rho_{atm} \cdot V_R^2 \cdot \cos\left(\alpha^{AD}\right) \cdot \left[\left(\frac{V_b}{V_R} - \cos\left(\alpha^{AD}\right)\right) \cdot \sigma_n + 2\cos\left(\alpha^{AD}\right)\right] \cdot dA \end{bmatrix} \quad [94]$$

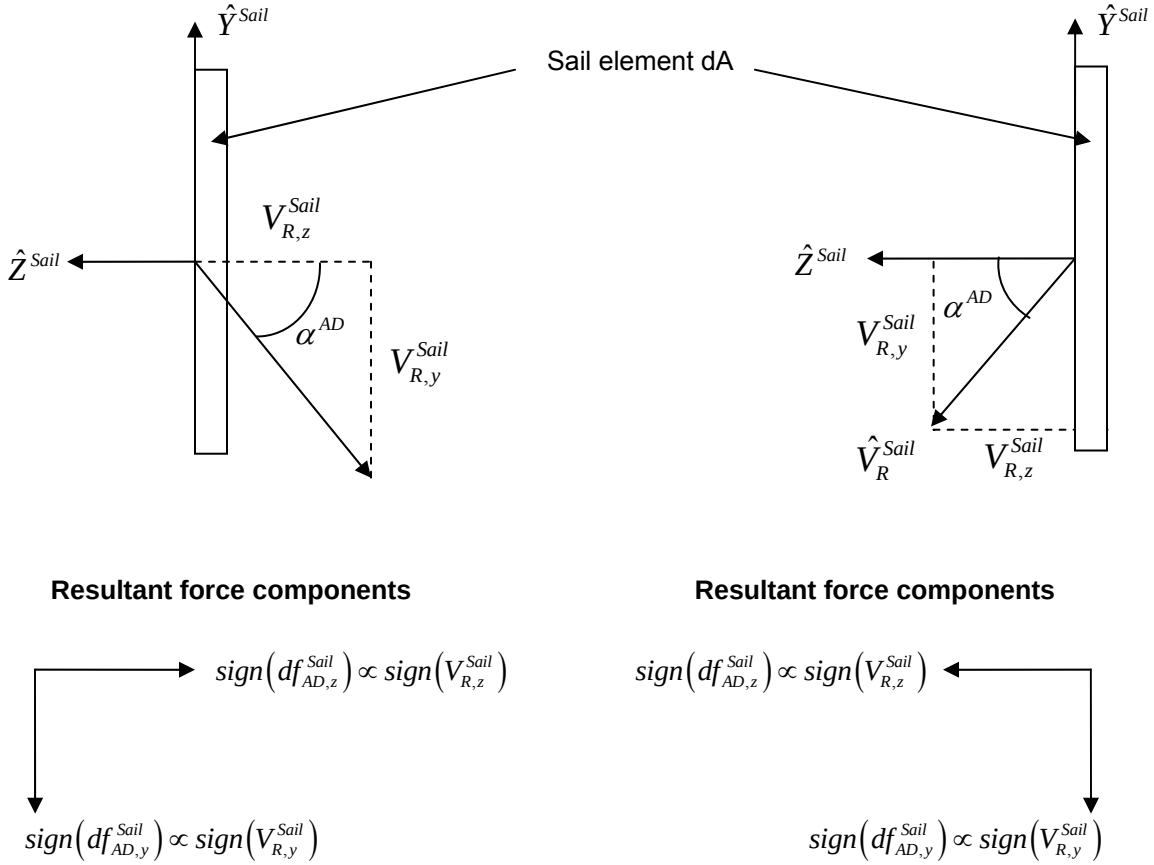

Figure 70. Aerodynamic drag force sign diagram.

As mentioned previously, the subscript i shown in Figure 57 was dropped for clarity with the implicit understanding that the elemental aerodynamic drag force in the above equation is applied at each elemental area dA with a unique incidence angle α^{AD}, unique accommodation coefficients σ_n and σ_t computed for the specific α^{AD}, and the atmospheric density specific to the altitude of each dA.

As discussed earlier, there are a number of factors, including angle of incidence, atmospheric temperature and composition, surface material and contamination, and others that contribute to estimating the coefficient of drag or, equivalently the accommodation coefficients. Several previous studies assumed that $\sigma_n = \sigma_t \approx 0.8$ [61,62,65], regardless of the above-mentioned factors. Gaposchkin[63] combined and extended the work of several previous models and presented the following result for a flat plate at 800 km altitude for Helium, as shown in Figure 71. Since the sail surface will be discretized along its length, forming rectangles which are 78 mm in width and Δr in height, the flat plate assumption is appropriate. The final altitude for the mission has not been selected, but is predicted to fall between 600 and 1000 km, thus validating the results for 800 km. Lastly, at altitudes of interest, the dominant atmospheric constituents are helium and atomic oxygen, thus making the presented results relatively representative of the conditions (results for atomic oxygen are not available). Furthermore, the presented model assumed a wall temperature of 300 K, which is a reasonable assumption for the typical operating temperature of the CubeSail spacecraft (predicted operating temperature is discussed in Appendix B). The nomenclature used in Figure 71 compares to previous notation by the following relationships: $\sigma \triangleq \sigma_t$, $\sigma' \triangleq \sigma_n$, $\bar{\alpha}^{AD} \triangleq 90^\circ - \alpha^{AD}$. For example, at an angle α^{AD} of 20°, the corresponding value of

$\bar{\alpha}^{AD} = 70^{\circ}$, and the accommodation coefficients can be read from Figure 71 as $\sigma_n = 0.599$, and $\sigma_t = 0.294$.

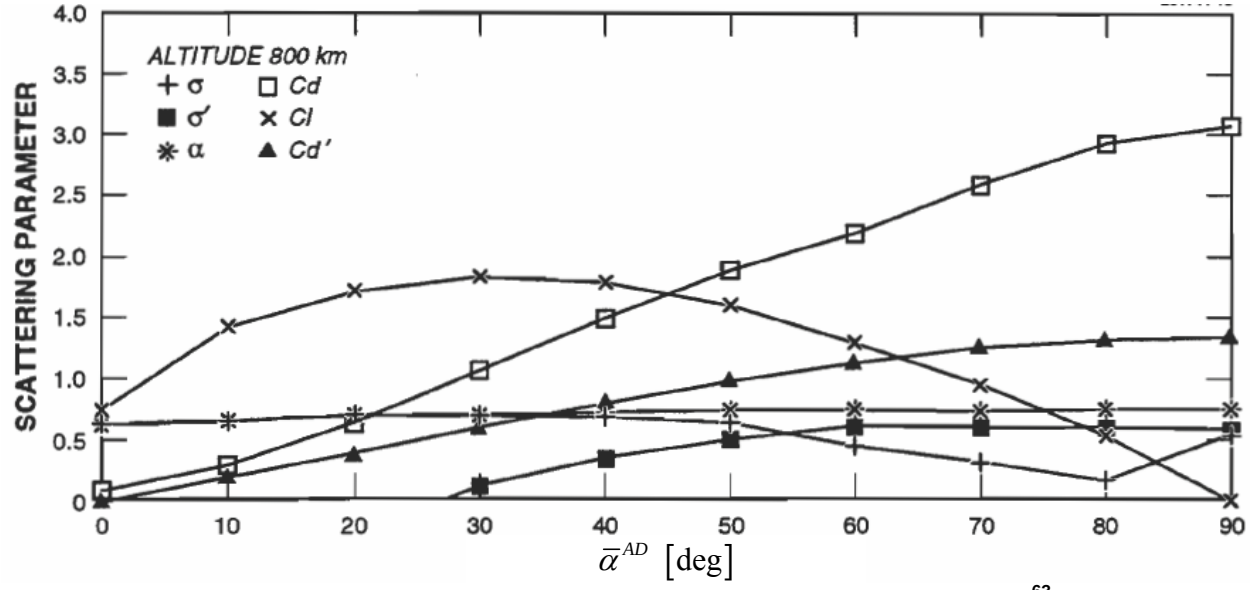

Figure 71. Accommodation coefficients for a flat plate for helium.[63]

The data from the plot can be fitted as shown in Figure 72. The accommodation coefficient in the normal direction is fitted with a sigmoidal function (whose general shape and equation is shown in Figure 73) with the following values computed using Nonlinear Least Squares function in Matlab:

$$\sigma_n(\bar{\alpha}^{AD}) = \frac{0.5959}{1 + e^{-\frac{(\bar{\alpha}^{AD} - 38.61)}{6.085}}} \qquad [95]$$

The accommodation coefficient in the tangential direction is fitted using a 7th order polynomial function with the following form:

$$\begin{aligned}\sigma_t(\bar{\alpha}^{AD}) = {} & 3.429\times10^{-13}\cdot(\bar{\alpha}^{AD})^7 - 3.494\times10^{-11}\cdot(\bar{\alpha}^{AD})^6 - 2.99\times10^{-9}\cdot(\bar{\alpha}^{AD})^5 \\ & +6.147\times10^{-7}\cdot(\bar{\alpha}^{AD})^4 - 3.844\times10^{-5}\cdot(\bar{\alpha}^{AD})^3 + 9.798\times10^{-4}\cdot(\bar{\alpha}^{AD})^2 \\ & -5.955\times10^{-3}\cdot(\bar{\alpha}^{AD}) + 6.24\times10^{-1}\end{aligned} \qquad [96]$$

Equations 95 and 96 compute the normal and tangential accommodation coefficients given a complement of the incidence angle, $\bar{\alpha}^{AD}$, in degrees.

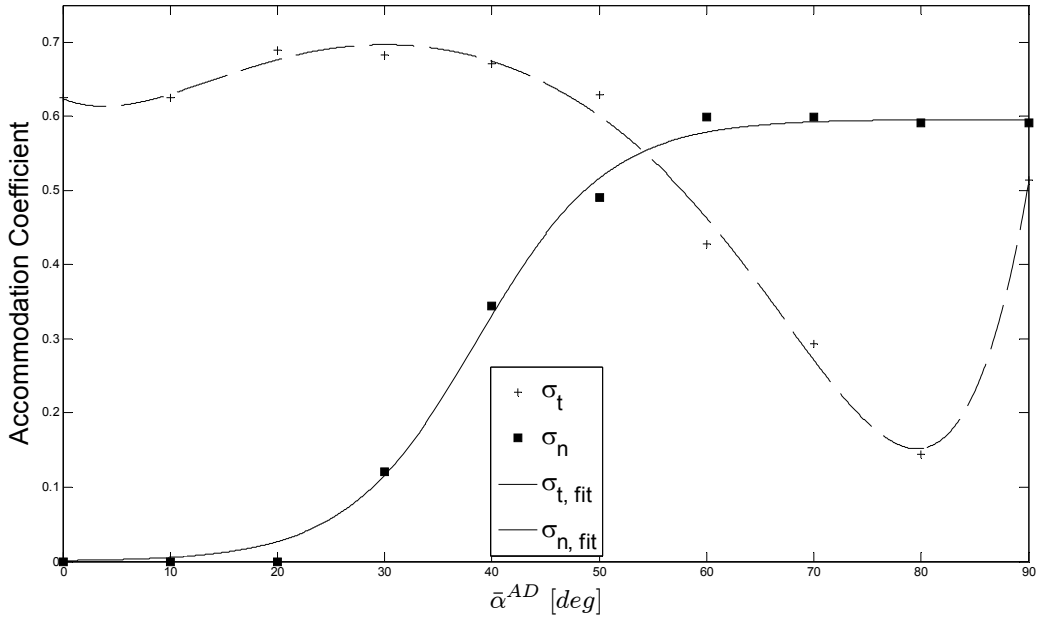

Figure 72. Curve fitted accommodation coefficients vs. $\bar{\alpha}^{AD}$ for a flat plate at 800 km for He.

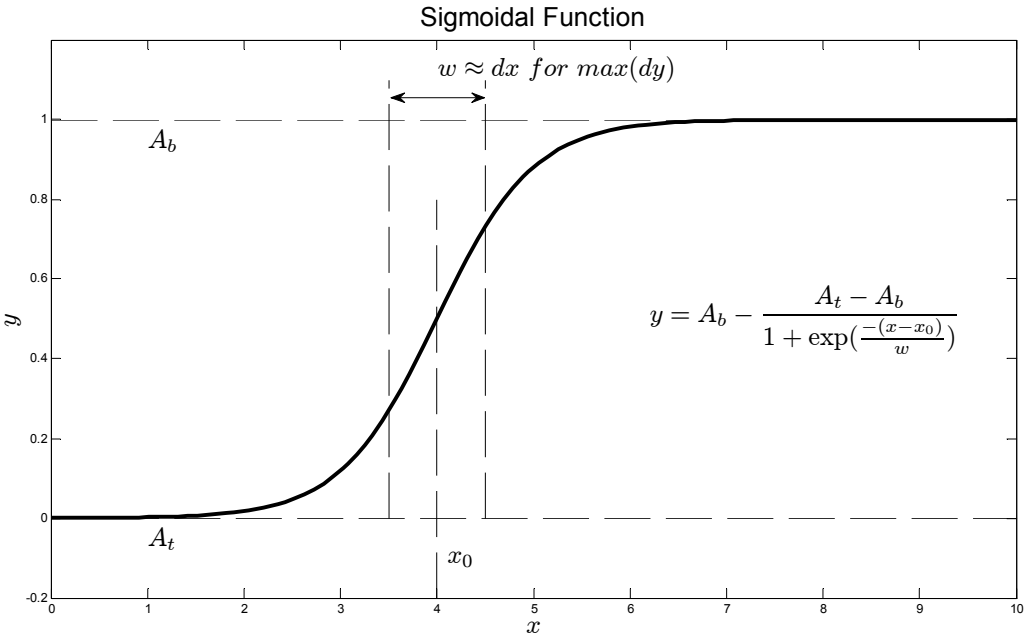

Figure 73. General definition of a sigmoidal function.

4.3.2 Comparison of Coefficient of Drag Models for a Flat Plate

In order to compare the flat plate assumption of constant C_D of 2.2 with the above accommodation coefficient model, we assume that the sail is neither billowed out nor pitched and sum the aerodynamic drag forces along this 'flat plate' surface. With

the 'flat plate' assumption, the 'Sail' and 'SAT' frames are the same and it is possible to write:

$$A_{SAT}^{Sail} \cdot A_{ORB}^{SAT} = A_{ORB}^{SAT} \quad [97]$$

with A_{ORB}^{SAT} as defined in Equation 79. For illustration purposes, a satellite with the following orbital and attitude parameters is chosen:

Table 10. Parameters for Sample Calculation.

Symbol	Variable	Value
R	Orbital Radius [km]	6378.132 + 800
V_{orb} †	Orbital Speed (circular) [km/s]	7.4518
e	Orbital eccentricity	0
i	Orbital Inclination [deg]	60
ω	Orbital Argument of Perigee [deg]	0
Ω	Orbital Right Ascension of the Ascending Node [deg]	45
f	Orbital True Anomaly [deg]	100
t	Epoch [yr mo day hr min sec]	[2010 7 1 12 0 0]
θ	Satellite/Sail Pitch [deg]	0→90
ϕ	Satellite/Sail Roll [deg]	0
ψ	Satellite/Sail Yaw [deg]	0
ρ_{atm} *	Atmospheric Density [kg/m^3]	6.2683e-015
V_b	Mean kinetic energy of diffusely reflected particles.	$0.05 \cdot V_R$

The parameters are sufficient to calculate the normal and tangential components of the aerodynamic drag force. The steps are as follows:

1. Compute $\vec{V}_R$ from Equation 85.
2. Compute α^{AD} from Equation 84.
3. Compute $\sigma_n(\bar{\alpha}^{AD})$ and $\sigma_t(\bar{\alpha}^{AD})$ from Equations 95 and 96 respectively.
4. Compute ρ_{atm} using the NRLMSISE00 model.
5. Sum over the entire surface area to compute $\vec{f} = \vec{f}_n + \vec{f}_t$ from Equation 93.
6. Compute the magnitude of the aerodynamic force from $f_{AD} = \sqrt{f_n^2 + f_t^2}$.

The above steps are used to compute the magnitude of the aerodynamic force and are compared to results obtained using Equation 82 with a constant C_D of 2.2. It is

† Corresponds to value at R

important to note that the area, A_{cs}, in Equation 82 is the cross sectional area exposed to the velocity direction and must be computed taking the projection onto the velocity vector. The so-called 'vector area' is computed by taking the dot product between the surface normal and the vector onto which the area is projected. If the sail is flying in any orientation other than the zero pitch/roll/yaw configuration, the normal vector must be rotated appropriately. This can be done by using the rotation matrix shown in Equation 79 and replacing the pitch angle, θ, with its complement ($\bar{\theta} = 90^{\circ} - \theta$) to correct for the fact that the vector area uses the angle between surface normal, while the pitch angle is defined from surface tangential as shown in Figure 74. Roll and yaw angles do not require any modifications.

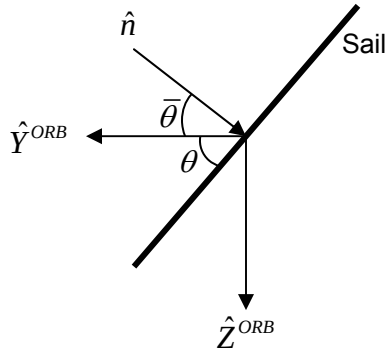

Figure 74. Circular orbit geometry of a pitched flat sail.

Assuming that the spacecraft is in a circular orbit, the velocity vector coincides with the $\hat{Y}^{ORB}$ direction and the sail area projected onto this vector can be written as:

$$A_{cs} = A_{\max} \cdot \left(A_{ORB}^{SAT}\left(\bar{\theta}, \phi, \psi\right) \cdot \begin{bmatrix} 0 \\ 0 \\ 1 \end{bmatrix} \right)^{T} \cdot \begin{bmatrix} 0 \\ 1 \\ 0 \end{bmatrix} \qquad [98]$$

Applying these results to Equation 82 results in the following plot for the magnitude of the aerodynamic drag:

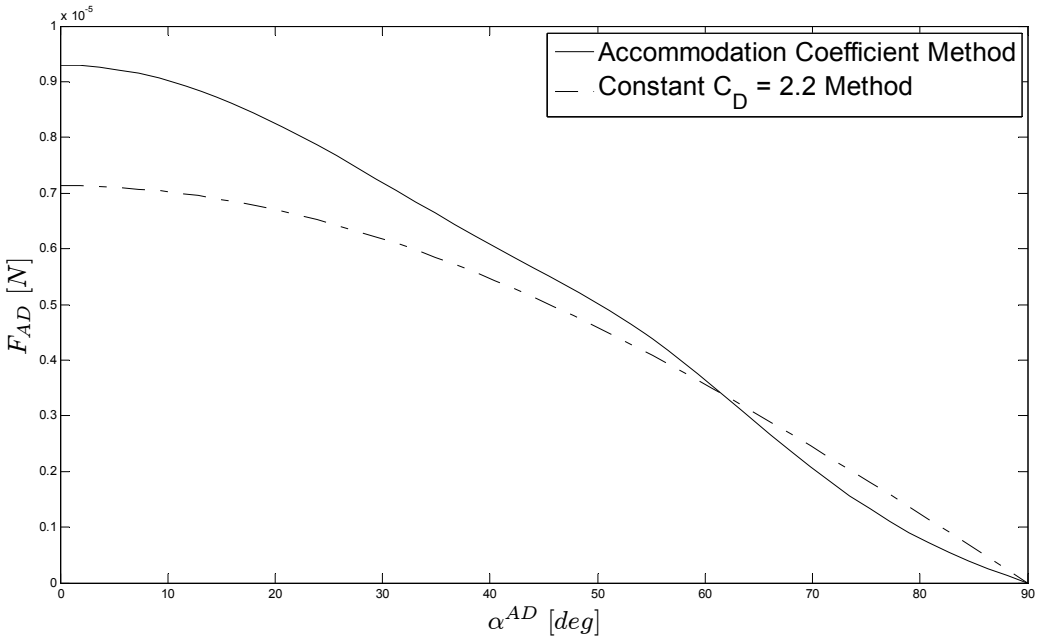

Figure 75. Comparison of aerodynamic drag force models for a flat plate CubeSail geometry.

As can be seen from the above figure, the classical method of assuming a constant coefficient of drag underestimates the force for all but large (> 60º) angles of incidence (edge-on configurations). Interestingly, matching the coefficient of drag in Equation 82 to achieve the force computed using the accommodation coefficient method, results in Figure 76. The value of C_D varies between 2.87 and 1.24 and is in line with the results of previous studies of a) NASA[62] shown in Figure 65 and of b) Moe and Moe[66] shown in Figure 77.

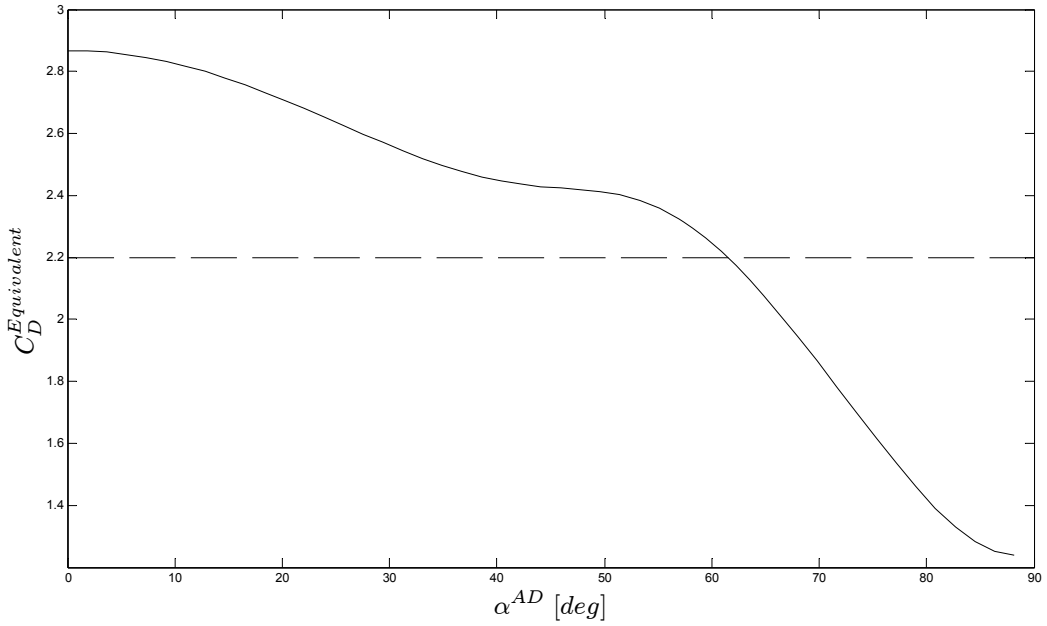

Figure 76. $C_D^{Equivalent}$ **obtained by matching aerodynamic forces computed using accommodation coefficients and constant** $C_D = 2.2$**.**

Looking at Figure 65 is important to remember that the numbers on the curves correspond to angles of attack and are complements of the incident angle α^{AD} (ie. $\theta \propto \overline{\alpha}^{AD} = 90^\circ - \alpha^{AD}$). As a result, for a specular reflection at an angle of attack of 30º ($\alpha^{AD} = 70^\circ$), the coefficient of drag varies between 1 and 1.9 depending on the thermal accommodation coefficient. In comparison, the value of $C_D^{Equivalent}$ from Figure 76 is approximately 1.87.

Figure 77 illustrates a fully diffuse reflection for a flat plate with $\alpha^{AD} = 0^\circ$, albeit at lower altitudes than those of CubeSail. Nevertheless, the trend shows a significant departure from the classical assumption of $C_D = 2.2$. For example, at an altitude of 300 km and assuming completely diffuse reflection, a plate normal to the velocity direction will have a $C_D = 2.43$. The comparable value of $C_D^{Equivalent}$ from Figure 76 is approximately 2.87, but is computed at 800 km. These results also agree with results

shown in Figure 65 where the coefficient of drag for a fully diffuse reflection of a flat plate at $\alpha^{AD} = 0^{\circ}$ ($\theta = 90^{\circ}$) varies between 3.3 and 2.1 depending on the thermal accommodation coefficient.

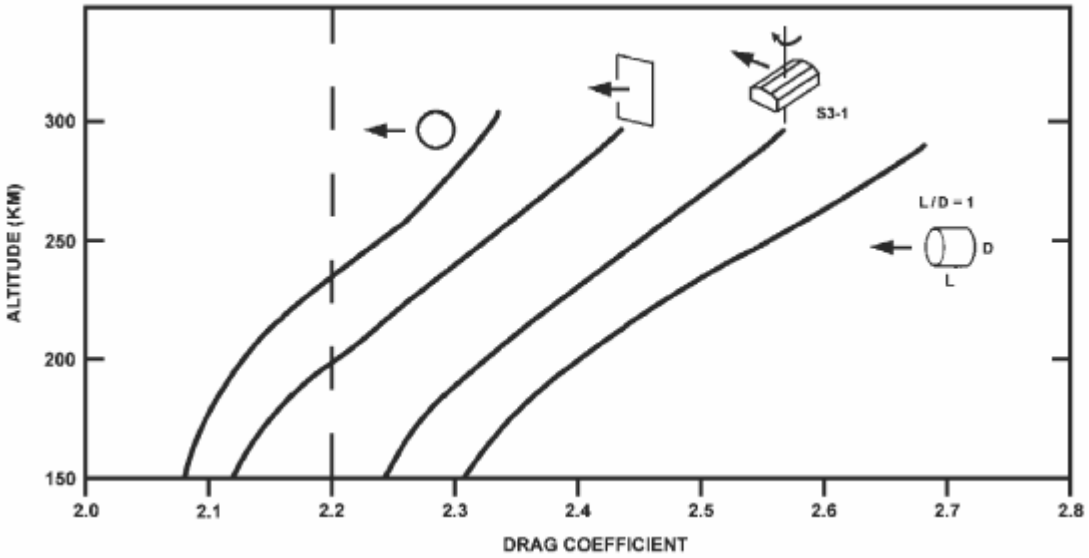

Figure 77. Drag coefficients of a sphere, a flat plate at normal incidence, the spinning S3-1 Satellite, and a short cylinder with a flat plate in front. The above curves have been calculated from Sentman's model[67,68], which assumes diffuse reemission, using parameters measured in orbit at times of low solar activity.[66]

4.3.3 Atmospheric Density Model

Due to CubeSail's relatively large surface area and deployment into low Earth orbit, the aerodynamic drag is a significant perturbation force and affects both the attitude as well as the orbital position of the spacecraft. In order to accurately model these effects, a high-fidelity atmospheric density model called NRLMSISE-00 (2001 United State Naval Research Laboratory Mass Spectrometer and Incoherent Scatter Radar Exosphere)[69] is used in the simulations.

The NRLMSISE-00 empirical atmosphere model was developed by Mike Picone, Alan Hedin, and Doug Drob based on the MSISE-90 model[70, 71, 72]. The primary improvements include: (1) the extensive use of drag and accelerometer data on total mass density, (2) the addition of a component to the total mass density that accounts for

possibly significant contributions of O+ and hot oxygen at altitudes above 500 km, and (3) the inclusion of the SMM UV occultation data on $[O_2]$.[69]

The MSISE-90 model describes the neutral temperature and densities in Earth's atmosphere from ground to thermospheric heights. Below 72.5 km the model is primarily based on the MAP Handbook[73] tabulation of zonal average temperature and pressure by Barnett and Corney, which was also used in the CIRA-86 model.[74] Below 20 km these data were supplemented with averages from the National Meteorological Center (NMC). In addition, pitot tube, falling sphere, and grenade sounder rocket measurements from 1947 to 1972 were taken into consideration. Above 72.5 km MSISE-90 is essentially a revised MSIS-86 model[75] taking into account data derived from space shuttle flights and newer incoherent scatter results.

The NRLMSISE-00 model was originally written in Fortran and later ported to Matlab/Simulink environment and is included in the Aerospace Toolbox. The code is accessed by a function call shown in Figure 78 with the inputs summarized in Table 11.

```
[T rho] = atmosnrlmsise00(h, lat, lon, year, doy, sec, 'Oxygen')
[T rho] = atmosnrlmsise00(h, lat, lon, year, doy, sec, f107a, f107, aph, flags, 'Oxygen')
```

Figure 78. Command-line NRLMSISE-00 function call.[42]

Table 11. NRLMSISE-00 Input Parameters.[42]

Input Variable	Description
h (m)	m x 3 array containing latitude, longitude, and altitude (LLA). Latitude and Longitude are geodetic (not geocentric) and are in degrees. Longitude should be between ±180º. Altitude is in meters.
Year	m x 1 array containing year at which the output is computed.
DOY	m x 1 array containing day of year.
UT	m x 1 array containing seconds in day in universal time (UT).
F107A	m x 1 array containing 81 day average of F10.7 flux, centered on the DOY. If this value is specified, one must also specify F107 and aph. The effects of F107A are not large or established below 80km; therefore, the default value is 150.
F107	m x 1 array containing F10.7 flux for previous day. If this value is specified, one must also specify F107A and aph. The effects of F107A are not large or established below 80km; therefore, the default value is 150.
aph	m x 7 array containing magnetic index information. If aph is specified, one must also specify F107A and F107.
Flags	23 x 1 array to enable or disable particular variations for the outputs. For detailed description of the flags, see Ref [42].
'Oxygen'	Indicates that total mass density outputs include anomalous oxygen number density.

The effects of solar flux and magnetic indices below altitudes of 80 km are minimal, but should not be ignored for typical CubeSail altitudes of approximately 750 km. During typical spacecraft operation, the relevant solar data must be downloaded daily, parsed, and used in the NLRMSISE-00 model.

In the majority of the ADCS code, the position of the satellite is expressed in the Earth-Centered-Fixed (ECF) reference frame. As a result, a method to convert these position measurements into geocentric longitude, latitude, and altitude is necessary. Although several methods exist to achieve this goal, the method used here is an iterative scheme taken from the *Astronomical Almanac*[76] and combines good accuracy and speed of execution. The relevant geometry is depicted in Figure 79.

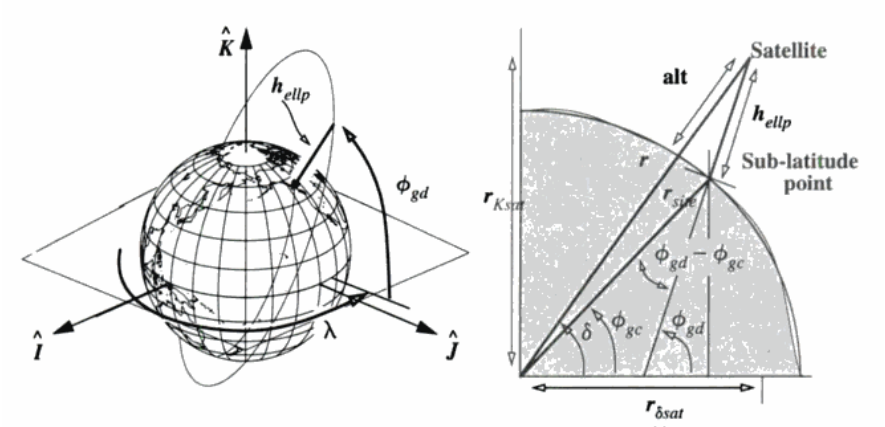

Figure 79. Oblate Earth geometry.[83]

The algorithm starts by computing the equatorial projection of the satellite's position vector as follows:

$$r_{\delta sat} = \sqrt{r_1^2 + r_2^2} \qquad \text{given} \qquad \vec{r}_{ECF} = \begin{bmatrix} r_1 & r_2 & r_3 \end{bmatrix} \tag{99}$$

The longitude, λ, can be found from geometry as:

$$\sin(\lambda) = \frac{r_2}{r_{\delta sat}} \quad \text{and} \quad \cos(\lambda) = \frac{r_1}{r_{\delta sat}}, \quad \text{thus} \quad \lambda = \arctan\left(\frac{r_2}{r_1}\right) \tag{100}$$

The latitude is slightly more difficult to compute and requires an iterative process. The process begins by assuming that at the first iteration, the geodetic latitude, ϕ_{gd}, is equal to satellite's declination, δ, which is computed using the following equation:

$$\delta = \arctan\left(\frac{r_3}{r_{\delta sat}}\right) \tag{101}$$

Next, an auxiliary quantity $C_\oplus$, known as the *radius of curvature in the meridian* is computed using the following equation:

$$C_\oplus = \frac{R_\oplus}{\sqrt{1 - e_\oplus^2 \sin^2\left(\phi_{gd}\right)}} \tag{102}$$

The new geodetic latitude is finally computed from:

$$\phi_{gd} = \arctan\left(\frac{r_3 + C_{\oplus} e_{\oplus}^2 \sin\left(\phi_{gd}\right)}{r_{\delta sat}} \right) \qquad [103]$$

The iterative process is repeated until $\phi_{gd} - \phi_{gd,\,old} < tolerance$.

Lastly, the altitude is simply the 2-norm of the position vector, which can be written as:

$$alt = \sqrt{r_1^2 + r_2^2 + r_3^2} \qquad [104]$$

The solar radiation has a strong impact on atmospheric density above 80 km and must thus be included in the calculations. The solar flux values, along with an excellent description reproduced below, are taken from Reference [77].

> "The sun emits radio energy with a slowly varying intensity. This radio flux, which originates from atmospheric layers high in the sun's chromosphere and low in its corona, changes gradually from day-to-day, in response to the number of spot groups on the disk. Radio intensity levels consist of mission from three sources: from the undisturbed solar surface, from developing active regions, and from short-lived enhancements above the daily level.
>
> Solar flux density at 2800 megaHertz has been recorded routinely by radio telescope near Ottawa since February 14, 1947. Each day, levels are determined at local noon (1700 GMT) and then corrected to within a few percent for factors such as antenna gain, atmospheric absorption, bursts in progress, and background sky temperature. Beginning in June 1991, the solar flux density measurement source is Penticton, B.C., Canada.
>
> The tables contain fluxes from the entire solar disk at a frequency of 2800 megaHertz in units of 10 to the -22 Joules/second/square meter/Hertz. Each number has been multiplied by 10 to suppress the decimal point. Three sets of fluxes--the observed, the adjusted, and the absolute--are summarized. Of the three, the observed numbers are the least refined, since they contain fluctuations as large as 7% that arise from the changing sun-earth distance. In contrast, adjusted fluxes have this variation removed; the numbers in these tables equal the energy flux received by a detector located at the mean distance between sun and earth. Finally, the absolute levels carry the error reduction one step further; here each adjusted value is multiplied by 0.90 to compensate for uncertainties in antenna gain and in waves reflected from the ground."

The data downloaded from the ftp server has the format shown in Figure 80 and is first parsed using *xy_plot.exe* to yield a more usable format. The parsing program requires and input file (ex. 1950.OBS) and the year of the file (ex. 1950). The answer to the last question is 'no.' The associated output file (1950OBS.PLT) will have the structure shown in Figure 81. Missing data will be represented as ---. The data are

displayed as the flux value multiplied by ten (same as the table format). For example, 1324 converts to 132.4 solar flux units for Jan 1, 1950. The symbol '*' after any entry indicates corrections for burst in progress and letter 'E' indicates corrections for snow on the antenna.

2001 ABSOLUTE DAILY SOLAR FLUX 2001
Penticton 2800 MHz Series D (Multiplied by Ten) 2000 UT

Day	Jan	Feb	Mar	Apr	May	Jun	Jul	Aug	Sep	Oct	Nov	Dec
1	1488	1406	1161	2315	1686#	1231	1260	1114	1686	1952	2088	1936
2	1532	1454	1147	2051	1611	1240	1249	1119	1671	1810	1891	2143
3	1478	1431	1236	2008	1576	1346	1227	1219	1819	1726	1912	2054
4	1519	1296	1248	1845	1607	1425	1181	1374	1999	1678	2011	2039
5	1534	1446	1380	1870*	1471	1422	1113	1445	1996	1591	2075	2071
6	1561	1488	1399	1728#	1420	1462	1082	1515	2031	1622	2099	2155
7	1538	1436	1566	1620	1268	1528	1096	1539	2065	1552	2375	1973
8	1454	1371	1483	1527	1180	1671	1175	1544	2278	1537	2188	1925
9	1447	1423	1433	1488	1187	1642	1209	1510	2156	1583	2390	1957
10	1417	1409	1422	1534	1197	1512	1209	1482	2230	1603	2169	1911
11	1445	1327	1402	1443	1255	1507	1226	1525	2276	1567	2064	1925
12	1552	1268	1401	1348	1269	1545	1245	1476	2143	1606	2004	2065
13	1605	1240	1310	1240	1277	1684	1240	1400	2183	1608	2041	1920
14	1535	1211	1266	1256	1271	1808	1309	1360	2154	1717	1913	1889#
15	1474	1186	1212	1216	1307	1829	1322	1354	1995	1726	1822	1899
16	1410	1139	1247	1119	1269	1928	1392	1316	1884	1852	1779	1823
17	1323	1141	1196	1144	1357	1900	1354	1336	1810	1943	1746	1791
18	1320	1161	1247	1197	1273	2056	1329	1439	1852	2042	1654	1845
19	1329	1206	1312	1313	1302	1816	1322	1451	1805	2210	1681	1814
20	1335	1281	1369	1639	1304	1845	1325	1438	2058	2182	1625	1926
21	1320	1265	1424	1737	1384	1862	1291	1475	2164	1998	1617	2041
22	1414	1285	1637	1752	1402	1893	1304	1487	2313	2074	1667#	2114
23	1458	1280	1610	1788	1465	1917	1330	1561	2342	2017	1556	2217
24	1505	1211	1957	1762	1572	1812	1231	1608	2529	2124	1517	2390
25	1471	1190	1941	1767	1495	1696	1238	1829	2489	2125	1491	2253
26	1445	1195	2363	1789	1362	1561	1145	1744	2556	2102	1532	2331
27	1456	1153	2452	1740	1358	1376	1126	1764	2435	2190	1668	2390
28	1463	1164	2454	1714	1322	1304	1071	1828	2570	2017	1738	2291#
29	1445		2349	1751	1281	1301	1084	1808	2162	1915	1894	2301
30	1394		2306	1716	1224	1271	1062	1827	2127	2005	1976	2146
31	1340		2207		1229		1083	1730		1960		2137
Mean	1452	1288	1585	1614	1368	1613	1220	1504	2126	1859	1873	

* 2300UT Value, Burst IP at 2000UT
\# 1700 or 1800UT Value, Burst IP at 2000UT

Figure 80. Sample absolute daily solar flux file format.

```
1950 01 01  1324
1950 01 02   ---
1950 01 03  1351
1950 01 04  1306
```

Figure 81. Sample output format of *xy_plot*.exe.

The parsed files can now be used to find the 80-day average (F107A input in the NRLMSISE-00) and the flux data for a day prior to DOY (F107 input). It is important to note that the F107A input is an 81-day average centered on the DOY. In typical operations, however, the solar flux data is not available for future 40 days after the DOY and for purposes of the CubeSail mission will be linearly extrapolated to obtain the F107A average.

The last remaining inputs needed in the computation of the atmospheric density are magnetic indices *K*, *Kp*, and *Ap*. Variations in the magnetic field are caused by several factors, including solar radiation changes, interactions of the solar wind with the Earth's magnetosphere, by the magnetosphere itself, by the interactions between magnetosphere and ionosphere, and by the ionosphere itself.[78] Reference [78] includes a succinct description of the indices used to describe these daily variations and is reproduced below.

> "The K-index is quasi-logarithmic local index of the 3-hourly range in magnetic activity relative to an assumed quiet-day curve for a single geomagnetic observatory site. First introduced by J. Bartels in 1938, it consists of a single-digit 0 thru 9 for each 3-hour interval of the universal time day (UT).
> The planetary 3-hour-range index Kp is the mean standardized K-index from 13 geomagnetic observatories between 44 degrees and 60 degrees northern or southern geomagnetic latitude. The scale is O to 9 expressed in thirds of a unit, e.g. 5- is 4 2/3, 5 is 5 and 5+ is 5 1/3. This planetary index is designed to measure solar particle radiation by its magnetic effects. The 3-hourly ap (equivalent range) index is derived from the Kp index as follows:
>
> Kp = 0o 0+ 1- 1o 1+ 2- 2o 2+ 3- 3o 3+ 4- 4o 4+
> ap = 0 2 3 4 5 6 7 9 12 15 18 22 27 32
> Kp = 5- 5o 5+ 6- 6o 6+ 7- 7o 7+ 8- 8o 8+ 9- 9o
> ap = 39 48 56 67 80 94 111 132 154 179 207 236 300 400"

The NRLMSISE-00 magnetic index input consists of the following information:

- Daily magnetic index (AP)
- 3 hour AP for current time
- 3 hour AP for 3 hours before current time
- 3 hour AP for 6 hours before current time
- 3 hour AP for 9 hours before current time
- Average of eight 3 hour AP indices from 12 to 33 hours before current time
- Average of eight 3 hour AP indices from 36 to 57 hours before current time

The AP values can be obtained from the web. The National Geophysical Data Center (NGDC) updates the magnetic index files approximately once every month once the values have been verified and refined. These values can be downloaded from Reference [79] and should be used when available. The format of these files is given in Figure 82.

FORMAT FOR RECORDS OF SELECTED GEOMAGNETIC AND SOLAR ACTIVITY INDICES

COLUMNS	FMT	DESCRIPTION
1- 2	I2	YEAR
3- 4	I2	MONTH
5- 6	I2	DAY
7-10	I4	BARTELS SOLAR ROTATION NUMBER--a sequence of 27-day intervals counted continuously from February 8, 1832.
11-12	I2	NUMBER OF DAY within the Bartels 27-day cycle.
13-14	I2	Kp or PLANETARY 3-HOUR RANGE INDEX for 0000 - 0300 UT.
15-16	I2	Kp or PLANETARY 3-HOUR RANGE INDEX for 0300 - 0600 UT.
17-18	I2	Kp or PLANETARY 3-HOUR RANGE INDEX for 0600 - 0900 UT.
19-20	I2	Kp or PLANETARY 3-HOUR RANGE INDEX for 0900 - 1200 UT.
21-22	I2	Kp or PLANETARY 3-HOUR RANGE INDEX for 1200 - 1500 UT.
23-24	I2	Kp or PLANETARY 3-HOUR RANGE INDEX for 1500 - 1800 UT.
25-26	I2	Kp or PLANETARY 3-HOUR RANGE INDEX for 1800 - 2100 UT.
27-28	I2	Kp or PLANETARY 3-HOUR RANGE INDEX for 2100 - 2400 UT.
29-31	I3	SUM of the eight Kp indices for the day expressed to the nearest third of a unit.
32-34	I3	ap or PLANETARY EQUIVALENT AMPLITUDE for 0000 - 0300 UT.
35-37	I3	ap or PLANETARY EQUIVALENT AMPLITUDE for 0300 - 0600 UT.
38-40	I3	ap or PLANETARY EQUIVALENT AMPLITUDE for 0600 - 0900 UT.
41-43	I3	ap or PLANETARY EQUIVALENT AMPLITUDE for 0900 - 1200 UT.
44-46	I3	ap or PLANETARY EQUIVALENT AMPLITUDE for 1200 - 1500 UT.
47-49	I3	ap or PLANETARY EQUIVALENT AMPLITUDE for 1500 - 1800 UT.
50-52	I3	ap or PLANETARY EQUIVALENT AMPLITUDE for 1800 - 2100 UT.
53-55	I3	ap or PLANETARY EQUIVALENT AMPLITUDE for 2100 - 2400 UT.
56-58	I3	Ap or PLANETARY EQUIVALENT DAILY AMPLITUDE--the arithmetic mean of the day's eight ap values.
59-61	F3.1	Cp or PLANETARY DAILY CHARACTER FIGURE--a qualitative estimate of overall level of magnetic activity for the day determined from the sum of the eight ap amplitudes. Cp ranges, in steps of one-tenth, from 0 (quiet) to 2.5 (highly disturbed).
62-62	I1	C9--a conversion of the 0-to-2.5 range of the Cp index to one digit between 0 and 9.
63-65	I3	INTERNATIONAL SUNSPOT NUMBER. Records contain the Zurich number through December 31,

Figure 82. Magnetic index file format.

For day-to-day operations, however, the AP values at the current time (and averages from previous several hours) are needed. The Space Weather Prediction Center, a branch of National Oceanic and Atmospheric Administration provides the unrefined values that can be used in the NRLMSISE_00 model. The daily values can be obtained from Ref [80].

The output from NRLMSISE-00 is given in the following format[42]:

Table 12. NRLMSISE-00 output format.[42]

Output Variable	Description
T	m x 2 array of temperatures in Kelvin. The first column is the exospheric temperature, while the second is the temperature at altitude.
rho	m x 9 array of densities either in $1/m^3$ or kg/m^3. Depending on units selected. The columns are as follows: • Density of He, in $1/m^3$ • Density of O, in $1/m^3$ • Density of N2, in $1/m^3$ • Density of O2, in $1/m^3$ • Density of Ar, in $1/m^3$ • Total mass density, in kg/m^3 • Density of H, in $1/m^3$ • Density of N, in $1/m^3$ • Anomalous oxygen number density, in $1/m^3$ rho(6), total mass density, is defined as the sum of the mass densities of He, O, N2, O2, Ar, H, and N. Optionally, rho(6) can include the mass density of anomalous oxygen making rho(6), the effective total mass density for drag.

A quantitative impact of the variations in the atmospheric density along the film is shown in Figure 83. The sail is assumed to be undeformed and deployed along the local vertical. The latitude, longitude, and altitude are assumed to be 58.6767751º, 54.9927768º, and 800 km (at the sail center) respectively. The epoch is selected as [2010 7 1 12 0 0] and the sail flies with zero roll, pitch, and yaw attitude.

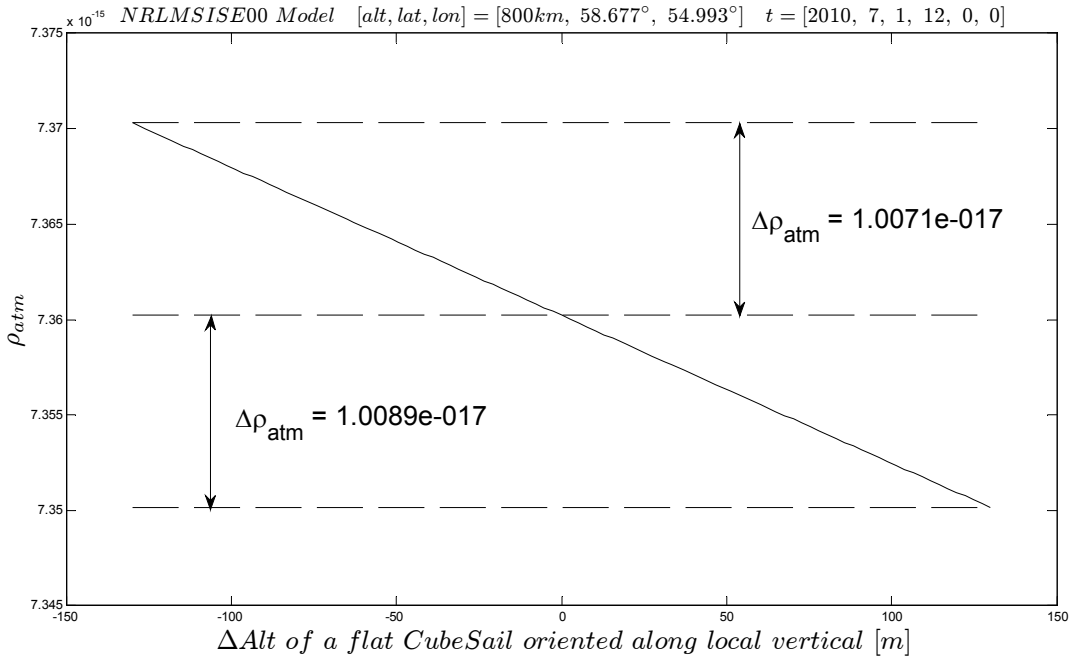

Figure 83. Variation in ρ_{atm} over sail length for undeformed sail aligned with local vertical.

The above figure demonstrates that for the proposed CubeSail mission altitude, the variations in the atmospheric density along the sail are very small. As a result, it is sufficiently accurate to assume a constant atmospheric density in the aerodynamic drag calculations. The density at the spacecraft's center of mass is used for this purpose.

It is important to note that the inclusion of all input parameters, including solar flux and magnetic indices, is still necessary as the density can vary by as much as two orders of magnitude depending on the time within the solar cycle, time of the day, altitude, etc., as discussed previously in section 3.4.1.

4.3.4 Solar Radiation Pressure

Considering a non-ideal solar sail, we must include effects of reflection, absorption and re-radiation by the sail in order to develop an accurate solar radiation force model. The governing force equation can be written as:

$$\vec{f}_{SP} = \vec{f}_r + \vec{f}_a + \vec{f}_e \qquad [105]$$

where $\vec{f}_r$ is the force due to photon reflection, $\vec{f}_a$ is the force due to absorption, and $\vec{f}_e$ is the force due to emission by re-radiation. These three forces depend on the optical properties of the film through the following coefficients: the reflection coefficient, $\tilde{r}$, the absorption coefficient, a, and the transmission coefficient, τ. The following constraint must be enforced:

$$\tilde{r} + a + \tau = 1 \qquad [106]$$

Since the reflective side of the sail allows no transmission (i.e. $\tau = 0$), the above constraint equation simplifies to:

$$a = 1 - \tilde{r} \qquad [107]$$

Similarly to the aerodynamic drag force derivation, the goal is to develop force equations in the normal and tangential directions applicable at each of the elemental section of height Δr and width of 78 mm shown in Figure 57. The following derivation is adopted from Ref [8].

Taking a cross sectional area (through the sail thickness) of a sample elemental section i, as shown in Figure 84, it is convenient to define several vectors and angles. The unit vector in the direction of incident photons is defined as $\vec{u}_i$, the unit vector in the direction of specularly reflected photons is defined as $\vec{s}_i$, the surface normal and tangential unit vectors are defined as $\vec{n}_i$ and $\vec{t}_i$ respectively. The angle of incidence (measured from the surface normal) is defined as α_i^{SP}, where the superscript SP is used to differentiate it from the angle of incidence of thermospheric constituent molecules used in the aerodynamic drag calculation (α^{AD}). The resultant force due to solar pressure will act in the direction $\vec{m}_i$ at an angle ϕ_i^{SP} from the surface normal.

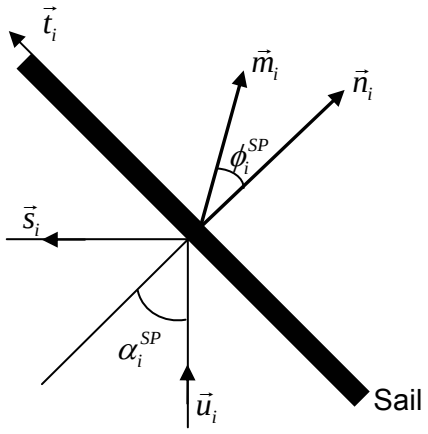

Figure 84. Non-ideal solar sail geometry.

The incident and specularly reflected unit vectors can be written in terms of normal and tangential components as:

$$\begin{aligned} \vec{u}_i &= \cos\left(\alpha_i^{SP}\right)\vec{n} + \sin\left(\alpha_i^{SP}\right)\vec{t} \\ \vec{s}_i &= -\cos\left(\alpha_i^{SP}\right)\vec{n} + \sin\left(\alpha_i^{SP}\right)\vec{t} \end{aligned} \qquad [108]$$

The force exerted on the elemental solar sail area dA due to absorbed photos can be written as $P \cdot \cos(\alpha^{SP})\vec{u} \cdot dA$, which can be rewritten using the above equation in the normal and tangential components as:

$$d\vec{f}_a = P \cdot \left[\cos^2(\alpha^{SP})\vec{n} + \cos(\alpha^{SP}) \cdot \sin(\alpha^{SP})\vec{t}\right] \cdot dA \qquad [109]$$

where the subscript i has been dropped for clarity and is understood to be applied at each elemental area dA. P in the above equation is the pressure exerted on a perfectly reflecting solar sail, which at 1 AU, is equal to $9.121 \times 10^{-6}\ N \cdot m^{-2}$ (assuming the mean value of solar energy flux of $W_E = 1368\ Js^{-1}m^{-2}$).

A fraction $\tilde{r}$ of the incoming photons will be reflected from the surface either in a specular or semi-diffuse way. Of that fraction, let s be the fraction that reflects

specularly in the $\vec{s}$ direction, thus providing the force in the opposite direction which can be written as:

$$d\vec{f}_r^{\,Specular} = -\tilde{r} \cdot s \cdot P \cdot \cos\left(\alpha^{SP}\right) \vec{s} \cdot dA \qquad [110]$$

The remaining fraction $(1-s)$ will be reflected in a semi-diffuse fashion, the extent of which is dictated by the coefficient B_f. If the surface appears equally bright from all viewing angles, the reflection is called Lambertian or fully diffuse and $B_f = 1$. Typically, the aluminum coating makes the solar sailing surface non-Lambertian, resulting in the elemental reflected force being written as:

$$d\vec{f}_r^{\,Non-Lambertian} = \tilde{r} \cdot (1-s) \cdot P \cdot B_f \cdot \cos\left(\alpha^{SP}\right) \vec{n} \cdot dA \qquad [111]$$

Combining the specular and non-Lambertian (or semi-diffuse) reflection forces and writing them in terms of the normal and tangential direction results in the following elemental force equation:

$$d\vec{f}_r = P \cdot \cos\left(\alpha^{SP}\right) \cdot \left[\left(\tilde{r} \cdot s \cdot \cos\left(\alpha^{SP}\right) + \tilde{r} \cdot (1-s) \cdot B_f \right) \vec{n} - \left(\tilde{r} \cdot s \cdot \cos\left(\alpha^{SP}\right) \cdot \sin\left(\alpha^{SP}\right) \right) \vec{t} \right] \cdot dA \qquad [112]$$

Lastly, we must find the elemental force due to emission through re-radiation of photons from the front and back surfaces. The overall thermal balance of a solar sail elemental area is shown in Figure 85. The power emitted from a unit area of the sail at temperature T is $\varepsilon \tilde{\sigma} T^4$, where $\tilde{\sigma}$ is the Stefan-Boltzmann constant and ε is the surface emissivity. Since the sail is extremely thin it has almost no thermal capacity, and temperature changes are therefore assumed instantaneous. The sail equilibrium temperature as a function of sail orientation, the sail optical properties and heliocentric distance can be calculated from the following equation:

$$T = \left[\frac{1-\tilde{r}}{\varepsilon_f + \varepsilon_b} \frac{W_E}{\tilde{\sigma}} \left(\frac{R_E}{r} \right)^2 \cos\left(\alpha^{SP}\right) \right]^{1/4} \quad [113]$$

where ε_f and ε_b are the front and back emissivities respectively, R_E is the Sun-Earth distance, and r is the distance from the Sun.

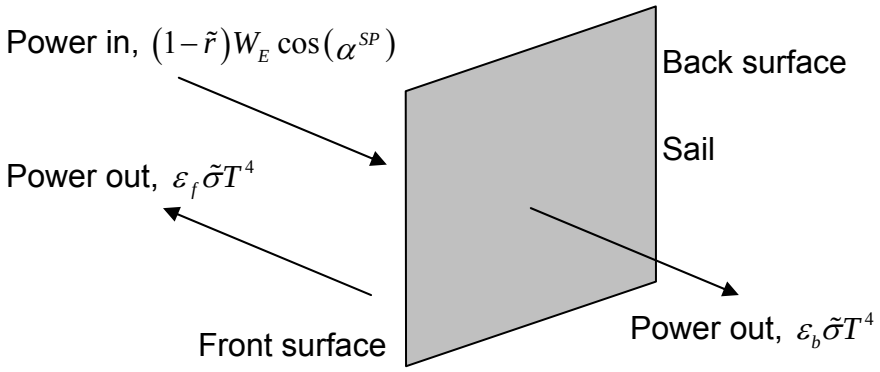

Figure 85. Solar sail thermal balance.

The elemental force due to emission by re-radiation that takes into account the non-Lambertian reflection of the front and back surfaces is given by:

$$d\vec{f}_e = \frac{\tilde{\sigma} \cdot T^4}{c} \left(\varepsilon_f \cdot B_f - \varepsilon_b \cdot B_b \right) \vec{n} \cdot dA \quad [114]$$

Upon substitution of the sail equilibrium temperature, the final elemental force due to emission is:

$$d\vec{f}_e = P \cdot (1-\tilde{r}) \cdot \frac{\varepsilon_f \cdot B_f - \varepsilon_b \cdot B_b}{\varepsilon_f + \varepsilon_b} \cdot \cos\left(\alpha^{RP}\right) \vec{n} \cdot dA \quad [115]$$

where the fact that $P \triangleq W / c$ was used with c as the speed of light.

Combining the elemental forces due to reflection, absorption, and emission, it is possible to write the elemental force due to solar pressure as:

$$d\vec{f}_{SP} = \left\{ P \cdot \cos\left(\alpha^{SP}\right) \cdot \left[(1+\tilde{r} \cdot s) \cdot \cos\left(\alpha^{SP}\right) + \tilde{r} \cdot (1-s) \cdot B_f + (1-\tilde{r}) \cdot \frac{\varepsilon_f \cdot B_f - \varepsilon_b \cdot B_b}{\varepsilon_f + \varepsilon_b} \right] \right\} \vec{n} \cdot dA + \left\{ P \cdot (1-\tilde{r} \cdot s) \cdot \cos\left(\alpha^{SP}\right) \cdot \sin\left(\alpha^{SP}\right) \right\} \vec{t} \cdot dA \quad [116]$$

Similarly to the aerodynamic drag development, it is important to obtain the correct sign of the solar radiation pressure in the *Sail* frame. Referring to Figure 86, the correct sign of the differential force components can be written as:

$$d\vec{f}_{SP}^{\,Sail} = \begin{bmatrix} 0 \\ -sign\left(r_{\odot,y}^{Sail}\right)\cdot P\cdot(1-\tilde{r}\cdot s)\cdot\cos\left(\alpha^{SP}\right)\cdot\sin\left(\alpha^{SP}\right)\cdot dA \\ -sign\left(r_{\odot,z}^{Sail}\right)\cdot P\cdot\cos\left(\alpha^{SP}\right)\cdot\left[(1+\tilde{r}\cdot s)\cdot\cos\left(\alpha^{SP}\right)+\tilde{r}\cdot(1-s)\cdot B_f+(1-\tilde{r})\cdot\dfrac{\varepsilon_f\cdot B_f-\varepsilon_b\cdot B_b}{\varepsilon_f+\varepsilon_b}\right]\cdot dA \end{bmatrix} \quad [117]$$

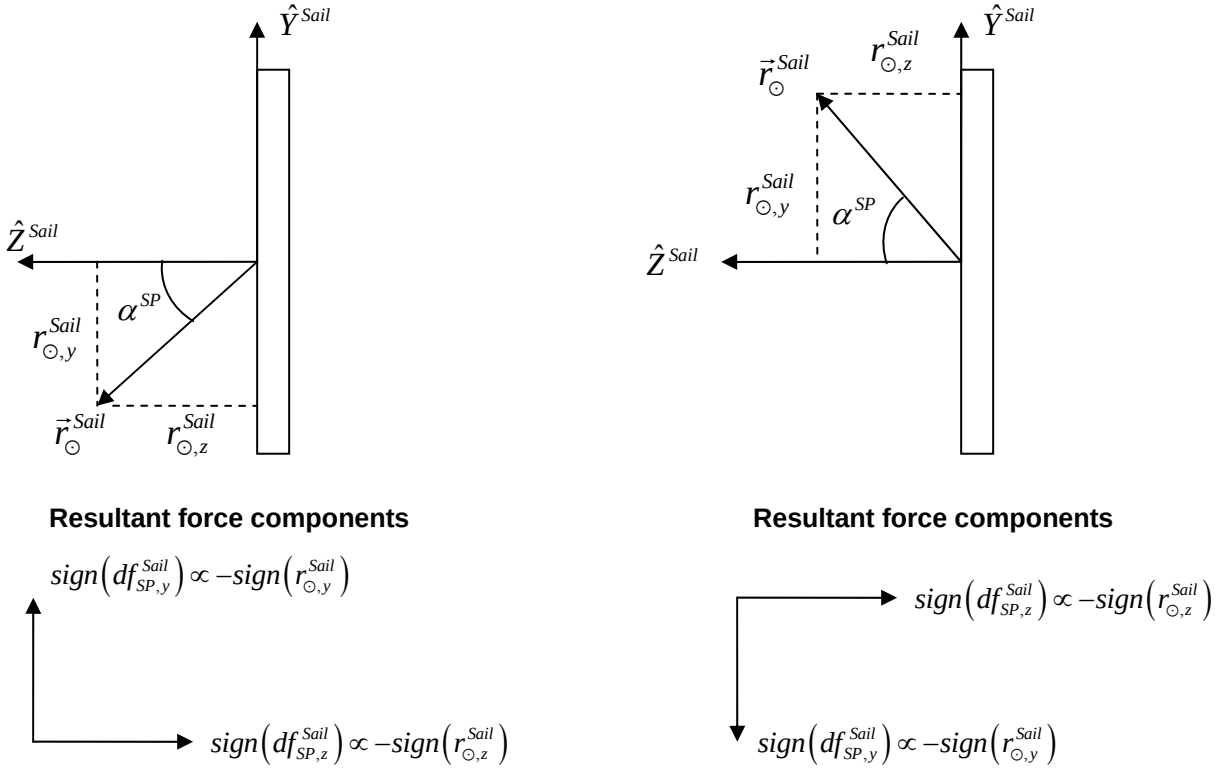

Figure 86. Solar radiation pressure force sign diagram.

As mentioned previously, the subscript i is dropped for clarity with the implicit understanding that the elemental solar radiation force in the above equation is applied at each elemental area dA with a unique incidence angle α^{SP}.

In order to relate the above result to the resultant force in the $\vec{m}$ direction shown in Figure 84, we notice the following relations:

$$d\vec{f}^{SP} = df^{SP}\vec{m} \quad \text{where} \quad df^{SP} = \sqrt{\left(df_n^{SP}\right)^2 + \left(df_t^{SP}\right)^2} \tag{118}$$

and

$$\phi^{SP} = \arctan\left(\frac{df_t^{SP}}{df_n^{SP}}\right) \tag{119}$$

Again the subscript i is suppressed.

Before the actual forces due to solar pressure can be computed, it is necessary to obtain realistic values for the sail optical coefficients. The combination of film substrate of the front and back coatings has not been finalized yet, but preliminary analysis indicates either Mylar or CP1 substrate coated with aluminum on one side and a high emissivity coating on the other will be used. Table 13 shows optical coefficients of an ideal sail and of two designs that use comparable films.[8,81] Until the film selection is finalized, optical coefficients of the Heliogyro will be used in simulations.

Table 13. Optical coefficient of sample solar sails.[8,18,81,82]

	$\tilde{r}$	s	ε_f	ε_b	B_f	B_b
Ideal sail	1	1	0	0	2/3	2/3
JPL Square sail	0.88	0.94	0.05	0.55	0.79	0.55
JPL Heliogyro	0.88	0.94	0.05	0.55	0.79	0.55

An important factor that has been ignored thus far is that the solar radiation pressure acts only during sun-lit portions of the orbit. It is necessary to develop a method of determining when the spacecraft is illuminated and how to calculate the sun incidence angle α^{SP}.

The problem of finding whether a satellite is in sunlight or shadow is equivalent to determining whether there exists a line of sight (LOS) between the satellite and the Sun. The following derivation assumes a spherical Earth model and yields conservative

values (fewer lines of sight than actual) because its polar radius is almost 20 km larger than the actual.[83]

The overall geometry of the line of sight between the satellite and the Sun is shown in Figure 87. The vector from the center of the Earth to the satellite is defined as $\vec{r}_{sat}$, and the vector between the center of the Earth and the Sun is defined as $\vec{r}_{\odot}$. The angle between these two vectors, defined by θ, can be computed using the dot product:

$$\cos(\theta) = \frac{\vec{r}_{sat} \bullet \vec{r}_{\odot}}{\left|\vec{r}_{sat}\right|\left|\vec{r}_{\odot}\right|} \qquad [120]$$

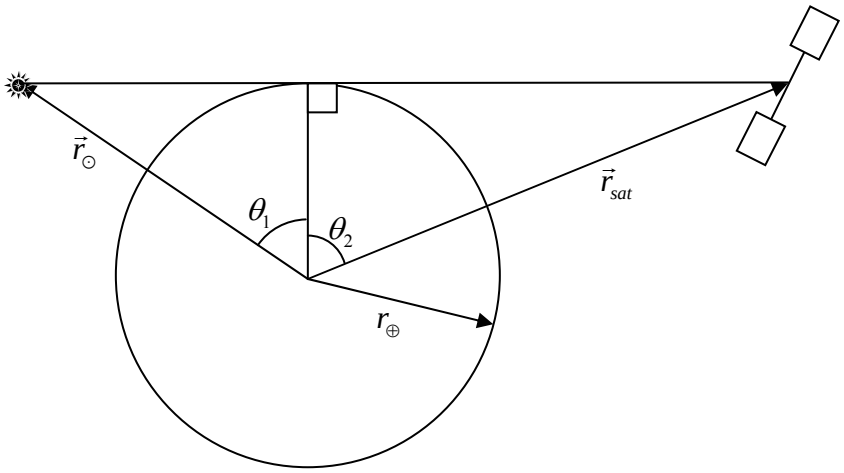

Figure 87. Satellite—Sun line of sight geometry.

From the above geometry, it is also possible to write the following two equalities:

$$\cos(\theta_1) = \frac{r_{\oplus}}{\left|\vec{r}_{\odot}\right|} \quad \text{and} \quad \cos(\theta_2) = \frac{r_{\oplus}}{\left|\vec{r}_{sat}\right|} \qquad [121]$$

An easy check whether the satellite is shadowed is to first compute the above three angles and then check if $\theta_1 + \theta_2 \leq \theta$. If the inequality is true, then CubeSail has no LOS with the Sun and is in eclipse.

The position vector of the satellite, $\vec{r}_{sat}$, is easily obtained by propagating the latest Two Line Element set to the desired time and converting it to the ECI frame. The

last remaining step, therefore, is to calculate Earth-Sun vector, $\vec{r}_{\odot}$, in the ECI coordinates.

When formulating the sun vector in the ECI frame, one must remember that the ecliptic plane is inclined to the equatorial plane by an angle $\varepsilon_{\oplus}$, known as the obliquity of the ecliptic. This can be seen in Figure 88. Displayed is also the longitude of the sun vector, $\lambda_{ecliptic}$, which is measured from the direction of vernal equinox along the ecliptic plane.

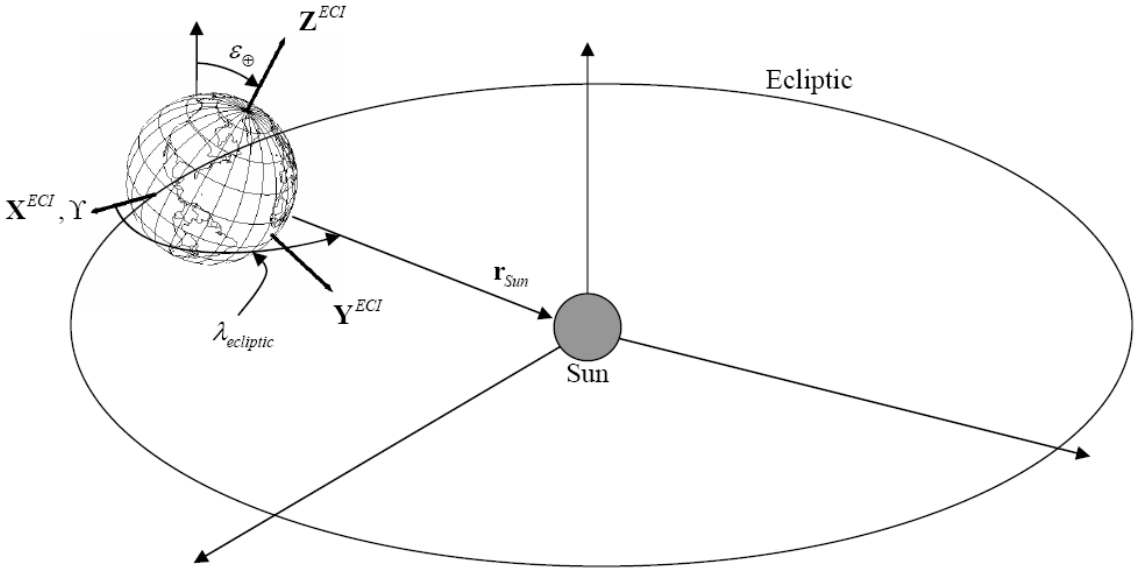

Figure 88. The Ecliptic Plane with Respect to the ECI Frame

As an intermediate step, it useful to define a quantity called mean longitude of the Sun as:

$$\lambda_{M_{\odot}} = 280.4606184° + 36,000.77005361 \cdot T_{UT1} \qquad [122]$$

where T_{UT1} is the desired time expressed in Universal Time and which can be computed from the Julian Day using the following equation:

$$T_{UT1} = \frac{JD_{UT1} - 2,451,545.0}{36,525} \qquad [123]$$

The subscript '1' refers to the form of the Universal Time that corrects for polar motion and is independent of station location. For more in-depth explanation on the differences in UT refer to Ref [83].

Next, it is necessary to compute the mean anomaly of the Sun, $M_{\odot}$, using the following equation:

$$M_{\odot} = 357.5277233° + 35{,}999.05034 \cdot T_{TDB} \quad [124]$$

where T_{TDB} is the barycentric dynamical time‡, which can be acceptably estimated as T_{UT1}. Combining the above equations, it is possible to write the ecliptic longitude of the Sun, $\lambda_{ecliptic}$, as:

$$\lambda_{ecliptic} = \lambda_{M_{\odot}} + 1.914666471° \cdot \sin\left(M_{\odot}\right) + 0.019994643 \cdot \sin\left(2 \cdot M_{\odot}\right) \quad [125]$$

Again using the assumption that $T_{TDB} \approx T_{UT1}$, the obliquity of the equator can be accurately estimated as:

$$\varepsilon_{\oplus} = 23.439291° - 0.0130042 \cdot T_{TDB} \quad [126]$$

The magnitude of the sun position vector in AU is calculated from:

$$r_{\odot} = 1.000140612 - 0.016708617 \cdot \cos\left(M_{\odot}\right) - 0.000139589 \cdot \cos\left(2 \cdot M_{\odot}\right) \quad [127]$$

It is finally possible to write the Sun vector in the ECI frame, represented in the astronomical units, in the following form:

$$\vec{r}_{\odot}^{\,ECI} = \begin{bmatrix} r_{\odot} \cdot \cos\left(\lambda_{ecliptic}\right) \\ r_{\odot} \cdot \cos\left(\varepsilon_{\oplus}\right) \cdot \sin\left(\lambda_{ecliptic}\right) \\ r_{\odot} \cdot \sin\left(\varepsilon_{\oplus}\right) \cdot \sin\left(\lambda_{ecliptic}\right) \end{bmatrix} \quad [128]$$

‡ The acronym for barycentric dynamical time, TDB, is ordered after the French translation, *Temps Dynamic Barycentric*

It is convenient to note that 1 AU is equal to 149,597,870.0 km.

Lastly, to compute the sun incidence angle, α^{SP}, it is necessary to convert the sun vector from the ECI to the 'Sail' frame and take the dot product with the sail normal as follows:

$$\cos\left(\alpha^{SP}\right) = \frac{\vec{r}_{\odot}^{\,Sail} \bullet \hat{n}}{\left|\vec{r}_{\odot}^{\,Sail}\right|} \quad \text{where} \quad \vec{r}_{\odot}^{\,Sail} = A_{SAT}^{Sail} \cdot A_{ORB}^{SAT} \cdot A_{ECI}^{ORB} \cdot \vec{r}_{\odot}^{\,ECI} \qquad [129]$$

4.3.5 Gravity Gradient

The gravitation potential of a mass m located at a distance R from the Earth as shown in Figure 89 is given by[83]:

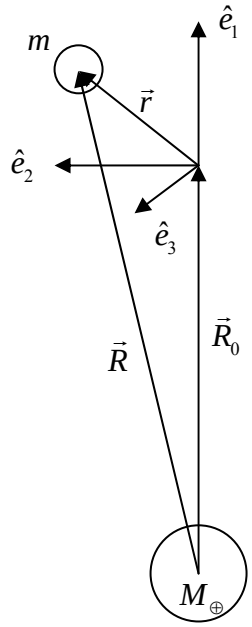

Figure 89. Gravity gradient inertial frame.

$$U = -\frac{\mu_{\oplus} \cdot m}{R}\left[1 - \sum_{l=2}^{\infty} J_l \cdot \left(\frac{R_{\oplus}}{R}\right)^l \cdot P_l\left(\sin\left(\phi_{gc,\,sat}\right)\right) + \sum_{l=2}^{\infty}\sum_{m=1}^{l}\left(\frac{R_{\oplus}}{R}\right)^l \cdot P_{l,m}\left(\sin\left(\phi_{gc,\,sat}\right)\right) \cdot \left\{C_{l,m}\cos\left(m\lambda_{sat}\right) + S_{l,m}\sin\left(m\lambda_{sat}\right)\right\}\right] \qquad [130]$$

where $\phi_{gc,\,sat}$ is the geocentric latitude of the subsatellite point, λ_{sat} is the longitude of the satellite, P_l and $P_{l,m}$ are the Legendre polynomials. It is important to notice that the parenthesis of the Legendre polynomial represent the argument of the polynomial and not multiplication. The polynomials are obtained from the following equations:

$$P_l(\beta) = \frac{1}{2^l \cdot l!}\frac{d^l\left(\beta^2-1\right)^l}{d\beta^l}$$
$$P_{l,m}(\beta) = \frac{1}{2^l \cdot l!}\left(1-\beta^2\right)^{m/2}\frac{d^{l+m}}{d\beta^{l+m}}\left(\beta^2-1\right)^l \qquad [131]$$

$C_{l,m}$ and $S_{l,m}$ are gravitational coefficients that represent mathematical modeling of Earth's mass distribution using spherical harmonics. The coefficients are empirically determined from observation and are available from several sources, for example the NASA EGM-96 gravitational model[84]. The J_l terms in Equation 130 are referred to as zonal harmonics and are computed from the coefficients as: $J_l = -C_{l,0}$.

The form of the aspherical-potential given in Equation 130 conveniently allows for separation of the spherical harmonics into zonal, sectorial, and tesseral harmonics. The zonal harmonics are defined by zeroth order ($m = 0$) and result in elimination of the dependence on longitude symmetry of the field around the polar axis. The strongest zonal harmonic is the J_2, which is approximately 1000 times larger than the next largest coefficient, J_3. The sectorial harmonics occur when $l = m$ and divide the sphere into $2l$ 'slices' or sectors along the meridians. The tesseral harmonics occur when $l \neq m \neq 0$ and create a tile-looking distribution. All three spherical harmonics are shown in Figure 90.

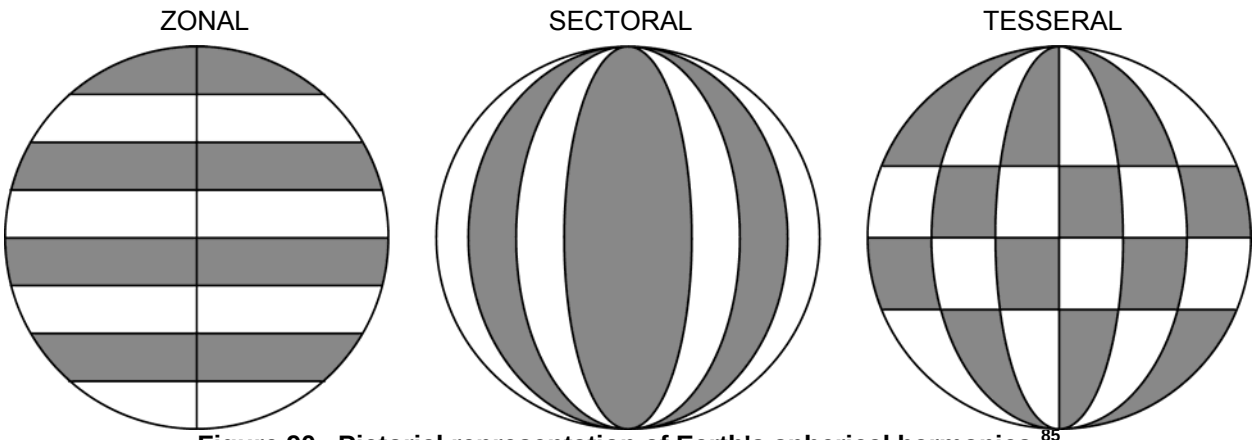

Figure 90. Pictorial representation of Earth's spherical harmonics.[85]

The gravitation acceleration is calculated by taking negative gradient of the gravitational potential with respect to $\vec{R}$, which in an inertial frame is written as:

$$\vec{a}_g = -\nabla U \qquad [132]$$

As a first approximation, it is possible to ignore the spherical harmonics terms that depend on either longitude or latitude and obtain a simple 2-body approximation. The goal is to derive the gradient of the gravitational acceleration that is used in the derivation of the sail deployment and steady-state sail shape.

From Figure 89 the vector $\vec{R}$ can also be written as $\vec{R} = \vec{R}_0 + \vec{r}$, which results in the following equation for the gravitational acceleration:

$$\vec{a}_g = -\frac{\mu_\oplus\left(\vec{R}_0+\vec{r}\right)}{\left[\left(\vec{R}_0+\vec{r}\right)\cdot\left(\vec{R}_0+\vec{r}\right)\right]^{3/2}} = -\frac{\mu_\oplus\left(\vec{R}_0+\vec{r}\right)}{\left[\vec{R}_0\cdot\left(1+\frac{\vec{r}}{\vec{R}_0}\right)\cdot\vec{R}_0\cdot\left(1+\frac{\vec{r}}{\vec{R}_0}\right)\right]^{3/2}} = -\frac{\mu_\oplus\left(\vec{R}_0+\vec{r}\right)}{R_0^3\left[\left(1+\frac{\vec{r}}{\vec{R}_0}\right)\cdot\left(1+\frac{\vec{r}}{\vec{R}_0}\right)\right]^{3/2}} \qquad [133]$$

Using the fact that $\vec{R}_0 \cdot \vec{R}_0 = R_0^2$ and expanding the denominator results in:

$$\vec{a}_g = -\frac{\mu_\oplus\left(\vec{R}_0+\vec{r}\right)}{R_0^2\left[1+2\cdot\frac{\vec{r}}{\vec{R}_0}+\left(\frac{r}{R_0}\right)^2\right]^{3/2}} = -\frac{\mu_\oplus\left(\vec{R}_0+\vec{r}\right)}{R_0^2\left[1+2\cdot\frac{\vec{R}_0\cdot\vec{r}}{R_0^2}+\left(\frac{r}{R_0}\right)^2\right]^{3/2}} \qquad [134]$$

Using a binomial expansion of $(1+x)^{\alpha} = 1+\alpha\cdot x+\frac{\alpha(\alpha-1)}{2!}x^2+\cdots$ in the denominator (with $x \propto 2\cdot\frac{\vec{R}_0\cdot\vec{r}}{R_0^2}+\left(\frac{r}{R_0}\right)^2$) results in:

$$\vec{a}_g = -\frac{\mu_{\oplus}\left(\vec{R}_0+\vec{r}\right)}{R_0^3}\left[1-\frac{3}{2}\left(2\cdot\frac{\vec{R}_0\cdot\vec{r}}{R_0^2}+\left(\frac{r}{R_0}\right)^2\right)+H.O.T.\right]$$

$$\vec{a}_g = -\frac{\mu_{\oplus}}{R_0^3}\left[\vec{R}_0+\vec{r}-\frac{3\left(\vec{R}_0+\vec{r}\right)\left(\vec{R}_0\cdot\vec{r}\right)}{R_0^2}-\frac{3}{2}\left(\vec{R}_0+\vec{r}\right)\cdot\left(\frac{r}{R_0}\right)^2\right] \quad [135]$$

$$\vec{a}_g = -\frac{\mu_{\oplus}}{R_0^3}\left[\vec{R}_0+\vec{r}-\frac{3\left(\vec{R}_0\cdot\vec{r}\right)}{R_0^2}\vec{R}_0-\frac{3\left(\vec{R}_0\cdot\vec{r}\right)}{R_0^2}\vec{r}-\frac{3}{2}\left(\vec{R}_0+\vec{r}\right)\cdot\left(\frac{r}{R_0}\right)^2\right]$$

Looking at Figure 89 it is possible to write: $\vec{R}_0 = R_0\hat{e}_1$ and $\vec{r} = r_1\hat{e}_1+r_2\hat{e}_2+r_3\hat{e}_3$. Substituting for the two vectors into the above equation and ignoring higher order terms results in:

$$\vec{a}_g = -\frac{\mu_{\oplus}}{R_0^3}\left[\vec{R}_0+\vec{r}-\frac{3\left(\vec{R}_0\cdot\vec{r}\right)}{R_0^2}\vec{R}_0-\frac{3\left(\vec{R}_0\cdot\vec{r}\right)}{R_0^2}\vec{r}-\frac{3}{2}\left(\vec{R}_0+\vec{r}\right)\cdot\left(\frac{r}{R_0}\right)^2\right]$$

$$\vec{a}_g = -\frac{\mu_{\oplus}}{R_0^3}\left[R_0\hat{e}_1+r_1\hat{e}_1+r_2\hat{e}_2+r_3\hat{e}_3-3r_1\hat{e}_1+H.O.T\right] \quad [136]$$

$$\vec{a}_g \approx -\frac{\mu_{\oplus}}{R_0^3}\left[\left(R_0-2r_1\right)\hat{e}_1+r_2\hat{e}_2+r_3\hat{e}_3\right]$$

Taking the gradient of the acceleration results in the gravity gradient force of the following form:

$$\nabla\vec{a}_g = \left[\frac{\partial\vec{a}_g}{\partial r_1} \quad \frac{\partial\vec{a}_g}{\partial r_2} \quad \frac{\partial\vec{a}_g}{\partial r_3}\right] = \left[\frac{2\mu_{\oplus}}{R_0^3} \quad -\frac{\mu_{\oplus}}{R_0^3} \quad -\frac{\mu_{\oplus}}{R_0^3}\right] \quad [137]$$

The above equation represents the first order gravity gradient field. Second and higher-order terms can typically be ignored, unless the added precision is deemed necessary. For example, for an approximate CubeSail target orbit with 800 km altitude,

$R_0 = \left(6378.13 + 800\right)\ km$, and a maximum displacement of $r \approx 0.260\ km$, results in a ratio of $r / R_0 \approx 3.6 \times 10^{-5}$.

If the reference frame is not inertial, but instead rotates at an angular velocity $\vec{\omega}$ (as in the case of the ORB reference frame), a rotational acceleration field is present and gradients from it must be added to the gravity gradients to form the total gradient. A general expression for the acceleration of mass m in an inertial frame can be written as:

$$\vec{a} = \vec{a}_0 + \ddot{\vec{r}}' + \vec{\omega} \times \left(\vec{\omega} \times \vec{r}\right) + \dot{\vec{\omega}} \times \vec{r} + 2\vec{\omega} \times \dot{\vec{r}}' \qquad [138]$$

where $\vec{a}_0$ is the acceleration of the origin of the rotating reference frame, $\ddot{\vec{r}}'$ and $\dot{\vec{r}}'$ are the acceleration and (relative) velocity in the rotating reference frame respectively, $\dot{\vec{\omega}}$ and $\vec{\omega}$ are the angular acceleration and velocity of the rotating frame respectively, and $\vec{r}$ is the position in the rotating frame. Solving for the acceleration in the rotating frame results in:

$$\ddot{\vec{r}}' = \vec{a} - \left[\vec{a}_0 + \vec{\omega} \times \left(\vec{\omega} \times \vec{r}\right) + \dot{\vec{\omega}} \times \vec{r} + 2\vec{\omega} \times \dot{\vec{r}}'\right] \qquad [139]$$

Since only terms involving $\vec{r}$ contribute to the gradient, the above equation simplifies to:

$$\vec{a}_{rot} = -\vec{\omega} \times \left(\vec{\omega} \times \vec{r}\right) - \dot{\vec{\omega}} \times \vec{r} \qquad [140]$$

For a circular orbit that rotates around the $\hat{e}_3$ axis at a constant rate the angular velocity vector is written as $\vec{\omega} = \omega_0 \hat{e}_3$ and the position of mass m is defined as before by $\vec{r} = r_1 \hat{e}_1 + r_2 \hat{e}_2 + r_3 \hat{e}_3$. With these definitions, Equation 140 can be written as:

$$\vec{a}_{rot} = \left(\omega_0^2 \cdot r_1\right)\hat{e}_1 + \left(\omega_0^2 \cdot r_2\right)\hat{e}_2 \qquad [141]$$

Taking the gradient of the above equation and using the fact that for a circular orbit the magnitude of the angular velocity can be written as $\omega_{0,\,circ}^2 = \mu_\oplus / R_0^3$ results in:

$$\nabla \vec{a}_{rot} = \left[\frac{\partial \vec{a}_{rot}}{\partial r_1} \quad \frac{\partial \vec{a}_{rot}}{\partial r_2} \quad \frac{\partial \vec{a}_{rot}}{\partial r_3} \right] = \left[\frac{\mu_\oplus}{R_0^3} \quad \frac{\mu_\oplus}{R_0^3} \quad 0 \right] \qquad [142]$$

The rotational acceleration gradient can now be added to the gravity gradient, resulting in the total gradient field (to first order) of the form:

$$\nabla \vec{a} = \frac{\mu_\oplus}{R_0^3} \cdot \begin{bmatrix} 3 & 0 & -1 \end{bmatrix} \qquad [143]$$

4.3.6 Solar Wind

In addition to the solar radiation pressure, solar wind plasma consisting of protons, doubly charged helium ions, small number of other positively charged particles, and enough electrons to ensure the plasma is neutrally charged will contribute to the force acting on the CubeSail spacecraft. Since approximately 95% of the plasma consists of the protons[86], only their effects will be investigated. The solar wind pressure exerted on a sail can be estimated from the from momentum transport as:

$$P_{SW} \approx m_p \cdot \rho_p \cdot v_p^2 \qquad [144]$$

where m_p is the rest mass of the protons (1.67×10^{-27} kg), ρ_p is the mean proton density at 1 AU (8.7×10^6 m^{-3}), and v_p is the mean proton speed, which is equal to 468 km/s.[86] As a result, solar wind pressure is approximately 3.18×10^{-9} N/m^2, or consequently 10^{-4} smaller than the solar radiation pressure. Therefore, solar wind pressure is not taken into account when calculating total force on the CubeSail spacecraft.

4.4 Equilibrium Configurations in the Presence of SRP and GG Forces

As a first step in deriving the shape of a fully flexible film, it is advantageous to obtain the deformation of the film that is acted upon only by the gravity gradient and solar radiation pressure. By assuming the film has zero pitch along the sail length, it is reasonable to neglect aerodynamic drag force and obtain the deformation caused by solar radiation pressure. In all consequent derivations, the spacecraft is assumed to be in a sun-synchronous terminator orbit with the reflective side presented to the sun. As a result of the choice of the orbit and zero pitch attitude, it is also accurate to first order to assume that the sail is in equilibrium purely along the local vertical and the deformation occurs out of the orbital plane as shown in Figure 91. It is important to note that the constraint of sail alignment with the local vertical must be relaxed when including the effects of aerodynamic drag for a non-zero pitch attitude.

The derivation of the sail shape without aerodynamic drag is performed for two reasons. First, it represents a reasonably accurate approximation to the sail shape during nominal operations of the CubeSail spacecraft. Second, the shape obtained with the simplified model provides an initial guess for the numerical integrator used to solve the set of much more complicated equations of motion that include aerodynamic drag.

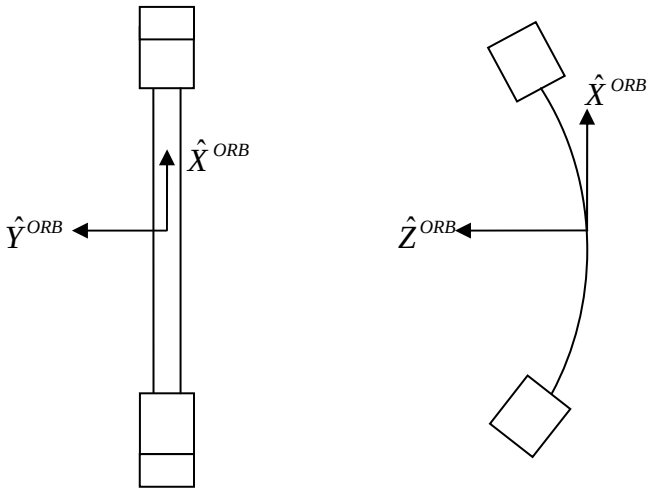

Figure 91. CubeSail out-of-plane billowing with no displacement away from local vertical.

Without loss of generality, the origin of the orbital frame is placed at the point of zero slope in the film, and the sail is assumed to be in static equilibrium. The free body diagram for a sail element, including all the forces, is shown in Figure 92.

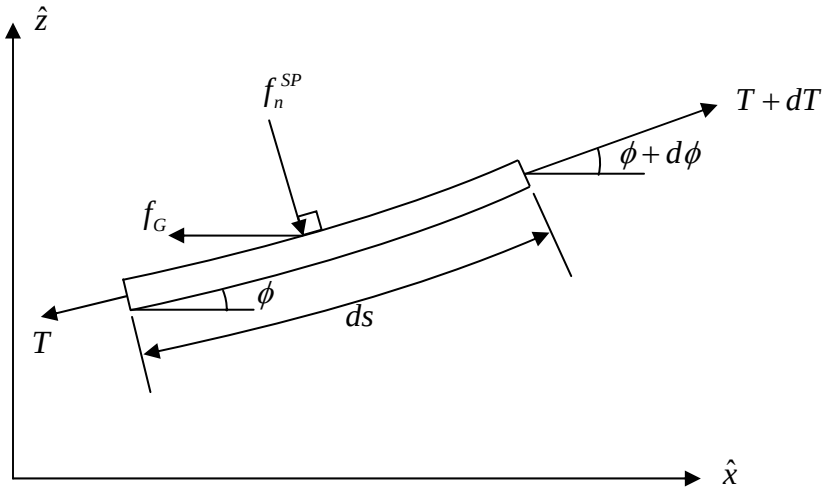

Figure 92. Forces on element of the sail.

The solar radiation pressure force in the Sail frame was derived previously as:

$$d\vec{f}_{SP}^{Sail} = \begin{bmatrix} 0 \\ -sign\left(r_{\odot,y}^{Sail}\right) \cdot P \cdot (1 - \tilde{r} \cdot s) \cdot \cos\left(\alpha^{SP}\right) \cdot \sin\left(\alpha^{SP}\right) \cdot dA \\ -sign\left(r_{\odot,z}^{Sail}\right) \cdot P \cdot \cos\left(\alpha^{SP}\right) \cdot \left[(1 + \tilde{r} \cdot s) \cdot \cos\left(\alpha^{SP}\right) + \tilde{r} \cdot (1 - s) \cdot B_f + (1 - \tilde{r}) \cdot \frac{\varepsilon_f \cdot B_f - \varepsilon_b \cdot B_b}{\varepsilon_f + \varepsilon_b} \right] \cdot dA \end{bmatrix} \quad [145]$$

The solar pressure force components must be transformed into the ORB frame, which is done using a single-axis rotation around the $\hat{y}$ axis by an angle ϕ, represented by the following rotation matrix:

$$A_{Sail}^{ORB}(\phi)=\begin{bmatrix} \mathrm{c}(\phi) & 0 & \mathrm{s}(\phi) \\ 0 & 1 & 0 \\ -\mathrm{s}(\phi) & 0 & \mathrm{c}(\phi) \end{bmatrix} \qquad [146]$$

Assuming that the sun incident rays are directed perfectly along the $\hat{Z}^{ORB}$ axis, the incidence angle, α^{SP}, which is measure with respect to the sail normal, is equivalent to the rotation angle ϕ.

For notational simplicity, let:

$$A \triangleq P \cdot w_{sail} \qquad B \triangleq (1+\tilde{r}\cdot s)$$
$$C \triangleq \tilde{r}\cdot(1-s)\cdot B_f + (1-\tilde{r})\cdot\frac{\varepsilon_f \cdot B_f - \varepsilon_b \cdot B_b}{\varepsilon_f + \varepsilon_b} \qquad D \triangleq (1-\tilde{r}\cdot s) \qquad [147]$$

Resulting in:

$$d\vec{f}_{SP}^{\,Sail} = \begin{bmatrix} 0 \\ -sign\left(r_{\odot,y}^{Sail}\right)\cdot A\cdot D\cdot\cos(\phi)\cdot\sin(\phi)\cdot ds \\ -sign\left(r_{\odot,z}^{Sail}\right)\cdot A\cdot\cos(\phi)\cdot\left[B\cdot\cos(\phi)+C\right]\cdot ds \end{bmatrix} \qquad [148]$$

Applying the transformation to the ORB frame results in:

$$d\vec{f}_{SP}^{\,ORB} = A_{Sail}^{ORB}(\phi)\cdot d\vec{f}_{SP}^{\,Sail} \triangleq \begin{bmatrix} f_x^{SP} \\ f_y^{SP} \\ f_z^{SP} \end{bmatrix} \qquad [149]$$

The gravity gradient force is given by:

$$\vec{f}_g = -f_g\hat{x}$$
$$f_g = 3\mu_{sail}\cdot\omega_{0,\,circ}^2\cdot x \qquad [150]$$

where μ_{sail} is the sail mass per unit length.

The equilibrium shape of the sail is derived by first summing the forces on the elemental sail section ds in the $\hat{x}$ and $\hat{z}$ direction, resulting in:

$$\begin{cases} (T+dT)\cdot\cos(\phi+d\phi)-T\cdot\cos(\phi)+f_x^{SP}\cdot ds-f_G\cdot ds=0 \\ (T+dT)\cdot\sin(\phi+d\phi)-T\cdot\sin(\phi)+f_z^{SP}\cdot ds=0 \end{cases} \quad [151]$$

The above equations are set to zero in order to obtain the equilibrium (zero acceleration) configuration. Expanding the sine and cosine functions results in the following:

$$\begin{cases} (T+dT)\cdot\left[\cos(\phi)\cdot\cos(d\phi)-\sin(\phi)\cdot\sin(d\phi)\right]-T\cdot\cos(\phi)+f_x^{SP}\cdot ds-f_G\cdot ds=0 \\ (T+dT)\cdot\left[\sin(\phi)\cdot\cos(d\phi)+\cos(\phi)\cdot\sin(d\phi)\right]-T\cdot\sin(\phi)+f_z^{SP}\cdot ds=0 \end{cases}$$

$$\begin{cases} (T+dT)\cdot\left[\cos(\phi)-\sin(\phi)\cdot d\phi\right]-T\cdot\cos(\phi)+f_x^{SP}\cdot ds-f_G\cdot ds=0 \\ (T+dT)\cdot\left[\sin(\phi)+\cos(\phi)\cdot d\phi\right]-T\cdot\sin(\phi)+f_z^{SP}\cdot ds=0 \end{cases}$$

$$\begin{cases} \cancel{T\cdot\cos(\phi)}-T\cdot d\phi\cdot\sin(\phi)+dT\cdot\cos(\phi)-\cancel{dT\cdot d\phi\cdot\sin(\phi)}-\cancel{T\cdot\cos(\phi)}+f_x^{SP}\cdot ds-f_G\cdot ds=0 \\ \cancel{T\cdot\sin(\phi)}+T\cdot d\phi\cdot\cos(\phi)+dT\cdot\sin(\phi)+\cancel{dT\cdot d\phi\cdot\cos(\phi)}-\cancel{T\cdot\sin(\phi)}+f_z^{SP}\cdot ds=0 \end{cases} \quad [152]$$

$$\begin{cases} dT\cdot\cos(\phi)-T\cdot d\phi\cdot\sin(\phi)+f_x^{SP}\cdot ds-f_G\cdot ds=0 \\ dT\cdot\sin(\phi)+T\cdot d\phi\cdot\cos(\phi)+f_z^{SP}\cdot ds=0 \end{cases}$$

By multiplying the first equation by $\cos(\phi)$ and the second by $\sin(\phi)$ and adding them together results in:

$$\begin{cases} dT\cdot\cos(\phi)-T\cdot d\phi\cdot\sin(\phi)+f_x^{SP}\cdot ds-f_G\cdot ds=0 & \times\cos(\phi) \\ dT\cdot\sin(\phi)+T\cdot d\phi\cdot\cos(\phi)+f_z^{SP}\cdot ds=0 & \times\sin(\phi) \end{cases}$$

$$\begin{cases} dT\cdot\cos^2(\phi)-T\cdot d\phi\cdot\sin(\phi)\cdot\cos(\phi)+f_x^{SP}\cdot\cos(\phi)\cdot ds-f_G\cdot\cos(\phi)\cdot ds=0 \\ dT\cdot\sin^2(\phi)+T\cdot d\phi\cdot\sin(\phi)\cdot\cos(\phi)+f_z^{SP}\cdot\sin(\phi)\cdot ds=0 \end{cases} \quad [153]$$

$$\frac{dT}{ds}=-f_x^{SP}\cdot\cos(\phi)+f_G\cdot\cos(\phi)-f_z^{SP}\cdot\sin(\phi)$$

Similarly, multiplying the first equation by $-\sin(\phi)$ and the second by $\cos(\phi)$, results in:

$$\begin{cases} dT\cdot\cos(\phi)-T\cdot d\phi\cdot\sin(\phi)+f_x^{SP}\cdot ds-f_G\cdot ds=0 & \times\ -\sin(\phi) \\ dT\cdot\sin(\phi)+T\cdot d\phi\cdot\cos(\phi)+f_z^{SP}\cdot ds=0 & \times\cos(\phi) \end{cases}$$

$$\begin{cases} -dT\cdot\sin(\phi)\cdot\cos(\phi)+T\cdot d\phi\cdot\sin^2(\phi)-f_x^{SP}\cdot\sin(\phi)\cdot ds+f_G\cdot\sin(\phi)\cdot ds=0 \\ dT\cdot\sin(\phi)\cdot\cos(\phi)+T\cdot d\phi\cdot\cos^2(\phi)+f_z^{SP}\cdot\cos(\phi)\cdot ds=0 \end{cases} \qquad [154]$$

$$\frac{d\phi}{ds}=\frac{1}{T}\left[f_x^{SP}\cdot\sin(\phi)-f_G\cdot\sin(\phi)-f_z^{SP}\cdot\cos(\phi)\right]$$

The above derivation results in two differential equations for the tether tension, T, and the deflection angle, ϕ, which are rewritten along with two additional geometrical relations as:

$$\begin{aligned} \frac{dT}{ds}&=-f_x^{SP}\cdot\cos(\phi)+f_G\cdot\cos(\phi)-f_z^{SP}\cdot\sin(\phi) \\ \frac{d\phi}{ds}&=\frac{1}{T}\left[f_x^{SP}\cdot\sin(\phi)-f_G\cdot\sin(\phi)-f_z^{SP}\cdot\cos(\phi)\right] \\ \frac{dx}{ds}&=\cos(\phi)\qquad\text{and}\qquad\frac{dz}{ds}=\sin(\phi) \end{aligned} \qquad [155]$$

The equations are solved numerically as a boundary value problem using the built-in Matlab solver (*bvp4c.m*). Initial conditions are set at $s=0$ located at the point of zero slope of the film, while the final conditions are set at $s=l_{sail}/2$ as follows:

$$\begin{aligned} &T\left(s=l_{sail}/2\right)=f_{g,\,satL} \\ &\phi(s=0)=0 \\ &x(s=0)=z(s=0)=0 \end{aligned} \qquad [156]$$

where $f_{g,satL}$ is the gravity gradient force on the lower satellite and is estimated as:

$$f_{g,\,satL}=3m_{sat}\cdot\omega_{circ}^2\cdot l_{sail}/2 \qquad [157]$$

Equations 155 are integrated for three different cases shown in Table 14 with the resulting shapes shown in Figure 93 and Figure 94.

Table 14. Sail configurations.

Configuration	Related parameters
Massless ideal film	$\mu_{sail} = 0$, $\tilde{r} = s = 1$, $\varepsilon_f = \varepsilon_b = 0$, $B_f = B_b = 2/3$
Massless non-ideal film	$\mu_{sail} = 0$, $\tilde{r} = 0.88$, $s = 0.94$, $\varepsilon_f = 0.05$, $\varepsilon_b = 0.55$, $B_f = 0.79$, $B_b = 0.55$
Non-ideal film with mass	$\mu_{sail} = 6.87 \times 10^{-4}$, $\tilde{r} = 0.88$, $s = 0.94$, $\varepsilon_f = 0.05$, $\varepsilon_b = 0.55$, $B_f = 0.79$, $B_b = 0.55$

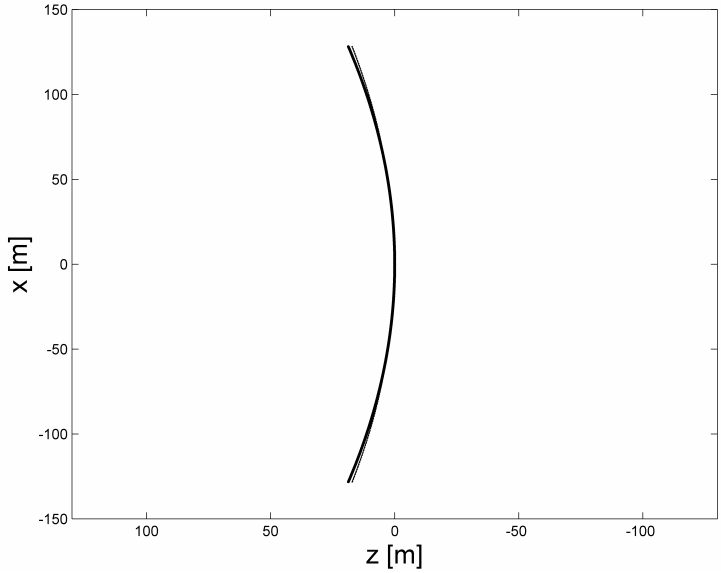

Figure 93. Sail shape for three different fidelity models and no aerodynamic drag.

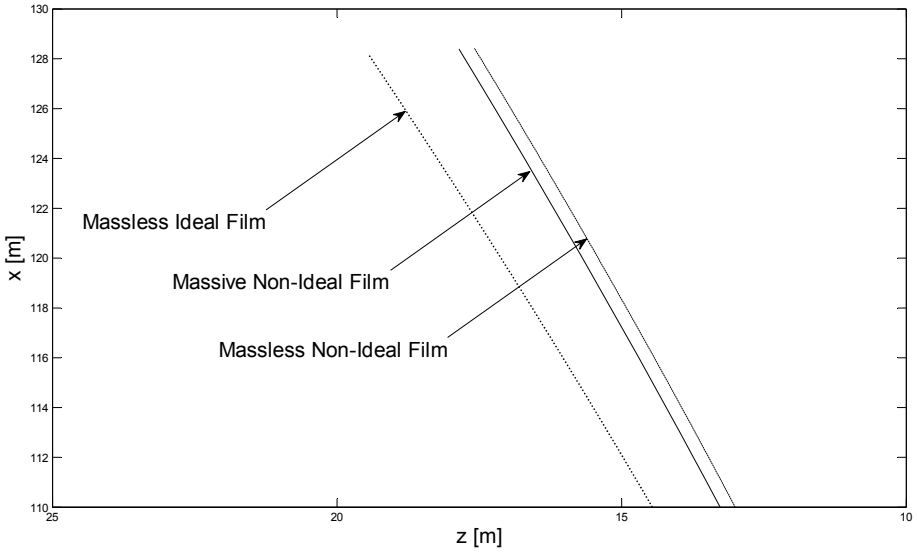

Figure 94. Zoom in of the shape at end of the sail.

The final conditions for all three configurations are listed in Table 15 and show, along with the above figures, that the sail is only moderately billowed in the out-of-plane direction by a maximum of approximately 18 m. The variation in the deflection angle ϕ is nearly linear from the film center to the tip satellite where it reaches a maximum value of approximately 15º from the vertical. In addition, the non-ideal sail effects have much higher impact on the sail shape than inclusion of its mass, primarily due to low mass of the film, equal to 0.69 g/m. It is also interesting to point out that the shape of the sail which includes the film mass is less deformed than its massless counterpart (when non-ideal sail effects are included) due to the massive sail having more inertia and resisting the billowing effects of the solar radiation pressure to a greater extent.

Table 15. Deformed film conditions at sail ends, excluding effects of aerodynamic drag.

Configuration	x_{max} [m]	z_{max} [m]	ϕ_{max} [deg]
Massless ideal film	128.09	19.42	16.31
Massless non-ideal film	128.43	17.59	14.89
Non-ideal film with mass	128.39	17.86	14.88

4.5 Equilibrium Configurations in the Presence of SRP, GG, and AD Forces

The above analysis derived the shape of the film during nominal operations when the sail is edge on to the velocity direction and the aerodynamic drag force can be neglected. In the case of a pitched sail, the area presented into the velocity direction becomes non-negligible and contributions from aerodynamic drag must be included in the derivation. In addition, the assumption of sail alignment with the local vertical must be relaxed and the in-plane deflection must be taken into account in the equations of static equilibrium.

Since the in-plane deflection away from the local vertical is not known apriori and, furthermore, the out-of-plane deflection is not necessarily symmetrical along the x-axis,

it is more appropriate to temporarily place the origin of the frame at the center of mass of the upper satellite.

The derivation is similar to the previously-presented method. However, each of the elemental areas of length ds is deflected not only in the out-of-plane direction by an angle ϕ at one end of the segment and $\phi + d\phi$ at the other end, but is also deflected in the orbital plane by angle ψ and $\psi + d\psi$ at respective ends. The geometry for a single element of length ds is shown in Figure 95.

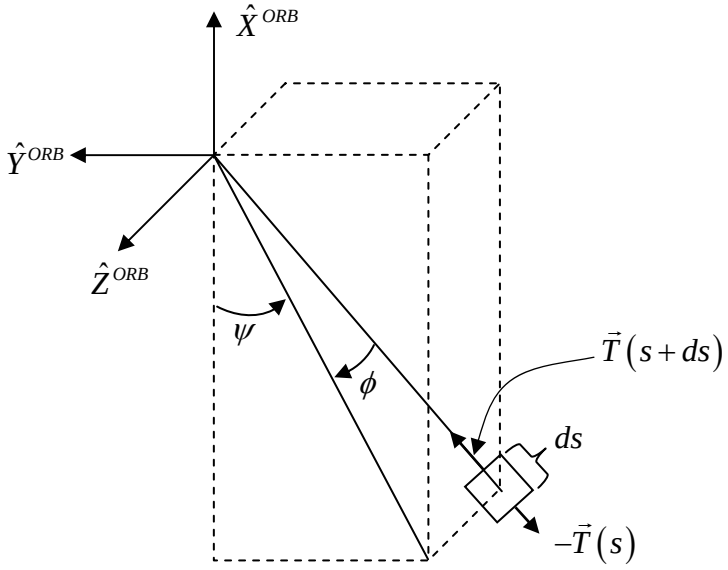

Figure 95. Geometry of an element ds of a fully deformed sail in the Orbital reference frame.

In the most general terms, the force balance equation on a sail element ds can be written as:

$$\vec{T}(s+ds) - \vec{T}(s) + \vec{F} \cdot ds = 0 \qquad [158]$$

where $\vec{F}$ combines all the forces on the sail element and includes gravity, centrifugal, aerodynamic drag, and solar radiation pressure, while $\vec{T}(s+ds)$ and $\vec{T}(s)$ are the tension at respective ends of the element. The equation is set to zero to indicate a no

acceleration (equilibrium) condition. The above equation is conveniently rewritten in the spherical coordinates as:

$$\begin{cases} (T+dT)\cdot\cos(\psi+d\psi)\cdot\cos(\phi+d\phi)-T\cdot\cos(\psi)\cdot\cos(\phi)+F_x\cdot ds=0 \\ (T+dT)\cdot\sin(\psi+d\psi)\cdot\cos(\phi+d\phi)-T\cdot\sin(\psi)\cdot\cos(\phi)+F_y\cdot ds=0 \\ (T+dT)\cdot\sin(\phi+d\phi)-T\cdot\sin(\phi)+F_z\cdot ds=0 \end{cases} \quad [159]$$

Since the tension is always assumed to be tangential to the element, the rotation along the local x-axis does not appear in the tension terms. In other words, rotation along the tension vector does not change its magnitude or direction. The rotation along the local x-axis, which is equivalent to the pitch of the sail, must, however, be included in the force terms as it has a direct impact on the incidence angles α^{AD} and α^{SP}.

If the sail elements are sufficiently small, the angular variations over its length are small. Furthermore, ignoring higher order terms, it is possible to write:

$$\sin(d\psi)=d\psi \quad \sin(d\phi)=d\phi \quad \cos(d\psi)=\cos(d\phi)=1 \quad [160]$$
$$d\psi\cdot d\phi=d\psi\cdot dT=d\phi\cdot dT=0$$

Expanding the sine and cosine function in Equation 159 and substituting the above assumptions results in:

$$\begin{cases} dT\cdot\cos(\psi)\cdot\cos(\phi)-T\cdot d\psi\cdot\sin(\psi)\cdot\cos(\phi)-T\cdot d\phi\cdot\cos(\psi)\cdot\sin(\phi)+F_x\cdot ds=0 \\ dT\cdot\sin(\psi)\cos(\phi)+T\cdot d\psi\cdot\cos(\psi)\cdot\cos(\phi)-T\cdot d\phi\cdot\sin(\psi)\cdot\sin(\phi)+F_y\cdot ds=0 \\ dT\cdot\sin(\phi)+T\cdot d\phi\cdot\cos(\phi)+F_z\cdot ds=0 \end{cases} \quad [161]$$

Solving the last of the three equations for dT results in:

$$dT=-\csc(\phi)\cdot\left[T\cdot d\phi\cdot\cos(\phi)+F_z\cdot ds\right] \quad [162]$$

Substituting this result into the first two equations results in:

$$\begin{cases} \left[-T \cdot d\psi \cdot \sin(\psi) \cdot \cos(\phi) + d\phi \cdot \left(-T \cdot \cos(\psi) \cdot \cos(\phi) \cdot \cot(\phi) - T \cdot \cos(\psi) \cdot \sin(\phi) \right) \right. \\ \left. -F_z \cdot ds \cdot \cos(\psi) \cdot \cot(\phi) + F_x \cdot ds \right] = 0 \\ \left[T \cdot d\theta \cdot \cos(\psi) \cdot \cos(\phi) + d\phi \cdot \left(-T \cdot \sin(\psi) \cdot \cos(\phi) \cdot \cot(\phi) - T \cdot \sin(\psi) \cdot \sin(\phi) \right) \right. \\ \left. -F_z \cdot ds \cdot \sin(\psi) \cdot \cot(\phi) + F_y \cdot ds \right] = 0 \end{cases} \quad [163]$$

Multiplying the first equation by $\cos(\psi)$ and second equation by $\sin(\psi)$ and then adding them together results in:

$$-T \cdot d\phi \cdot \csc(\phi) + F_x \cdot ds \cdot \cos(\psi) + F_y \cdot ds \cdot \sin(\psi) - F_z \cdot ds \cdot \cot(\psi) = 0 \quad [164]$$

which can be solved for $d\phi$ as:

$$\frac{d\phi}{ds} = \frac{1}{T}\left[F_x \cdot \cos(\psi) + F_y \cdot \sin(\psi) - F_z \cdot \cot(\phi) \right] \cdot \sin(\phi) \quad [165]$$

The above equation can be substituted into either of the Equations 163 and solved for $d\psi$ to yield:

$$\frac{d\psi}{ds} = \frac{1}{T}\left[F_x \cdot \sin^2(\psi) - F_y \cdot \cos(\psi) \cdot \sin(\psi) \right] \cdot \csc(\psi) \cdot \sec(\phi) \quad [166]$$

Substituting the solution for $d\phi$ into the previously-computed equation for dT yields the last differential equation. The three equations are therefore:

$$\begin{cases} \dfrac{dT}{ds} = -F_x \cdot \cos(\psi) \cdot \cos(\phi) - F_y \cdot \sin(\psi) \cdot \cos(\phi) - F_z \cdot \sin(\phi) \\ \dfrac{d\psi}{ds} = \dfrac{1}{T}\left[F_x \cdot \sin(\psi) - F_y \cdot \cos(\psi) \right] \cdot \sec(\phi) \\ \dfrac{d\phi}{ds} = \dfrac{1}{T}\left[F_x \cdot \cos(\psi) + F_y \cdot \sin(\psi) - F_z \cdot \cot(\phi) \right] \cdot \sin(\phi) \end{cases} \quad [167]$$

It is important to note that in the case of zero in-plane deflection, $\psi = 0$, the above equations reduce to the previously-derived differential equations.

Additional three differential equations are obtained from spherical geometry as:

$$\frac{dx}{ds} = -\cos(\psi)\cos(\phi) \qquad \frac{dy}{ds} = -\sin(\psi)\cos(\phi) \qquad \frac{dz}{ds} = \sin(\phi) \qquad [168]$$

It is now necessary to write the force components, F_x, F_y, and F_z in the ORB frame based on the attitude of the sail.

The aerodynamic drag and solar radiation pressure force terms are written in the 'Sail' frame and must be rotated to the ORB. The following derivation varies slightly from the previously-shown method where an intermediate rotation from the ORB to the SAT reference was first determined and then a consequent rotation from SAT to Sail frame was performed. This approach was convenient when assuming the sail is potentially pitched, but otherwise undeformed (no billowing). In such a case, the center of each sail element of length Δr (or equivalently ds) was located on the line connecting the two tip satellites, and the rotation occurred along that line and was assumed to be linearly-varying from the tip satellite to the mid-point (length-wise).

In the current derivation, the sail elements are no longer located on this imaginary line connecting the two satellites, but are rather displaced in both in- and out-of-plane directions. Since the deformed shape is not known (and is the goal of this derivation), it is more convenient to define the transformation matrix from the ORB frame to rotated element ds directly. Furthermore, the tip satellites are not controlled in the roll and yaw directions, but rather are allowed to align themselves with the film at the slit, as shown in Figure 96. This configuration is allowed in order to prevent damage to the film by unnecessarily trying to align the SAT frames with the ORB frame, as well as to conserve power. The pitch of satellite will remain the only axis of active control throughout the mission, to either keep the sail edge-on into the velocity direction, or induce a twist in the film.

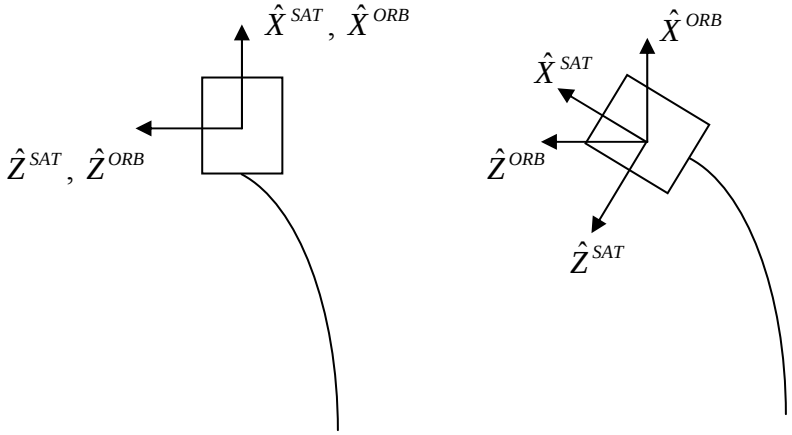

Figure 96. Tip satellite attitude with respect to film at the slit. Undesired (left), desired (right).

With the above assumptions, the direct rotation matrix from the ORB to the Sail frame of an element ds is written as:

$$A_{ORB}^{Sail} = R_3(\psi) \cdot R_2(\phi) \cdot R_1(\theta) \qquad [169]$$

It is important to note that the above is a concise notation that represents n different rotational matrices as the three angles vary along the sail length. The angles θ, ϕ, and ψ are exactly equal to the previously-introduced angles θ^{Sail}, ϕ^{Sail}, and ψ^{Sail}, where the superscript has been dropped for notational simplicity.

Historically, the rotation along the local x-axis (tangent to the film along its length) is assumed to vary linearly with a maximum value of θ^{Sat} at the upper satellite ($s = 0$) to zero pitch at the sail mid-section ($s = l_{sail}/2$), to finally a value of $-\theta^{Sat}$ at the lower satellite ($s = l_{sail}$) where l_{sail} is the length of deployed sail. This scheme was developed for the spinning UltraSail project and it resulted in either speeding up or slowing down of the rotational rate of the spacecraft. The equilibrium shapes for this configuration were investigated and are presented below. However, since the CubeSail spacecraft is not spin-stabilized, an alternative pitching scheme where both satellites are pitched in the

same direction is utilized. The variation in the pitch angle is assumed to vary linearly as in the UltraSail configuration. The pitch variation for both schemes can be concisely written as:

$$\theta^{Sail}_{\text{Opposite Pitch}}(s) = \theta^{Sat} \cdot \left(1 - \frac{2 \cdot s}{l_{sail}}\right)$$
$$\theta^{Sail}_{\text{Equal Pitch}}(s) = \theta^{Sat} \cdot \left|\left(1 - \frac{2 \cdot s}{l_{sail}}\right)\right| \quad [170]$$

The following derivation uses a general notation θ^{Sail} to refer to either scheme. The consequent results for both schemes will be presented and appropriate θ^{Sail} identified at that time.

The rotation matrices can be written as:

$$R_1(\theta) = \begin{bmatrix} 1 & 0 & 0 \\ 0 & \mathrm{c}(\theta^{Sail}) & s(\theta^{Sail}) \\ 0 & -\mathrm{s}(\theta^{Sail}) & \mathrm{c}(\theta^{Sail}) \end{bmatrix} \quad [171]$$

and

$$R_2(\phi) = \begin{bmatrix} \mathrm{c}(\phi) & 0 & -\mathrm{s}(\phi) \\ 0 & 1 & 0 \\ \mathrm{s}(\phi) & 0 & \mathrm{c}(\phi) \end{bmatrix} \quad R_3(\psi) = \begin{bmatrix} \mathrm{c}(\psi) & \mathrm{s}(\psi) & 0 \\ -\mathrm{s}(\psi) & \mathrm{c}(\psi) & 0 \\ 0 & 0 & 1 \end{bmatrix} \quad [172]$$

where s and c represent the sine and cosine functions respectively. The combined rotation matrix from the ORB to the Sail frame can therefore be written as:

$$A^{Sail}_{ORB} = \begin{bmatrix} \mathrm{c}(\phi)\mathrm{c}(\psi) & \mathrm{c}(\theta^{Sail})\mathrm{s}(\psi) + \mathrm{s}(\theta^{Sail})\mathrm{s}(\phi)\mathrm{c}(\psi) & \mathrm{s}(\theta^{Sail})\mathrm{s}(\psi) - \mathrm{c}(\theta^{Sail})\mathrm{s}(\phi)\mathrm{c}(\psi) \\ -\mathrm{c}(\phi)\mathrm{s}(\psi) & \mathrm{c}(\theta^{Sail})\mathrm{c}(\psi) - \mathrm{s}(\theta^{Sail})\mathrm{s}(\phi)\mathrm{s}(\psi) & \mathrm{s}(\theta^{Sail})\mathrm{c}(\psi) + \mathrm{c}(\theta^{Sail})\mathrm{s}(\phi)\mathrm{s}(\psi) \\ \mathrm{s}(\phi) & -\mathrm{s}(\theta^{Sail})\mathrm{c}(\phi) & \mathrm{c}(\theta^{Sail})\mathrm{c}(\phi) \end{bmatrix} \quad [173]$$

The forces due to aerodynamic drag and solar radiation pressure were previously derived in the Sail frame and must be converted to the ORB frame to complete the derivation of the sail shape. Using the fact that

$$\left(A_{ORB}^{Sail}\right)^{-1} = \left(A_{ORB}^{Sail}\right)^{T} = A_{Sail}^{ORB} \qquad [174]$$

the force vectors represented in the Sail frame are pre-multiplied by the transpose of the above matrix A_{ORB}^{Sail} to obtain the force in the orbital reference frame.

The solar radiation pressure force vector in the Sail frame was derived previously as:

$$d\vec{f}_{SP}^{\,Sail} = \begin{bmatrix} 0 \\ -sign\left(r_{\odot,y}^{Sail}\right)\cdot P\cdot(1-\tilde{r}\cdot s)\cdot\cos\left(\alpha^{SP}\right)\cdot\sin\left(\alpha^{SP}\right)\cdot dA \\ -sign\left(r_{\odot,z}^{Sail}\right)\cdot P\cdot\cos\left(\alpha^{SP}\right)\cdot\left[(1+\tilde{r}\cdot s)\cdot\cos\left(\alpha^{SP}\right)+\tilde{r}\cdot(1-s)\cdot B_f+(1-\tilde{r})\cdot\dfrac{\varepsilon_f\cdot B_f-\varepsilon_b\cdot B_b}{\varepsilon_f+\varepsilon_b}\right]\cdot dA \end{bmatrix} \qquad [175]$$

where the sun incidence angle, α^{SP}, is computed from:

$$\cos\left(\alpha^{SP}\right) = \frac{\vec{r}_{\odot}^{\,Sail}\bullet\hat{n}}{\left|\vec{r}_{\odot}^{\,Sail}\right|} \quad \text{where} \quad \vec{r}_{\odot}^{\,Sail} = A_{ORB}^{Sail}\cdot A_{ECI}^{ORB}\cdot\vec{r}_{\odot}^{\,ECI} \qquad [176]$$

given the sun vector in the ECI frame, $\vec{r}_{\odot}^{\,ECI}$, and position and velocity vectors of the spacecraft in the ECI frame in order to compute the A_{ECI}^{ORB} transformation matrix.

As before, for notational simplicity, let:

$$A \triangleq P\cdot w_{sail} \qquad B \triangleq (1+\tilde{r}\cdot s)$$
$$C \triangleq \tilde{r}\cdot(1-s)\cdot B_f+(1-\tilde{r})\cdot\frac{\varepsilon_f\cdot B_f-\varepsilon_b\cdot B_b}{\varepsilon_f+\varepsilon_b} \qquad D \triangleq (1-\tilde{r}\cdot s) \qquad [177]$$

Resulting in

$$d\vec{f}_{SP}^{\,Sail} = \begin{bmatrix} 0 \\ -sign\left(r_{\odot,y}^{Sail}\right)\cdot A\cdot D\cdot\cos\left(\phi\right)\cdot\sin\left(\phi\right)\cdot ds \\ -sign\left(r_{\odot,z}^{Sail}\right)\cdot A\cdot\cos\left(\phi\right)\cdot\left[B\cdot\cos\left(\phi\right)+C\right]\cdot ds \end{bmatrix} \qquad [178]$$

The elemental force components in the ORB frame are obtained by pre-multiplying the above vector by the full rotation matrix $A_{Sail}^{ORB}(\theta,\phi,\psi)$:

$$d\vec{f}_{SP}^{\,ORB} = A_{Sail}^{ORB}(\theta,\phi,\psi)\cdot d\vec{f}_{SP}^{\,Sail} \triangleq \begin{bmatrix} F_{SP,\,x}^{ORB} \\ F_{SP,\,y}^{ORB} \\ F_{SP,\,z}^{ORB} \end{bmatrix} \quad [179]$$

The aerodynamic drag force vector in the Sail frame was previously derived as:

$$d\vec{f}_{AD}^{\,Sail} = \begin{bmatrix} 0 \\ sign\left(V_{R,y}^{Sail}\right)\cdot\rho_{atm}\cdot V_R^2\cdot\cos\left(\alpha^{AD}\right)\cdot\sin\left(\alpha^{AD}\right)\cdot\sigma_t\cdot dA \\ sign\left(V_{R,z}^{Sail}\right)\cdot\rho_{atm}\cdot V_R^2\cdot\cos\left(\alpha^{AD}\right)\cdot\left[\left(\frac{V_b}{V_R}-\cos\left(\alpha^{AD}\right)\right)\cdot\sigma_n+2\cos\left(\alpha^{AD}\right)\right]\cdot dA \end{bmatrix} \quad [180]$$

The incidence angle of the incoming molecules, α^{AD}, is computed from:

$$\cos\left(\alpha^{AD}\right) = \hat{V}_R \bullet \vec{n} \quad [181]$$

The relative velocity, $\vec{V}_R$, is computed as before, with the small change of foregoing the intermediate transformation to the satellite frame discussed above:

$$\vec{V}_R^{\,Sail} = V_{orb}\left(1-\frac{\omega_E\cdot R\cdot\cos i}{V_{orb}}\right)\cdot A_{ORB:CubeSail}^{Sail}\cdot A_{ORB:Ravindran}^{ORB:CubeSail}\cdot\begin{bmatrix} -1 \\ \left(\frac{\omega_E\cdot R}{V_{orb}}\right)\cdot\sin i\cdot\cos f \\ 0 \end{bmatrix} \quad [182]$$

The corresponding aerodynamic drag force components in the orbital frame are computed similarly to the solar radiation pressure vector by applying the full rotation matrix:

$$d\vec{f}_{AD}^{\,ORB} = A_{Sail}^{ORB}(\theta,\phi,\psi)\cdot d\vec{f}_{AD}^{\,Sail} \triangleq \begin{bmatrix} F_{AD,\,x}^{ORB} \\ F_{AD,\,y}^{ORB} \\ F_{AD,\,z}^{ORB} \end{bmatrix} \quad [183]$$

The gravity gradient force (including contributions from the centrifugal acceleration) are written as before

$$\begin{aligned} \vec{F}_G &= -f_G \hat{x} \\ f_G &= 3\mu_{sail} \cdot \omega_{0,\,circ}^2 \cdot x \end{aligned} \qquad [184]$$

The force components in the differential equations are the sum of the individual forces due to gravity, solar radiation pressure, and aerodynamic drag written in component form as:

$$\begin{aligned} F_x &= -f_G + F_{SP,\,x}^{ORB} + F_{AD,\,x}^{ORB} \\ F_y &= F_{SP,\,\mathrm{y}}^{ORB} + F_{AD,\,\mathrm{y}}^{ORB} \\ F_z &= F_{SP,\,\mathrm{z}}^{ORB} + F_{AD,\,\mathrm{z}}^{ORB} \end{aligned} \qquad [185]$$

The equations are solved numerically as a boundary value problem using the built-in Matlab solver (*bvp4c.m*) and the following boundary conditions:

$$\begin{aligned} T\left(s = l_{sail}\right) &= \sqrt{f_{G,\,satL}^2 + f_{AD,\,satL}^2} \\ \psi\left(s = l_{sail}\right) &= \arctan\left(\frac{f_{AD,\,satL}}{f_{G,\,satL}}\right) \\ z\left(s = l_{sail}\right) &= 0 \\ x\left(s = 0\right) &= y\left(s = 0\right) = z\left(s = 0\right) = 0 \end{aligned} \qquad [186]$$

where the gravity gradient force and the aerodynamic drag on the lower satellite are estimated as:

$$f_{G,\,satL} = 3m_{sat} \cdot \omega_{circ}^2 \cdot l_{sail} \qquad [187]$$

and

$$f_{AD,\,satL} = \frac{1}{2}\rho_{atm} \cdot v^2 \cdot C_d \cdot A \qquad [188]$$

with $C_d = 2.2$ and the tip satellite cross sectional area is conservatively estimated as the maximum possible area presented into the velocity direction which is equal to 0.0212 m^2. The velocity v is estimated as orbital velocity to be equal to 7451.832 m/s (assuming a circular orbit with altitude of (800-0.26) km).

4.5.1 Sail Equilibrium in the Presence of SRP, GG, and AD Forces: Opposite Pitch Case

The results presented in this section all refer to the 'opposite pitch' case, described by:

$$\theta^{Sail}_{\text{Opposite Pitch}}(s) = \theta^{Sat} \cdot \left(1 - \frac{2 \cdot s}{l_{sail}}\right) \quad [189]$$

The resultant sail shape for a sample pitch angle of 15º is shown in Figure 97 through Figure 99. For this specific case, the out-of-plane angle, ϕ, varies nearly linearly between -13.32º at the upper satellite to 14.35º at the lower satellite, as shown in Figure 97 (left). The corresponding out-of-plane displacement, shown in Figure 97 (right), reaches a maximum value of 16.18 m at s = 132.63 m.

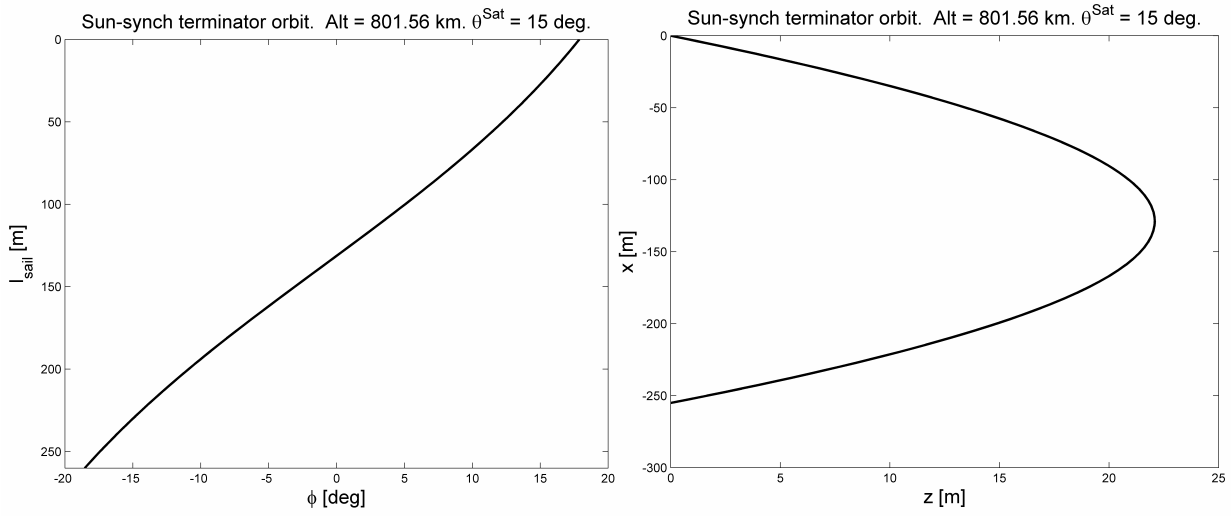

Figure 97. Out-of-plane sail deformation for $\theta^{Sat} = 15^{\circ}$ for the opposite pitch case. Angle ϕ (left) and displacement, z, (right). Note the difference is horizontal scales between the two figures.

The in-plane angle for the sample case of 15º pitch is shown Figure 98 (left), and demonstrates minimal deviation from the local vertical. The angle varies between -0.46º at the upper tip satellite and reaches 0.005º at the bottom satellite satisfying the final boundary condition, $\psi\left(s = l_{sail}\right) = \arctan\left(f_{AD,\,satL} \,/\, f_{G,\,satL}\right)$. The force of gravity on the lower satellite is several orders of magnitude larger than the maximum aerodynamic drag on the spacecraft, resulting in the final in-plane angle boundary conditions being always close to zero. The in-plane displacement, shown in Figure 98 (right), reaches a maximum value of only 3.57 m at the lower satellite.

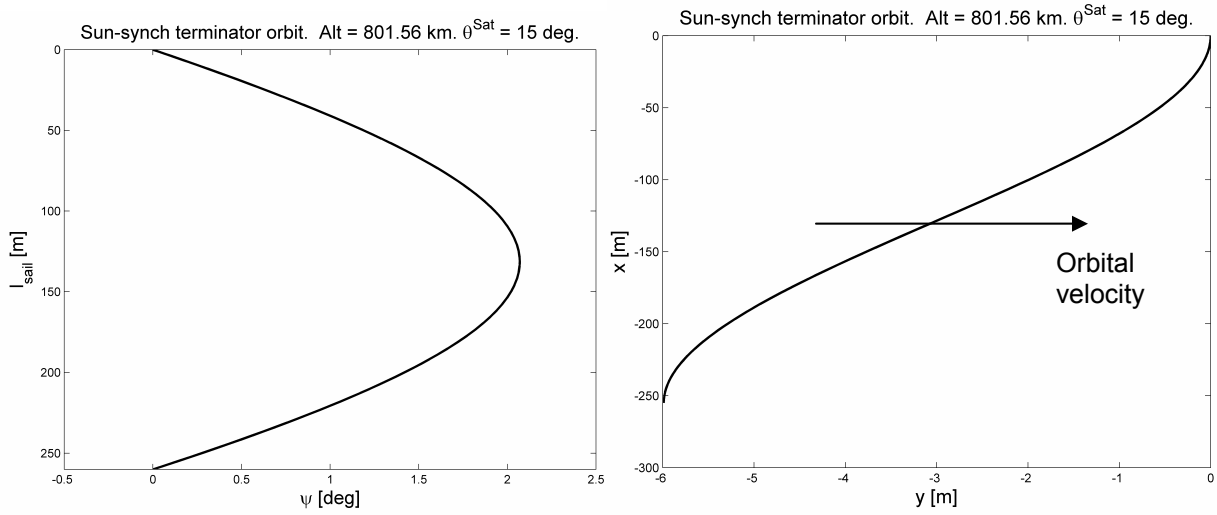

Figure 98. In-plane sail deformation for $\theta^{Sat} = 15^{\circ}$ for the opposite pitch case. Angle ψ (left) and displacement, y, (right).

The general trend of the tension along the film is shown in Figure 99 and is consistent with historical tether tension profiles shown, for example, in the works of Lorenzini[87], Misra[88]. The maximum tension occurs at the upper satellite and is due to the added contributions of the lower satellite, film with mass, and all external forces acting on the sail.

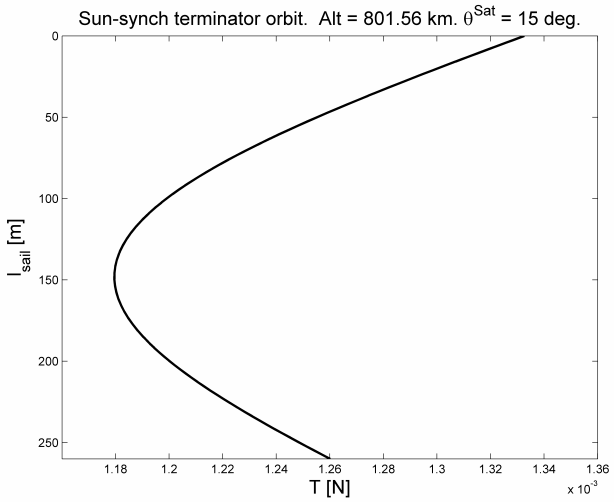

Figure 99. Tension along the deformed film for $\theta^{Sat} = 15^{\circ}$ for the opposite pitch case.

4.5.2 Variations of Sail Shape with Satellite Pitch: Opposite Pitch Case

The above results presented characteristics of a deformed sail for a single case of 15º pitch. It is interesting to investigate the behavior of the sail, both in terms of the sail shape and tension, as the pitch angle varies between 0 and 45º—the maximum allowed pitch.

Figure 100 and Figure 101 illustrate the variation of the out-of-plane angle and displacement for varying pitch angles θ^{Sat}. Intuitively, as the spacecraft is flying in a sun-synchronous terminator orbit with the surface normal of the reflective face in the direction of the sun, zero-pitch configuration results in maximum out-of-plane deflection. As the pitch angle increases, the solar pressure incidence angle α^{SP} decreases, thus decreasing the out-of-plane component of the solar radiation force. The resultant shape of the film has therefore reduced out-of-plane angle ϕ and displacement z as shown in the figures.

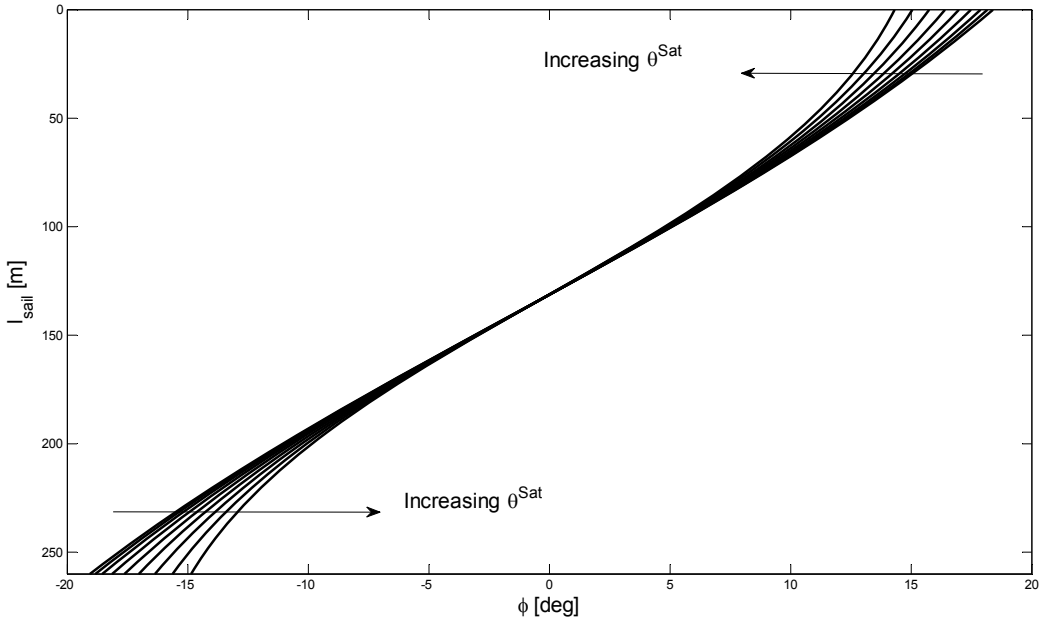

Figure 100. Variations in the out-of-plane angle for various pitch angles. The opposite pitch case.

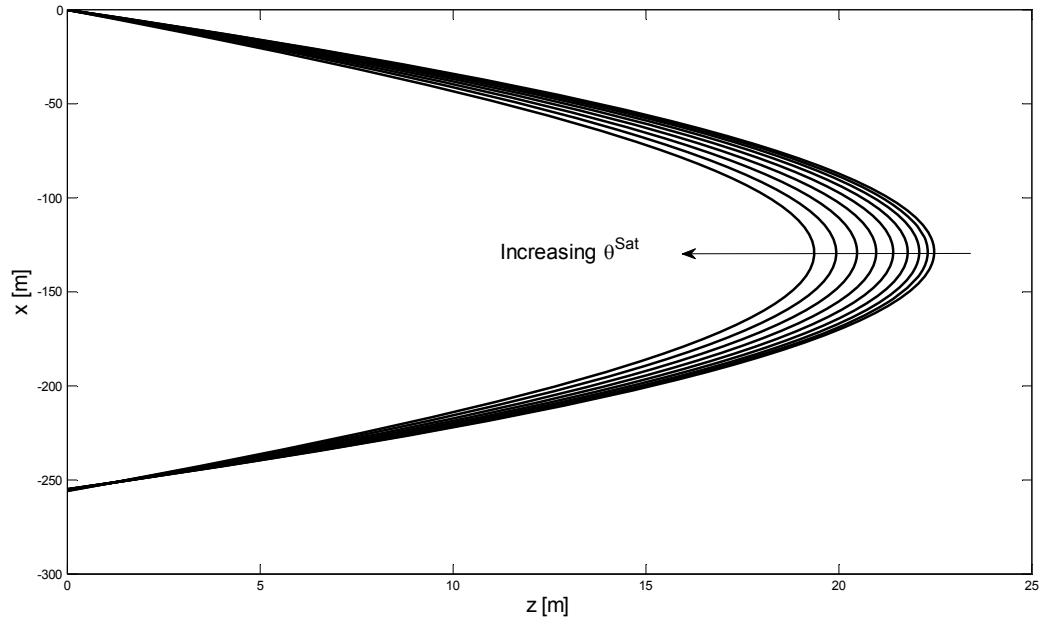

Figure 101. Variations in the out-of-plane displacement for various pitch angles. The opposite pitch case.

In contrast to the out-of-plane angle variation, the in-plane angle ψ increases with increasing pitch angle. Since zero pitch attitude corresponds to edge-on to the velocity direction configuration, any variations in the pitch angle will cause increased cross-sectional area presented in the ram direction. As a result, the aerodynamic force

will deform the sail as shown for selected cases of $\theta^{Sat} = \left(0^\circ, 15^\circ, 20^\circ, 25^\circ, 30^\circ, 35^\circ, 40^\circ, 45^\circ\right)$ in Figure 102 and Figure 103. It is important to note that the in-plane deflections are small, but their magnitude is dependent on the insertion altitude and date. The results presented in this section are all done for an insertion altitude of 800 km and for an epoch that is relatively close to the solar minimum. The resultant atmospheric density and thus the aerodynamic drag force is sufficiently small to have a correspondingly small effect on the in-plane deflection of the sail.

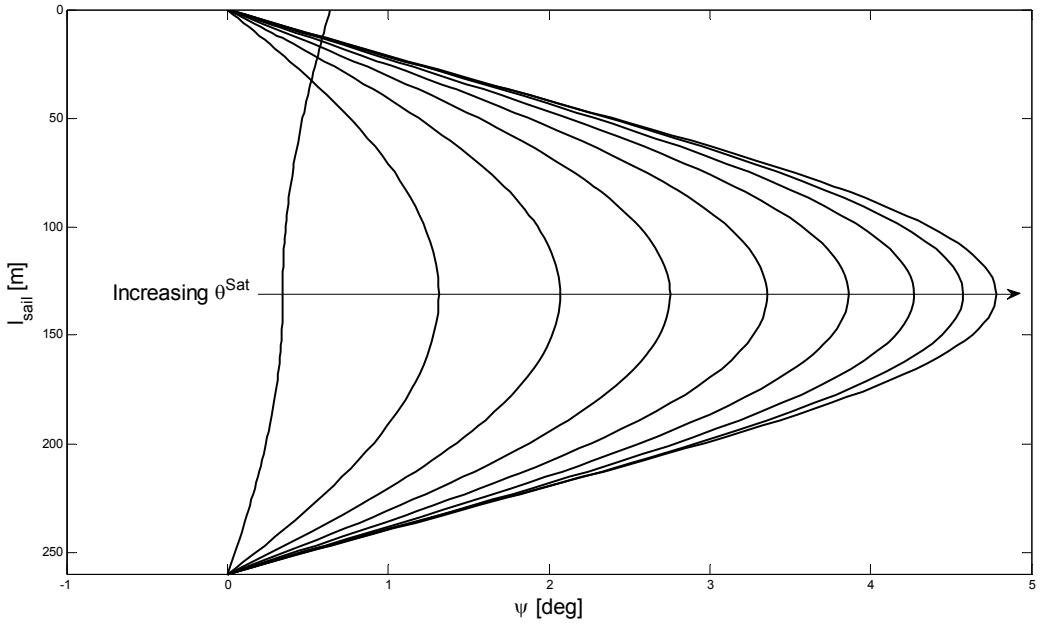

Figure 102. Variations in the in-plane angle for various pitch angles. The opposite pitch case.

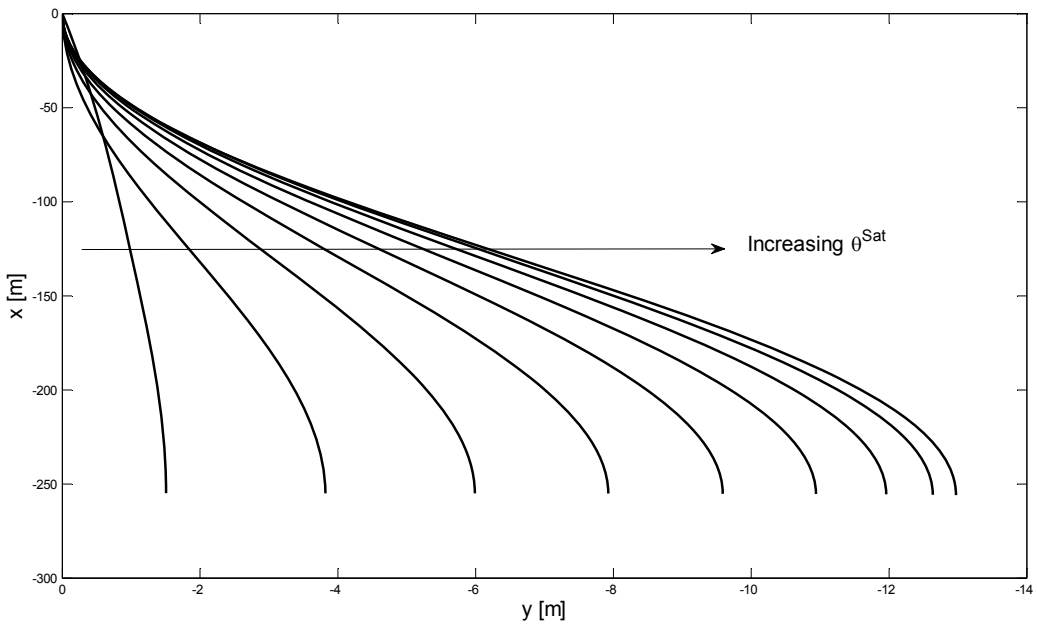

Figure 103. Variations in the in-plane displacement for various pitch angles. The opposite pitch case.

The variations in the film tension for various pitch angles are shown in Figure 104. Although the trend of increasing tension with increasing pitch angle is clearly shown, it is altitude dependent and intuitive explanations must be made with care. The pitching of the spacecraft results in a decrease in the SRP force and an increase in the AD force, however disproportionate magnitude of the two forces might result in either increase or decrease in the tension. For example, in the limiting case of sufficiently high altitude that results in no aerodynamic drag, any pitching will result in a decrease in the SRP force, but no corresponding increase in the AD force and net loss of tension. As the altitude is decreased, the aerodynamic drag force increases and the effects on decreasing tension with increasing pitch are less pronounced. In other words, the loss of SRP force (as the satellites are pitched) is being augmented by a gain in AD force resulting in a smaller loss of tension. There also exists a critical altitude where, for a given pitch angle (or equivalently sail attitude), the aerodynamic drag force exceeds the

solar radiation pressure force and results in the increase in the tension. It is important to note that the increase is not significant and that it does diminish the in-plane deflection to a small extent.

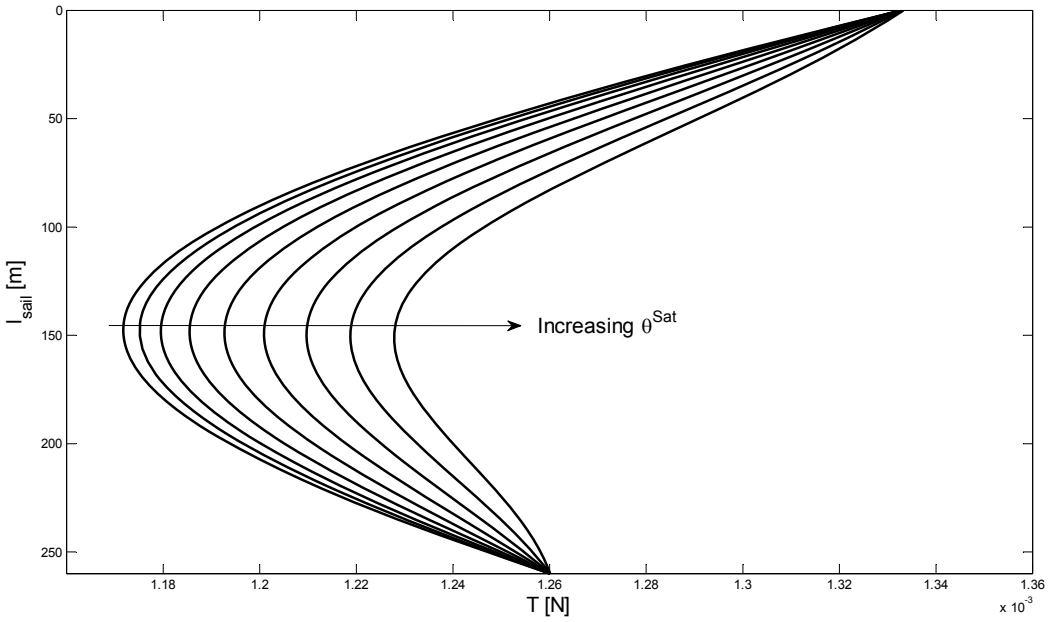

Figure 104. Variations in the film tension for various pitch angles. The opposite pitch case.

4.5.3 Sail Equilibrium in the Presence of SRP, GG, and AD Forces: Equal Pitch Case

The results presented in this section all refer to the 'equal pitch' case, described by:

$$\theta^{Sail}_{\text{Equal Pitch}}(s) = \theta^{Sat} \cdot \left| \left(1 - \frac{2 \cdot s}{l_{sail}} \right) \right| \qquad [190]$$

Analogous to the previous section the variations of the equilibrium shapes for selected pitch angles are shown in Figure 105 through Figure 109. As expected, the out-of plane deflection is comparable for the two pitching schemes as the normal component is unchanged. As the film pitch angle increases, that magnitude of the out-

of-plane force diminishes and the film is less deformed as shown in Figure 105 and Figure 106.

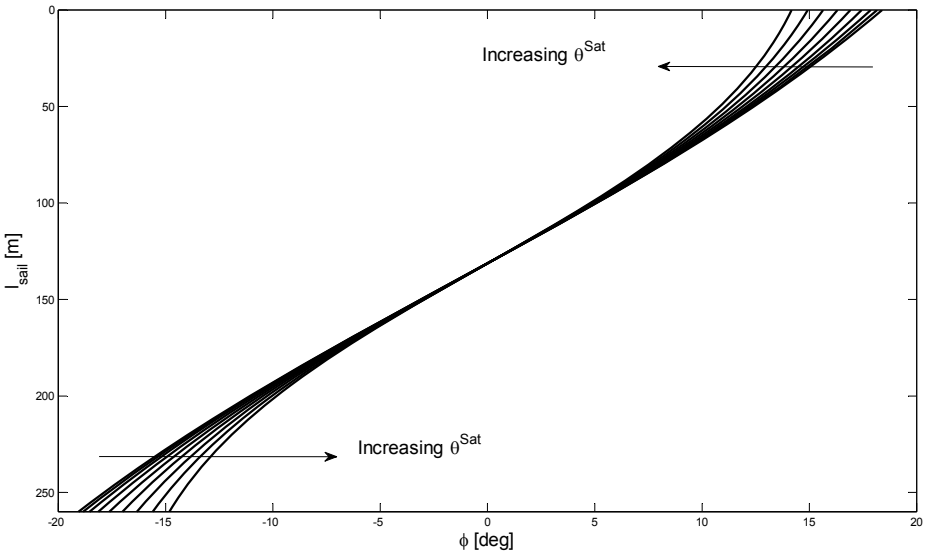

Figure 105. Variations in the out-of-plane angle for various pitch angles. The eqaul pitch case.

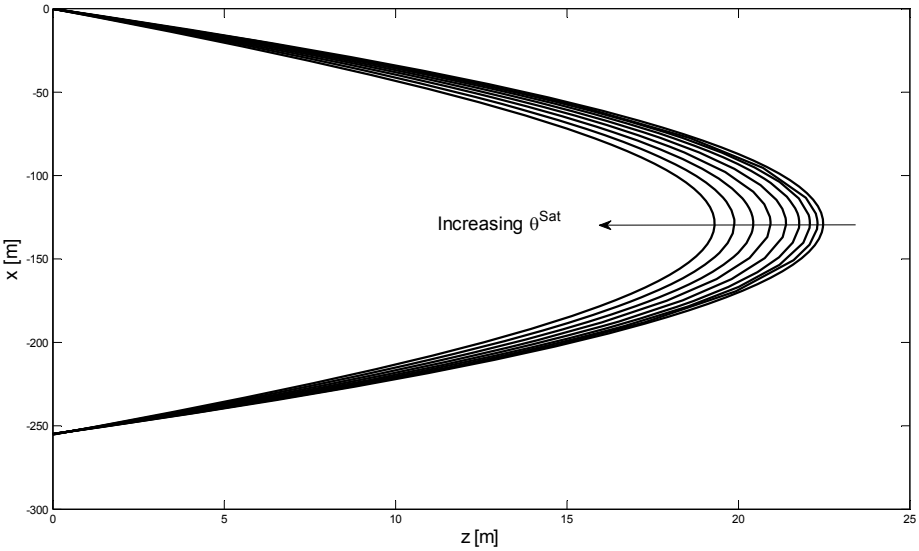

Figure 106. Variations in the out-of-plane displacement for various pitch angles. The eqaul pitch case.The in-plane deformation is the one that exhibits substantial departure from the opposite pitch behavior.

In the opposite pitch case, the top half of the sail had a net force in the positive $\hat{Y}^{ORB}$ direction and a negative net force in the $\hat{Y}^{ORB}$ direction for the bottom half of the sail. In the equal pitch case, the net force is always positive along the length of the sail, resulting in a in-plane deformation shown in Figure 107 and Figure 108.

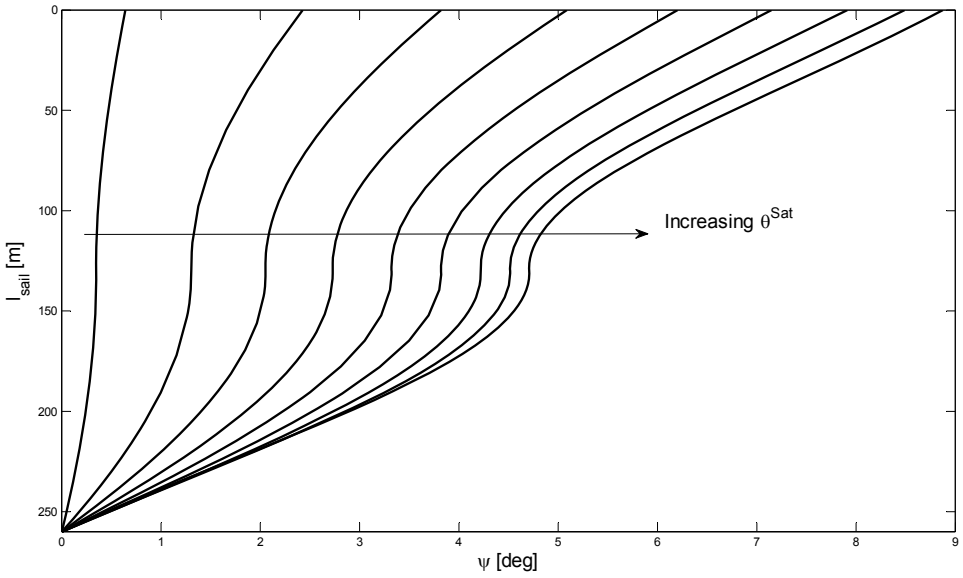

Figure 107. Variations in the in-plane angle for various pitch angles. The equal pitch case.

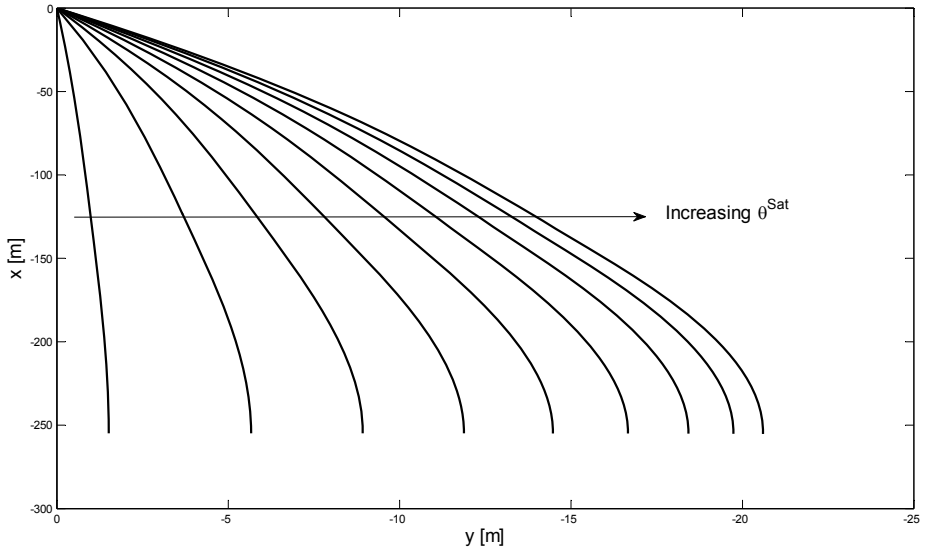

Figure 108. Variations in the in-plane displacement for various pitch angles. The equal pitch case.

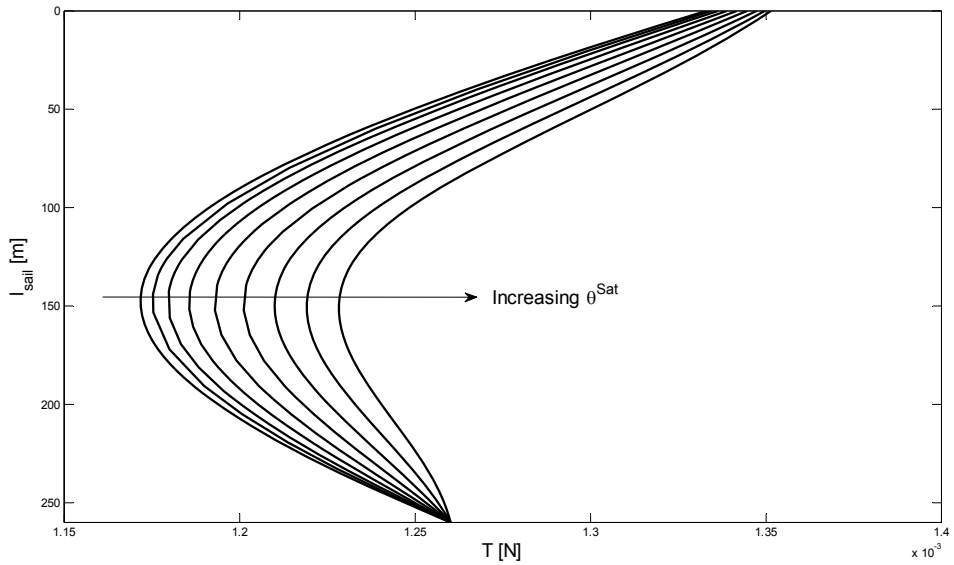

Figure 109. Variations in the film tension for various pitch angles. The opposite pitch case.

4.6 Sail Deployment in the Presence of AD, SRP, and GG Forces

The analysis of the sail deployment in the presence of aerodynamic drag, solar radiation pressure, and gravity is accomplished using the Lagrange formulation. As shown in the previous section, the sail deformations in the presence of all disturbing forces are small and it is reasonable to assume the sail is straight during the deployment. The forces of aerodynamic drag, solar radiation pressure, gravity, and centrifugal acceleration due to orbital motion are included in the following derivation, as is the film mass. It assumed that the center of mass of the system travels in a Keplerian orbit. In keeping with previous notation, superscripts refer to the coordinate frame, while subscripts refer either to the type of the force, individual axis of a particular frame, or to either of the three masses: lower satellite (satL), upper satellite (satU), or a sail element (sail). The geometry of the system is shown in Figure 110.

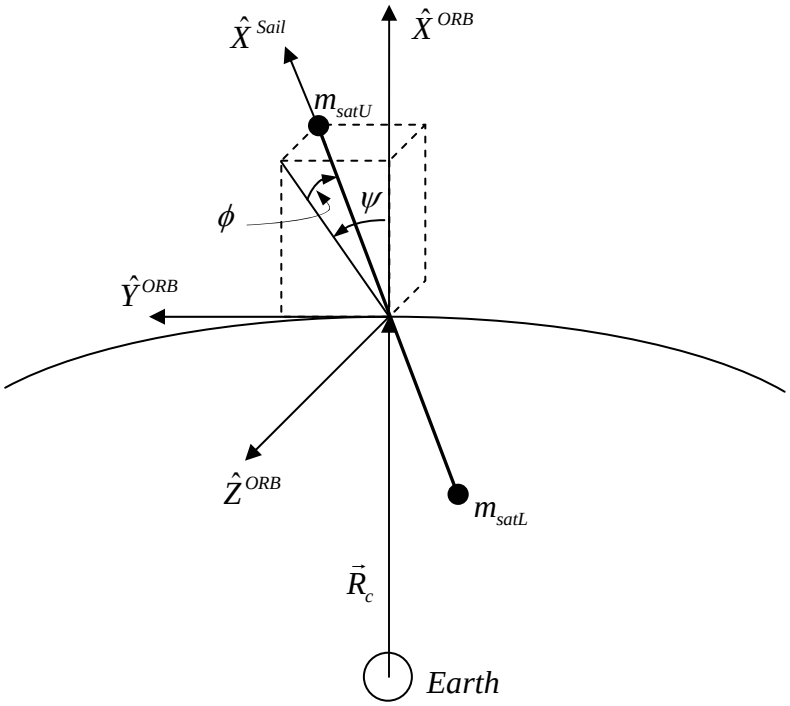

Figure 110. Gravity gradient deployment geometry.

The position of the upper satellite, lower satellite, and an elemental mass of the sail with respect to the center of Earth are given by:

$$\vec{R}_{satU} = \vec{R}_c + \vec{r}_{satU} \qquad \vec{R}_{satL} = \vec{R}_c + \vec{r}_{satL} \qquad \vec{R}_{sail} = \vec{R}_c + \vec{r}_{sail} \tag{191}$$

where $\vec{R}_c$ is the position vector of the center of mass of the system with respect to the center of Earth, and $\vec{r}_{satU}$, $\vec{r}_{satL}$, and $\vec{r}_{sail}$ respectively represent the position vectors of the upper satellite, lower satellite, and elemental sail mass with respect to the center of mass of the system (equivalently the ORB frame).

By the definition of the center of mass, it is possible to write:

$$m_{satU} \cdot \vec{r}_{satU} + m_{satL} \cdot \vec{r}_{satL} + \int_{m_{sail}} \vec{r}_{sail} \cdot dm_{sail} = 0 \tag{192}$$

The position vectors are conveniently written in the ‘Sail’ coordinate frame as:

$$\vec{r}_{satL}^{\,Sail} = -r_{satL}\hat{X}^{Sail} \qquad \vec{r}_{satU}^{\,Sail} = r_{satU}\hat{X}^{Sail} = \left(l - r_{satL}\right)\hat{X}^{Sail} \qquad \vec{r}_{sail}^{\,Sail} = r_{sail}\hat{X}^{Sail} = \left(s - r_{satL}\right)\hat{X}^{Sail} \tag{193}$$

where s is a spatial variable measured along the film from the lower satellite. The quantities r_{satL}, and r_{satU}, and r_{sail} are magnitudes of the corresponding vectors $\vec{r}_{satL}$, $\vec{r}_{satU}$, and $\vec{r}_{sail}$. Substituting Equations 193 into Equation 192 and noting that the instantaneous sail mass can be written as $m_{sail} = \mu_{sail} \cdot l$, results in:

$$\begin{aligned} m_{satU} \cdot (l - r_{satL}) - m_{satL} \cdot r_{satL} + \mu_{sail} \cdot \int_0^l (s - r_{satL})\, ds = 0 \\ -m_{satU} \cdot r_{satL} + m_{satU} \cdot l - m_{satL} \cdot r_{satL} + \mu_{sail} \cdot \left(\frac{1}{2} l^2 - r_{satL} \cdot l \right) = 0 \\ -r_{satL} \cdot (m_{satU} + m_{satL} + m_{sail}) + m_{satU} \cdot l + \frac{1}{2} l \cdot m_{sail} = 0 \\ r_{satL} = \frac{l \cdot (m_{satU} + m_{sail}/2)}{M} \end{aligned} \qquad [194]$$

where $M \triangleq m_{satU} + m_{satL} + m_{sail}$. The remaining two position magnitudes are obtained by substituting the above result into Equations 193 to yield:

$$r_{satU} = \frac{l \cdot (m_{satL} + m_{sail}/2)}{M} \quad \text{and} \quad r_{sail} = s - \frac{l \cdot (m_{satU} + m_{sail}/2)}{M} \qquad [195]$$

The velocities of the tip satellites and an elemental mass area are found by differentiating Equation 191:

$$\dot{\vec{R}}_{satU} = \dot{\vec{R}}_c + \dot{\vec{r}}_{satU} \qquad \dot{\vec{R}}_{satL} = \dot{\vec{R}}_c + \dot{\vec{r}}_{satL} \qquad \dot{\vec{R}}_{sail} = \dot{\vec{R}}_c + \dot{\vec{r}}_{sail} \qquad [196]$$

The inertial position of the center of mass of the system written in the ORB frame is:

$$\vec{R}_c = R_c \hat{X}^{ORB} \qquad [197]$$

which, after differentiating and assuming the center of mass moves in a constant altitude Keplerian orbit is:

$$\dot{\vec{R}}_c = \cancel{\dot{R}_c} \hat{X}^{ORB} + R_c \cdot \omega_{orb} \hat{Z}^{ORB} \qquad [198]$$

The velocity of the tip satellites and elemental sail mass with respect to the center of mass is calculated according to:

$$\dot{\vec{r}}_{satL}^{ORB} = \dot{\vec{r}}_{satL}^{Sail} + \vec{\omega} \times \vec{r}_{satL}^{Sail} \qquad \dot{\vec{r}}_{satU}^{ORB} = \dot{\vec{r}}_{satU}^{Sail} + \vec{\omega} \times \vec{r}_{satU}^{Sail} \qquad \dot{\vec{r}}_{sail}^{ORB} = \dot{\vec{r}}_{sail}^{Sail} + \vec{\omega} \times \vec{r}_{sail}^{Sail} \qquad [199]$$

The rotational velocity of the system, $\vec{\omega}$, expressed in the Sail frame using spherical coordinates is given by:

$$\vec{\omega} = \left[-\left(\omega_{orb} + \dot{\psi}\right) \cdot \sin\left(\phi\right) \quad \dot{\phi} \quad \left(\omega_{orb} + \dot{\psi}\right) \cdot \cos\left(\phi\right) \right]^T \qquad [200]$$

The derivatives of the position magnitudes of the tip satellites and elemental sail mass in the Sail frame are calculated by differentiating Equations 193 and noting that the total mass M is constant, that $\dot{s} = \dot{l}$, that the rate of change of the sail mass can be written as $\dot{m}_{sail} = \mu_{sail} \cdot \dot{l} = m_{sail} \cdot \left(\dot{l} / l\right)$, and that the sail is deployed evenly from both the upper and lower satellites, resulting in $\dot{m}_{satU} = \dot{m}_{satL} = -\dot{m}_{sail} / 2$. Incorporating these relations, the rates of change of the position vectors in the Sail frame can be written as follows:

$$\dot{r}_{satU} = \frac{\dot{l} \cdot \left(m_{satL} + m_{sail} / 2\right) + l \cdot \left(\dot{m}_{satL} + \dot{m}_{sail} / 2\right)}{M}$$
$$\dot{r}_{satU} = \frac{\dot{l} \cdot \left(m_{satL} + m_{sail} / 2\right)}{M} \qquad [201]$$

$$\dot{r}_{satL} = \frac{\dot{l} \cdot \left(m_{satU} + m_{sail} / 2\right) + l \cdot \left(\dot{m}_{satU} + \dot{m}_{sail} / 2\right)}{M}$$
$$\dot{r}_{satL} = \frac{\dot{l} \cdot \left(m_{satU} + m_{sail} / 2\right)}{M} \qquad [202]$$

and

$$\dot{r}_{sail} = \dot{s} - \frac{\dot{l}\cdot\left(m_{satU} + m_{sail}/2\right) + l\cdot\left(\dot{m}_{satU} + \dot{m}_{sail}/2\right)}{M} = \frac{\dot{l}\cdot\left(M - m_{satU} - m_{sail}/2\right)}{M}$$
$$\dot{r}_{sail} = \frac{\dot{l}\cdot\left(m_{satL} + m_{sail}/2\right)}{M} \qquad [203]$$

Combining the results, it is possible to write the velocity vectors in the ORB frame as:

$$\dot{\vec{r}}_{satL}^{ORB} = \dot{\vec{r}}_{satL}^{Sail} + \vec{\omega}\times\vec{r}_{satL}^{Sail} = \begin{bmatrix} -\dot{r}_{satL} \\ 0 \\ 0 \end{bmatrix} + \begin{bmatrix} -\left(\omega_{orb} + \dot{\psi}\right)\cdot\sin\left(\phi\right) \\ \dot{\phi} \\ \left(\omega_{orb} + \dot{\psi}\right)\cdot\cos\left(\phi\right) \end{bmatrix} \times \begin{bmatrix} -r_{satL} \\ 0 \\ 0 \end{bmatrix}$$
$$\dot{\vec{r}}_{satL}^{ORB} = \begin{bmatrix} -\dfrac{\dot{l}\cdot\left(m_{satU} + m_{sail}/2\right)}{M} \\ -\dfrac{l\cdot\left(\omega_{orb} + \dot{\psi}\right)\cdot\cos\left(\phi\right)\left(m_{satU} + m_{sail}/2\right)}{M} \\ \dfrac{l\cdot\dot{\phi}\cdot\left(m_{satU} + m_{sail}/2\right)}{M} \end{bmatrix} \qquad [204]$$

$$\dot{\vec{r}}_{satU}^{ORB} = \dot{\vec{r}}_{satU}^{Sail} + \vec{\omega}\times\vec{r}_{satU}^{Sail} = \begin{bmatrix} -\dot{r}_{satU} \\ 0 \\ 0 \end{bmatrix} + \begin{bmatrix} -\left(\omega_{orb} + \dot{\psi}\right)\cdot\sin\left(\phi\right) \\ \dot{\phi} \\ \left(\omega_{orb} + \dot{\psi}\right)\cdot\cos\left(\phi\right) \end{bmatrix} \times \begin{bmatrix} -r_{satU} \\ 0 \\ 0 \end{bmatrix}$$
$$\dot{\vec{r}}_{satU}^{ORB} = \begin{bmatrix} \dfrac{\dot{l}\cdot\left(m_{satL} + m_{sail}/2\right)}{M} \\ \dfrac{l\cdot\left(\omega_{orb} + \dot{\psi}\right)\cdot\cos\left(\phi\right)\left(m_{satL} + m_{sail}/2\right)}{M} \\ -\dfrac{l\cdot\dot{\phi}\cdot\left(m_{satL} + m_{sail}/2\right)}{M} \end{bmatrix} \qquad [205]$$

and

$$\dot{\vec{r}}_{sail}^{ORB} = \dot{\vec{r}}_{sail}^{Sail} + \vec{\omega} \times \vec{r}_{sail}^{Sail} = \begin{bmatrix} -\dot{r}_{sail} \\ 0 \\ 0 \end{bmatrix} + \begin{bmatrix} -(\omega_{orb} + \dot{\psi}) \cdot \sin(\phi) \\ \dot{\phi} \\ (\omega_{orb} + \dot{\psi}) \cdot \cos(\phi) \end{bmatrix} \times \begin{bmatrix} -r_{sail} \\ 0 \\ 0 \end{bmatrix}$$

$$\dot{\vec{r}}_{sail}^{ORB} = \begin{bmatrix} \dfrac{\dot{l} \cdot (m_{satL} + m_{sail}/2)}{M} \\ \dfrac{l \cdot (\omega_{orb} + \dot{\psi}) \cdot \cos(\phi)(m_{satL} + m_{sail}/2)}{M} \\ -\dfrac{l \cdot \dot{\phi} \cdot (m_{satL} + m_{sail}/2)}{M} \end{bmatrix} \quad [206]$$

The total kinetic energy of the system is written as:

$$\begin{aligned} T &= T_{satU} + T_{satL} + T_{sail} \\ &= \frac{1}{2} m_{satU} \langle \dot{\vec{R}}_{satU}, \dot{\vec{R}}_{satU} \rangle + \frac{1}{2} m_{satL} \langle \dot{\vec{R}}_{satL}, \dot{\vec{R}}_{satL} \rangle + \frac{1}{2} \int_{m_{sail}} \langle \dot{\vec{R}}_{sail}, \dot{\vec{R}}_{sail} \rangle dm_{sail} \\ &= \frac{1}{2} m_{satU} \langle \dot{\vec{R}}_c + \dot{\vec{r}}_{satU}, \dot{\vec{R}}_c + \dot{\vec{r}}_{satU} \rangle + \frac{1}{2} m_{satL} \langle \dot{\vec{R}}_c + \dot{\vec{r}}_{satL}, \dot{\vec{R}}_c + \dot{\vec{r}}_{satL} \rangle \\ &\quad + \frac{1}{2} \int_{m_{sail}} \langle \dot{\vec{R}}_c + \dot{\vec{r}}_{sail}, \dot{\vec{R}}_c + \dot{\vec{r}}_{sail} \rangle dm_{sail} \end{aligned} \quad [207]$$

where the $\langle \cdot \rangle$ notation represents a vector dot product. Expanding the dot products and grouping terms results in:

$$\begin{aligned} T &= \frac{1}{2} M \langle \dot{\vec{R}}_c, \dot{\vec{R}}_c \rangle + \langle \dot{\vec{R}}_c, \left[m_{satU} \dot{\vec{r}}_{satU} + m_{satL} \dot{\vec{r}}_{satL} + \int_{m_{sail}} \dot{\vec{r}}_{sail} dm_{sail} \right] \rangle \\ &\quad + \frac{1}{2} \left[m_{satU} \langle \dot{\vec{r}}_{satU}, \dot{\vec{r}}_{satU} \rangle + m_{satL} \langle \dot{\vec{r}}_{satL}, \dot{\vec{r}}_{satL} \rangle + \int_{m_{sail}} \langle \dot{\vec{r}}_{sail}, \dot{\vec{r}}_{sail} \rangle dm_{sail} \right] \end{aligned} \quad [208]$$

By definition of the center of mass given in Equation 192, the quantity in bracket of the second term is zero, resulting in the kinetic energy of the system of the form:

$$T = \frac{1}{2} M \langle \dot{\vec{R}}_c, \dot{\vec{R}}_c \rangle + \frac{1}{2} \left[m_{satU} \langle \dot{\vec{r}}_{satU}, \dot{\vec{r}}_{satU} \rangle + m_{satL} \langle \dot{\vec{r}}_{satL}, \dot{\vec{r}}_{satL} \rangle + \int_{m_{sail}} \langle \dot{\vec{r}}_{sail}, \dot{\vec{r}}_{sail} \rangle dm_{sail} \right] \quad [209]$$

The vector dot products can be written as:

$$\langle \dot{\vec{R}}_c, \dot{\vec{R}}_c \rangle = R_c^2 \cdot \omega_{orb}^2$$

$$\langle \dot{\vec{r}}_{satL}^{ORB}, \dot{\vec{r}}_{satL}^{ORB} \rangle = \frac{\left(2m_{satU} + m_{sail}\right)^2 \cdot \left[\dot{l}^2 + l^2\left(\dot{\phi}^2 + \left(\omega_{orb} + \dot{\psi}\right)^2 \cdot \cos^2\left(\phi\right)\right)\right]}{4M^2} \qquad [210]$$

$$\langle \dot{\vec{r}}_{satU}^{ORB}, \dot{\vec{r}}_{satU}^{ORB} \rangle = \frac{\left(2m_{satL} + m_{sail}\right)^2 \cdot \left[\dot{l}^2 + l^2\left(\dot{\phi}^2 + \left(\omega_{orb} + \dot{\psi}\right)^2 \cdot \cos^2\left(\phi\right)\right)\right]}{4M^2}$$

and

$$\int_{m_{sail}} \langle \dot{\vec{r}}_{sail}^{ORB}, \dot{\vec{r}}_{sail}^{ORB} \rangle dm_{sail} = \frac{\int_{m_{sail}} \left(2m_{satL} + m_{sail}\right)^2 dm_{sail} \cdot \left[\dot{l}^2 + l^2\left(\dot{\phi}^2 + \left(\omega_{orb} + \dot{\psi}\right)^2 \cdot \cos^2\left(\phi\right)\right)\right]}{4M^2} \qquad [211]$$

$$= \frac{\left(4m_{satL}^2 \cdot m_{sail} + 2m_{satL} \cdot m_{sail}^2 + m_{sail}^3 / 3\right) \cdot \left[\dot{l}^2 + l^2\left(\dot{\phi}^2 + \left(\omega_{orb} + \dot{\psi}\right)^2 \cdot \cos^2\left(\phi\right)\right)\right]}{4M^2}$$

Substituting the above results into the equation for kinetic energy and collecting terms results in:

$$T = \frac{1}{2} M \cdot R_c^2 \cdot \omega_{orb}^2 + \frac{1}{2} M_e \cdot \left[\dot{l}^2 + l^2\left(\dot{\phi}^2 + \left(\omega_{orb} + \dot{\psi}\right)^2 \cdot \cos^2\left(\phi\right)\right)\right] \qquad [212]$$

where M_e is a time-dependent equivalent mass defined as:

$$M_e = \frac{m_{sail}^3 + 12m_{satL} \cdot m_{satU} \cdot \left(m_{satL} + m_{satU}\right) + 3m_{sail}^2 \cdot \left(m_{satL} + 3m_{satU}\right) + 12m_{sail} \cdot m_{satU} \cdot \left(2m_{satL} + m_{satU}\right)}{12M^2} \qquad [213]$$

It is important to note that this equation differs somewhat from the equations presented in many of the tether analysis by Nixon[89], Misra[90] , Pasca[91,92,93], or Modi[94] where one or several of the following simplifying assumptions were made: the tether deployment occurred from only one end body (typically the Shuttle or larger satellite), external forces which are included in the current derivation and are presented shortly were ignored, or only in-plane motion was considered.

The potential energy of the system due to gravitational field of the Earth is written as:

$$V = -\mu_{\oplus}\left[\frac{m_{satU}}{\left|\vec{R}_{satU}\right|} + \frac{m_{satL}}{\left|\vec{R}_{satL}\right|} + \int_{m_{sail}} \frac{dm_{sail}}{\left|\vec{R}_{sail}\right|}\right]$$
$$= -\mu_{\oplus}\left[\frac{m_{satU}}{\left|\vec{R}_c + \vec{r}_{satU}\right|} + \frac{m_{satL}}{\left|\vec{R}_c + \vec{r}_{satL}\right|} + \int_{m_{sail}} \frac{dm_{sail}}{\left|\vec{R}_c + \vec{r}_{sail}\right|}\right] \quad [214]$$

where $\mu_{\oplus}$ is the gravitational constant of Earth.

It is possible to write the first term as:

$$\frac{1}{\left|\vec{R}_c + \vec{r}_{satU}\right|} = \langle \vec{R}_c + \vec{r}_{satU}, \vec{R}_c + \vec{r}_{satU} \rangle^{-\frac{1}{2}} = \left[R_c^2 + 2\langle \vec{R}_c, \vec{r}_{satU} \rangle + \langle \vec{r}_{satU}, \vec{r}_{satU} \rangle\right]^{-\frac{1}{2}}$$
$$= R_c^{-1}\left[1 + \frac{2}{R_c}\langle \hat{X}^{ORB}, \vec{r}_{satU} \rangle + \frac{1}{R_c^2}\langle \vec{r}_{satU}, \vec{r}_{satU} \rangle\right]^{-\frac{1}{2}} \quad [215]$$

where we used the fact that $\vec{R}_c = R_c \hat{X}^{ORB}$. Similar to the gravity gradient derivation, the above equation is rewritten using binomial expansion $(1+x)^{\alpha} = 1 + \alpha \cdot x + \frac{\alpha(\alpha-1)}{2!}x^2 + \cdots$ after third and higher order powers of $\left|r_{satU}\right| / R_c$ are ignored, results in:

$$\frac{1}{\left|\vec{R}_c + \vec{r}_{satU}\right|} = R_c^{-1}\left[1 - \frac{2}{R_c}\langle \hat{X}^{ORB}, \vec{r}_{satU} \rangle - \frac{\langle \vec{r}_{satU}, \vec{r}_{satU} \rangle - 3\langle \hat{X}^{ORB}, \vec{r}_{satU} \rangle^2}{2R_c^2}\right] \quad [216]$$

The corresponding equations for $1/\left|\vec{R}_c + \vec{r}_{satL}\right|$ and $1/\left|\vec{R}_c + \vec{r}_{sail}\right|$ are obtained in a similar fashion. Substituting the above results and rearranging, the potential energy is written as:

$$V = -\frac{\mu_{\oplus} M}{R_c} - \frac{\mu_{\oplus}}{R_c^2}\langle \hat{X}^{Sail}, \left[m_{satU}\vec{r}_{satU} + m_{satL}\vec{r}_{satL} + \int_{m_{sail}} \vec{r}_{sail} dm_{sail}\right]\rangle +$$
$$\frac{\mu_{\oplus}}{2R_c^3}\left\{m_{satL}\left[\langle \vec{r}_{satL}, \vec{r}_{satL} \rangle - 3\langle \hat{X}^{Sail}, \vec{r}_{satL} \rangle^2\right] + m_{satU}\left[\langle \vec{r}_{satU}, \vec{r}_{satU} \rangle - 3\langle \hat{X}^{Sail}, \vec{r}_{satU} \rangle^2\right]\right. \quad [217]$$
$$\left. + \int_{m_{sail}}\left[\langle \vec{r}_{sail}, \vec{r}_{sail} \rangle - 3\langle \hat{X}^{Sail}, \vec{r}_{sail} \rangle^2\right] dm_{sail}\right\}$$

By definition of the center of mass (Equation 192), the quantity in the bracket of the second term is equal to zero. Before the remaining terms can be evaluated, the unit vector $\hat{X}^{ORB}$ must be expressed in the 'Sail' frame. This is accomplished by noting that for a straight sail the 'Sail' and 'SAT' frames coincide. Furthermore, since the sail is deployed edge-on to the velocity direction, the pitch angle is zero ($\theta^{SAT} = 0 = \theta^{Sail}$) and the unit vector along the orbital x-axis, represented in the 'Sail' frame is written as:

$$\hat{X}^{Sail} = A_{ORB}^{Sail}\hat{X}^{ORB} = \begin{bmatrix}\cos(\psi)\cos(\phi) & -\sin(\psi)\cos(\phi) & \sin(\phi)\end{bmatrix} \quad [218]$$

The remaining undefined dot products can be written as follows:

$$\begin{aligned}\langle \vec{r}_{satL}, \vec{r}_{satL} \rangle &= \begin{bmatrix}-r_{satL} & 0 & 0\end{bmatrix}\begin{bmatrix}-r_{satL} & 0 & 0\end{bmatrix}^T = r_{satL}^2 \\ \langle \vec{r}_{satL}, \vec{r}_{satL} \rangle &= \frac{l^2 \cdot \left(m_{satU} + m_{sail}/2\right)^2}{M^2}\end{aligned} \quad [219]$$

$$\langle \vec{r}_{satU}, \vec{r}_{satU} \rangle = \frac{l^2 \cdot \left(m_{satL} + m_{sail}/2\right)^2}{M^2} \quad [220]$$

$$\begin{aligned}\int_{m_{sail}} \langle r_{sail}, r_{sail} \rangle dm_{sail} &= \int_{m_{sail}} \frac{l^2\left(m_{satL} + m_{sail}/2\right)^2}{M^2} dm_{sail} \\ \int_{m_{sail}} \langle r_{sail}, r_{sail} \rangle dm_{sail} &= \frac{l^2}{M^2}\left[m_{satL}m_{sail} + \frac{m_{satL}m_{sail}^2}{2} + \frac{m_{sail}^3}{12}\right]\end{aligned} \quad [221]$$

$$\langle \hat{X}^{Sail}, \vec{r}_{satU} \rangle = \begin{bmatrix}\cos(\psi)\cos(\phi) & -\sin(\psi)\cos(\phi) & \sin(\phi)\end{bmatrix}\begin{bmatrix}-r_{satU} \\ 0 \\ 0\end{bmatrix}$$

$$\begin{aligned}\langle \hat{X}^{Sail}, \vec{r}_{satU} \rangle^2 &= r_{satU}^2 \cdot \cos^2(\psi) \cdot \cos^2(\phi) \\ \langle \hat{X}^{Sail}, \vec{r}_{satU} \rangle^2 &= \frac{l^2 \cdot \cos^2(\psi) \cdot \cos^2(\phi) \cdot \left(m_{satL} + m_{sail}/2\right)^2}{M^2}\end{aligned} \quad [222]$$

$$\begin{aligned}\langle \hat{X}^{Sail}, \vec{r}_{satL} \rangle^2 &= r_{satL}^2 \cdot \cos^2(\psi) \cdot \cos^2(\phi) \\ \langle \hat{X}^{Sail}, \vec{r}_{satL} \rangle^2 &= \frac{l^2 \cdot \cos^2(\psi) \cdot \cos^2(\phi) \cdot \left(m_{satU} + m_{sail}/2\right)^2}{M^2}\end{aligned} \quad [223]$$

$$\int_{m_{sail}} \langle \hat{X}^{Sail}, r_{sail} \rangle^2 dm_{sail} = \int_{m_{sail}} \frac{l^2 \cdot \cos^2(\psi) \cdot \cos^2(\phi) \left(m_{satL} + m_{sail}/2\right)^2}{M^2} dm_{sail}$$

$$\int_{m_{sail}} \langle \hat{X}^{Sail}, r_{sail} \rangle^2 dm_{sail} = \frac{l^2 \cdot \cos^2(\psi) \cdot \cos^2(\phi) \cdot \left(m_{satL} m_{sail} + \frac{m_{satL} m_{sail}^2}{2} + \frac{m_{sail}^3}{12} \right)}{M^2} \quad [224]$$

Substituting the above results into the potential energy equation and collecting terms results in:

$$V = -\frac{\mu_{\oplus} \cdot M}{R_c} + \frac{\mu_{\oplus} \cdot M_e \cdot l^2}{2R_c^3} \left[1 - 3\cos^2(\psi)\cos^2(\phi)\right] \quad [225]$$

The equations of motion are obtained using the classical Lagrangian formulation written as:

$$\frac{d}{dt}\left(\frac{\partial L}{\partial \dot{q}_i}\right) - \frac{\partial L}{\partial q_i} = Q_i \quad [226]$$

where $L \triangleq T - V$ and Q_i are the generalized forces associated with each of the generalized coordinates $q = \{\psi, \phi, l\}$.

$$L = \frac{1}{2} M \cdot R_c^2 \cdot \omega_{orb}^2 + \frac{1}{2} M_e \cdot \left[\dot{l}^2 + l^2 \left(\dot{\phi}^2 + \left(\omega_{orb} + \dot{\psi}\right)^2 \cdot \cos^2(\phi)\right)\right] + \frac{\mu_{\oplus} \cdot M}{R_c} - \frac{\mu_{\oplus} \cdot M_e \cdot l^2}{2R_c^3}\left[1 - 3\cos^2(\psi)\cos^2(\phi)\right] \quad [227]$$

The equation of motion associated with the generalized coordinate ψ is:

$$\frac{d}{dt}\left[M_e \cdot l^2 \cdot \cos^2(\phi) \cdot \left(\omega_{orb} + \dot{\psi}\right)\right] + \frac{\mu_{\oplus} \cdot M_e \cdot l^2}{2R_c^3}\left[6\cos(\psi) \cdot \sin(\psi) \cdot \cos^2(\phi)\right] = Q_{\psi}$$

$$\left(\ddot{\psi} + \dot{\omega}_{orb}\right) + 2\left(\dot{\psi} + \omega_{orb}\right) \cdot \left[\frac{\dot{l}}{l} - \dot{\phi} \cdot \tan(\phi)\right] + \frac{3\mu_{\oplus}}{R_c^3}\cos(\psi) \cdot \sin(\psi) = \frac{Q_{\psi}}{M_e \cdot l^2 \cdot \cos^2(\phi)} \quad [228]$$

The equation of motion associated with the generalized coordinate ϕ is:

$$\frac{d}{dt}\left[M_e \cdot l^2 \cdot \dot{\phi}\right] + \left[M_e \cdot l^2 \cdot \left(\dot{\psi} + \omega_{orb}\right)^2 \cdot \cos\left(\phi\right) \cdot \sin\left(\phi\right) + \frac{3\mu_{\oplus} \cdot M_e \cdot l^2}{R_c^3} \cos^2\left(\psi\right) \cdot \cos\left(\phi\right) \cdot \sin\left(\phi\right)\right] = Q_{\phi}$$

$$\ddot{\phi} + \frac{2\dot{\phi} \cdot \dot{l}}{l} + \left[\left(\dot{\psi} + \omega_{orb}\right)^2 + \frac{3\mu_{\oplus}}{R_c^3} \cos^2\left(\psi\right)\right] \cdot \cos\left(\phi\right) \cdot \sin\left(\phi\right) = \frac{Q_{\phi}}{M_e \cdot l^2} \quad [229]$$

Lastly, the equation of motion associated with the generalized coordinate l is:

$$\frac{d}{dt}\left[M_e \cdot \dot{l}\right] - M_e \cdot l \cdot \left(\left(\dot{\psi} + \omega_{orb}\right)^2 \cdot \cos^2\left(\phi\right) + \dot{\phi}^2\right) + \frac{\mu_{\oplus} \cdot M_e \cdot l}{R_c^3}\left(1 - 3\cos^2\left(\psi\right) \cdot \cos^2\left(\phi\right)\right) = Q_l$$

$$\ddot{l} - l \cdot \left(\left(\dot{\psi} + \omega_{orb}\right)^2 \cdot \cos^2\left(\phi\right) + \dot{\phi}^2\right) + \frac{\mu_{\oplus} \cdot l}{R_c^3}\left(1 - 3\cos^2\left(\psi\right) \cdot \cos^2\left(\phi\right)\right) = \frac{Q_l}{M_e} \quad [230]$$

Combining the three second-order differential equations, the system's dynamics are described by:

$$\left(\ddot{\psi} + \dot{\omega}_{orb}\right) + 2\left(\dot{\psi} + \omega_{orb}\right) \cdot \left[\frac{\dot{l}}{l} - \dot{\phi} \cdot \tan\left(\phi\right)\right] + \frac{3\mu_{\oplus}}{R_c^3} \cos\left(\psi\right) \cdot \sin\left(\psi\right) = \frac{Q_{\psi}}{M_e \cdot l^2 \cdot \cos^2\left(\phi\right)}$$

$$\ddot{\phi} + \frac{2\dot{\phi} \cdot \dot{l}}{l} + \left[\left(\dot{\psi} + \omega_{orb}\right)^2 + \frac{3\mu_{\oplus}}{R_c^3} \cos^2\left(\psi\right)\right] \cdot \cos\left(\phi\right) \cdot \sin\left(\phi\right) = \frac{Q_{\phi}}{M_e \cdot l^2} \quad [231]$$

$$\ddot{l} - l \cdot \left(\left(\dot{\psi} + \omega_{orb}\right)^2 \cdot \cos^2\left(\phi\right) + \dot{\phi}^2\right) + \frac{\mu_{\oplus} \cdot l}{R_c^3}\left(1 - 3\cos^2\left(\psi\right) \cdot \cos^2\left(\phi\right)\right) = \frac{Q_l}{M_e}$$

4.6.1 Generalized Forces

The generalized forces Q_{ψ}, Q_{ϕ}, and Q_l are calculated from the virtual work done by the external forces through virtual displacements. The virtual work is conveniently expressed in the ORB frame and corresponding components of the external forces. The desired general forces are then obtained by a transformation to the generalized coordinates[49,95]. The virtual work is written as:

$$\delta W = F_x^{ORB} \delta x^{ORB} + F_y^{ORB} \delta y^{ORB} + F_z^{ORB} \delta z^{ORB} \quad [232]$$

Referring to Figure 110, the position of the sail element written in the generalized coordinates is:

$$
\begin{aligned}
x^{ORB} &= l \cdot \cos(\psi)\cos(\phi) \\
y^{ORB} &= l \cdot \sin(\psi)\cos(\phi) \\
z^{ORB} &= -l \cdot \sin(\phi)
\end{aligned}
\qquad [233]
$$

The virtual displacements are therefore:

$$
\begin{aligned}
\delta x^{ORB} &= -l \cdot \sin(\psi)\cos(\phi)\delta\psi - l \cdot \cos(\psi)\sin(\phi)\delta\phi + \cos(\psi)\cos(\phi)\delta l \\
\delta y^{ORB} &= l \cdot \cos(\psi)\cos(\phi)\delta\psi - l \cdot \sin(\psi)\sin(\phi)\delta\phi + \sin(\psi)\cos(\phi)\delta l \\
\delta z^{ORB} &= -l \cdot \cos(\phi)\delta\phi - \sin(\phi)\delta l
\end{aligned}
\qquad [234]
$$

Substituting the virtual displacement equations into the equation of virtual work results in:

$$
\begin{aligned}
\delta W = {} & F_x^{ORB} \cdot \left[-l \cdot \sin(\psi)\cos(\phi)\delta\psi - l \cdot \cos(\psi)\sin(\phi)\delta\phi + \cos(\psi)\cos(\phi)\delta l \right] \\
& + F_y^{ORB} \cdot \left[l \cdot \cos(\psi)\cos(\phi)\delta\psi - l \cdot \sin(\psi)\sin(\phi)\delta\phi + \sin(\psi)\cos(\phi)\delta l \right] \\
& + F_z^{ORB} \cdot \left[-l \cdot \cos(\phi)\delta\phi - \sin(\phi)\delta l \right]
\end{aligned}
\qquad [235]
$$

and collecting related terms results in:

$$
\begin{aligned}
\delta W = {} & \left[-F_x^{ORB} \cdot l \cdot \sin(\psi)\cos(\phi) + F_y^{ORB} \cdot l \cdot \cos(\psi)\cos(\phi) \right]\delta\psi \\
& + \left[-F_x^{ORB} \cdot l \cdot \cos(\psi)\sin(\phi) - F_y^{ORB} \cdot l \cdot \sin(\psi)\sin(\phi) - F_z^{ORB} \cdot l \cdot \cos(\phi) \right]\delta\phi \\
& + \left[F_x^{ORB} \cdot \cos(\psi)\cos(\phi) + F_y^{ORB} \cdot \sin(\psi)\cos(\phi) - F_z^{ORB} \cdot \sin(\phi) \right]\delta l \\
\delta W = {} & Q_\psi \delta\psi + Q_\phi \delta\phi + Q_l \delta l
\end{aligned}
\qquad [236]
$$

The last remaining task is to re-write the previously derived forces in the orbital frame in the form of generalized forces, Q_ψ, Q_ϕ, Q_l shown above. The first-order gravity gradient force on a mass element dm is written from Equation 137 in the orbital frame as:

$$F_{gg^1,x}^{ORB} = 2\frac{\mu_\oplus}{R_c^3}\cdot x^{ORB}\cdot dm$$
$$F_{gg^1,y}^{ORB} = -\frac{\mu_\oplus}{R_0^3}\cdot y^{ORB}\cdot dm \qquad [237]$$
$$F_{gg^1,z}^{ORB} = -\frac{\mu_\oplus}{R_0^3}\cdot z^{ORB}\cdot dm$$

Substituting the expressions for generalized coordinates from Equation 233 into the above equation results in:

$$F_{gg^1,x}^{ORB} = 2\frac{\mu_\oplus}{R_c^3}\cdot l\cdot\cos(\psi)\cos(\phi)\cdot dm$$
$$F_{gg^1,y}^{ORB} = -\frac{\mu_\oplus}{R_0^3}\cdot l\cdot\sin(\psi)\cos(\phi)\cdot dm \qquad [238]$$
$$F_{gg^1,z}^{ORB} = \frac{\mu_\oplus}{R_0^3}\cdot l\cdot\sin(\phi)\cdot dm$$

Subsequently, substituting the above result into the equation for generalized force results in:

$$Q_{gg^1,\,\psi} = -3\frac{\mu_\oplus}{R_c^3}\cdot l^2\cdot\cos^2(\phi)\sin(\psi)\cos(\psi)\,dm$$
$$Q_{gg^1,\,\phi} = -3\frac{\mu_\oplus}{R_c^3}\cdot l^2\cdot\cos^2(\psi)\sin(\phi)\cos(\phi)\,dm \qquad [239]$$
$$Q_{gg^1,\,l} = \frac{\mu_\oplus}{R_c^3}\cdot l\cdot\left[3\cos^2(\psi)\cos^2(\phi)-1\right]dm$$

Integrating the above equations over all particles in the dynamical system and using the fact that the sail has a constant density per unit length, $m_{sail} = \mu_{sail}\cdot l$ ($dm_{sail} = \mu_{sail}\cdot dl_{sail}$) results in the final generalized force equations for the first-order gravity gradient force:

$$
\begin{aligned}
Q_{gg^1,\,\psi} &= -\left(6m_{sat} + m_{sail}\right)\frac{\mu_\oplus}{R_c^3}\cdot l^2\cdot\cos^2\left(\phi\right)\sin\left(\psi\right)\cos\left(\psi\right) \\
Q_{gg^1,\,\phi} &= -\left(6m_{sat} + m_{sail}\right)\frac{\mu_\oplus}{R_c^3}\cdot l^2\cdot\cos^2\left(\psi\right)\sin\left(\phi\right)\cos\left(\phi\right) \\
Q_{gg^1,\,l} &= \left(2m_{sat} + \frac{m_{sail}}{2}\right)\frac{\mu_\oplus}{R_c^3}\cdot l\cdot\left[3\cos^2\left(\psi\right)\cos^2\left(\phi\right) - 1\right]
\end{aligned}
\qquad [240]
$$

The second order gravity-gradient is relatively small and is not included in the presented analysis. However, if the added precision is deemed necessary, the force components in the orbital frame are given by (the derivation of generalized forces is omitted):

$$
\begin{aligned}
F_{gg^2,x}^{ORB} &= 3\frac{\mu_\oplus}{R_c^3}\cdot\frac{x^{ORB}\cdot z^{ORB}}{R_c}\cdot dm \\
F_{gg^2,y}^{ORB} &= -3\frac{\mu_\oplus}{R_0^3}\cdot\frac{y^{ORB}\cdot z^{ORB}}{R_c}\cdot dm \\
F_{gg^2,z}^{ORB} &= -\frac{\mu_\oplus}{R_0^3}\cdot\left[-\frac{3}{2}\left(\frac{\left(x^{ORB}\right)^2 + \left(z^{ORB}\right)^2}{R_c} + \frac{3\left(z^{ORB}\right)^2}{R_c}\right)\right] z^{ORB}\cdot dm
\end{aligned}
\qquad [241]
$$

The generalized forces associated with the aerodynamic drag and solar radiation pressure are easily obtained by substituting the previously-derived force components expressed in the orbital frame into the equation for generalized work, resulting in:

$$
\begin{aligned}
Q_{AD,\,\psi} &= -F_{AD,x}^{ORB}\cdot l\cdot\sin\left(\psi\right)\cos\left(\phi\right) + F_{AD,y}^{ORB}\cdot l\cdot\cos\left(\psi\right)\cos\left(\phi\right) \\
Q_{AD,\,\phi} &= -F_{AD,x}^{ORB}\cdot l\cdot\cos\left(\psi\right)\sin\left(\phi\right) - F_{AD,y}^{ORB}\cdot l\cdot\sin\left(\psi\right)\sin\left(\phi\right) - F_{AD,z}^{ORB}\cdot l\cdot\cos\left(\phi\right) \\
Q_{AD,\,l} &= F_{AD,x}^{ORB}\cdot\cos\left(\psi\right)\cos\left(\phi\right) + F_{AD,y}^{ORB}\cdot\sin\left(\psi\right)\cos\left(\phi\right) - F_{AD,z}^{ORB}\cdot\sin\left(\phi\right)
\end{aligned}
\qquad [242]
$$

and

$$
\begin{aligned}
Q_{SP,\,\psi} &= -F_{SP,x}^{ORB}\cdot l\cdot\sin\left(\psi\right)\cos\left(\phi\right) + F_{SP,y}^{ORB}\cdot l\cdot\cos\left(\psi\right)\cos\left(\phi\right) \\
Q_{SP,\,\phi} &= -F_{SP,x}^{ORB}\cdot l\cdot\cos\left(\psi\right)\sin\left(\phi\right) - F_{SP,y}^{ORB}\cdot l\cdot\sin\left(\psi\right)\sin\left(\phi\right) - F_{SP,z}^{ORB}\cdot l\cdot\cos\left(\phi\right) \\
Q_{SP,\,l} &= F_{SP,x}^{ORB}\cdot\cos\left(\psi\right)\cos\left(\phi\right) + F_{SP,y}^{ORB}\cdot\sin\left(\psi\right)\cos\left(\phi\right) - F_{SP,z}^{ORB}\cdot\sin\left(\phi\right)
\end{aligned}
\qquad [243]
$$

The total generalized force components can therefore be written as:

$$
\begin{aligned}
Q_{\psi} &= Q_{gg^1,\,\psi} + Q_{AD,\,\psi} + Q_{SP,\,\psi} \\
Q_{\phi} &= Q_{gg^1,\,\phi} + Q_{AD,\,\phi} + Q_{SP,\,\phi} \\
Q_{l} &= Q_{gg^1,\,l} + Q_{AD,\,l} + Q_{SP,\,l}
\end{aligned}
\qquad [244]
$$

It is important to note that the above force components must be expressed in units of force (N), and represent the total force applied to the spacecraft.

4.6.2 CubeSail Deployment Control Law

The deployment of the film requires an active control system, implemented by varying the reel motor speed. Although a large number of different control schemes have been developed in the tether community for both deployment and retrieval, the CubeSail design is limited to non-feedback control laws due to inability to accurately sense tension. As a result, the control law adopted here is the so-called exponential law, in which the deployment length is ramped up exponentially during an initial phase until it reaches a maximum value (dictated by the hardware), then remains constant for a prescribed duration, until it is finally reduced (exponentially) back to zero. The exponential law can be summarized as:

$$
\begin{cases}
\dot{l} = \dot{l}_0 + \alpha \cdot l & l_0 < l \le l_1 \\
\dot{l} = c = const. & l_1 < l \le l_2 \\
\dot{l} = \alpha \cdot \left(l_f + l_0 - l \right) & l_2 < l \le l_f
\end{cases}
\qquad [245]
$$

where l_0 is the initial separation distance and is set to 2 cm, l_f is the final length and is equal to 260 m, and c is the constant velocity and due to hardware restriction cannot exceed 10 cm/s. The remaining parameters can be chosen to obtain the desired performance. The parameter $\dot{l}_0$ is the initial separation velocity achieved by appropriate selection of the separation springs, α is the ramp-up and –down

acceleration of the motor, l_1 is the length at which the control law switches from exponential rate to constant rate, and $l_2 = l_f - l_1$.

The accelerations during the three phases are obtained by differentiating the above equations resulting in:

$$\begin{cases} \ddot{l} = \alpha^2 \cdot l & l_0 < l \le l_1 \\ \ddot{l} = 0 & l_1 < l \le l_2 \\ \ddot{l} = -\alpha^2 \cdot l & l_2 < l \le l_f \end{cases} \quad [246]$$

4.6.3 Numerical Simulation Results of Gravity Gradient Deployment

The three second-order differential equations describing the motion of the system were derived in section 4.6 as:

$$\begin{aligned} &\left(\ddot{\psi} + \dot{\omega}_{orb}\right) + 2\left(\dot{\psi} + \omega_{orb}\right) \cdot \left[\frac{\dot{l}}{l} - \dot{\phi} \cdot \tan\left(\phi\right)\right] + \frac{3\mu_{\oplus}}{R_c^3} \cos\left(\psi\right) \cdot \sin\left(\psi\right) = \frac{Q_{\psi}}{M_e \cdot l^2 \cdot \cos^2\left(\phi\right)} \\ &\ddot{\phi} + \frac{2\dot{\phi} \cdot \dot{l}}{l} + \left[\left(\dot{\psi} + \omega_{orb}\right)^2 + \frac{3\mu_{\oplus}}{R_c^3} \cos^2\left(\psi\right)\right] \cdot \cos\left(\phi\right) \cdot \sin\left(\phi\right) = \frac{Q_{\phi}}{M_e \cdot l^2} \\ &\ddot{l} - l \cdot \left(\left(\dot{\psi} + \omega_{orb}\right)^2 \cdot \cos^2\left(\phi\right) + \dot{\phi}^2\right) + \frac{\mu_{\oplus} \cdot l}{R_c^3}\left(1 - 3\cos^2\left(\psi\right) \cdot \cos^2\left(\phi\right)\right) = \frac{Q_l}{M_e} \end{aligned} \quad [247]$$

These equations are first converted to a set of first-order differential equations as follows:

$$\begin{aligned} x_1 &= \psi \quad \dot{x}_1 = x_4 \\ x_2 &= \phi \quad \dot{x}_2 = x_5 \\ x_3 &= l \quad \dot{x}_3 = x_6 \end{aligned}$$

$$\begin{aligned} \dot{x}_4 &= \frac{Q_{\psi}}{M_e \cdot x_3^2 \cdot \cos^2\left(x_2\right)} - 2\left(x_4 + \omega_{orb}\right) \cdot \left[\frac{x_6}{x_3} - x_5 \cdot \tan\left(x_2\right)\right] - \frac{3\mu_{\oplus}}{R_c^3} \cos\left(x_1\right) \cdot \sin\left(x_1\right) \\ \dot{x}_5 &= \frac{Q_{\phi}}{M_e \cdot x_3^2} - \frac{2x_5 \cdot x_6}{x_3} - \left[\left(x_4 + \omega_{orb}\right)^2 + \frac{3\mu_{\oplus}}{R_c^3} \cos^2\left(x_1\right)\right] \cdot \cos\left(x_2\right) \cdot \sin\left(x_2\right) \\ \dot{x}_6 &= \frac{Q_l}{M_e} + x_3 \cdot \left[\left(x_4 + \omega_{orb}\right)^2 \cdot \cos^2\left(x_2\right) + x_5^2\right] - \frac{\mu_{\oplus} \cdot x_3}{R_c^3}\left(1 - 3\cos^2\left(x_1\right) \cdot \cos^2\left(x_2\right)\right) \end{aligned} \quad [248]$$

By using the above-discussed control scheme, the equation for $\ddot{l}$ and the term $\dot{l}$ are replaced by the commanded sail deployment acceleration and rate. It is advantageous to notice that the generalized force along the generalized coordinate l is identically the tension in the film, $Q_l \triangleq T$. It is therefore possible to ensure that the deployment never results in negative tension, which would indicate that there exits slack in the film.

The above equations are integrated using a built-in Matlab solver *ode45*. The previously discussed 'free' parameters are chosen to obtain zero relative separation velocity at full deployment, steady-state configuration reasonably close to the local vertical (both in- and out-of-plane), and such that the separation velocity does not exceed 10 cm/s dictated by the reel motors. Although several combination of acceptable parameters exist, the below results are obtained using the values listed in Table 16 and combine the above-discussed performance and relatively short deployment time of approximately 100 minutes.

Table 16. Parameters used in the gravity gradient deployment simulation.

Parameter	Value
l_0 [m]	0.02
l_1 [m]	18.0
l_2 [m]	242.0
l_f [m]	260.0
$\dot{l}_0$ [m/s]	0.05
α [1/s]	3.695×10^{-3}
c [m/s]	0.05
ψ_0 [deg]	2
ϕ_0 [deg]	-2

The results of the simulation are shown in Figure 111 through Figure 114. The dashed lines on all plots indicate when full deployment has been reached, and occurs

102.65 minutes. The differential equations are propagated for an additional 150 minutes to demonstrate stability of the spacecraft after the reel motors have been stopped.

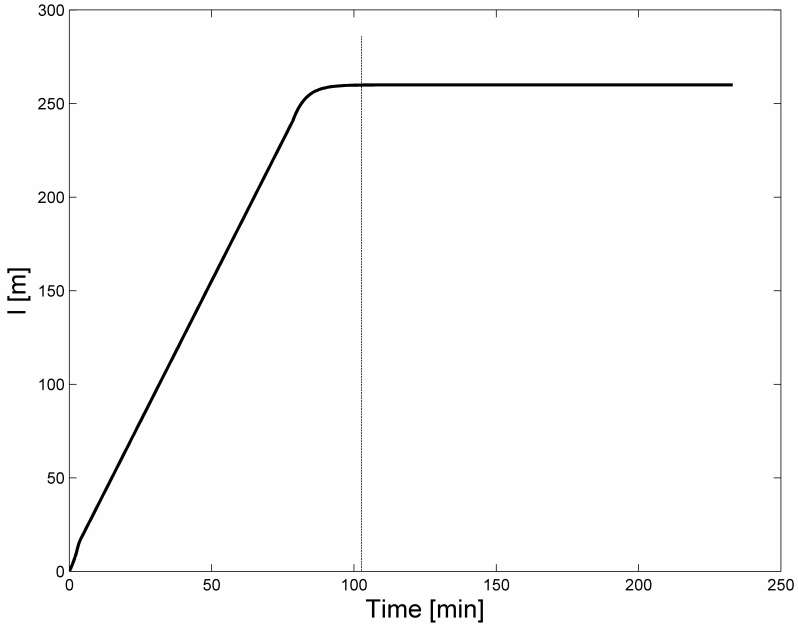

Figure 111. Time history of the sail length during gravity gradient deployment.

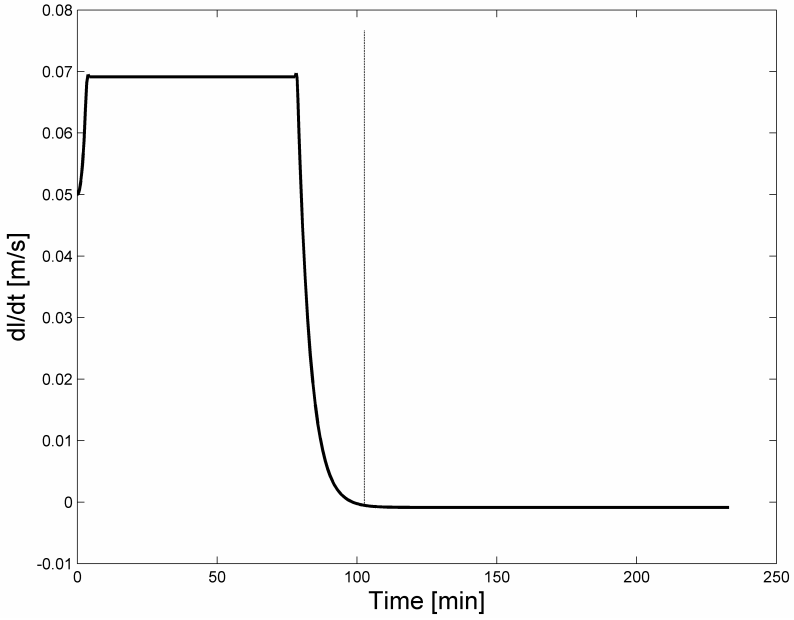

Figure 112. Time history of the rate of the sail length during gravity gradient deployment.

The in- and out-of-plane angles, shown in Figure 113, stabilize to 0º and -1º respectively and have small oscillations of approximately ±0.6º around those values. The tension, shown in Figure 114, reaches a final value of approximately 6.3×10^{-4} N, which corresponds exactly to the steady-state tension calculated in section 4.5.

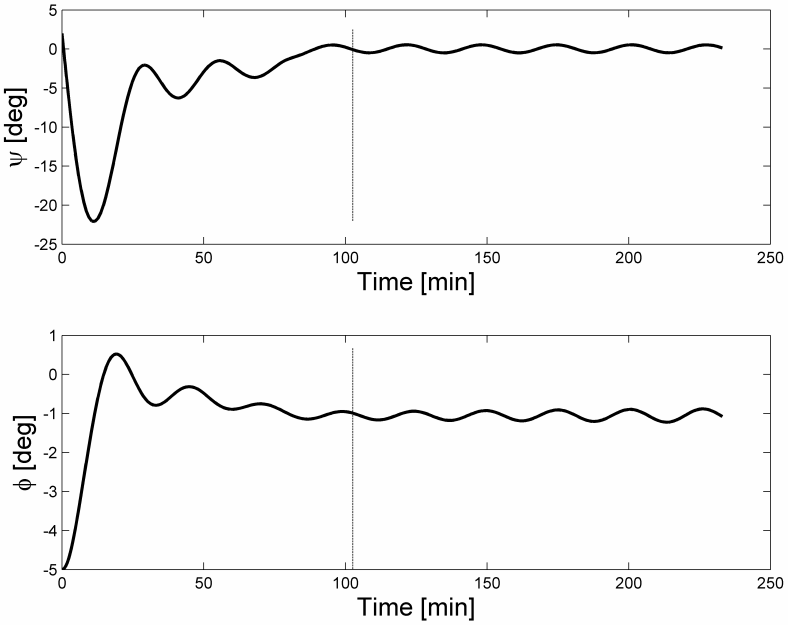

Figure 113. Time history of the in-plane and out-of-plane orbital angles during gravity gradient deployment.

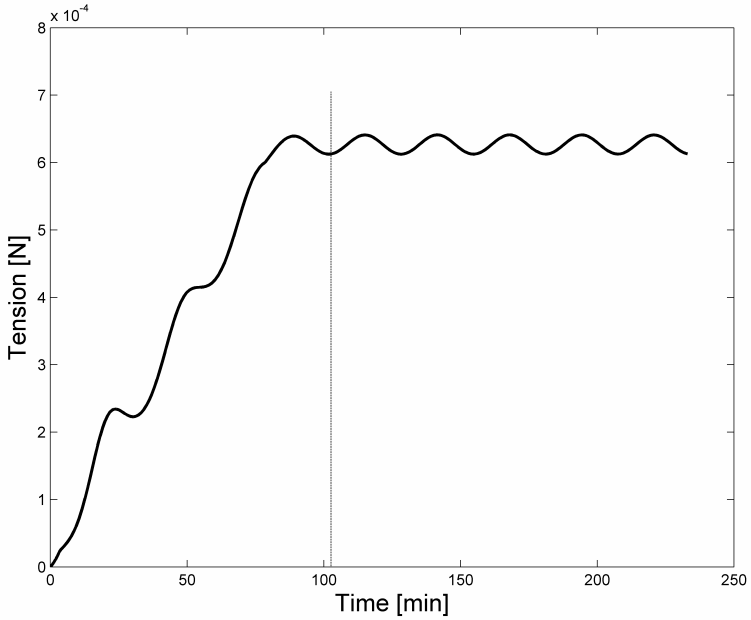

Figure 114. Time history of the tension in the film during gravity gradient deployment.

CHAPTER 5

ORBITAL MANEUVERING

5.1 Gauss Variation of Parameters Equations of Orbital Motion

The variation in the orbital elements due to disturbing accelerations is computed using the Gaussian form of the Variation of Parameters (VOP) equations, which are written as[83]:

$$\begin{aligned}
\frac{da}{dt} &= \frac{2}{n\sqrt{1-e^2}}\left[e\cdot\sin(f)\cdot F_x + \frac{p}{r}F_y\right] \\
\frac{de}{dt} &= \frac{\sqrt{1-e^2}}{n\cdot a}\left[\sin(f)\cdot F_x + \left(\frac{e+\cos(f)}{1+e\cdot\cos(f)}\right)\cdot F_y\right] \\
\frac{di}{dt} &= \frac{r\cdot\cos(u)}{n\cdot a^2\sqrt{1-e^2}}F_z \\
\frac{d\Omega}{dt} &= \frac{r\cdot\sin(u)}{n\cdot a^2\cdot\sin(i)\sqrt{1-e^2}}F_z \\
\frac{d\omega}{dt} &= \frac{\sqrt{1-e^2}}{n\cdot a\cdot e}\left[-\cos(f)\cdot F_x + \sin(f)\left(1+\frac{r}{p}\right)\cdot F_y\right] - \frac{r\cdot\cot(i)\cdot\sin(u)}{h}F_z \\
\frac{dM_0}{dt} &= \frac{1}{n\cdot a^2\cdot e}\left[\left(p\cdot\cos(f)-2\cdot e\cdot r\right)\cdot F_x - \left(p+r\right)\cdot\sin(f)\cdot F_y\right]
\end{aligned} \qquad [249]$$

where a is the semi-major axis, e is the eccentricity, i is the inclination, Ω is the right ascension of the ascending node, ω is the argument of perigee, M is the mean anomaly, and r is the magnitude of the position vector. The additional quantities are defined as follows: u is the argument of latitude, n is the mean motion, p is the semiparameter, and h is the magnitude of the angular momentum. The additional parameters are computed from the following equations:

$$\begin{aligned}
u &= \omega + f \qquad p = a\left(1-e^2\right) \qquad n = \sqrt{\frac{\mu_\oplus}{a^3}} \\
h &= \sqrt{\mu_\oplus\cdot p} \qquad M = M_0 + n\cdot\Delta t
\end{aligned} \qquad [250]$$

The perturbing specific (N/m or units of acceleration) forces resolved in the orbital frame are written as:

$$\vec{F}_{pert} = F_x \hat{X}^{ORB} + F_y \hat{Y}^{ORB} + F_z \hat{Z}^{ORB} \qquad [251]$$

In the general case of elliptic orbits, the Gaussian form of the VOP equations is easily propagated in time and can be used with non-conservative forces such as aerodynamic drag. However, since CubeSail's desired insertion orbit is a circular sun-synchronous terminator orbit, the low values of eccentricity in the differential equation for ω and M cause numerical singularities. To avoid problems with low values of eccentricity, the above equations are rewritten in terms of the so-called *equinoctial variables* by replacing the classical elements e, Ω, i, and ω with P_1, P_2, Q_1, and Q_2. The new set of differential equations becomes:

$$\begin{aligned}
\frac{da}{dt} &= \frac{2a^2}{h}\left[\left(P_2\sin(L) - P_1\cos(L)\right)\cdot F_x + \frac{p}{r}F_y\right] \\
\frac{dP_1}{dt} &= \frac{r}{h}\left\{-\frac{p}{r}\cos(L)\cdot F_x + \left[P_1 + \left(1+\frac{p}{r}\right)\sin(L)\right]\cdot F_y - P_2\left(Q_1\cos(L) - Q_2\sin(L)\right)\cdot F_z\right\} \\
\frac{dP_2}{dt} &= \frac{r}{h}\left\{\frac{p}{r}\sin(L)\cdot F_x + \left[P_2 + \left(1+\frac{p}{r}\right)\cos(L)\right]\cdot F_y + P_1\left(Q_1\cos(L) - Q_2\sin(L)\right)\cdot F_z\right\} \\
\frac{dQ_1}{dt} &= \frac{r}{2h}\left(1+Q_1^2+Q_2^2\right)\sin(L)\cdot F_z \qquad [252] \\
\frac{dQ_2}{dt} &= \frac{r}{2h}\left(1+Q_1^2+Q_2^2\right)\cos(L)\cdot F_z \\
\frac{dl}{dt} &= n - \frac{r}{h}\left\{\left[\frac{a}{a+b}\left(\frac{p}{r}\right)\left(P_1\sin(L) + P_2\cos(L)\right) + \frac{2b}{a}\right]\cdot F_x\right. \\
&\quad \left. + \frac{a}{a+b}\left(1+\frac{p}{r}\right)\left(P_1\cos(L) - P_2\sin(L)\right)\cdot F_y + \left(Q_1\cos(L) - Q_2\sin(L)\cdot F_z\right)\right\}
\end{aligned}$$

where

$$b = a\sqrt{1 - P_1^2 - P_2^2} \qquad h = nab \qquad \frac{p}{r} = 1 + P_1 \sin(L) + P_2 \cos(L)$$
$$\frac{r}{h} = \frac{h}{\mu_\oplus \left(1 + P_1 \sin(L) + P_2 \cos(L)\right)} \qquad [253]$$

The true longitude, L, is computed from the mean longitude, l, by first solving the Kepler's equation:

$$l = K + P_1 \cos(K) - P_2 \sin(K) \qquad [254]$$

for the eccentric longitude, K and then determining r from the following equation:

$$r = a\left(1 - P_1 \sin(K) - P_2 \cos(K)\right) \qquad [255]$$

Finally, L is computed from the following equation:

$$\sin(L) = \frac{a}{r}\left[\left(1 - \frac{a}{a+b} P_2^2\right)\sin(K) + \frac{a}{a+b} P_1 \cdot P_2 \cdot \cos(K) - P_1\right] \qquad [256]$$

with

$$\frac{a}{a+b} = \frac{1}{1 + \sqrt{1 - e^2}} \qquad [257]$$

The classical orbital elements are easily recovered using the following identities:

$$e^2 = P_1^2 + P_2^2 \qquad \tan^2\left(\frac{i}{2}\right) = Q_1^2 + Q_2^2 \qquad \tan(\Omega) = \frac{Q_1}{Q_2}$$
$$\tan(\tilde{\omega}) = \frac{P_1}{P_2} \qquad f = L - \tilde{\omega} \qquad \omega = \tilde{\omega} - \Omega \qquad [258]$$

where $\tilde{\omega} = \Omega + \omega$ and is called the longitude of pericenter.

The differential equations for the equinoctial elements are integrated forward in time starting from the initial conditions given typically in the form of classical elements (obtained from a TLE). To convert these initial classical orbital elements to equinoctial elements, the following equations are used:

$$\begin{aligned}
\tilde{\omega}_0 &= \omega_0 + \Omega_0 \\
P_{1,0} &= e_0 \cdot \sin\left(\tilde{\omega}_0\right) \\
P_{2,0} &= e_0 \cdot \cos\left(\tilde{\omega}_0\right) \\
Q_{1,0} &= \tan\left(\frac{i_0}{2}\right) \cdot \sin\left(\Omega_0\right) \\
Q_{2,0} &= \tan\left(\frac{i_0}{2}\right) \cdot \cos\left(\Omega_0\right) \\
l_0 &= \tilde{\omega}_0 + M_0
\end{aligned} \qquad [259]$$

where M_0 is the initial mean anomaly and is computed by first solving for initial eccentric anomaly, E_0, from

$$\tan\left(\frac{f_0}{2}\right) = \sqrt{\frac{1+e_0}{1-e_0}} \tan\left(\frac{E_0}{2}\right) \qquad [260]$$

and then noting that

$$M_0 = E_0 - e_0 \cdot \sin\left(E_0\right) \qquad [261]$$

5.2 Specific Forces During Orbital Maneuvering

The components of the perturbing accelerations come from the aerodynamic drag, solar radiation pressure, and Earth oblateness terms on the sail and the tip satellites. The total acceleration depends on (among other variables such as orbital position) on the sail shape, which, in turn is dependent on the force. The problem is approach as shown in Figure 115 (using classical flow chart symbols) by first computing the equilibrium sail shape as in Section 4.5, then finding the total perturbing specific force exerted on the spacecraft, and finally integrating the differential equations of orbital elements. Due to computational complexity of solving the nested ODEs, the equilibrium sail shape is not recomputed at every time step of the VOP integrator, but

rather it is held constant until the integrator reaches a prescribed critical time t_{cr}, which is described in more detail in a subsequent section.

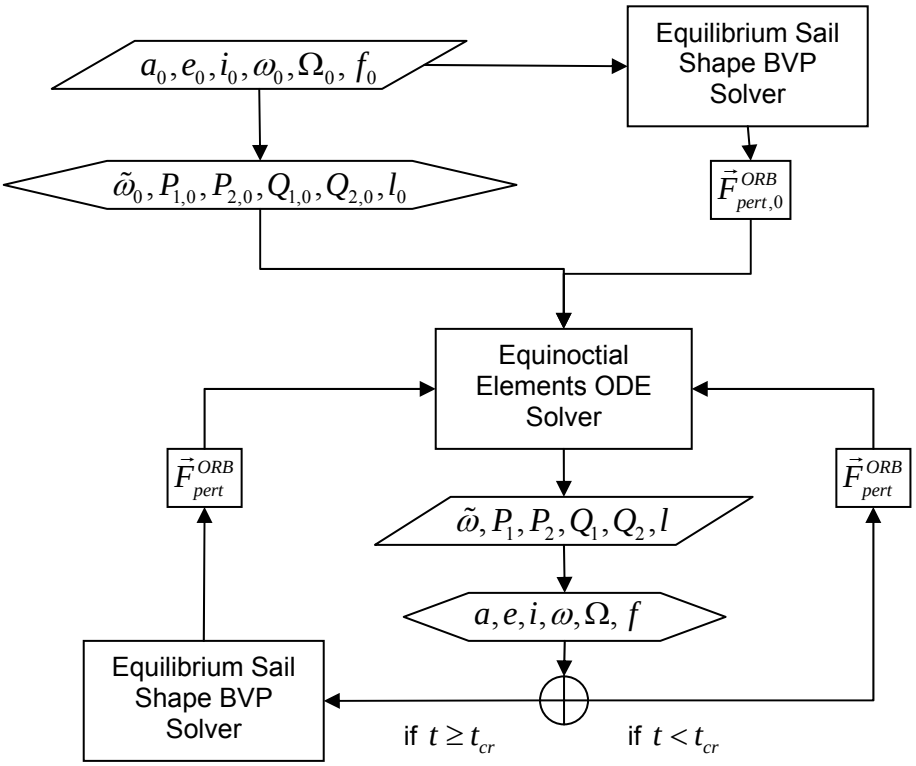

Figure 115. Orbital maneuvering flow diagram.

The force due to solar radiation pressure on a sail element in the orbital frame was derived in Section 4.5 as:

$$d\vec{f}_{SP}^{ORB} = A_{Sail}^{ORB} \begin{bmatrix} 0 \\ -sign\left(r_{\odot,y}^{Sail}\right) \cdot A \cdot D \cdot \cos\left(\alpha^{SP}\right) \cdot \sin\left(\alpha^{SP}\right) \cdot ds \\ -sign\left(r_{\odot,z}^{Sail}\right) \cdot A \cdot \cos\left(\alpha^{SP}\right) \cdot \left[B \cdot \cos\left(\alpha^{SP}\right) + C\right] \cdot ds \end{bmatrix} \quad [262]$$

where

$$A_{ORB}^{Sail} = \begin{bmatrix} \mathrm{c}(\phi)\mathrm{c}(\psi) & \mathrm{c}\left(\theta^{Sat} \cdot \left(1 - \frac{2 \cdot s}{l_{sail}}\right)\right)\mathrm{s}(\psi) + \mathrm{s}\left(\theta^{Sat} \cdot \left(1 - \frac{2 \cdot s}{l_{sail}}\right)\right)\mathrm{s}(\phi)\mathrm{c}(\psi) & \mathrm{s}\left(\theta^{Sat} \cdot \left(1 - \frac{2 \cdot s}{l_{sail}}\right)\right)\mathrm{s}(\psi) - \mathrm{c}\left(\theta^{Sat} \cdot \left(1 - \frac{2 \cdot s}{l_{sail}}\right)\right)\mathrm{s}(\phi)\mathrm{c}(\psi) \\ -\mathrm{c}(\phi)\mathrm{s}(\psi) & \mathrm{c}\left(\theta^{Sat} \cdot \left(1 - \frac{2 \cdot s}{l_{sail}}\right)\right)\mathrm{c}(\psi) - \mathrm{s}\left(\theta^{Sat} \cdot \left(1 - \frac{2 \cdot s}{l_{sail}}\right)\right)\mathrm{s}(\phi)\mathrm{s}(\psi) & \mathrm{s}\left(\theta^{Sat} \cdot \left(1 - \frac{2 \cdot s}{l_{sail}}\right)\right)\mathrm{c}(\psi) + \mathrm{c}\left(\theta^{Sat} \cdot \left(1 - \frac{2 \cdot s}{l_{sail}}\right)\right)\mathrm{s}(\phi)\mathrm{s}(\psi) \\ \mathrm{s}(\phi) & -\mathrm{s}\left(\theta^{Sat} \cdot \left(1 - \frac{2 \cdot s}{l_{sail}}\right)\right)\mathrm{c}(\phi) & \mathrm{c}\left(\theta^{Sat} \cdot \left(1 - \frac{2 \cdot s}{l_{sail}}\right)\right)\mathrm{c}(\phi) \end{bmatrix} \quad [263]$$

It is important to recognize that the above transformation matrix and associated force due to solar radiation pressure is computed for a specific sail element that is deformed according to set of roll-pitch-yaw angles (ϕ,θ,ψ) obtained from the film shape at every length along the sail s. As a result, the total specific force due to solar radiation pressure on the entire sail and excluding the tip satellites is written as:

$$\vec{F}_{SP,\,\text{sail}}^{ORB} = \frac{1}{m_{tot}} \sum_{k=1}^{N} A_{Sail}^{ORB}\left(\theta_k,\phi_k,\psi_k\right) \begin{bmatrix} 0 \\ -sign\left(r_{\odot,y}^{Sail}\right)\cdot A\cdot D\cdot\cos\left(\alpha_k^{SP}\right)\cdot\sin\left(\alpha_k^{SP}\right)\cdot ds \\ -sign\left(r_{\odot,y}^{Sail}\right)\cdot A\cdot\cos\left(\alpha_k^{SP}\right)\cdot\left[B\cdot\cos\left(\alpha_k^{SP}\right)+C\right]\cdot ds \end{bmatrix} \quad [264]$$

where N is the number of elements the sail has been divided into and subscript k has been added to indicate dependence of all variables on the attitude of each of the sail elements.

Similarly, the total specific force due to aerodynamic drag on the entire sail and excluding the tip satellites is written as:

$$\vec{F}_{AD,\,\text{sail}}^{ORB} = \frac{1}{m_{tot}} \sum_{k=1}^{N} A_{Sail}^{ORB}\left(\theta_k,\phi_k,\psi_k\right) \begin{bmatrix} 0 \\ sign\left(V_{R,y}^{Sail}\right)\cdot\rho_{atm}\cdot V_R^2\cdot\cos\left(\alpha_k^{AD}\right)\cdot\sin\left(\alpha_k^{AD}\right)\cdot\sigma_{t,k}\cdot dA \\ sign\left(V_{R,y}^{Sail}\right)\cdot\rho_{atm}\cdot V_R^2\cdot\cos\left(\alpha_k^{AD}\right)\cdot\left[\left(\frac{V_b}{V_R}-\cos\left(\alpha_k^{AD}\right)\right)\cdot\sigma_{n,k}+2\cos\left(\alpha_k^{AD}\right)\right]\cdot dA \end{bmatrix} \quad [265]$$

The effects of the solar radiation pressure on the tips satellites are small (due to relatively small surface area and low reflectivity coefficient of the solar cells) and are not taken into account.

In order to compute the specific force due to aerodynamic drag on each of the tip satellites, it is first necessary to compute the projections of the two long sides and one top side of the spacecraft onto the velocity vectors (here assumed to be $\hat{Y}^{ORB}$ axis) as:

$$A_{cs}^{SATU} = w_{sat} \cdot l_{sat} \cdot \left(A_{ORB}^{SAT}\left(\bar{\theta}_0, \phi_0, \psi_0\right) \cdot \begin{bmatrix} 0 \\ 0 \\ 1 \end{bmatrix} \right)^T \cdot \begin{bmatrix} 0 \\ 1 \\ 0 \end{bmatrix} + w_{sat} \cdot l_{sat} \cdot \left(A_{ORB}^{SAT}\left(\bar{\theta}_0, \phi_0, \psi_0\right) \cdot \begin{bmatrix} 0 \\ 1 \\ 0 \end{bmatrix} \right)^T \cdot \begin{bmatrix} 0 \\ 1 \\ 0 \end{bmatrix}$$
$$+ w_{sat} \cdot w_{sat} \cdot \left(A_{ORB}^{SAT}\left(\bar{\theta}_0, \phi_0, \psi_0\right) \cdot \begin{bmatrix} 1 \\ 0 \\ 0 \end{bmatrix} \right)^T \cdot \begin{bmatrix} 0 \\ 1 \\ 0 \end{bmatrix} \quad [266]$$

$$A_{cs}^{SATL} = w_{sat} \cdot l_{sat} \cdot \left(A_{ORB}^{SAT}\left(\bar{\theta}_f, \phi_f, \psi_f\right) \cdot \begin{bmatrix} 0 \\ 0 \\ 1 \end{bmatrix} \right)^T \cdot \begin{bmatrix} 0 \\ 1 \\ 0 \end{bmatrix} + w_{sat} \cdot l_{sat} \cdot \left(A_{ORB}^{SAT}\left(\bar{\theta}_f, \phi_f, \psi_f\right) \cdot \begin{bmatrix} 0 \\ 1 \\ 0 \end{bmatrix} \right)^T \cdot \begin{bmatrix} 0 \\ 1 \\ 0 \end{bmatrix}$$
$$+ w_{sat} \cdot w_{sat} \cdot \left(A_{ORB}^{SAT}\left(\bar{\theta}_f, \phi_f, \psi_f\right) \cdot \begin{bmatrix} 1 \\ 0 \\ 0 \end{bmatrix} \right)^T \cdot \begin{bmatrix} 0 \\ 1 \\ 0 \end{bmatrix} \quad [267]$$

where $\left(\theta_0, \phi_0, \psi_0\right)$ and $\left(\theta_f, \phi_f, \psi_f\right)$ are the initial and final attitude Euler angles provided from the equilibrium sail shape calculation. In addition, the complement of the pitch angle ($\bar{\theta} = 90^\circ - \theta$) is used to correct for the fact that the vector area uses the angle between surface normal, while the pitch angle is defined from the surface tangential as shown previously in Figure 74. The specific force components on the tip satellites due to aerodynamic drag, including the effects of rotation of the upper atmosphere, can be written as[96] :

$$\vec{F}_{AD,\text{ tip sat}}^{ORB} = -\frac{\rho_{atm} \cdot C_D}{2m_{tot}} \cdot \begin{bmatrix} 0 \\ \cos(i) \cdot \left(a_{SATU}^2 \cdot n_{SATU}^2 \cdot A_{cs}^{SATU} \cdot \left(1 - \frac{2\omega_\oplus}{n_{SATU}}\right) + a_{SATL}^2 \cdot n_{SATL}^2 \cdot A_{cs}^{SATL} \cdot \left(1 - \frac{2\omega_\oplus}{n_{SATL}}\right) \right) \\ \sin(i) \cdot \cos(u) \cdot \omega_\oplus \cdot \left(a_{SATU}^2 \cdot n_{SATU} \cdot A_{cs}^{SATU} + a_{SATL}^2 \cdot n_{SATL} \cdot A_{cs}^{SATL} \right) \end{bmatrix} \quad [268]$$

As discussed previously, the gravitational field of earth is not spherically symmetric, causing small perturbations to the Keplerian orbit. The most significant of

these perturbations is the first term in the latitude-dependent expansion of the field, or the so-called J_2 effect. The perturbing acceleration in the ORB frame can be written as:

$$\vec{F}_{obl}^{ORB} = -\frac{3\mu_{\oplus} \cdot J_2 \cdot R_{\oplus}^2}{R^4} \begin{bmatrix} \frac{1}{2}\left(1 - 3\sin^2(i) \cdot \sin^2(u)\right) \\ \sin^2(i) \cdot \sin(u) \cdot \cos(u) \\ \sin(i) \cdot \sin(u) \cdot \cos(i) \end{bmatrix} \quad [269]$$

The total perturbation on the spacecraft is therefore:

$$\vec{F}_{pert}^{ORB} = \vec{F}_{SP,\,\text{sail}}^{ORB} + \vec{F}_{AD,\,\text{sail}}^{ORB} + \vec{F}_{AD,\,\text{tip sat}}^{ORB} + \vec{F}_{obl}^{ORB} \quad [270]$$

5.3 Orbital Maneuvering Simulation Results

5.3.1 Comparison of Results with Edelbaum Orbital Transfer Analysis

The first orbital maneuvering simulation aims to compare results obtained using the Edelbaum analysis with the more accurate method described in the above section. Although the above derivation includes effects of aerodynamic drag (both on the sail and the tip satellites) as well as effects of Earth oblateness, these effects are neglected in this first simulation in order to make the result comparable. The simulation does, however, compute the steady-state deformed shape of the sail and applies the previously-described non-ideal sail effects. The equinoctial elements are propagated forward in time until the desired increase in altitude of 100 km is achieved.

Figure 116 shows the results of this run and demonstrate a transfer time of approximately 24.3 days. The transfer time computed using the Edelbaum analysis for the 100 km altitude increase was approximately 22.6 days. The discrepancy between the two results is small and it is attributed to the fact that the preliminary analysis assumed an undeformed ideal sail. Losses due to non-ideal sail effects as well as slight

deformation of the film contribute to the loss of thrust acceleration and, in turn, longer transfer times.

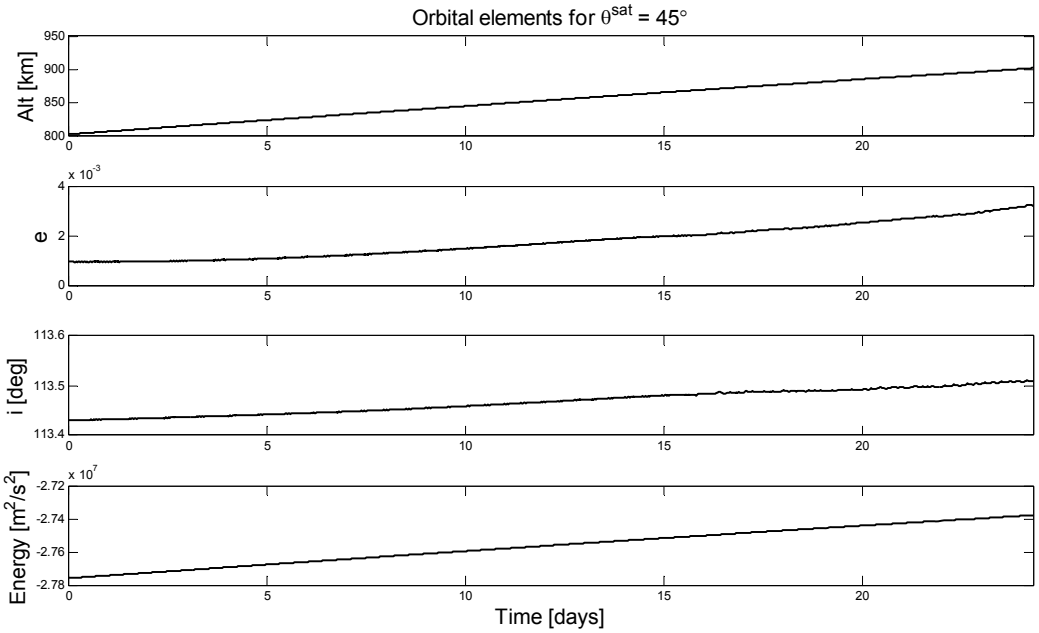

Figure 116. Time history of orbital elements for a 100 km altitude raise. Solar radiation pressure effects are included, however effects of aerodynamic drag and Earth oblateness are neglected.

5.3.2 Orbital Maneuvers Neglecting Earth Oblateness

It is beneficial to present limited number of results that exclude the effects of Earth oblateness on the spacecraft motion ($\vec{F}_{obl}^{ORB} = 0$). In order to retain the ability to compare the increased fidelity model to previous results, the following simulation uses identical starting ephemeris and pitch angle. Two separate simulations are run in order to illustrate the importance of the launch date within the solar cycle. As was shown in Section 3.4.1, the atmospheric density can vary by as much as two orders of magnitude between solar minima and solar maxima. The first simulation is run assuming the spacecraft is launched during a solar minimum and has an initial atmospheric density at 800 km of approximately 3.3×10^{-15} kg/m^3 (the exact value depends on latitude, longitude, time of the day, and actual solar flux). The second simulation uses the exact same

initial ephemeris, however, the date is set to match period of solar maximum, resulting in the approximate initial atmospheric density of 1.3×10^{-13} kg/m^3.

The equinoctial elements are propagated until a 100 km increase in altitude is achieved. The results from the first simulation (solar minimum) are shown in Figure 117 and yield a transfer time of 24.78 days. Interestingly, the transfer time is remarkably close to the transfer time computed without the effects of aerodynamic drag. This result is explained by looking at the force components in the y direction expressed in the orbital frame, $\hat{Y}^{ORB}$, for each of the forces. For example, the components at the initial time during a solar minimum are $F_{SP,y}^{ORB} = 8.25 \times 10^{-5} N$ and $F_{AD,y}^{ORB} = -1.36 \times 10^{-6} N$, demonstrating that the aerodynamic drag force is approximately only 1.6% of the solar radiation pressure and effectively has no impact on the transfer time. Additionally, the aerodynamic drag force, which in the present orbital geometry acts opposite the solar radiation pressure force, actually flattens out (decreases the billowing of) the film and thus slightly increases the net force.

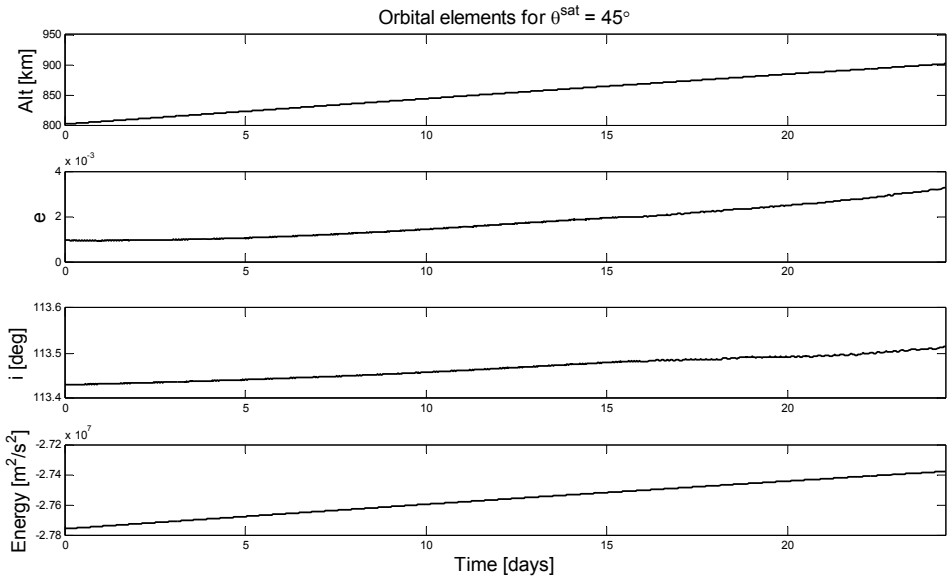

Figure 117. Time histories of orbital elements for a 100 km altitude change. Effects of aerodynamic drag during solar minimum and solar radiation pressure are included, however Earth oblateness effects are neglected.

The results for the 100 km altitude change maneuver during solar maximum are shown in Figure 118 and yield a transfer time of 54.24 days. The respective force components of the solar radiation pressure and aerodynamic drag expressed in the orbital are $F_{SP,y}^{ORB} = 8.28 \times 10^{-5} N$ and $F_{AD,y}^{ORB} = -6.90 \times 10^{-5} N$. The solar radiation pressure force is indeed larger than the aerodynamic drag force, however, the relative closeness in magnitude during periods of solar maxima of these two forces results in long transfer times.

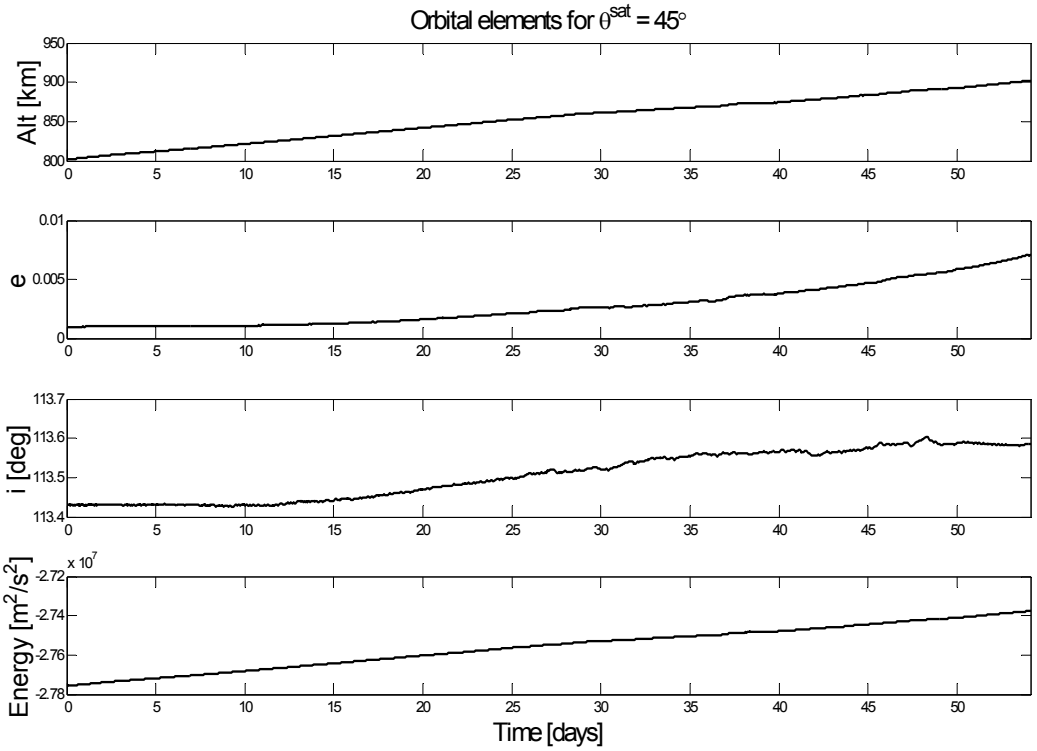

Figure 118. Time histories of orbital elements for a 100 km altitude change. Effects of aerodynamic drag during solar maximum and solar radiation pressure are included, however Earth oblateness effects are neglected.

5.3.3 Orbital Maneuvers Including Earth Oblateness

The previous section neglected effects of Earth oblateness in order to isolate the effects of aerodynamic drag during solar minimum and solar maximum. The results showed that the launch date within the solar cycle has a significant effect on the transfer

time, but that an 800 km orbit is sufficiently high to overcome aerodynamic drag effects and perform an orbit raising maneuver. This section repeats the above integration of the equinoctial elements, however it includes effects of Earth oblateness (J2 only) on the spacecraft motion.

The initial attempts at propagating the equinoctial element starting with the same initial ephemeris and pitch angle resulted in excessively long run times and minimal altitude increase. A 10-day time history of the orbital elements for a 0º pitch configuration is shown in Figure 119 and demonstrates an approximate 41 km altitude decrease.

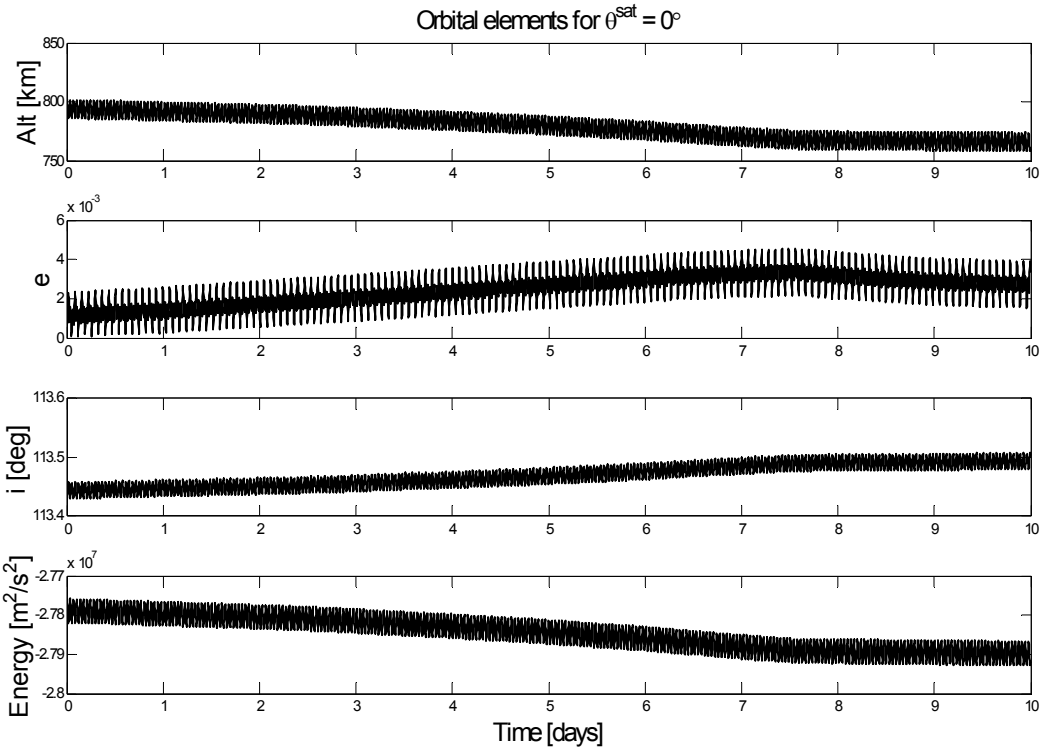

Figure 119. 10-day time histories of orbital elements. Effects of aerodynamic drag during solar minimum, solar radiation pressure, and Earth oblateness are included.

Upon closer inspection, this behavior is caused by relatively large magnitude of the perturbation force due to Earth's oblateness. The oblateness equation was given previously in section 5.2 and is repeated below for convenience.

$$\vec{F}_{obl}^{ORB} = -\frac{3\mu_{\oplus} \cdot J_2 \cdot R_{\oplus}^2}{R^4} \begin{bmatrix} \frac{1}{2}\left(1-3\sin^2(i)\cdot\sin^2(u)\right) \\ \sin^2(i)\cdot\sin(u)\cdot\cos(u) \\ \sin(i)\cdot\sin(u)\cdot\cos(i) \end{bmatrix} \quad [271]$$

For the suggested orbit with an initial altitude of 800 km, the pre-multiplier value is $3\mu_{\oplus} \cdot J_2 \cdot R_{\oplus}^2 / R^4 = 0.0199$. The maximum value that each of x-, y-, and z-component can achieve is 0.5, which can occurs at least once every orbit when $u = \omega + f = 45^\circ \text{ or } 215^\circ$ (the actual value depends on the inclination). As a result, the maximum value of the force due to Earth oblateness is approximately 0.0099, or two orders of magnitude greater than the force of solar radiation pressure on the entire film (given previously as $F_{SP,y}^{ORB} = 8.25\times10^{-5} N$ for $\theta^{Sat} = 45^\circ$).

Although it is possible to try to affect specific elements by varying the pitch profile along the orbit, the effects remain very small due to the limitation of thrust generated by a 20 m^2 sail. As an example of this approach, we inspect the Gauss Variation of Parameter equation for the change in inclination:

$$\frac{di}{dt} = \frac{r\cdot\cos(u)}{n\cdot a^2\sqrt{1-e^2}} F_z \quad [272]$$

During nominal operation, the $\hat{Z}^{ORB}$-component (directed out of the orbital plane) of the force is mainly dependent on the solar radiation pressure and the oblateness terms. The $\hat{Z}^{ORB}$-component of the solar radiation pressure is always positive, regardless of the pitch angle ($F_{SP,z}^{ORB} > 0$). The $\hat{Z}^{ORB}$-component of the oblateness term depends on inclination and the argument of latitude, u according to $-\sin(i)\cdot\sin(u)\cdot\cos(i)$. For the starting inclination of approximately 113º, $\sin(i)\cos(i) < 0$. The resultant change in

inclination is therefore dependent on the sign of the quantity: $\cos(u)\sin(u)$, which is positive for $0 \le u \le 90^\circ$ or $180^\circ \le u \le 270^\circ$ and is negative for $90^\circ < u < 180^\circ$ or $270^\circ < u < 360^\circ$. Although it is not possible to prevent the change of sign in the di/dt equation, it is possible to, for example, decrease the magnitude of the force by appropriate pitching when $\cos(u)\sin(u)$ is negative and maximize the magnitude of the force when $\cos(u)\sin(u)$ is positive. The net result is a net increase in the inclination. However, since the solar radiation pressure force is approximately two orders of magnitude less than the J2 perturbative force, the effect is very small.

Similar analysis can be performed for other VOP equations, although equivalently simple results are harder to obtain due to constantly changing geometry of the sun-incidence and aerodynamic drag-incidence angles, sail shape, etc. and dependence of VOP equations on more than one force component (typically F_x^{ORB} and F_y^{ORB}). Regardless, of the sophistication of the pitching scheme, the underlying difficulty resides in comparably low thrust generated by the sail as compared to perturbative acceleration of the Earth's oblate gravity field.

5.4 De-Orbiting Maneuver

At the end of the mission, the spacecraft is oriented such that maximum surface area is presented into the velocity direction ($\theta^{Sat} = 90^\circ$) and results in shortest orbital lifetime. In addition, if the incoming solar radiation pressure is not exactly perpendicular to the orbital plane (either due to orbital maneuvers or initial orbit insertion errors), it is possible to pitch the sail such that the $Y_{SP,y}^{ORB}$ is negative, further accelerating the deorbit maneuver. Figure 120 shows the 10-day time histories of a deorbit maneuver that

include the effect of solar radiation pressure (during a solar minimum), aerodynamic drag, and Earth oblateness. By pitching the spacecraft at 90º, the altitude loss in 10 days was approximately 79.3 km.

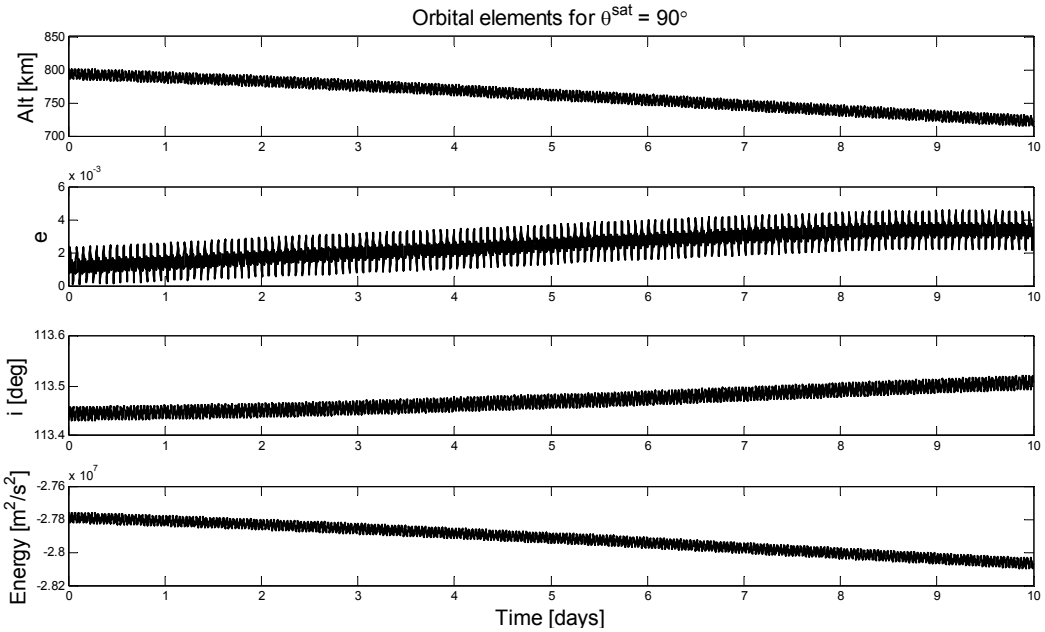

Figure 120. 10-day time histories of orbital elements for a deorbit burn. Effects of aerodynamic drag during solar minimum, solar radiation pressure, and Earth oblateness are included.

CHAPTER 6

FUTURE WORK

6.1 Re-optimization of Parameters

Following the spacecraft design freeze and confirmation of orbit insertion parameters, the majority of the above-presented analysis must be repeated. Fortunately, the derivation and methodology will remain unchanged, and only the already-existing code must be re-run with updated values. The re-optimization includes: $\mathbf{Q}$ and $\mathbf{R}$ matrices for the LQR controller during initial spacecraft stabilization, initial separation velocity required for deployment along the local vertical that does not exceed the reel motor specifications, prediction of disturbance torques and reaction wheel energy usage, orbital maneuvering scenarios and power consumption, and orbital lifetime predictions. Although this dissertation does not include specific software filenames or description, a supplementary document titled 'CubeSail Operational Guide for Attitude Control and Dynamics' provides those details.

6.2 Real Time Solar Flux Updates to NRLMSISE-00 Model

As discussed in section 4.3.3, the NRLMSISE-00 model requires daily updates of the solar flux and magnetic coefficients. The solar flux data must be averaged over 81 days in order to obtain the F107A input values and additional solar flux values from the previous days must be provided as the F107 input. The magnetic field coefficients *K*, *Kp*, and *Ap* are also needed and should be downloaded within the nearest 3 hours of the desired time. This process of downloading the data from the ftp sites (given in section 4.3.3), taking the necessary averages, and interfacing the data with the

NRLMSISE-00 function calls throughout the existing code should be automated prior to launch.

6.3 Prevention of Sail Twisting During Nominal Operations

A critical requirement necessary for mission success is prevention of twisting of the film by more than 45º at each satellite (in the opposing direction). This necessitates that the attitude determination sensors and algorithms be run continuously for the duration of the mission and any excessive deviation be corrected. The constant lighting conditions of the sun synchronous orbit simplify this task, but the frequency of the sensor sampling remains to be determined and implemented in the code. Care should be taken to check the attitude more frequently during increased solar activity and anomalous solar events.

6.4 Earth Albedo and Infrared Radiation Effects

Two additional sources of perturbations that have not been accounted for in the above analysis is the solar flux reflected from the Earth, referred to as Earth albedo, and the infrared radiation (IR) that is reemitted from the surface. Earth albedo radiation is approximately 30 ± 5% of direct solar flux (1367 W/m^2, mean) and the infrared radiation is approximately 237 ± 21 W/m^2.[97] Knocke et al. used a spherical harmonic expansion (up to second degree) to represent the albedo and IR emission as a function of latitude as:[98]

$$\begin{aligned} p_{albedo} &= 0.34 + \left[0.1 \cdot \cos\left(\omega JD - t_0\right)\right] \cdot \cos\left(\phi\right) + 0.29 \cdot \sin\left(\phi\right) \\ p_{IR\ \text{emission}} &= 0.68 + \left[-0.07 \cdot \cos\left(\omega JD - t_0\right)\right] \cdot \cos\left(\phi\right) - 0.18 \cdot \sin\left(\phi\right) \end{aligned} \quad [273]$$

where the base epoch, t_0, is December 22, 1981 (JD = 2,444,960.5) and ω establishes periodicity and is equal to $2\pi / 365.25$. The above equations give the solar radiation

pressure (either reflected or re-emitted) in the units of force per unit area, N/m^2. It should be noted that the longitude-dependent terms are significantly smaller and are not included in the formulation. The complication in evaluating the total acceleration, or heating in the case of calculating thermal equilibrium, arises when the above equations must be integrated over the entire Earth area visible by the satellite. This is typically done by dividing the visible area into segments which have equal projected areas, finding the vectors from the spacecraft to the center of each segment, and summing all contributions from the albedo and IR emissions.

6.5 Micrometeorite Impact

The low Earth orbit environment is becoming increasingly populated with both active and inactive payloads, debris which includes final stages of rockets, satellite deployment mechanisms, upper stage booster platforms, satellite fragmentation, dead satellites, as well as meteoroids. Table 17 illustrates the number of man-made orbiting and reentered payloads and debris starting with the first launch in 1957 and extending up to 2007[83].

Table 17. Orbiting and decayed satellites (1957—2007).[83]

	Orbiting			Reentered		
Country	**Payloads**	**Debris**	**Total**	**Payloads**	**Debris**	**Total**
Former Soviet Union	1408	2899	4307	2424	10561	12985
United States	1072	3119	4191	840	4133	4973
People's Republic of China	61	925	986	51	344	395
France	44	315	359	8	652	660
Japan	106	69	175	17	147	164
European Space Agency	42	35	77	6	14	20
Other	491	134	625	64	329	393

There exists a significant debate as to the actual number of hazardous objects in LEO due to limitation of ground radar on the detectable debris size of approximately 10 cm. The U.S. Space Command compiles a catalog of trackable debris using the Space Surveillance Network (SSN), which was initially developed to track large objects, and

was never envisioned to detect space debris. Recent campaigns with more sensitive radars confirmed that there is a significantly larger population of the 1 cm size objects than is cataloged.[97] In addition, object as small as 1 mm, which are believed to be the most populous in LEO, can cause significant damage to orbiting spacecraft. The high damage potential, even from small particles, results from typical impact velocities of 10 km/s for man-made debris and impact velocities of 19-20 km/s for meteoroids[§]. Knowledge of the particle population of millimeter- and micron-sized particles is typically gained from "dedicated in situ experiments or through the analysis of material that has been returned from space."[99]

A detailed analysis predicting probability of impact by space debris on the CubeSail spacecraft must be performed prior to launch. A useful and widely available debris model is the European Space Agency's Meteoroid and Space Debris Terrestrial Environment Reference (MASTER). A brief description of the model is given below:[100]

> MASTER (Meteoroid and Space Debris Terrestrial Environment Reference) is a software that can be used to analyze space debris flux and spatial densities. The following sources of debris are considered: launch and mission-related objects, explosion and collision fragments, solid rocket motor slag and dust, NaK droplets, surface degradation products, ejecta, and meteoroids. MASTER can deliver flux and spatial density analysis for all epochs between 1957 and 2055. For all historic epochs (up to the MASTER-2005 reference epoch - May 1st, 2005), the lower size threshold is one micron. The analysis of the future debris environment is possible based on three different future scenarios (business as usual, intermediate mitigation, full mitigation). The lower size threshold for future analysis is 1 millimetre. The MASTER-2005 software is delivered on a DVD, together with extensive documentation of the underlying models. The software is available for Windows, Linux, Solaris, and Apple.

Two similar models have been developed by NASA Johnson Spaceflight Center called ORDEM200 and LEGEND and provide debris characteristic including number, type, size distribution, spatial density distribution, velocity distribution, flux, etc. for orbits

[§] Leonid meteoroids impact velocity can be as high as 70 km/s due to their retrograde orbit which causes the collisions with Earth in nearly head-on fashion.

between 200 and 50,000 km. The minimum size threshold in the LEGEND model is 1 mm.[101]

6.6 CubeSat Bus Development

As of this writing, the IlliniSat-2 design which serves as the backbone of the CubeSail spacecraft requires significant advancement. The command and data handling (C&DH) circuit board has not yet been designed and requires significant investment of time to be developed, integrated, and tested with the existing system. The power board has been under development and considerable advances have been made in the last several months. It is estimated that the design of the power board is approximately 60% complete, however it must still undergo hardware-in-the-loop testing after fabrication.

The radio and the terminal node controller (TNC) initially selected as primary method of communication has been discontinued by the manufacturer. Recently, the decision was made to switch to a new model, which requires additional integration and testing with the existing IlliniSat-2 architecture.

Components of the IlliniSat-2's unique side panel assembly that include the solar cells, carbon-fiber backing, flex cable containing power system's connectors and circuitry, radiation shielding, and torque coils have undergone individual testing. They must, however, be assembled and undergo thermal, vacuum, and vibrational testing before launch.

Software is estimated to be approximately 50% completed and is typically the most time-intensive system to interface with existing hardware. In addition, the bus and battery thermal output must be modeled during nominal operations in the sun-

synchronous terminator orbit in order to determine spacecraft thermal equilibrium and determine the size and location of heat sinks or insulators.

Lastly, the complete bus must undergo comprehensive thermal, vacuum, vibrational, and operational testing to ensure mission success. Although the existing testing facilities and experience exists among the University of Illinois CubeSat team, any redesigns could potentially lead to lengthy delays.

6.7 CubeSail Payload Development

The development of the payload hardware is significantly farther along than the CubeSat bus design and is on schedule for the spring 2011 delivery date. The remaining tasks include performing the 'rail experiment' aimed at testing the separation release unit and selection of separation spring locations. The majority of the hardware for the rail experiment has been manufactured and assembled, and limited testing without the film material is currently in progress. After satisfactory reliability of the SRU is achieved and the separation is ensured to occur linearly, the same behavior must be verified in vacuum at the expected operating temperature. The thermo-vacuum tests will ensure that any thermal contraction or expansion of the SRU parts will not stress the motor and prevent separation. In addition, the mechanical team must select lubricants, if any, that will be used to ease the separation, but which do not contaminate the film material and are space-rated.

In addition, the SRU control circuit board must be re-designed and tested prior to launch. The current board, used primarily for the 'rail experiment,' relies on a wireless transmission to a USB-connected transceiver and does not fit the IlliniSat-2 bus

specifications. The interface software between the IlliniSat-2 C&DH protocol and the SRU controller board must also be developed.

The camera control circuit board must be designed and placed either in the payload section or along the IlliniSat-2's service stack. Placing the camera control board in the payload section of both satellites posses volumetric difficulties due to incorporation of the reaction wheels (one in both tip satellites) and SRU motor (on the lower tip satellite). It might be feasible to combine the SRU and camera controller circuitry on a single board to reduce volume and simplify interface to the bus.

Lastly, the CubeSail's unique two-satellite design must undergo vibrational testing to ensure that SRU sustains no damage during launch. The Illinois CubeSat program has performed 2U vibrational tests, however, two rigidly-coupled 1.5U satellites remain untested at this point.

6.8 Communication Infrastructure

The CubeSail mission will primarily rely on the University of Illinois CubeSat ground station located in Everitt Laboratory. Although the station is fully operational and primary responsibility for the communication architecture is placed on the IlliniSat-2 team, the interface protocol between the payload and bus operations has not been established. Items such as format of the command inputs to the torquers and the motors (two operating the reels and one operating the SRU), camera operations including storage, compression, and download of captured images must all be finalized.

In addition, the current radio/TNC architecture has not been designed for intra-satellite communication. In principle, since the two radios operate at different frequencies and the antennas are largely omni-directional, communication between the

satellites is possible. However, at this time the majority of the CubeSail operations are scheduled from the ground and can be sent independently to both spacecraft and intra-satellite communication is not required.

6.9 Spacecraft Charging Effects

The effects of spacecraft charging has been widely investigated in the tether community, both as a source of potentially dangerous charging/discharging as well as means of space propulsion—the so-called electrodynamic tether. The effect arises by flying a long, conductive wire (or aluminum-coated sailing film) through a magnetic field of Earth, accumulating electric charge. If the end of a tether is bare, it can contact the charged ionosphere and generate potentially high currents through the wire/film. If the charge is not equalized, for example by using an electron emitter, arcing can occur and damage electronic components.

The specific analysis of this behavior on the CubeSail spacecraft is beyond the scope of this dissertation, however it must be addressed before the launch.

CHAPTER 7

CONCLUSIONS

The presented design of the CubeSail spacecraft offers a low cost, scalable architecture for a solar sailing demonstration in low Earth orbit. The reel-based, gravity-gradient-stiffened design eliminates the need for external stiffening hardware such as booms, masts, or guy-wires while avoiding classical scaling issues such as Euler buckling. The conformity of the CubeSail spacecraft to the CalPoly CubeSat specifications allows for a highly reduced launch costs and increased launch availability as secondary payload. In doing so, this small-scale demonstration aims at breaking the paradigm of limited funding of poorly characterized solar sailing technology, by increasing the Technology Readiness Level of various subsystems.

The analysis showed that an LQR-based magnetic torque attitude actuation system is capable of detumbling and re-orienting the spacecraft regardless of the initial attitude or orbital position and for the worst expected body rotation rate. The use of a Genetic Algorithm in combination with an attitude control simulator allows for selection of robust Q and R weight matrices that ensure desired performance.

The desired insertion orbit is a sun-synchronous terminator orbit for which the lighting conditions remain constant. The constant lighting conditions eliminate the accordion-like changes in the sail billowing as the spacecraft comes in and out of shadow, reduce cyclic thermal loading on the film, and greatly simplify orbital maneuvering scheduling. In order to minimize the effects of aerodynamic drag, which vary by two orders of magnitude between solar minimum and solar maximum, the desired insertion altitude is above 800 km.

The equations governing the film deployment are highly nonlinear and numerical methods must be employed to obtain a solution. The model includes the mass of the tip satellites, the mass of the film, as well as the effects of gravity gradient, solar radiation pressure, and aerodynamic drag. The deployment rate is controlled with the reel motors and full deployment is achieved in approximately 100 minutes. The spacecraft settles into a stable configuration along the local vertical.

The steady-state equilibrium configuration of the fully deployed film is dependant on the pitch of the tip satellites. In nominal operations, the film is oriented with its edge into the velocity direction and face towards the sun, creating a minimal drag profile, but maximum out-of-plane billow due to solar radiation pressure. The maximum billowing during nominal operations is approximately 18 m for a 260 m-long film. Any configurations with nonzero pitch result in increased aerodynamic drag and a solar radiation pressure force component both in- and out-of-plane. The particular shapes associated with various pitch angles are presented in Chapter 4.

The preliminary analysis showed that an 800 km initial altitude orbit was sufficient to overcome effects of aerodynamic drag and achieve an altitude raising maneuver. Unfortunately this analysis neglected perturbation effects of Earth oblateness, which are much larger than the solar radiation force generated by the $20m^2$ CubeSail spacecraft. As a result, orbital maneuvers generally require a more involved approach by performing a series of pitching and de-pitching maneuvers at each tip satellite. The exact profile for the pitching maneuver depends whether the maneuver is an inclination change, which is most difficult in terms of delta-V budget but is also the simplest to

implement due to constant out-of-orbital-plane solar radiation pressure force, or an altitude maintenance/change maneuver.

Appendix A. DERIVATION OF SRU DYNAMICAL EQUATIONS

The angular momentum of the screw is summed up as follows:

$$H_{\text{lead screw}} = \left(I_{zz,\text{ solid cylinder}} + I_{zz,\text{ thick-wall cylinder}}\right)\cdot\omega_{\text{lead screw}} \triangleq I_{\text{lead screw}}\cdot\omega_{\text{lead screw}}$$
$$\dot{H}_{\text{lead screw}} = I_{\text{lead screw}}\cdot\left(-\alpha_{\text{lead screw}}\right) \qquad [274]$$

where the lead screw acceleration, $\alpha_{\text{lead screw}}$, is assumed constant and the moments of inertia of a solid and thick-wall cylinders were defined previously in Equation 63 based on Figure 48. At this stage of the deployment sequence, the film is not yet exposed to either the residual atmospheric drag nor to the solar radiation pressure. In addition, since the satellite center of mass is assumed to be located at the geometric center, the spacecraft can be assumed free of external torques. The analysis is performed along the single axis ($\hat{X}^{SAT}$) and assumes both the spacecraft and the lead screw rotate around this axis. As a result, it is possible to write:

$$\dot{H}_{sat} = -\dot{H}_{\text{lead screw}} \qquad [275]$$

The torque from the wheel is delivered between t_1 and t_2 when the motor is being accelerated. Assuming the satellite has no angular momentum at time t_1 ($H_{sat}(t_1) = 0$), integration of the above equation yields the angular momentum of the satellite as follows:

$$\dot{H}_{sat} = \frac{dH_{sat}}{dt} = -\dot{H}_{\text{lead screw}}$$
$$\int_{H_{sat}(t_1)}^{H_{sat}(t)} dH_{sat} = \int_{t_1}^{t} -\dot{H}_{\text{lead screw}}\cdot dt \qquad [276]$$
$$H_{sat}(t) = -\dot{H}_{\text{lead screw}}\cdot\left(t - t_1\right) + \cancel{H_{sat}(t_1)}$$

$$H_{sat}(t) = I_{\text{lead screw}}\cdot\alpha_{\text{lead screw}}\cdot\left(t - t_1\right) \quad \forall \quad t_1 \le t \le t_2 \qquad [277]$$

At time t_2, the angular momentum of the satellite is:

$$H_{sat}\left(t_2\right) = I_{\text{lead screw}} \cdot \alpha_{\text{lead screw}} \cdot \left(t_2 - t_1\right) \quad [278]$$

The angular momentum of the satellite is also equal to $I_{sat} \cdot \omega_{sat}$ with $\omega_{sat} = d\theta_{sat} / dt$. Assuming the satellite had zero pitch at time t_1 ($\theta_{sat}\left(t_1\right) = 0$), the satellite will rotate in the same period according to:

$$\begin{aligned} H_{sat}(t) &= -\dot{H}_{\text{lead screw}} \cdot \left(t - t_1\right) + \cancel{H_{sat}\left(t_1\right)} \\ I_{sat}\omega_{sat} &= I_{sat}\frac{d\theta_{sat}}{dt} = -\dot{H}_{\text{lead screw}} \cdot \left(t - t_1\right) \\ \int_{\theta_{sat}(t_1)}^{\theta_{sat}(t)} I_{sat} d\theta_{sat} &= \int_{t_1}^{t} -\dot{H}_{\text{lead screw}} \cdot \left(t - t_1\right) \cdot dt \\ I_{sat}\theta_{sat}(t) &= -\frac{1}{2}\dot{H}_{\text{lead screw}} \cdot \left(t - t_1\right)^2 + \cancel{I_{sat}\theta_{sat}\left(t_1\right)} \end{aligned} \quad [279]$$

$$\theta_{sat}(t) = \frac{1}{2I_{sat}} I_{\text{lead screw}} \cdot \alpha_{\text{lead screw}} \cdot \left(t - t_1\right)^2 \quad \forall \quad t_1 \le t \le t_2 \quad [280]$$

which at time t_2 is equal to:

$$\theta_{sat}\left(t_2\right) = \frac{1}{2I_{sat}} I_{\text{lead screw}} \cdot \alpha_{\text{lead screw}} \cdot \left(t_2 - t_1\right)^2 \quad [281]$$

The acceleration of the motor is taken directly from the manufacturer's data sheet and is equal to $1 \times 10^5 \ rad/s^2$. The maximum angular velocity at the output of the gear box is 24 RPM, which corresponds to motor output (gearbox input) angular velocity of 6288 RPM (262:1 ratio gearbox). At t_1 the motor is stationary and thus the time to accelerate it to the desired angular rate, t_2, is found as follows:

$$\begin{gathered}\alpha_{\text{motor}} = d\omega_{\text{motor}} / dt \\ \int_{t_1}^{t_2} \alpha_{\text{motor}} \cdot dt = \int_{t_1}^{t_2} d\omega_{\text{motor}} \\ \alpha_{\text{motor}} \cdot (t_2 - t_1) = \omega_{\text{motor}}(t_2) - \cancel{\omega_{\text{motor}}(t_1)} \\ t_2 = \frac{\omega_{\text{motor}}(t_2)}{\alpha_{\text{motor}}}\end{gathered} \quad [282]$$

Using the above values, the maximum angular velocity is reached in 0.066 seconds. The acceleration of the worm screw can be scaled by the gear ratio as well:

$$\begin{gathered}\alpha_{\text{lead screw}} = \frac{\Delta\omega_{\text{lead screw}}}{\Delta t} = \frac{\omega_{\text{lead screw}}(t_2) - \cancel{\omega_{\text{lead screw}}(t_1)}}{t_2 - \cancel{t_1}} \\ \alpha_{\text{lead screw}} = \omega_{\text{lead screw}}(t_2) \cdot \frac{1}{t_2} = \frac{\omega_{\text{motor}}(t_2)}{\text{gear ratio}} \cdot \frac{\alpha_{\text{motor}}}{\omega_{\text{motor}}(t_2)} \\ \alpha_{\text{lead screw}} = \frac{\alpha_{\text{motor}}}{\text{gear ratio}}\end{gathered} \quad [283]$$

Between time t_2 and $t_3 = 10 \text{ sec}$, the rotational rate of the lead screw is constant and equal to its value at t_2:

$$\omega_{\text{lead screw}}(t) = \omega_{\text{lead screw}}(t_2) \quad \forall \quad t_2 < t \le t_3 \quad [284]$$

As a result, the angular momentum of the lead screw is constant during this time. Remembering that the lead screw rotates in the negative direction, it is possible to write:

$$\begin{gathered}H_{\text{lead screw}}(t) = -I_{\text{lead screw}} \cdot \omega_{\text{lead screw}}(t) = -I_{\text{lead screw}} \cdot \omega_{\text{lead screw}}(t_2) \quad \forall \quad t_2 < t \le t_3 \\ H_{\text{lead screw}}(t) = H_{\text{lead screw}}(t_2) \quad \forall \quad t_2 < t \le t_3\end{gathered} \quad [285]$$

$$\begin{gathered}H_{sat}(t) = -H_{\text{lead screw}}(t) \\ H_{sat}(t) = I_{\text{lead screw}} \cdot \omega_{\text{lead screw}}(t_2) \quad \forall \quad t_2 < t \le t_3 \\ H_{sat}(t) = I_{\text{lead screw}} \cdot \alpha_{\text{lead screw}} \cdot (t_2 - t_1) \quad \forall \quad t_2 < t \le t_3\end{gathered} \quad [286]$$

Since there are no external torques acting on the satellite for $t_2 < t \le t_3$, the angular momentum must be conserved. It is therefore possible to write:

$$H_{total}\big|_{t_2} = H_{total}\big|_{t_2 \le t < t_3}$$

$$\cancel{H_{\text{lead screw}}(t_2)} + H_{sat}(t_2) = \cancel{H_{\text{lead screw}}(t)} + H_{sat}(t)$$

$$H_{sat}(t_2) = I_{sat}\frac{d\theta_{sat}}{dt}$$

$$\int_{t_2}^{t} H_{sat}(t_2)\,dt = \int_{\theta_{sat}(t_2)}^{\theta_{sat}(t)} I_{sat}\,d\theta_{sat} \qquad [287]$$

$$H_{sat}(t_2)\cdot(t-t_2) + I_{sat}\theta_{sat}(t_2) = I_{sat}\theta_{sat}(t)$$

$$\theta_{sat}(t) = \frac{H_{sat}(t_2)\cdot(t-t_2)}{I_{sat}} + \theta_{sat}(t_2) \quad \forall \quad t_2 < t \le t_3$$

$$\theta_{sat}(t) = \frac{I_{\text{lead screw}}\cdot\alpha_{\text{lead screw}}\cdot(t_2-t_1)\cdot(t-t_2)}{I_{sat}} + \theta_{sat}(t_2) \quad \forall \quad t_2 < t \le t_3 \qquad [288]$$

which at time t_3 is equal to:

$$\theta_{sat}(t_3) = \frac{I_{\text{lead screw}}\cdot\alpha_{\text{lead screw}}\cdot(t_2-t_1)\cdot(t_3-t_2)}{I_{sat}} + \theta_{sat}(t_2) \qquad [289]$$

$$H_{sat}(t_3) = I_{\text{lead screw}}\cdot\alpha_{\text{lead screw}}\cdot(t_2-t_1)$$

At $t = t_3$ the lead screw motor begins to decelerate until it reaches zero rotational velocity at $t = t_4$. The deceleration occurs in 0.0066 seconds during which the equations can be written as follows:

$$H_{sat}(t) = -\dot{H}_{\text{lead screw}}\cdot(t-t_3) + H_{sat}(t_3)$$

$$H_{sat}(t) = -I_{\text{lead screw}}\cdot\alpha_{\text{lead screw}}\cdot(t-t_3) + H_{sat}(t_3) \quad \forall \quad t_3 < t \le t_4 \qquad [290]$$

Similarly to previous derivation, the pitch angle can be computed as follows:

$$H_{sat}(t) = -\dot{H}_{\text{lead screw}} \cdot (t - t_3) + H_{sat}(t_3)$$

$$I_{sat}\omega_{sat} = I_{sat}\frac{d\theta_{sat}}{dt} = -\dot{H}_{\text{lead screw}} \cdot (t - t_3) + H_{sat}(t_3)$$

$$\int_{\theta(t_3)}^{\theta(t)} I_{sat}\, d\theta_{sat} = \int_{t_3}^{t} \left[-\dot{H}_{\text{lead screw}} \cdot (t - t_3) + H_{sat}(t_3) \right] \cdot dt \qquad [291]$$

$$I_{sat}\theta_{sat}(t) = -\frac{1}{2}\dot{H}_{\text{lead screw}} \cdot (t - t_3)^2 + H_{sat}(t_3) \cdot (t - t_3) + I_{sat}\theta_{sat}(t_3)$$

$$\theta_{sat}(t) = -\frac{I_{\text{lead screw}} \cdot \alpha_{\text{lead screw}} \cdot (t - t_3)^2}{2I_{sat}} + \frac{H_{sat}(t_3) \cdot (t - t_3)}{I_{sat}} + \theta_{sat}(t_3) \quad \forall \quad t_3 < t \le t_4$$

Combing the angular momentum and pitch angle equations for $t_1 \le t \le t_4$ results in the following set of equation:

$$H_{sat}(t) = \begin{cases} I_{\text{lead screw}} \cdot \alpha_{\text{lead screw}} \cdot (t - t_1) & \forall \quad t_1 \le t \le t_2 \\ I_{\text{lead screw}} \cdot \omega_{\text{lead screw}}(t_2) & \forall \quad t_2 < t \le t_3 \\ -I_{\text{lead screw}} \cdot \alpha_{\text{lead screw}} \cdot (t - t_3) + H_{sat}(t_3) & \forall \quad t_3 < t \le t_4 \end{cases} \qquad [292]$$

$$\theta_{sat}(t) = \begin{cases} \dfrac{I_{\text{lead screw}} \cdot \alpha_{\text{lead screw}} \cdot (t - t_1)^2}{2I_{sat}} & \forall \quad t_1 \le t \le t_2 \\ \dfrac{I_{\text{lead screw}} \cdot \alpha_{\text{lead screw}} \cdot (t_2 - t_1) \cdot (t - t_2)}{I_{sat}} + \theta_{sat}(t_2) & \forall \quad t_2 < t \le t_3 \\ -\dfrac{I_{\text{lead screw}} \cdot \alpha_{\text{lead screw}} \cdot (t - t_3)^2}{2I_{sat}} + \dfrac{H_{sat}(t_3) \cdot (t - t_3)}{I_{sat}} + \theta_{sat}(t_3) & \forall \quad t_3 < t \le t_4 \end{cases} \qquad [293]$$

Appendix B. SAIL THERMAL CONSIDERATIONS

In order to prevent damage to the sail material that is flying in a sun synchronous terminator orbit and facing the sun, an equilibrium temperature must not exceed design specifications of the base polymer. Accurate analysis includes non-ideal sail effects of reflection, absorption and re-radiation and assumes that the film has no thermal capacity (due to its minimal thickness) resulting in instantaneous temperature changes. Figure 85 (shown previously) demonstrates the overall thermal balance of the sail material. The power emitted from a unit area of the sail at temperature T is $\varepsilon\tilde{\sigma}T^4$, where $\tilde{\sigma}$ is the Stefan-Boltzmann constant and ε is the surface emissivity. The sail equilibrium temperature as a function of sail orientation, the sail optical properties and heliocentric distance can be calculated from the following equation[8]:

$$T = \left[\frac{1-\tilde{r}}{\varepsilon_f + \varepsilon_b} \frac{W_E}{\tilde{\sigma}} \left(\frac{R_E}{r} \right)^2 \cos\alpha \right]^{1/4} \qquad [294]$$

where $\tilde{r}$ is the reflection coefficient, ε_f and ε_b are the front and back emissivities respectively, W_E is the solar energy flux measured at the Earth's distance from the Sun (1369 $Js^{-1}m^{-2}$), R_E is the Sun-Earth distance, r is the distance from the Sun, α is the solar pitch angle (shown previously in Figure 84).

A typical reflection coefficient of aluminum is between 0.85 and 0.9[8] with the lower value used in the proceeding calculations. The back side of the film is coated with a high emittance paint (typically chromium, $\varepsilon_b = 0.55$) to keep the equilibrium sail temperature below physical melting point of the base polymer.[102] Figure 121 demonstrates a series of equilibrium temperature plots for several back emissivities as

a function of distance from the Sun. The following results are for a case with front emissivity of 0.05 and direct sun incidence ($\alpha = 0^\circ$).

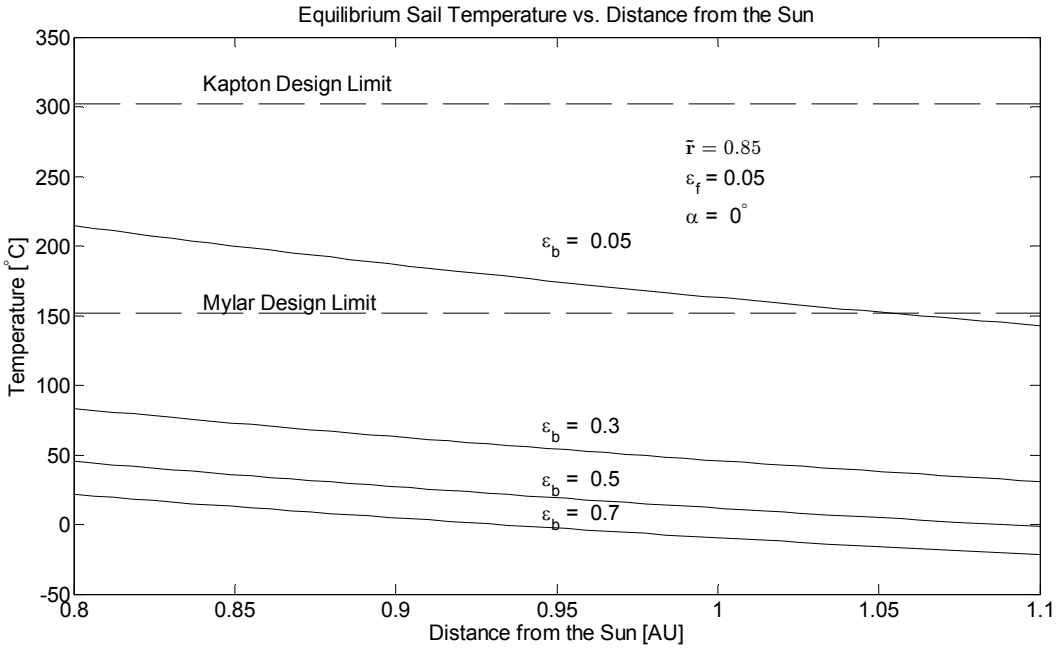

Figure 121. Equilibrium sail temperature as a function of distance from the Sun and back emissivity. ($\tilde{r} = 0.85$, $\varepsilon_f = 0.05$, $\alpha = 0^\circ$).

These above results demonstrate the necessity of an emissive coating in order to prevent damage to the base polymer.

REFERENCES

[1] Tsiolkovsky, K.E., *Extension of Man into Outer Space*, 1921.

[2] Tsiolkovsky, K.E., *Symposium Jet Propulsion*, No. 2, United Scientific and Technical Presses, 1936.

[3] Tsander, K., *From a Scientific Heritage*, NASA Technical Translation *TTF-541*, 1967.

[4] Wiley C. [pseudonym Sanders R.], "Clipper Ships of Space," *Astounding Science Fiction*, pp. 135, May 1951.

[5] Friedman, L., *Star Sailing: Solar Sails and Interstellar Travel*, Wiley Science Publications, New York, 1988.

[6] Garwin, R.L., "Solar Sailing—A Practical Method of Propulsion Within the Solar System," *Jet Propulsion*, 28, 188-190, 1958.

[7] Villers, P., "On the application of solar radiation momentum transfer to space vehicle propulsion," Thesis (M.S.), Massachusetts Institute of Technology Dept. of Mechanical Engineering, 1960.

[8] McInnes, C. R., *Solar Sailing: Technology, Dynamics, and Mission Applications*, Springer-Praxis Publishing, Chichester, UK, 1999.

[9] Young, R., "Enhanced Heliostorm Warning Mission: Enhancements Based on New Technology," 48th AIAA/ASME/ASCE/AHS/ASC Structures, Structural Dynamics, and Materials Conference 23 - 26 April 2007, Honolulu, Hawaii. AIAA 2007-2249.

[10] Liewer, P.C. et. al., "Solar Polar Imager: Observing Solar Activity from a New Perspective," Progress in Astronautics and Aeronautics. Vol. 224, pp. 1-40. 2008.

[11] Mewaldt, R.A. and Liewer P.C., "An *interstellar probe mission* to the boundaries of the heliosphere and nearby *interstellar* space," AIAA Space 2000 Conference and Exposition, Long Beach, CA; 19-21 Sept. 2000.

[12] Melnikov, Vitali M., and Vladimir A. Koshelev. *Large Space Structures Formed by Centrifugal Forces*. Amsterdam: Gordon and Breach Science Publishers, 1998.

[13] Planetary Society, "Projects: LightSail—Solar Sailing LightSail-1," http://www.planetary.org/programs/projects/solar_sailing/lightsail1.html

[14] NASA, Small Satellite Missions: NanoSail-D, http://www.nasa.gov/mission_pages/smallsats/nanosaild.html.

[15] NASA Marshall Space Flight Center, "Release: 09-102, NASA and Contractor Team Develop One Fast Satellite," http://www.nasa.gov/centers/marshall/news/news/releases/2009/09-102.html.

[16] JAXA, IKAROS Project, http://www.jspec.jaxa.jp/e/activity/ikaros.html.

[17] Solar Sail Wiki, http://wiki.solarsails.info/images/2/29/Square.jpg.

[18] Wright, J.L., *Space Sailing*, Gordon & Breach Science Publishers, Philadelphia, 1992.

[19] Solar Sail Wiki, http://wiki.solarsails.info/images/6/60/Disk2.jpg

[20] Xu, Yan. "Fold methods and deployment analysis of deployable membrane structure." Gongcheng Lixue, Vol. 25, No. 5, pp. 176-181, 2008.

[21] U3P, "The MFPP folding of the sail," http://www.u3p.net/.

[22] Burton, R. et al., "UltraSail – Ultra-Lightweight Solar Sail Concept," 41st AIAA/ASME/SAE/ASEE Joint Propulsion Conference & Exhibit; Tucson, AZ; USA; 10-13 July 2005. pp. 1-12. 2005.

[23] Hargens-Rysanek, J. et al., "Orbital Precession via Cyclic Pitch for the UltraSail System," 17th Annual Space Flight Mechanics Meeting; Sedona, AZ; USA; 28 Jan.-1 Feb. 2007.

[24] Botter, T. et al., "Structural Dynamics Of A Spin-Stabilized, Mast-Free Solar Sail Design," dvances in the Astronautical Sciences. Vol. 124, no. II, pp. 1935-1954. 2006.

[25] Hargens-Rysanek, J., *The Dynamics and Control of the UltraSail System*, Ph.D. Thesis, UIUC Dept. of Aerospace Engineering, 2006.

[26] Ertmer, K., *Design and Operation of a Thin-Film Vacuum Deployment Experiment for UltraSail Concept Validation* , MS Thesis, UIUC Dept. of Aerospace Engineering, May, 2006.

[27] CubeSat Design Specifications Revision 12, http://cubesat.org/images/developers/cds_rev12.pdf.

[28] CubeSat P-POD Mark II Rendering, http://cubesat.org/index.php/media/pictures/55-p-pod-mk-ii-renderings.

[29] Warner, J., *Attitude Determination and Control of Nano-Satellites*, M.S. Thesis, UIUC Dept. of Aerospace Engineering, 2009.

[30] Wertz, J., *Spacecraft Attitude Determination and Control*, Dordrecht Reidel, 1978.

[31] Shuster, M.D. and Oh, S.D., "Three-Axis Attitude Determination from Vector Observations," Journal of Guidance and Control, vol. 4, No. 1, pp. 70-77, 1981.

[32] Pukniel, A., et al., "A Preliminary Study of the Dynamics and Control of the CubeSail Spacecraft," AAS 09-417, Presented at the AAS/AIAA Conference, Pittsburgh, PA, August 9-13, 2009.

[33] International Geomagnetic Reference Field, International Association of Geomagnetism and Aeronomy (IAGA), http://www.ngdc.noaa.gov/IAGA/vmod/igrf.html.

[34] W.H. Campbell, *Introduction to Geomagnetic Fields,* New York: Cambridge, 1997

[35] C. Roithmayr, "Contributions of Spherical Harmonics to Magnetic and Gravitational Fields," NASA Johnson Space Center, Tech. Rep. EG2-96-02, Jan.23, 1996.

[36] Bryson and Ho, *Applied Optimal Control,* Hemisphere Publishing Corporation, 1975.

[37] Brogan, W. L., *Modern Control Theory*. Englewood Cliffs: Prentice Hall, 1991.

[38] Psiaki, M., "Magnetic Torquer Attitude Control via Asymptotic Periodic Linear Quadratic Regulation," *Journal of Guidance, Control, and Dynamics*, vol. 24, pp. 386-394, March-April 2001.

[39] Hughes, P.C., *Spacecraft Attitude Dynamics*, Wiley, New York, 1986.

[40] Pukniel, A., "Attitude Determination and Three-Axis Control System for Nanosatellites with Magnetic Torque Actuation," M.S. Thesis, Dept. of Aerospace Engineering at the University of Illinois at Urbana-Champaign, 2006.

[41] Naval Research Lab NRLMSISE-00, http://www.nrl.navy.mil/content.php?P=03REVIEW105.

[42] MathWorks Matlab Documentation, http://www.mathworks.com/access/helpdesk/help/toolbox/aerotbx/ug/atmosnrlmsise00.html.

[43] Goldberg, D., *Genetic Algorithms in Search, Optimization and Machine Learning,* Kluwer Academic Publishers, Boston, MA, 1989.

[44] Mathworks Matlab Documentation, http://www.mathworks.com/access/helpdesk/help/toolbox/gads/ga.html

[45] Pitel, G., "Performance Analysis of Lithium Ion Batteries," M.S. Thesis, Department of Electrical Engineering at University of Illinois at Urbana-Champaign, 2005.

[46] Linear Technology LTC1779 Data Sheet, http://cds.linear.com/docs/Datasheet/1779f.pdf.

[47] Matlab Central File Exchange, Grabit.m, http://www.mathworks.com/matlabcentral/fileexchange/7173-grabit.

[48] Rose Batteries Specification Sheet for LI-2S1P-2200 Battery, http://www.rosebatteries.com/pdfs/LI-2S1P-2200.PDF

[49] Greenwood, D.T., *Principals of Dynamics*, Prentice Hall, 1988.

[50] Lakso, J. J. and Coverstone, V. L., "Optimal Tether Deployment/Retrieval Trajectories Using Direct Collocation," AIAA/AAS Astrodynamics Specialist Conference; 14-17 August 2000 Denver, CO, AIAA 2000-4349.

[51] Bainum, P. M., Kumar, V. K., "Optimal Control of the Shuttle-Tethered-Subsatellite System," Acta Astronautica, Vol. 7, 1980, pp. 1333-1348.

[52] Stuiver, W., "Dynamics and Configuration Control of Two-Body Satellite System," *J. Spacecraft Rockets,* Vol. 11 No. 8, pp. 545-546 (Synoptic); also full paper available as—*A method for configuration control of Earth co-orbiting satellites. Presented at the 5th World Congress of the IFAC. Paris, June, 1972.*

[53] MathWorks Matlab Documentation, http://www.mathworks.com/access/helpdesk/help/techdoc/index.html?/access/helpdesk/help/techdoc/math/f1-713877.html&http://www.mathworks.com/cgi-bin/texis/webinator/search/

[54] Howard, Ronald and Abbas, Ali, "*The Foundations of Decision Analysis," (*Manuscript in Progress).

[55] Straker, Dave, "A Toolbook for Quality Improvement and Problem Solving,' http://syque.com/quality_tools/toolbook/Force/when.htm

[56] Hecht, H. and Hecht, M., "Reliability Prediction for Spacecraft," RADC Report RADC-TR-85-229. Rome Air Development Center, NY: Department of Defense, 1985.

[57] Chobotov, V., "Orbital Mechanics, 3rd Edition," AIAA Education Series.

[58] Edelbaum, T. N., "Optimum Low-Thrust Transfer between Circular and Elliptic Orbits," Proc. Fourth Nat. Cong. Appl. Mech., (ASME, N. Y.) 1962, pp. 137–141.

[59] Faulhaber 1524-012SR DC Micromotor Data Sheet, http://www.faulhaber.com/uploadpk/EN_1524SR_DFF.pdf.

[60] Faulhaber 15/5 262:1 gearbox Data Sheethttp://www.faulhaber.com/uploadpk/EN_155_165_MIN.pdf.

[61] Wiggins, L.E., "Relative Magnitudes of the Space-Environment Torques on a Satellite," AIAA, Vol. 2, No. 4, pp. 770-771, April 1964.

[62] NASA Space Vehicle Design Criteria Guidance and Control, "Spacecraft Aerodynamic Torques," Report: NASA-SP-8058, Jan 1971.

[63] Gaposchkin, E.M., "Calculation of Satellite Drag Coefficients," Technical Report 998, Lincoln Laboratory, MIT, Lexington, Massachusetts, 18 July, 1994.

[64] Ravindran, R. and Hughes, P.C., "Optimal Aerodynamic Attitude Stabilization of Near-Earth Satellites," *Journal of Spacecraft and Rockets*, Vol. 9, No. 7, pp 499-506, July 1972.

[65] Gargasz, M.L. and Titus, N.A., "Spacecraft Attitude Control Using Aerodynamic Torques," *17th AAS/AIAA Space Flight Mechanics Meeting*, AAS 07-178, Sedona, AZ, Feb. 2007.

[66] Moe, K. and Moe, M.M., "Gas–surface interactions and satellite drag coefficients," *Planetary and Space Science*, 53, pp 793–801, 2005.

[67] Sentman, L.H., "Free Molecule Flow Theory and Its Application to the Determination of Aerodynamic Forces," Lockheed Missile and Space Co., LMSC-448514, AD 265-409 (available from National Technical Information Service, Springfield, VA), 1961.

[68] Sentman, L.H., "Comparison of the exact and approximate methods for predicting free molecule aerodynamic coefficients," ARS J. 31, 1576–1579.

[69] NRLMSISE-00 Model 2001, Community Coordinated Modeling Center, Goddard Space Flight Center, http://ccmc.gsfc.nasa.gov/modelweb/atmos/nrlmsise00.html.

[70] MSISE Model 1990, Community Coordinated Modeling Center, Goddard Space Flight Center, http://ccmc.gsfc.nasa.gov/modelweb/atmos/msise.html.

[71] A. E. Hedin, Extension of the MSIS Thermospheric Model into the Middle and Lower Atmosphere, J. Geophys. Res. 96, 1159, 1991.

[72] J.M. Picone, A.E. Hedin, D.P. Drob, and A.C. Aikin, NRLMSISE-00 empirical model of the atmosphere: Statistical comparisons and scientific issues, J. Geophys. Res., 107(A12), 1468, doi:10.1029/2002JA009430, 2002.

[73] K. Labitzke, J. J. Barnett, and B. Edwards (eds.), Handbook MAP 16, SCOSTEP, University of Illinois, Urbana, 1985.

[74] COSPAR International Reference Atmosphere: 1986 (0 km to 120 km), http://ccmc.gsfc.nasa.gov/modelweb/atmos/cospar1.html

[75] MSIS Model 1986, Community Coordinated Modeling Center, Goddard Space Flight Center, http://ccmc.gsfc.nasa.gov/modelweb/atmos/msis.html.

[76] Seidelmann, K.P., "Explanatory Supplement to the Astronomical Almanac," University Science Books, 1992.

[77] National Geophysical Data Center, National Oceanic and Atmospheric Administration, Solar Flux Data Repository, ftp://ftp.ngdc.noaa.gov/STP/SOLAR_DATA/SOLAR_RADIO/FLUX/

[78] National Geophysical Data Center, "Geomagnetic kp and ap Indices," http://www.ngdc.noaa.gov/stp/GEOMAG/kp_ap.html.

[79] National Geophysical Data Center, National Oceanic and Atmospheric Administration, Magnetic Field Data Repository, ftp://ftp.ngdc.noaa.gov/STP/GEOMAGNETIC_DATA/INDICES/KP_AP/.

[80] National Oceanic and Atmospheric Administration, Space Weather Prediction Center, Geomagnetic and Solar Indices, http://www.swpc.noaa.gov/alerts/solar_indices.html.

[81] Rowe, W.M., "Sail Film Materials and Supporting Structures for a Solar Sail—a Preliminary Design, Vol. IV," Jet Propulsion Laboratory, Pasadena, California, October, 1978.

[82] Wie, B., "Solar Sail Attitude Control and Dynamics, Part 1," Journal of Guidance, Control, and Dynamics, Vol. 27, No.4, July-August 2004.

[83] Vallado, D., *Fundamentals of Astrodynamics and Application,* Microcosm Press, 2001.

[84] NASA EGM96 Model, http://cddis.nasa.gov/926/egm96/egm96.html.

[85] The Defense Mapping Agency Technical Report, "Geodesy for the Layman," DMA TR 80-003, https://www1.nga.mil/ProductsServices/GeodesyGeophysics/Related%20Documents/Geo4lay.pdf.

[86] Jursa, A.S., "Handbook of Geogphysics and the Space Environment," Air Force Geophysics Laboratory, 1985.

[87] Lorenzini, E.C. et al., " Low Altitude Tethered Mars Probe," Acta Astronautica, Vol. 21, No. 1, pp. 1-12, 1990.

[88] Misra, A.K. et al., " Nonlinear Dynamics of Two-Body Tethered Satellite Systems: Constant Length Case, " Journal of Astronautical Sciences , Vol. 49, No. 2, pp. 219-236, April-June, 2001.

[89] Nixon, Melina, " Nonlinear Dynamics and Chaos of Tethered Satellite Systems," Master's Thesis, Department of Mechanical Engineering of the McGill University, Montreal, Canada, 1996.

[90] Misra, A.K., " Dynamics and Control of Tethered Satellite Systems, " Acta Astronautica 63, pg. 1169-1177, 2008.

[91] Pasca, M. and Lorenzini, E.C., "Collection of Martian Atmospheric Dust with a Low Altitude Tethered Probe," Advances in the Astronautical Sciences, Vol. 75, pp. 1124-1139, 1991.

[92] Pasca, M. and Lorenzini, E.C., "Optimization of a Low Altitude Tethered Probe for Martian Atmospheric Dust Collection," Journal of the Astronautical Sciences, Vol. 44, No. 2, pp. 191-205, April-June, 1996.

[93] Pasca, M. and Lorenzini, E.C., "Two Analytical Models for the Analysis of a Tethered Satellite System in Atmosphere," Meccanica, Vol. 32, pp. 263-277, 1997.

[94] Modi, V.J. et al., "On the Control of the Space Shuttle Based Tethered Systems," Acta Atronautica, Vol. 9, No.6-7, pp. 437-443, 1992.

[95] Baker, W. P. et al., "Thethered Subsatellite Study," NASA Marshall Space Flight Center Technical Memorandum, TMX-73314, March 1976.

[96] Prussing, J. and Conway, B., *Orbital Mechanics*, Oxford University Press, 1993.
[97] Wertz, J.R. and Larson W.J., *Space Mission Analysis and Design Third Edition*, Space Technology Library, 1999.

[98] Knocke, P.C. et al., "Earth Radiation Pressure Effects on Satellites," Proceedings of the AIAA/AAS Astrodynamics Conference, Washington D.C. pp. 577-586, 1988.

[99] Drolshagen G. et. al, "Optical survey of micrometeoroid and space debris impact features on EURECA," Planetary and Space Science, Vol. 44, No. 4, pp. 317-340, 1996.

[100] European Space Agency, "Meteoroid and Space Debris Terrestrial Environment Reference Model," http://www.master-2005.net/index.html.

[101] NASA Johnson Spaceflight Center Orbital Debris Program Office, http://orbitaldebris.jsc.nasa.gov/model/modeling.html.

[102] Rowe, W.M., "Sail Film Materials and Supporting Structures for a Solar Sail—a Preliminary Design, Vol. IV," October, 1978, Jet Propulsion Laboratory, Pasadena, California.